Open Research Online

The Open University's repository of research publications
and other research outputs

Synthesis and characterisation of metal oxides and fluorinated perovskite-related oxides

Thesis

How to cite:

Ren, Xiaolin (2005). Synthesis and characterisation of metal oxides and fluorinated perovskite-related oxides. PhD thesis The Open University.

For guidance on citations see FAQs.

© 2005 The Author

Version: Version of Record

Copyright and Moral Rights for the articles on this site are retained by the individual authors and/or other copyright owners. For more information on Open Research Online's data policy on reuse of materials please consult the policies page.

oro.open.ac.uk

Unrestricted

Synthesis and Characterisation of Metal Oxides and Fluorinated Perovskite-Related Oxides

Submitted by

Xiaolin Ren

(MSc)

as a Thesis for the Degree of
Doctor of Philosophy
In The Open University

February 2005

I certify that all material in this thesis which is not my own work has been identified and that no material has been previously submitted and approved for the award of a Degree by this or any other University.

AUTHOR No: U3368978
Submission date 15 February 2005
Award date: 8 April 2005

Abstract

Perovskite-related materials of composition $LaFe_{1-x}Co_xO_3$ prepared by conventional calcination methods and mechanical milling are shown by temperature programmed reduction to be more susceptible to reduction in a flowing mixture of hydrogen and nitrogen by the incorporation of cobalt. X-ray powder diffraction and Mössbauer spectroscopy show that in iron-rich systems the limited reduction of iron and cobalt leads to the segregation of discrete metallic phases without destruction of the perovskite structure. In cobalt-rich systems, the reduction of Co^{3+} to Co^{o} precedes complete reduction of Fe^{3+} and the segregation of alloy and metal phases is accompanied by destruction of the perovskite structure. Phases made by milling techniques were of smaller particle size and are more susceptible to hydrogen reduction than their counterparts made by conventional techniques. Materials of the type $La_{0.5}Sr_{0.5}MO_3$ (M= Fe, Co) made by calcination methods are more susceptible to reduction when the transition metal M is cobalt as compared to iron.

Perovskite-related oxides of composition $La_{1-x}Sr_xFe_{1-y}Co_yO_3$ have been fluorinated by reaction with poly(vinylidene fluoride). The materials have been characterised by X-ray powder diffraction and Mössbauer spectroscopy. Fluorination induces a reduction in the oxidation state of iron from Fe^{4+} to Fe^{3+}. The fluorinated materials were magnetically ordered at 298 K.

Compounds of the type $SrFe_{1-x}Sn_xO_3$ were found to contain Fe^{5+} and Fe^{3+}. Fluorination resulted in reduction of the transition metal to Fe^{3+} and, in iron-rich systems, magnetic order. The compound Ba_2SnO_4 which adopts the K_2NiF_4-type structure has also been

fluorinated by reaction with zinc fluoride. X-ray powder diffraction shows an enlargement of the unit cell of the fluorinated phase along the *c*-axis.

Small particle iron- and vanadium- antimonate have been prepared by mechanical milling methods. The phases have been examined by Mössbauer spectroscopy and can be formulated $M^{3+}Sb^{5+}O_4$ (M = Fe, V). Thermal analysis suggests that the vanadium animonate formed by milling V_2O_5 and Sb_2O_3 in an inert atmosphere may be oxygen deficient. X-ray powder diffraction shows that milling also induces the phase transformation of the cubic senarmontite Sb_2O_3 form to the orthorhombic valentinite Sb_2O_3 form and of α-Sb_2O_4 to β-Sb_2O_4.

Acknowledgements

I would like to thank my supervisors, Professor Frank J Berry and Dr Michael Mortimer for their continual guidance and encouragement throughout my research.

Thanks to The Open University for financial support.

Thanks to Dr J. F. Marco of Instituto de Química-Física 'Rocasolano', Consejo Superior de Investigaciones Científicas, in Madrid for recording low temperature ^{57}Fe Mössbauer spectra reported in Chapter 4 and for initially showing me how to compute the XANES and EXAFS data.

Thanks to Dr Michael F. Thomas for providing access to facilities in The University of Liverpool to record ^{119}Sn Mössbauer spectrum and low temperature ^{57}Fe Mössbauer spectra reported in Chapter 5 as well as ^{121}Sb Mössbauer spectra recorded in Chapter 6.

Also thanks to Dr Peter Slater of The University of Surrey for instruction on the fluorination of oxides and for discussions on the structural characterisation of these materials.

I am grateful to Dr D. C. Apperley, EPSRC solid-state NMR Service, Department of Chemistry, University of Durham for recording the ^{19}F MAS NMR spectra.

Thanks to my wife and daughter for emotional support as well as all my relatives and friends in China for their wishes.

CONTENTS

Chapter 1

INTRODUCTION

Chapter 1

INTRODUCTION

1.1 AIMS

The aims of the work reported in this thesis are to:

1. Prepare by conventional and milling methods perovskite-related phases of the type $La_{1-x}Sr_xFe_{1-y}Co_yO_3$ and examine their reduction properties,
2. Prepare by solid state reactions oxide fluorides with perovskite-related structures and examine some structural and properties,
3. Prepare by milling techniques rutile-related phase of the type $MSbO_4$ (M= V, Fe).

1.2 PEROVSKITES

1.2.1 Structure of Perovskite $CaTiO_3$

Perovskites adopt the composition ABO_3, for example $CaTiO_3$. The structure is shown in Figure 1.1.

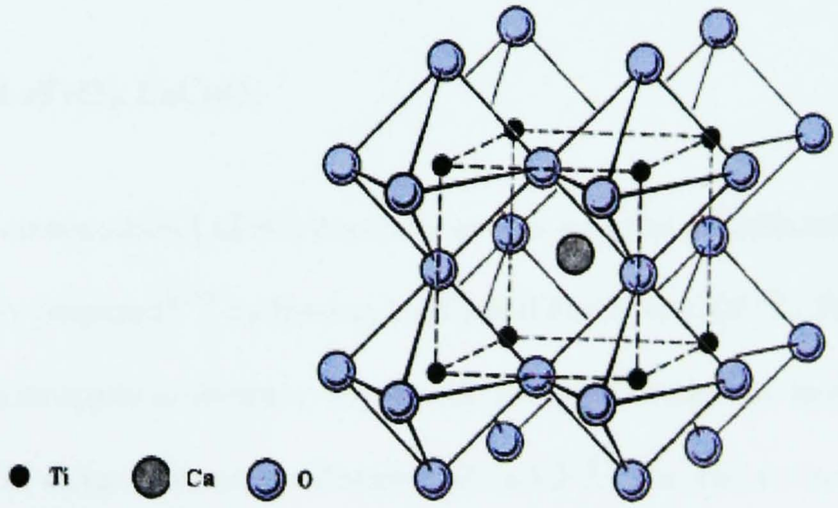

Figure 1.1 Structure of $CaTiO_3$

Titanium atoms occupy the corners of the unit cell, a calcium atom is at its centre and the oxygen atoms lie at the mid-points of its edges. Each calcium is 12- and each titanium 6-coordinated by oxygen neighbours whilst each oxygen atom is linked to four calcium and two titanium atoms. The unit cell is cubic.

1.2.2 Rare Earth Orthoferrites

Perovskite-related rare earth orthoferrites have been investigated in the past because of their potential for use as logic-or memory-components or as laser and light modulators in optical materials [1, 2]. The solids are also catalytically active for hydrocarbon oxidation and combustion [3] and can be used in sensors [4-6] and solid electrolytes [7-9].The materials, which contain only trivalent metal ions in the structure, are amenable systems for isovalent substitution and systems of the type $LaFe_{1-x}Co_xO_3$ have attracted interest in recent years [10-12] because of their potential for electroceramic and catalytic oxidation applications. Applications such as these require operation under reducing conditions but the nature of the reduced phases in these systems is a matter of sparse investigation (see 1.2.6).

1.2.2.1 Structure of $LaFeO_3$, $LaCoO_3$

Lanthanum ferrite of composition $LaFeO_3$ normally occurs with the orthorhombic structure and is usually prepared[13,14] by heating La_2O_3 and Fe_2O_3 at 1200 °C. The orthorhombic $LaFeO_3$ structure is shown in Figure 1.2. In this structure, the lanthanum ion is surrounded by 12 oxygen atoms at a distance of *ca.*3.5 Å. The iron cations are surrounded by 6 oxygen atoms at *ca.*2.2 Å. The Fe-O octahedra are slightly tilted as compared with the situation in the cubic perovskite ABO_3, such as a $CaTiO_3$.

It is also known that that $LaFeO_3$ occurs in a cubic form [15] as shown in Figure 1.3. In the ideal cubic $LaFeO_3$ perovskite structure the larger lanthanum cation is surrounded by twelve equidistant oxygen atoms at *ca.*2.8 Å, and the smaller iron atom is at the centre of an undistorted oxygen octahedron at *ca.*2.2 Å.

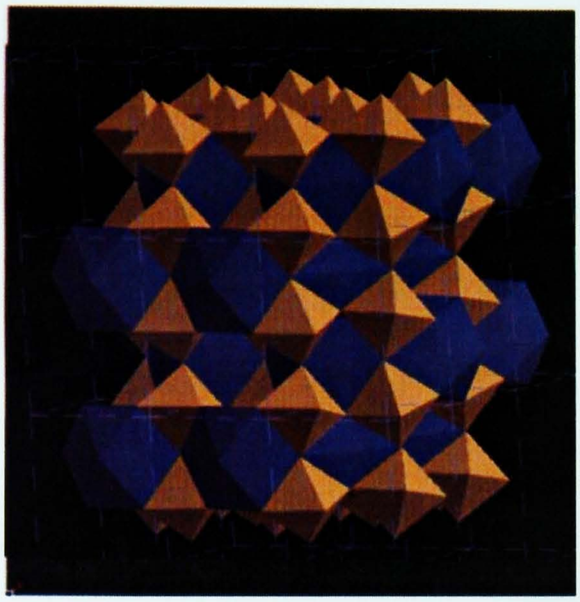

Figure 1.2 Orthorhombic structure of $LaFeO_3$ **Figure 1.3 Cubic structure of $LaFeO_3$**

(iron and lanthanum are located with the orange and blue units respectively.)

$LaCoO_3$ normally occurs with the hexagonal structure[16] and is usually prepared by heating La_2O_3 and CoO at 1000 °C. The hexagonal $LaCoO_3$ structure is

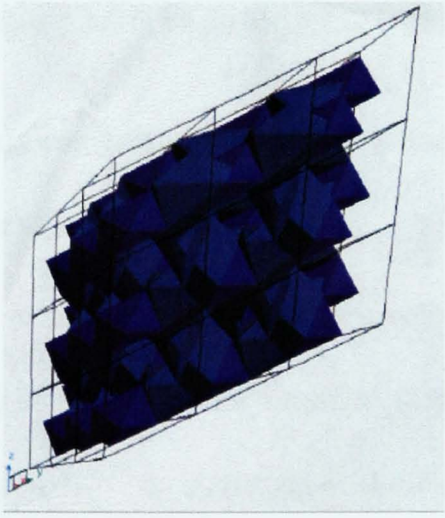

Figure 1.4 Hexagonal structure of $LaCoO_3$

(cobalt and lanthanum are located with the deep blue and blue units respectively.)

shown in Figure 1.4. In this structure, the lanthanum ions are surrounded by 12 oxygen atoms at *ca.*2.9 Å. Each cobalt ion is surrounded by 6 oxygen atoms at *ca.*2.0 Å. $LaCoO_3$ also occurs with a cubic structure above 800K[17].

1.2.3 Structure of $SrFeO_3$

The rare earth element in the rare earth orthoferrites can be replaced by an alkaline earth metal such as strontium to give compounds of the type $SrFeO_3$ in which iron is present as Fe^{4+}. The cubic structure of $SrFeO_3$[18] is shown in Figure 1.5. Each iron atom is surrounded by six oxygen atoms at 1.93 Å and each strontium atom surrounded by twelve oxygen atoms at 2.72 Å.

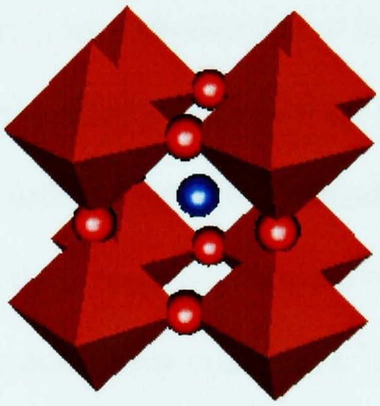

Figure 1.5 The cubic structure of $SrFeO_3$

Pure $SrFeO_3$ is difficult to prepare, and even preparations under oxygen can lead to some oxygen deficiency such that the Fe^{4+} oxidation state is observed with some Fe^{3+}.[19,20] Initial investigations[5,19] of materials of the type $SrFeO_{3-y}$ by Mössbauer spectroscopy showed the oxidation state of iron to vary with composition of the perovskite phase when $y < 0.25$. The material was cubic for $y < 0.12$ and tetragonal for $0.15 < y < 0.25$. Subsequently structural studies[21-24] have determined crystallographic features of this system and tentative structural models have been proposed.

$SrFeO_3$[25] is a metallic conductor with a Néel temperature of 134K. The absence of Jahn-Teller distortion in this high spin $3d^4$ state was explained by the high electrical conductivity where the e_g iron orbitals are broadened into an electronic conduction band.

1.2.4 $La_{1-x}Sr_xFeO_3$

The perovskite series $La_{1-x}Sr_xFeO_{3-\delta}$ ($0 \leq x \leq 1$) was first studied by Waugh[26] who observed complex phase changes from orthorhombic at low x through rhombohedral to cubic as the stoichiometry approached $SrFeO_3$ ($\delta = 0$). Since the distortions were very small, no further structural information was obtained by Waugh although the complex magnetic properties of these materials were subsequently investigated[27]. Preliminary Mössbauer measurements were undertaken[28]; at high values of x, characteristic Fe^{4+} lines were observed with an isomer shift relative to that of ^{57}Co in stainless steel of 0.1 to 0.2 mm sec^{-1}. Lower values of x, however, gave broad and varying linewidths which were attributed to an intermediate Fe^{3+}/Fe^{4+} valence state.

An extensive range of compounds in the $La_{1-x}Sr_xFeO_{3-\delta}$ ($0 \leq x \leq 1$, $0 \leq \delta \leq 0.5$) system was recently reported.[14] When $\delta \approx 0$ the system is composed of three crystallographically different regions: orthorhombic for $0 \leq x \leq 0.2$, rhombohedral for $0.4 \leq x \leq 0.7$, and cubic for $0.8 \leq x \leq 1.0$. Products were characterized by thermogravimetric analysis and Mössbauer spectroscopy yielding information on oxygen stoichiometry and iron oxidation state. At 4.2K, the Mössbauer spectra showed the coexistence of Fe^{3+} and Fe^{5+} in the orthorhombic and rhombohedral, and

Fe^{4+} and Fe^{3+} in the cubic region. High resolution powder neutron diffraction data were collected on samples annealed under high-pressure oxygen, and full structure refinements were carried out using the Rietveld method. Accurate bond length data obtained for all phases showed that the iron coordination geometry becomes more regular with increasing Sr, and hence Fe^{4+}, content. A phase diagram for the full range of lanthanum/strontium and oxygen stoichiometry was proposed.

1.2.5 K_2NiF_4–Type Structure

The K_2NiF_4–type structure is illustrated in Figure 1.6[29]. Each nickel atom is surrounded by six fluorine atoms at *ca.* 2.00 Å. Each potassium atom is surrounded by nine fluorine atoms, which involve one fluorine atom at 2.63 Å, four fluorine atoms at 2.77 Å and four other fluorine atoms at 2.84 Å.

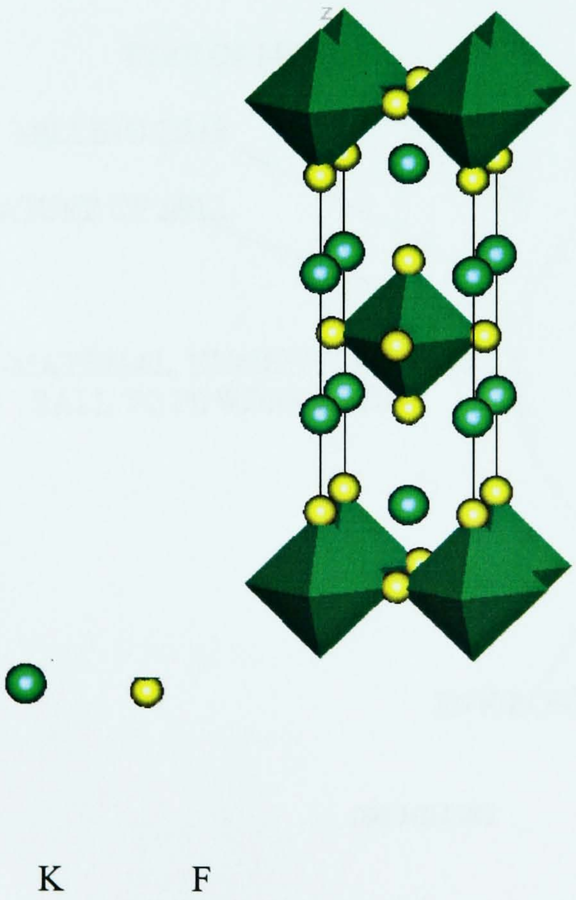

Figure 1.6 The Structure of K_2NiF_4

1.2.6 Synthesis of Perovskite-Related Structures

Perovskite-related oxides have frequently been prepared by conventional solid state reactions between component oxides at elevated temperatures. For example, orthorhombic $LaFeO_3$ can be made by heating La_2O_3 and Fe_2O_3 at 1200 °C.[13] Precipitation[30] and sol-gel[30] methods have also been used. More recently, mechanical milling techniques have been applied to the preparation of perovskite-related phases. For example, *ca.* 25 nm $CaTiO_3$ was made by milling CaO and TiO_2.[31]

1.2.7 Milling

The fundamental process in mechanical alloying has been described[32] as ''the repeated welding, fracturing and rewelding of a mixture of powder particles''. The milling conditions are generally considered[33-36] to have a strong influence on the

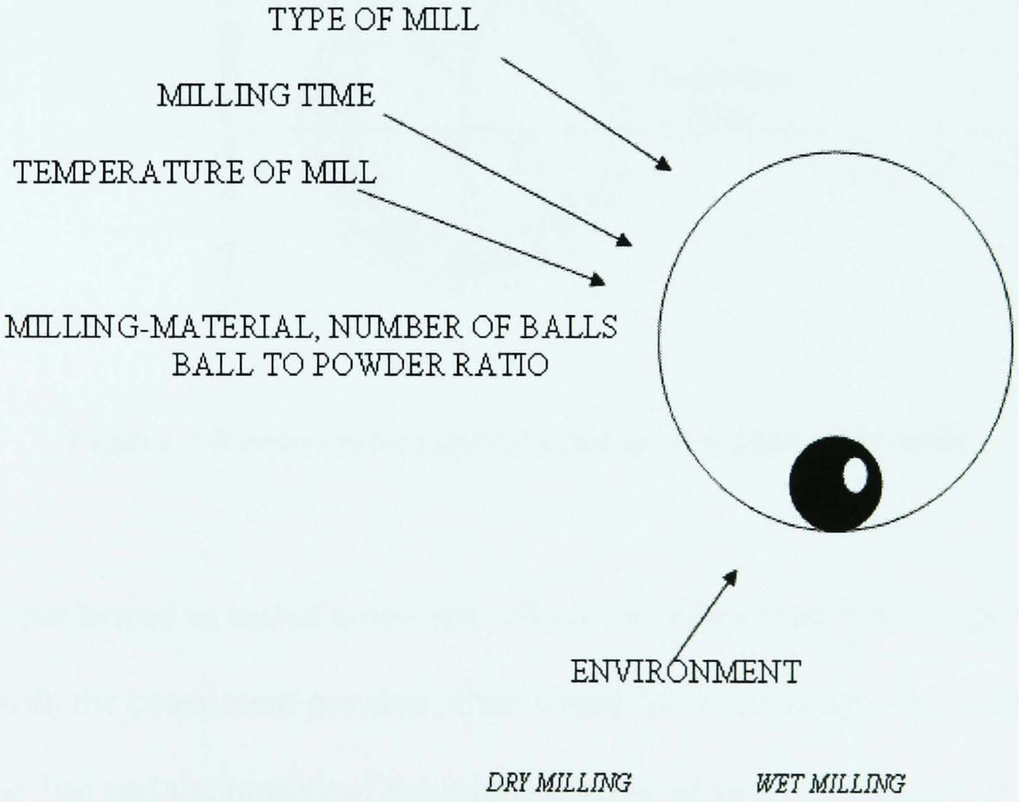

Figure 1.7 Factors to be considered in a ball milling experiment

properties of the product such as the particle size distribution and the final stoichiometry. A summary of the main factors which should be considered in carrying out ball milling experiments is presented schematically in Figure 1.7.

The first comprehensive analysis of the different types of mills which can be used in mechanically alloying was presented[34] in 1990. The majority of the mills used for experimental research and for the production of small batches of materials are variants of the ball mill. The main types of mill currently used in the field of mechanical alloying include attritors, vibratory mills, planetary (vertical) mills and rotary (horizontal) mills.

Some of the work reported in this thesis was performed in a planetary mill (see Figure 1.8).

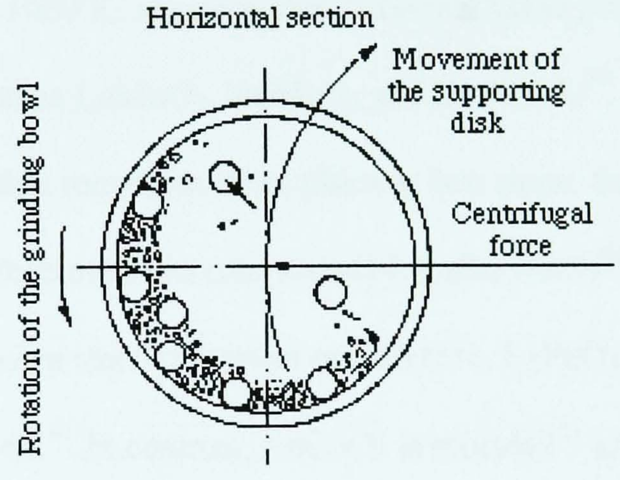

Figure 1.8 Schematic representation of a planetary mill.

Milling is performed in sealed bowls into which the appropriate ball charge is placed together with the constituent powders. Centrifugal forces caused by the rotation of the supporting disc and the turning of the grinding bowl act on the medium and the grinding container. Because the turning directions of the supporting disc and the bowl are opposed, the centrifugal forces are alternately synchronised and opposed. Thus the grinding balls and the charge alternately roll on the inner wall of the bowl and are lifted and thrown across the container at high speed. The milling process takes place mainly as a result of impact and friction. Overviews of the characteristics and applications of planetary mills in mechanical alloying have been published.[36,37]

1.2.8 Reduction Properties of Perovskite-Related Phases

Temperature-programmed reduction (tpr) studies have been carried out to investigate the reduction properties of some perovskite-related materials.[38,41] The temperature representing the maximum of the TPR peak, T_{max}, is an important parameter which indicates whether or not a material is easy to reduce. Some perovskites[38] such as $BaPb_{1-x}Bi_xO_3$, $BaPb_{1-x-y}Bi_xCu_yO_3$, $YBa_2Cu_3O_3$ and $Tl_2CaBa_2Cu_2O_{14}$ have one TPR peak in the range 473-1000 K, showing that reduction takes place in a single stage. Other perovskites, such as $LaMnO_3$, $NdMnO_3$ and $SmMnO_3$[39], have two peaks in their TPR profile showing that reduction takes place in two steps. Similar results were recorded from initial studies of the compounds $La_{0.8}Sr_{0.2}FeO_3$[40] and $La_{0.8}Sr_{0.2}CoO_3$[40] and other work has shown that lanthanum orthoferrite, $LaFeO_3$, retains its perovskite structure upon reduction.[41] In contrast, $LaCoO_3$ is reported[41] to be more easily reduced to a compound with a K_2NiF_4-type structure, La_2CoO_4.

1.2. 9 Oxide Fluorides

In recent years the insertion of fluorine into high T_c copper oxide superconductors to change structural and physical properties has attracted significant attention.[42, 43] This has resulted in a resurgence of interest in the syntheses of other and new oxide fluorides unrelated to superconductivity.[44] In summary, the fluorination of oxides to oxide fluorides can result in (i) the substitution of one fluorine for one oxygen; (ii) the incorporation of two fluorine atoms for each oxygen atom lost; (iii) the insertion of fluorine into interstitial sites. This results in structural changes [(ii) and (iii)], electronic changes [(i) and (iii)] as well as either oxidation (iii) or reduction (i) of the metal ions during fluorination.

1.2.9.1 ABO_3-Type Oxide Fluorides

$La_{1-x}Sr_xMnO_{3-2x+\delta}F_{2x}$ has been made[45,46] in which the fluorine atoms randomly occupy oxygen positions in the rhombohedral structure. The crystal structures and giant magnetoresistance properties of fluorinated $Nd_{0.67}Sr_{0.33}MnO_3$[47] and $La_{0.67}Ca_{0.33}MnO_3$ have been investigated [45,48]. Perovskite-type $La_{1-x}Sr_xFeO_{3-\delta}X_\delta$ (X=F, Cl) catalysts have also been reported[49] and have been found to have good selectivity for the oxidation of ethane to ethene.

1.2.9.2 K_2NiF_4–Type Oxide Fluorides

Much work[42, 43, 50-52] has recently been performed on fluorinating K_2NiF_4–type materials. The new oxide fluoride $Ba_2ZrO_3F_2 \cdot xH_2O$ has been made from the reaction of Ba_2ZrO_4 with NH_4F or transition metal difluorides (CuF_2, ZnF_2) at low temperatures (250 °C).[50] The fluorination reaction represents a substitution of 1 oxygen atom by 2 fluorine atoms.

A similar result has been achieved with the synthesis of the new oxide fluoride $Sr_2TiO_3F_2$ from the low temperature reaction of Sr_2TiO_4 with fluorinating agents NH_4F or transition metal difluorides.[51] The compound $Sr_2CuO_2F_{2+\delta}$ has also been made by the same method.[52] Sr_2FeO_3F has been prepared and investigated by powder neutron diffraction methods. The structure is one in which the anions are fully ordered giving iron oxygen square pyramids separated by rock salt type layers of strontium fluoride.[53] The material $LaSrMnO_4F$[54] has been synthesised and shown to have a staged structure in which the insertion of F atoms into the parent $LaSrMnO_4$ structure occurs only in alternate (La,Sr)O rocksalt blocks. An improved route[55] to the synthesis of K_2NiF_4-related inorganic oxide fluorides, such as $Sr_2TiO_3F_2$ and $Ca_2CuO_2F_2$, has involved the low-temperature fluorination of precursor oxides with poly(vinylidene fluoride). A summary of the use of low-temperature fluorinating agents including gaseous F_2, NH_4F, XeF_2, CuF_2 and ZnF_2, has been published.[55]

1.3 RUTILE

1.3.1 Titanium Dioxide

The rutile structure is illustrated by TiO_2. (Figure 1.9)

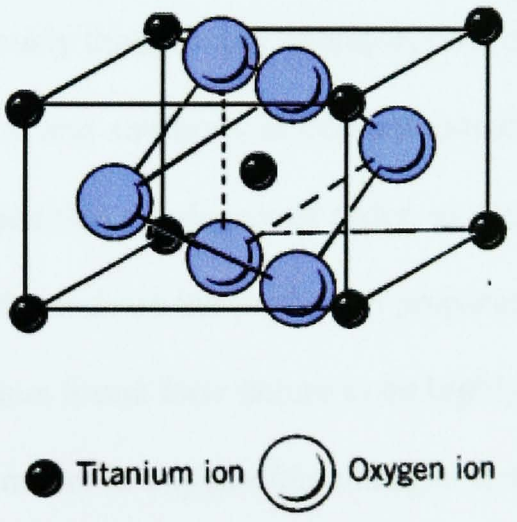

Figure 1.9 Rutile structure of TiO_2

In this structure each titanium atom is surrounded by six oxygen neighours, while the three titanium atoms co-ordinate each oxygen atom in a trigonal plane. TiO_6 octahedra share edges in chains along the *c*-axis, with edge-sharing chains being linked by vertices. The unit cell is tetragonal.

1.3.2 Metal Antimonates

Rutile-related metal antimonates have been known for many years, for example iron antimonate of composition $FeSbO_4$ was first reported [56] in 1943 during an investigation of rutile-related solids of composition ABO_4 and $VSbO_4$ was characterised [57] in1951. The materials have normally been prepared by high temperature calcination of Sb_2O_3 with either α-Fe_2O_3 or V_2O_5, or by the calcination of precipitates containing the elements at elevated temperatures. The fundamental properties of the materials have attracted a steady degree of attention over the past fifty years with, for example, the structural properties normally being associated with a random distribution of the cations over the cationic sites in oxygen octahedra. However, more recent studies have shown that the materials are more complex in nature than previously thought. For example, convergent beam electron diffraction[58] has shown that iron and antimony in iron antimonate are ordered in a triple rutile-related structure and that the degree of order, as well as the nature of cationic oxidation states, depends on the method of preparation[59]. Studies of vanadium antimonate [60,61] have found their nature to be highly dependent on the atmosphere in which they were made. In oxygen-free nitrogen a rutile-type antimony deficient compound of composition $VSb_{1-y}O_{4-3/2y}$ ($0<y<0.1$) was formed whereas in commercial nitrogen or in evacuated sealed tubes biphasic products composed of $VSb_{1-y}O_{4-2y}$ ($0<y<0.1$) and α-Sb_2O_4 were formed. Materials prepared in oxygen gave oxidised products of formulation $V_{1-y}\ Sb_{1-y}O_4$ ($0<y<0.1$). The materials have also attracted interest because of their activity as catalysts for hydrocarbon oxidation [62-65] but new applications now seem possible given recent reports [66] which have described their potential for gas sensing applications. One of the disadvantages of the high calcination temperatures involved in the conventional synthetic routes is that they produce large particles with low surface areas.

REFERENCES

1. C. Vasques, P Kogerler and M.A. Lopez-Quintela, *J. Mater. Res.,* 1998, **13,** 451
2. A.S. Moskvin, N. S. Ovanesyan and V.A. Trukhtarnov, *Hyperfine Interactions,* 1975, **1**, 265
3. J. G. McCarty and H. Wise, *Catalysis Today,* 1990, **8**, 231
4. Y. Shimizu, M Shimabukuro, H. Arai, and T, Seiyama, *Chem. Lett.,* 1985, 917
5. T. Arakawa, H. Kurachi,and J. Shiokawa, *J.Mater.Sci.,* 1985, **4**, 1207
6. Y. Matsuura, S. Matsushima, M.Sakamoto and Y. Sadoaka, *J. Mater. Chem.,* 1993, **3**, 767
7. F. G. Karlsson, *Electrochem. Acta,* 1985, **30**, 1555
8. T. Nekamura, G. Petzow and L. J. Gancker, *Mater. Res.Bull.,* 1979, **14**, 649
9. J. Mizusaki, T. Sisamoto, W. K. Cannon and H. K. Bowen, *J. Amer. Ceram.* Soc., 1982, **65**, 363.
10. Y.Sadaoka, E.Traversa, P. Nunziante, M.Sakamoto, *J. Alloy Comp.,* 1997, **261**, 182
11. E. Traversa, P. Nunziante, M. Sakamoto, Y.Sodoaka and R. Montanar, *Mater Res.Bull.,* 1998, **33**, 673
12. V. R.Choudhary, B. S. Uphade, S.G. Pataskar, *Fuel,* 1999, **78**, 919
13. M. Marezio, *Mater. Res. Bull.,* 1971, **6**, 23
14. S. E. Dann, D. B. Currie and M. T. Weller, M. F. Thomas and A. D. Al-Rawwas, *J. Solid State Chem.,* 1994, **109**, 134
15. W. C. Koehler, E. O. Wollan, *J. Phys. Chem. Solids,* 1957, **4**, 100
16. G. Thornton, *J. Solid State Chem.,* 1986, **61**, 301
17. A. N. Petrov, *Solid State Ionics,* 1995, **80**, 189
18. J.P. Hodges, S. Short, J.D. Jorgensen, X. Xiong, B. Dabrowski, S. M. Mini and C. W. Kimball, *J. Solid State Chem.,* 2000, **151**, 190

19. P.Gallagher, J.B. Mac Chesney and D.N.E. Buchanan, *J. Chem. Phys.,* 1964, **41**, 2429
20. M. Takano, T. Okita, N. Nakayama, Y. Bando, Y. Takeda, O. Yamamoto and J. B. Goodenough, *J. Solid State Chem.,* 1988, **73**, 14
21. B.C Tofield, C. Greaves and B.E.F. Fender, *Mat.Res.Bull.,* 1975, **10**, 737
22. A.Ea, Doctoral Thesis, Université de Bordeaux, 1983
23. T. C. Gibb, *J. Chem. Soc. Dalton Trans.,* 1985, 1455
24. Y. Takeda, K. Kanno, T. Takada, O. Yamamoto, M. Takano, N. Nakayama and Y. Bando, *J. Solid State Chem.,* 1986, **63**, 237
25. T. Takeda, Y. Yamaguchi and H. Watanabe, *J. Phys. Soc. Jpn.,* 1972, **33**, 967
26. J. S. Waugh, M. I. T.Lab. for Insulation Res. Technical No. 1960, 152
27. W. F. Kelly, M. S. *Thesis,* M.I.T., 1961
28. U. Shimony and J. M. Knudsen, *Phys. Rev.,* 1966, **144**, 361
29. D. Babel, E. Herdtweck, *Zeitschrift fuer Anorganische und Allgemeine Chemie,* 1982, **487**, 75
30. X. Chu and S. Pietro, *Sensors and Actuator B,* 2003, **94,** 197
31. F.J. Berry, P. Wynn, J. Jiang and S. Mørup, *J. Mater. Sci.,* 2001, **36,** 3637
32. P.S. Gilman and J.S. Benjamin, *Ann. Rev. Mater. Sci.,* 1993, **13**, 280
33. P. Pochet, L.Chaffron and E. Martin, *Mater. Sci. Forum,* 1998, **91**, 179
34. D. R. Maurice and T. H. Courtney, *Metall. Trans.,* 1990, **21A**, 289.
35. A. N. Streletskii, *Proc. Second International Conference on the Structural Applications of Mechanical Alloying,* J. J. de Barbadillo, F. H. Fores, R. Schwarz, eds., p.51, SM, Materials Park, Ohio, 1993
36. M. Abdellaoni and E. Gaffet, *Mater. Sci. Forum,* 1995, **339**, 179
37. J. Uchcrin, R. Uchcrin and E. G. McCormick, *Metall. Trans,* 1991, **22A**, 3019

38. R. Sumathi, K. Johnson, B. Viswanathan, T. K. Varadarajan, *Applied Catalysis A,* 1998, **175**, 15

39. P. Ciambelli, *Applied Catalysis B*, 2000, **24,** 243

40. D. Ferri and L. Forni, *Applied Catalysis B,* 1998, **16**, 339

41. A. Lindstedt, D. Strömberg and M. A. Milh, *Applied Catalysis A,* 1994, **116**, 109

42. M. G. Francesconi and C. Greaves, *Supercond. Sci. Techol.,* 1997, **10**, A29

43. C.Greaves and M. G. Francesconi, *Current Opinion in Solid State and Materials,* 1998, **3**, 132

44. A.C.Needs, M. T. Weller, M. Scheler and R.K.Harns, *J. Mater. Chem.,* 1996, **6**, 1219

45. V. Maxim, A.M. Lobanova, A. V. Abakumov, M. G. Sidorovaa, O. G. Rozovaa, E. V. D'yachenkoa, J. H. Antipova, and V. T. Gustaaf, *Solid State Sci.,* 2002, **4**, 19

46. Y. Guo , X. Zhang and R. Wappling, *J. Alloys Comp.,* 2000, **306**, 133

47. Y.Q. Guo, Y.C. Liu, K. Tao, H.P. Zhou, R. Wappling, *J. Solid State Chem.,* 1999, **148**, 236

48. Y.Q. Guo, K. Tao, Y.C. Liu, H.P. Zhou and R. Wappling, *J. Alloys Comp.,* 2000, **296**, 33

49. H. X. Dai , C. F. Ng and C.T. Au , *J. Catal.,* 2000, **52**, 189

50. P. R. Slater and R. K. B. Gover, *J. Mater. Chem.,* 2001, **11**, 2035

51. P. R. Slater and R. K. B. Gover, *J. Mater. Chem.,* 2002, **12**, 291

52. M. Al-Mamouri, C. Greaves, P. P. Edwards and M. Slaski, *Nature,* 1994, **369,** 382

53. A. L. Hector, A. J. Hutchings, R. L. Needs, M. F. Thomas and M. T. Weller, *J. Mater. Chem.,* 2001, **11**, 527

54. L. D. Aikens, R. K. Li and C. Greaves, *Chem. Commun.*, 2000, 2129

55. P. R. Slater, *J. Fluorine Chem.,* 2002, **117,** 43

56. K.Brandt, *Ark. Kemi Mineral. Geol. A*, 1943, **17**, 15

57. L. W. Vernon and W. O. Milligan, *Tex. J. Sci.,* 1951, 82

58. F. J. Berry, J. G. Holden, and M. H. Loretto, *J. Chem. Soc. Faraday Trans.,* 1987, **83**, 615

59. F. J. Berry, J. G. Holden, M. H. Loretto and D. S. Urch. *J. Chem. Soc. Dalton Trans.*, 1987, 1727

60. F. J. Berry, M.E. Brett and W.R. Patterson, *J. Chem. Soc. Dalton Trans.*, 1983, 9

61. F. J. Berry, M.E. Brett and W.R. Patterson, *J. Chem. Soc. Dalton Trans.*, 1983,13

62. Brit. Pat.1336136

63. Brit. Pat.1377211

64. Brit. Pat.1324693

65. Brit. Pat.1363455

66. Z. Tianshu and P. Hing, *J. Mater.Sci.*, 1999, **10**, 509

Chapter 2

THEORY OF EXPERIMENTAL TECHNIQUES

Chapter 2

THEORY OF EXPERIMENTAL TECHNIQUES

2.1 X-RAY POWDER DIFFRACTION (XRD)

XRD has been used routinely for the characterisation of crystalline solids for many years. The theory of X-ray diffraction has been understood since the early part of the 20th century and the use of X-ray diffraction as a structural technique has been explained in detail in standard textbooks[1-3].

2.1.1 Theory of XRD

When an X-ray beam strikes an atom, the interaction between the X-radiation and the electrons in the atom results in a scattering of X-rays in all directions. If the diffracted X-rays are in phase then constructive interference can occur and if they are out of phase then destructive interference will occur. An incident X-ray beam will be diffracted by a crystal if Bragg's Law is obeyed.

Bragg's approach was to consider the crystals as being built in layers, or planes, such that each acts as a semi-transparent mirror. The planes allow some of the X-ray beams to be reflected at the same angle as the angle of incidence (Figure 2.1).

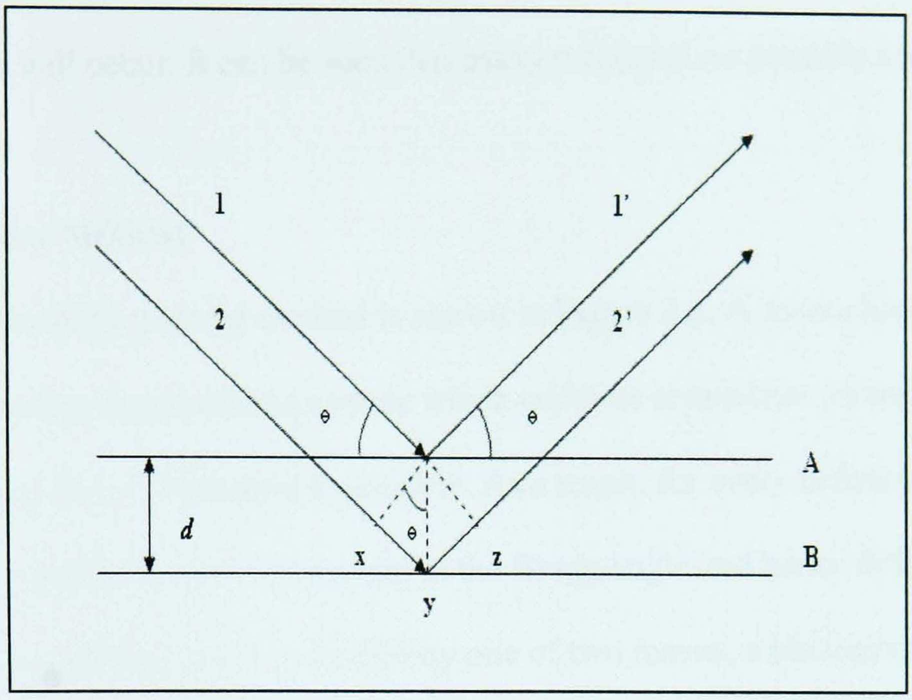

Figure 2.1 Schematic representation of derivation of Bragg's law

The incident beams1 and 2 are reflected by planes A and B to form beams1' and 2', the condition under which these beams are in phase with each other is approached as follows. Beam 2 2', shown in Figure 2.1, has to travel a further distance, xyz as compared to 1 1'. For 1' and 2' to be in phase with each other *xyz* must equal $n\lambda$, where n is an integer and λ is the wavelength. The perpendicular spacing, *d*, and angle of incidence, θ, called the Bragg angle, are related by:

$$xy = yz = d\sin\theta \quad (2.1)$$

=> $$xyz = 2d\sin\theta \quad (2.2)$$

Since $$xyz = n\lambda \quad (2.3)$$

=> $$n\lambda = 2d\sin\theta \quad (2.4)$$

When the above equation, (2.4) Bragg's Law, is satisfied the reflected beams are in phase and thus constructively interfere. If the angle is not correct, then usually interference of a destructive nature will occur. It can be seen that many solutions are possible i. e. n = 1, 2, 3.

2.1.2 The Powder Method

The basic principle of the powder method is shown in Figure 2.2. A monochromatic beam of X-rays strikes the powdered sample which contains crystallites arranged randomly such that every orientation is possible. As a result, for every diffraction plane, there are some crystallites correctly oriented at the Bragg angle and hence diffraction occurs. The diffracted beam can be detected by one of two means, a photographic plate surrounding the sample, or a moveable detector, connected to a computer. The original photographic method, called the Debye-Scherrer method, is little used in modern X-ray diffraction pactices. A modern diffractometer can collect accurate positional and intensity

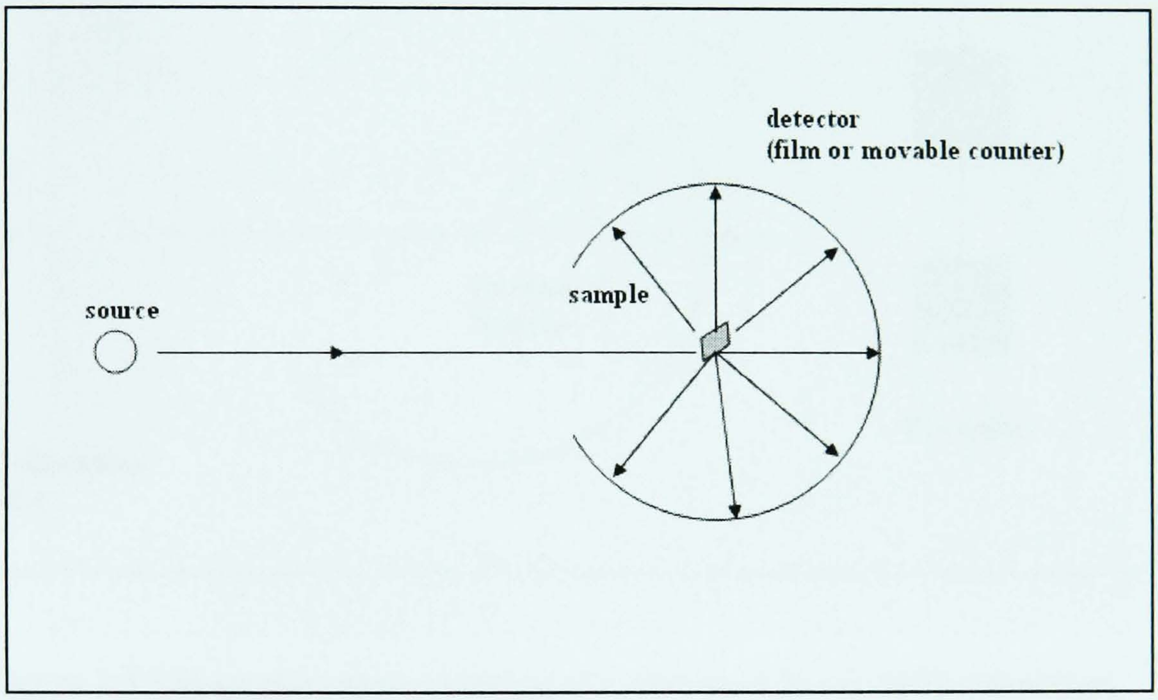

Figure 2.2 A schematic representation of the powder method

data both quickly and easily. This can enable the phase composition to be determined in less than an hour, with the recorded pattern being matched against standard patterns.

2.1.3 Diffractometer

The collection of X-ray powder diffraction data is routinely carried out on a diffractometer, such as shown in Figure 2.3.

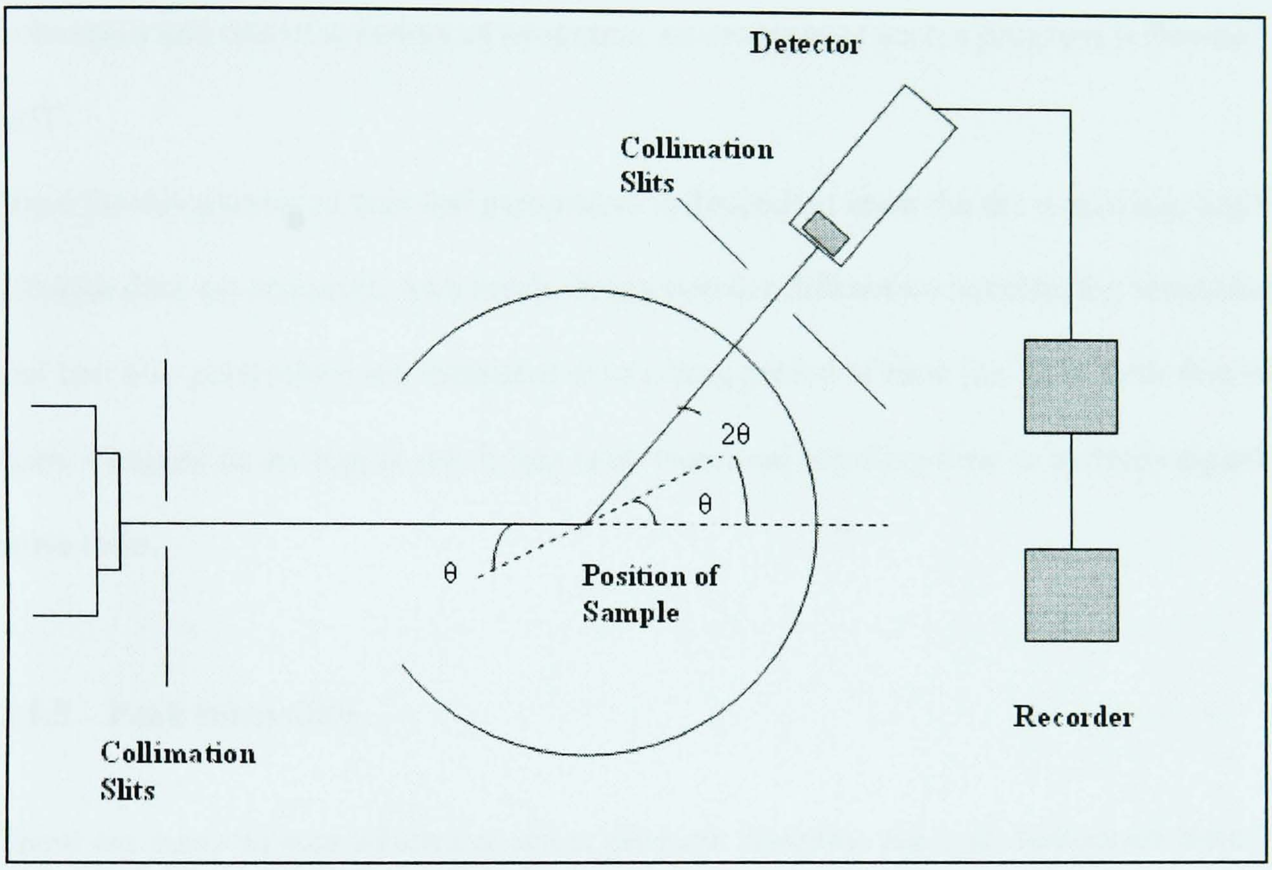

Figure 2.3 Schematic representation of a standard X-ray diffractometer.

The X-rays are generated in an X-ray tube, where electrons are bombarded against a metal target, usually copper. This bombardment results in the evolution of X-rays, which are collimated into a pencil like beam. The beam then passes through the sample, which is rotated around a central axis, and is diffracted. This diffracted beam passes through a further set of collimation slits to remove X-ray scattering. The X-rays are counted in a detector moving around the central axis, at an angle of rotation twice that of the sample.

2.1.4 Unit Cell Sizes

The calculation of unit cell parameters is usually carried out using computer modelling techniques and one of a variety of programs, an example of such a program is Powder Cell[4].

Since the calculation of unit cell parameters is dependent upon the the d-spacing, highly accurate data are required. As a result, X-ray powder diffraction patterns for determining unit cell size parameters are measured over a long period of time (*ca.* 12 h) with fine step sizes. Coupled to the higher resolution is an increased counting time to increase signal to noise ratio.

2.1.5 Peak Intensities

There are many factors which can affect the peak intensity, the main factors are described below.

i) Structure Factor

The peak intensity is influenced by the position of the atoms in the unit cell and the atom type. If an atom has a high atomic number then it will scatter X-rays better than an element with a low atomic number, e.g. Cs scatters better than Li giving greater intensity.

ii) Multiplicity Factor

For a cubic system, lattice planes such as (013), (031), (103), (130) all have the same d-spacing where $a = b = c$. In a powder XRD pattern the variable co-ordinate is the d-spacing, therefore reflections which give rise to the same d-spacing will be superimposed. As a result a more intense peak will be observed.

iii) Preferred Orientation

This occurs if the powder is poorly ground or the powder is not oriented randomly. This effect can cause some intensities to be increased while others are decreased.

iv) Temperature Factor

Thermal vibrations of atoms cause a decrease in the observed peak intensity with an increase in background scatter. This effect is usually only important for experiments performed at high temperature.

2.1.6 Crystallite Size Measurement

It is possible to measure the crystallite size from X-ray powder diffraction patterns using the effect of line broadening in the diffraction pattern. The relationship between the mean dimension of the crystallites in a powder, D, and the pure X-ray diffraction broadening, β, was first determined by Scherrer, and is discussed in detail by Klug and Alexander[5]. Scherrer related the mean dimension, D, to the pure diffraction broadening, β, by the equation;

$$D = k\lambda / \beta\cos\theta \qquad (2.5)$$

where k is a constant approximately equal to unity, θ is the diffraction angle and λ is the wavelength of the X-radiation.

2.2 MÖSSBAUER SPECTROSCOPY

2.2.1 Theory of Mössbauer Spectroscopy

Mössbauer Spectroscopy is a technique which involves the resonant absorption and emission of gamma rays by nuclei. This phenomenon was first observed by Rudolf Mössbauer in ^{158}Ir in 1958, and led to the development of the technique which now bears his name. Many detailed accounts of the theory and instrumentation of Mössbauer spectroscopy can be found in the literature [6-8].

In Mössbauer spectroscopy the γ-ray source consists of a solid matrix in which a radioactive isotope is embedded. The isotope then decays into the Mössbauer isotope in an excited state which subsequently relaxes with the emission of a γ-ray. For resonant absorption the energy of the γ-ray must not be influenced by nuclear recoil, to achieve this Mössbauer nuclei are held in a rigid crystal lattice. If the energy of the nuclear recoil associated with the absorption and emission of a γ-ray is small in comparison with the lowest quantised lattice vibration, recoil free transitions suitable for a Mössbauer experiment can occur. In the case of ^{57}Fe the γ-ray energy is small (14.4 keV) and thus recoil effects are small.

The energy of the transition between the excited and ground state of the Mössbauer nucleus is usually different in the source and the absorber. Therefore, rarely does the energy of the incident γ-ray correspond to the energy transition of the absorber Mössbauer nucleus. The γ-ray energy is therefore modified by the Doppler effect and this is achieved by vibration of the source at a velocity of millimetres per second. Thus, a Mössbauer spectrum consists of a plot of γ-ray counts against γ-ray energy. The γ-ray energy is presented in terms of the velocity of the source. A typical Mössbauer spectrum obtained from a sample in which the Mössbauer atoms are in the same cubic environment in both source and absorber is presented in Figure 2.4.

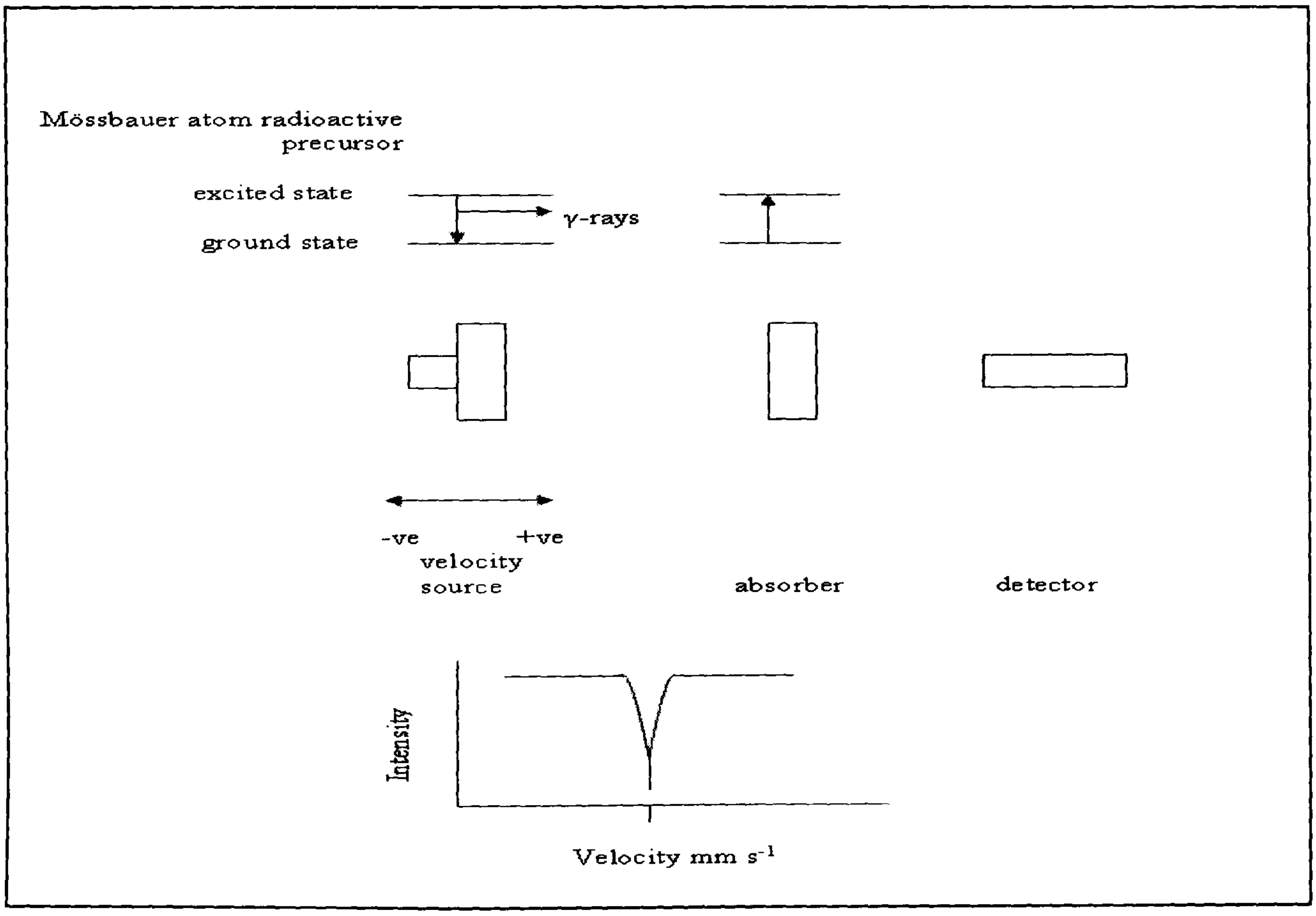

Figure 2.4 Schematic representation of Mössbauer spectroscopy experiment.

Differing environments around the nucleus in the absorber give rise to hyperfine interactions which give the parameters known as isomer shift, quadrupole splitting and magnetic hyperfine splitting. These arise because of the electric monopole interaction, electric quadrupole interaction and magnetic dipole interaction respectively.

2.2.2 Isomer Shift

To understand the origin of the isomer shift it is useful to consider a nucleus stripped of its electrons. In such a nucleus the energy of the transition between ground and excited states may be represented as E, in Figure 2.5 (a).

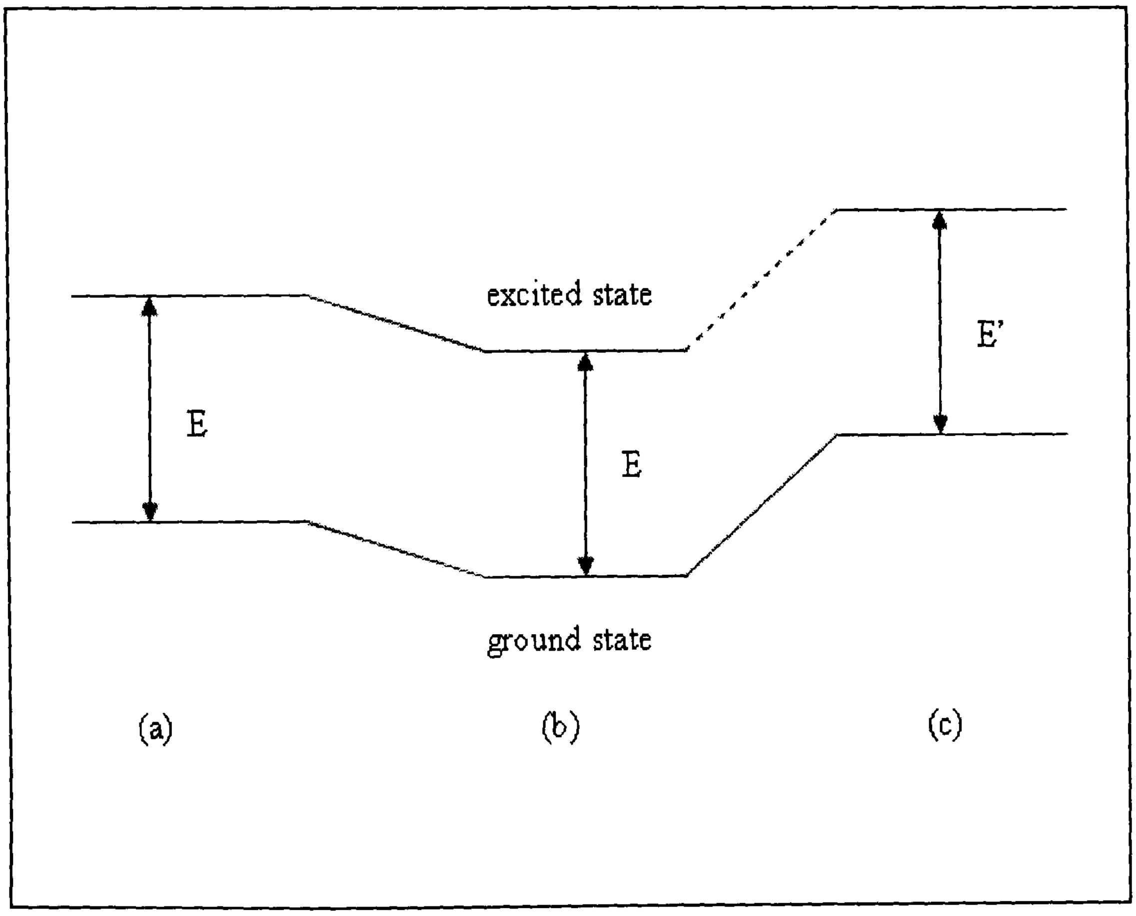

Figure 2.5 Nuclear energy level of (a) bare nucleus, and a nucleus in which the excited and ground states are (b) the same size and (c) differing size

If the nucleus is surrounded by electrons a Coulombic attraction between the nuclear and the electronic charges occurs which modifies the nuclear energy levels. If, in both the excited and ground states, the sizes of the nuclei are the same, then the interaction of these states with electrons will be the same. Hence the energy levels will be changed by the same amount, as will the energy of the transition E, Figure 2.5 (b). If, alternately, the sizes of the nuclei in the two states are different, as usually arises, the energies of the ground and excited states will be modified to a different extent, consequently the energy of the transition will be modified to a new value E', Figure 2.5 (c).

The nuclear energy levels depend upon the electronic environment. Therefore, if the source and absorber nuclei are in different electronic environments then the nuclear energy levels will be modified to differing degrees, Figure 2.6 (a). The energy of the emitted γ-ray is then modified by the Doppler effect and the Mössbauer spectrum will exhibit a resonant absorption shifted from zero velocity, Figure 2.6 (b). This is known as the isomer shift or chemical isomer shift, δ.

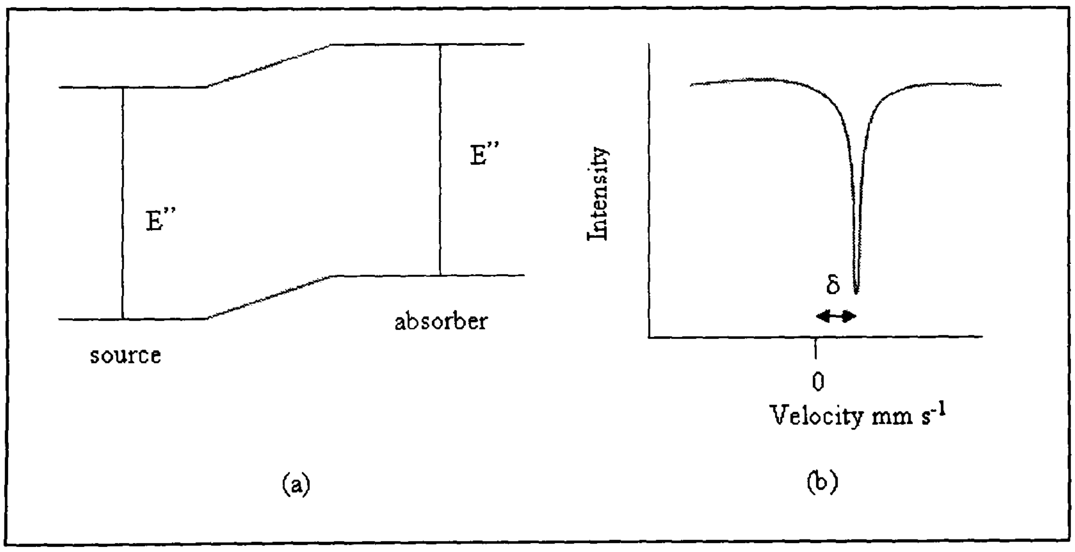

Figure 2.6 (a) Nuclear energy levels with source and absorber atoms in different electronic environments, (b) the resultant spectrum.

The isomer shift can be related to the electronic properties by the equation

$$\delta = \text{constant}\ \frac{\Delta R}{R}\ (\Psi_s^2(o)_A - \Psi_s^2(o)_s)$$

where $\Delta R/R$ is $(R_e - R_g)/R_g$ and R_e and R_g are the radii of the excited and ground state nuclei respectively and $\Psi_s^2(o)_A$ and $\Psi_s^2(o)_S$ are the s- electron densities at the absorber- and source-nuclei, respectively. $\Psi_s^2(o)$ is dependent primarily on the population of the s-orbitals, but will also be influenced by the occupation of other types of orbitals. This is due to the outer electrons shielding the interaction of the s-elections from the nucleus. For any particular source the value of $\Psi_s^2(o)_S$ will be constant, and therefore any change in the isomer shift will reflect changes in $\Psi_s^2(o)_A$. Hence, information about the electronic environment of the absorber is obtained which can then be used as a probe of oxidation state.

For ^{57}Fe Mössbauer spectroscopy the value of $\Delta R/R$ is negative. Hence higher s-electron densities at iron nuclei are reflected by a decrease in isomer shift. Another influence on the isomer shift in iron compounds is the effect of shielding. As d-electron removal effectively increases the s-electron density at the iron nuclei, iron (II) species with a d^6 configuration have a more positive isomer shift than iron (III) species with a d^5 configuration. In ^{57}Fe nuclei the magnitude of $\Delta R/R$ is sufficiently large for a range of isomer shifts to exist.

2.2.3 Quadrupole Splitting

If a nucleus has a spin *I* greater than 1/2 then it will have an asymmetric charge distribution, which gives rise to a nuclear quadrupole moment. It is then possible for the nuclear quadrupole moment to interact with an asymmetric electric field represented by an electric field gradient. This results in the partial or complete splitting of the nuclear energy levels. As more than one nuclear transition may occur, a multi-line Mössbauer spectrum results. For nuclear transitions the selection rule is $\Delta m_I = 0, \pm 1$. ^{57}Fe has excited and ground state spins of 3/2 and 1/2 respectively which, for this isotope, means that the presence of an electric field gradient gives rise to a two line spectrum, shown in Figure 2.7. The distance between the peaks is the quadrupole splitting, Δ.

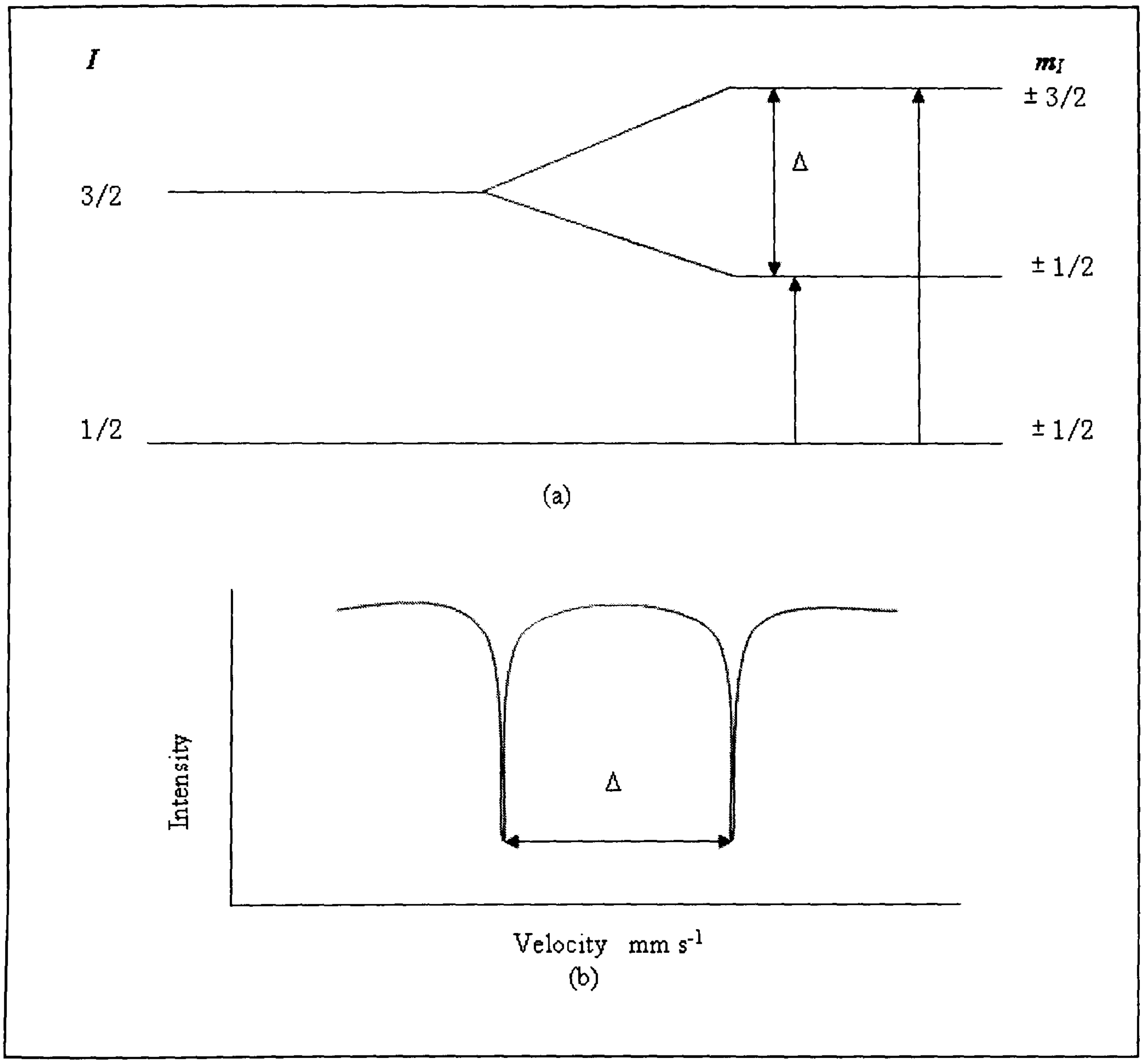

Figure 2.7 (a) Splitting of nuclear energy levels for ^{57}Fe nuclei in the presence of an electric field gradient and (b) resultant spectum.

Different components contribute to the electric field gradient. One is from the electronic environment about the nucleus, called the valence term. The valence term can be envisaged as arising from the valence electrons of the Mössbauer atom and originates from asymmetry in the electronic structure which derives from the unfilled or partially filled electron shells occupied by the valence electrons. The main contribution to the valence term is the asymmetric *p*- and *d*- electron populations, as the s-electron density is principally symmetric about the nuclear volume. A lattice contribution, arising from surrounding charged entities, also contributes to the electric field gradient. This arises from asymmetry in the arrangement of atoms around the Mössbauer nuclei. Further contributions to the electric field gradient include the effects of molecular orbitals and any polarisation of the core electrons of the Mössbauer atom.

Hence, quadrupole splitting reflects the symmetry of the bonding environment and local structure in the vicinity of the Mössbauer atom. Used in conjunction with chemical isomer shift data, the quadrupole splitting can be used to elucidate the oxidation states, electronic configuration and ligand arrays.

2.2.4 Magnetic Splitting

A nucleus of spin $I > 0$ has a magnetic moment which may interact with a magnetic field via a magnetic dipole interaction. Such a magnetic interaction induces splitting of the nuclear energy levels. Degeneracy of the nuclear state is removed by interaction of the nucleus with the magnetic field, and the levels subsequently split into $2I+1$ substates. In ^{57}Fe the ground state with $I = 1/2$ splits into two substates, and the excited state with $I = 3/2$ splits into four substates. For these spin states the selection rule, $\Delta m_I = 0, \pm 1$, gives rise to a symmetric six line Mössbauer spectrum. In such a spectrum the isomer shift is given as the centroid of the six peaks. The magnetic splitting of the ground and excited states for ^{57}Fe and the resultant spectrum is illustrated in Figure 2.8.

The total magnetic field experienced by the nucleus is a vector sum of the magnetic hyperfine and any external applied field. The magnetic hyperfine field arises from the spin of any unpaired electrons and is dependent upon the oxidation- and spin-state of that atom. Hence, interpretation of the magnetically split Mössbauer spectrum can give information about electronic structure and magnetic properties in a system. It is possible to modify the hyperfine field by application of an externally applied magnetic field, which distinguishes the hyperfine field from the other Mössbauer hyperfine interactions. Altering the applied field can change the appearance of the spectrum and aid interpretation. The occurrence of magnetically split ^{57}Fe Mössbauer spectra is common among ferro- and antiferro- magnetic materials. Paramagnetic materials cooled to below their Curie temperatures also exhibit a magnetically split Mössbauer spectrum.

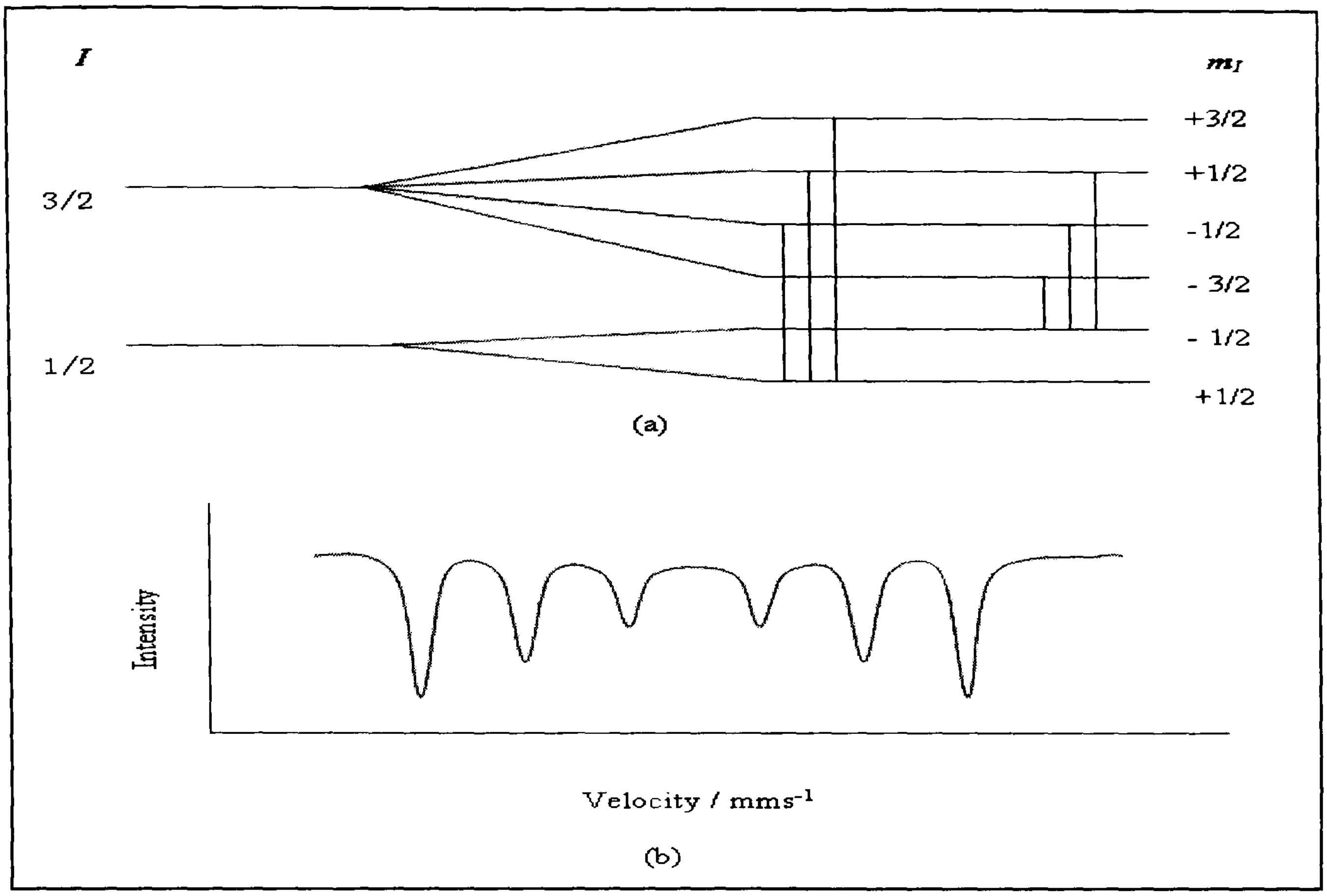

Figure 2.8 (a) Splitting of nuclear energy levels by a magnetic field (b) and resultant spectrum.

2.3 TEMPERATURE PROGRAMMED REDUCTION (TPR)

2.3.1 Theory

Temperature programmed reduction (tpr) [9,10] is a thermal analytical technique used to probe the reducibility of solid compounds. Typically a dilute hydrogen mixture is passed over a sample and the uptake of hydrogen is monitored as the temperature is raised in a linear fashion with time.

2.3.2 Instrumentation

The procedure involves flowing a gas mixture through the reference arm of a kathrometer detector of a gas chromatograph and then over the sample under investigation with the gas mixture returning via a drying tube to the other arm of the kathrometer. Consumption of hydrogen (and therefore reduction) is detected as a voltage imbalance between the two arms of the kathrometer. This is displayed schematically in Figure 2.9

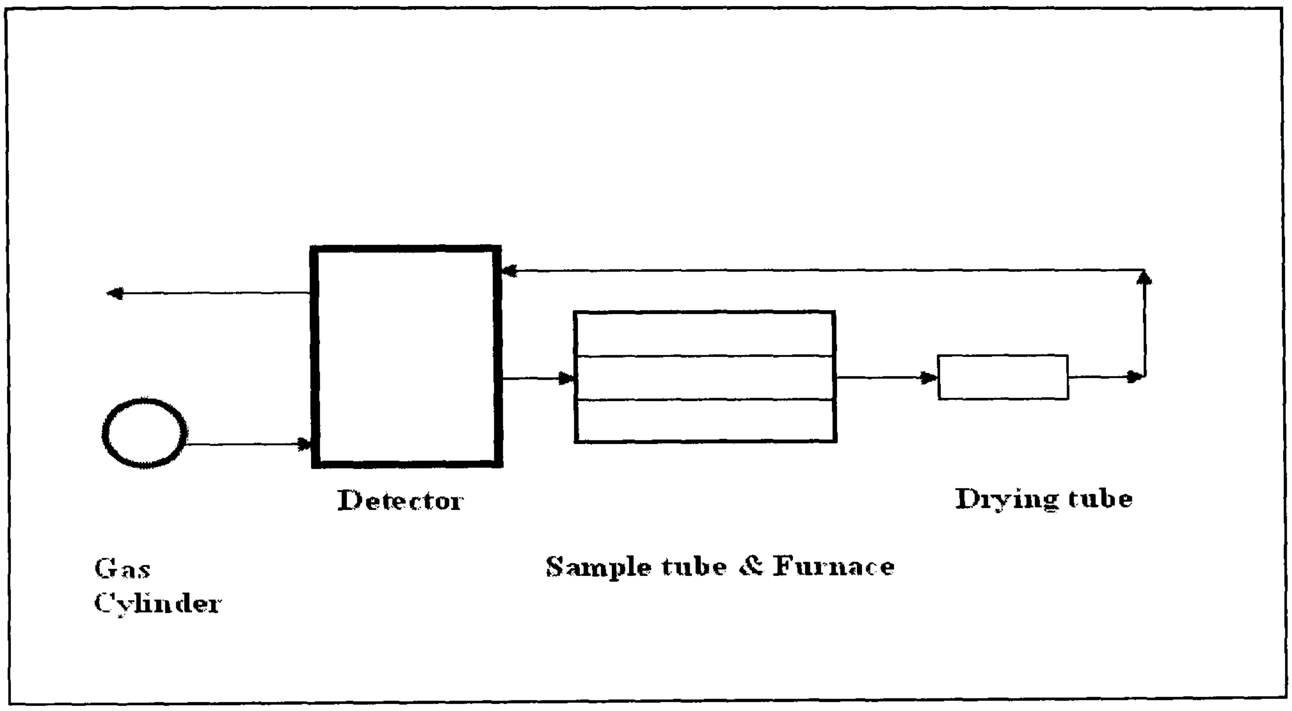

Figure 2.9 Schematic diagram of apparatus used for tpr experiment

2.4 X-RAY ABSORPTION NEAR EDGE STRUCTURE (XANES) AND EXTENDED X-RAY ABSORPTION FINE STRUCTURE (EXAFS)

The use of X-ray absorption spectroscopy for structural determination has been known for about sixty years but only in the last 20 years, with the development of synchrotron radiation sources, has EXAFS been developed as a powerful tool for the chemist. The technique allows structural information to be derived from solids, whether crystalline or amorphous, liquids, gases and fluid-solid interfaces. Detailed descriptions of the theory, instrumentation and applications of EXAFS have been published.[11-17]

2.4.1 Theory

In X-ray absorption spectroscopy the excitation of core electrons of the atom under investigation gives rise to an X-ray absorption spectrum which exhibits sharp edges. For example, the X-ray absorption spectrum obtained from transition metals can be separated into 3 distinct regions. (Figure 2.10)

1) Pre-edge absorption features which occur a few eV below the steep absorption edge. These appear to be associated with electronic transitions from the 1s core orbital to the molecular orbitals.

2) The steep absorption edge and the features as much as 40eV beyond the edge may be due to 1s transitions similar to those in region 1 or due to 1s transitions to more continuum-like states, not localised on the metal ion.

In the X-ray absorption spectrum these two regions are termed the XANES (X-ray Absorption near Edge Structure). XANES may be used to probe a specific ion environment and different oxidation states and coordination environments of the element cause shifts in the position of the edge.

3) The absorption cross section in the region from 40eV to 1000eV or more above the absorption edge is known as the post edge region and is observed to oscillate. These oscillations are termed the Extended X-ray Absorption Fine Structure, or EXAFS. This is also known as the Kronig structure, Figure 2.10.

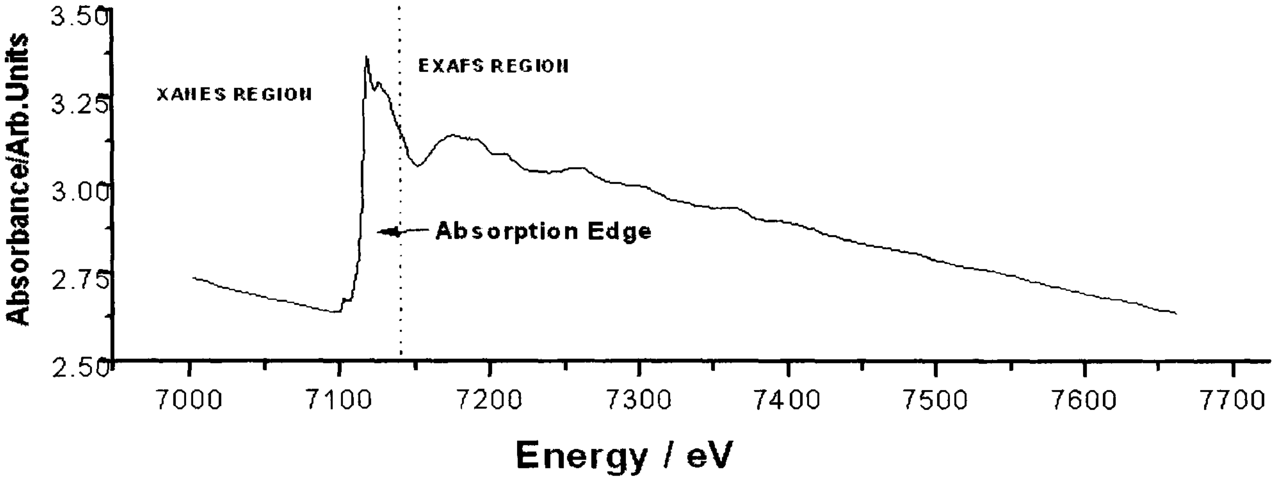

Figure 2.10 Regions containing the XANES and EXAFS information and the position of the absorption edge

The EXAFS, normally expressed in terms of absorption coefficient, μ, can be determined from a measurement of the attenuation of X-ray intensities. The absorbance is given by Beer's Law:

$$\mu x = \ln I_0/I$$

where x is the thickness of the material and I_0 and I are the incident and emergent X-ray intensities respectively . When the energy of an X-ray photon, E, of the monochromatic beam is tuned to the binding energy of a core electronic level of an atom in the material, an increase in the absorption coefficient is observed, known as the absorption edge. At the edge the energy is sufficient to cause an electron to be ejected from the sample atom. This electron will be from either the K or the L shells and the X-ray energies will be 1-40keV. If there is any further increase in X-ray energy, this will be translated into the kinetic energy of the ejected photoelectron.

The EXAFS can be explained by considering the outgoing photoelectron as a spherical wave originating from the absorbing atom. When an excited atom is surrounded by other atoms, the outgoing spherical wave is reflected back towards the origin by the surrounding scatterers. The wavelength of the photoelectron and the atomic number of the scatterers determine the phase of the reflected wave. This reflected wave undergoes self-interference with the outgoing wave, Figure 2.11, and depending on the wavelength of the photoelectron, outgoing and back-scattered waves may interfere constructively or destructively. A sinusoidal variation of the absorption coefficient, μ, as a function of photon energy results from the interference. Quantum mechanically the photoelectron interference effect in the final state modifies the absorption cross-section and results in modulations of the transmitted X-ray intensity beyond the absorbing edge.

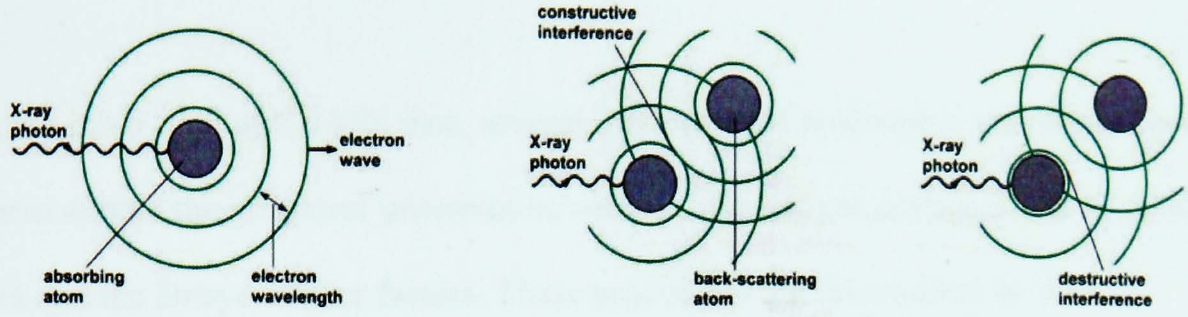

a) b)

An outgoing photoelectron wave caused by the absorption of an X-ray photon.

Outgoing photoelectron waves and backscattered waves from neighbouring atoms, interacting
a) constructively, and b) destructively.

Figure 2.11 Diagram illustrating constructive and destructive interference of an outgoing wave

The frequency of the EXAFS oscillations depends on the distance between the absorbing atom and the scattering atoms, since the wave travels from the absorber to the scatterer and returns. During this period the photoelectron undergoes a phase shift. If the phase shift can be determined either from model compounds such as standards of known structure with atoms in similar electronic and structural environments or by calculation, then interatomic distances can be calculated for the immediate vicinity of the absorber atom. The amplitude of each modulation depends on several factors; the atomic number, back scattering power of the neighbouring atoms, as well as their number and bonding distance from the absorber. Bond distance and coordination number can be determined from this amplitude.

Having recorded a set of EXAFS data, several mathematical procedures may be followed in order to extract the structural information, such as inter-atomic distances, coordination numbers and the Debye-Waller factors. These procedures are determined by the mathematical theory of EXAFS as detailed in the literature.[13, 15]

Initially the data should be normalised so that the EXAFS modulation $\chi(E)$ can be observed. It is therefore necessary to subtract the background spectrum leaving the EXAFS oscillations. This consists of several stages.

1) Firstly, the position of the absorption edge E_0 is found which is then used as a standard against which the EXAFS oscillations can be based. This value is not fixed but allowed to iterate to provide more accurate inter-atomic distance determination.

2) The pre-edge absorption is fitted to a linear polynomial function and extrapolated across the EXAFS region.

3) The post-edge absorption is fitted to a set of polynomials which model μ_0, the atomic absorption factor. This passes smoothly through the EXAFS oscillations, which effectively models the post-edge as it would appear without the EXAFS oscillations. This procedure then produces isolated EXAFS oscillations.

Having carried out the pre- and post- edge subtractions, the x-axis is converted from energy space, E, into photoelectron wave vector space, *k*. Finally a Fourier transformation using a k^3 weighting factor is carried out. This results in a radial distribution function being produced, with peaks appearing at certain distances away from the core atom, Figure 2.12. Further manipulation is carried out using window functions. At this stage the structural information is obtained by producing a theoretical model which is iterated to match the experimental data using a series of curve fitting routines.

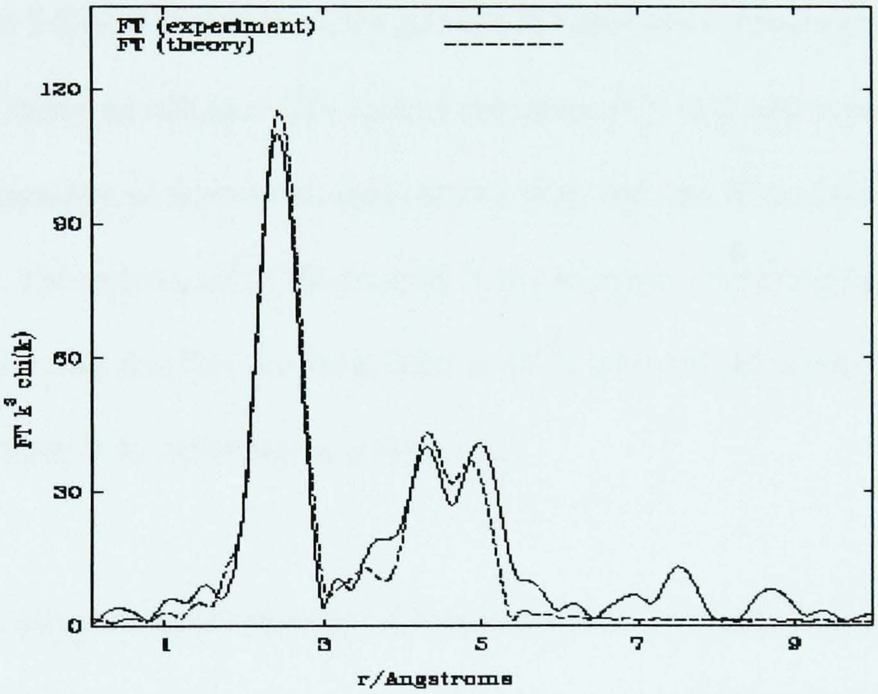

Figure 2.12 Fourier transformed EXAFS data showing experimental data (solid line) and modelled data (dashed line)

2.4.2 Instrumentation

Many methods for measuring EXAFS have been developed. These differ mainly in the detection technique employed, sample geometry and choice of X-ray detectors. The transmission mode directly measures the incident and transmitted X-rays and gives a direct measurement of the absorption coefficient. As the absorption of X-rays is limited to the creation of an electron vacancy it is possible to determine the absorption coefficient. The vacancy can be filled by an outer shell electron which is accompanied by emission of fluorescence radiation or Auger electrons, both of which can yield EXAFS information. In the fluorescence mode, the fluorescence yield increases with increasing atomic number. The advantage of this method is that background radiation can be measured with suitable filters, increasing the sensitivity of the method. If the fluorescence method fails, then the Auger method may be useful which is particularly good in the analysis of surfaces (SEXAFS). In EXAFS the most commonly used source is the synchrotron. Synchrotron radiation has many advantages. The energy spectrum of X-rays generated by synchrotron radiation is smooth and continuous and extends from the end of the infra-red to the hard X-ray region. This allows all of the desired X-ray energies to be investigated. Also the beam is intense, and the flux can be as high as 10^{12} photons per second, allowing the EXAFS spectrum to be collected in a short time.

Synchrotrons are particle accelerators. Charged particles, usually electrons, are accelerated to high velocities, then stored in a storage ring. Whilst in this ring they are subjected to a magnetic field which maintains the electrons in an orbit, but places an accelerating force upon them. As a result of this, the electrons emit intense white electromagnetic radiation covering all frequencies.

A monochromator allows the X-ray beam to be separated into its component frequencies. The monochromator consists of two single crystals of silicon aligned along defined planes. These crystals can be rotated so that the path length between them changes and allows differing energies of X-rays to be scanned. The single crystals are slightly offset to allow rejection of the harmonics which are detrimental to the data quality. The monochromator is enclosed in a helium filled chamber with beryllium windows. A typical transmission EXAFS configuration is shown in Figure 2.13.

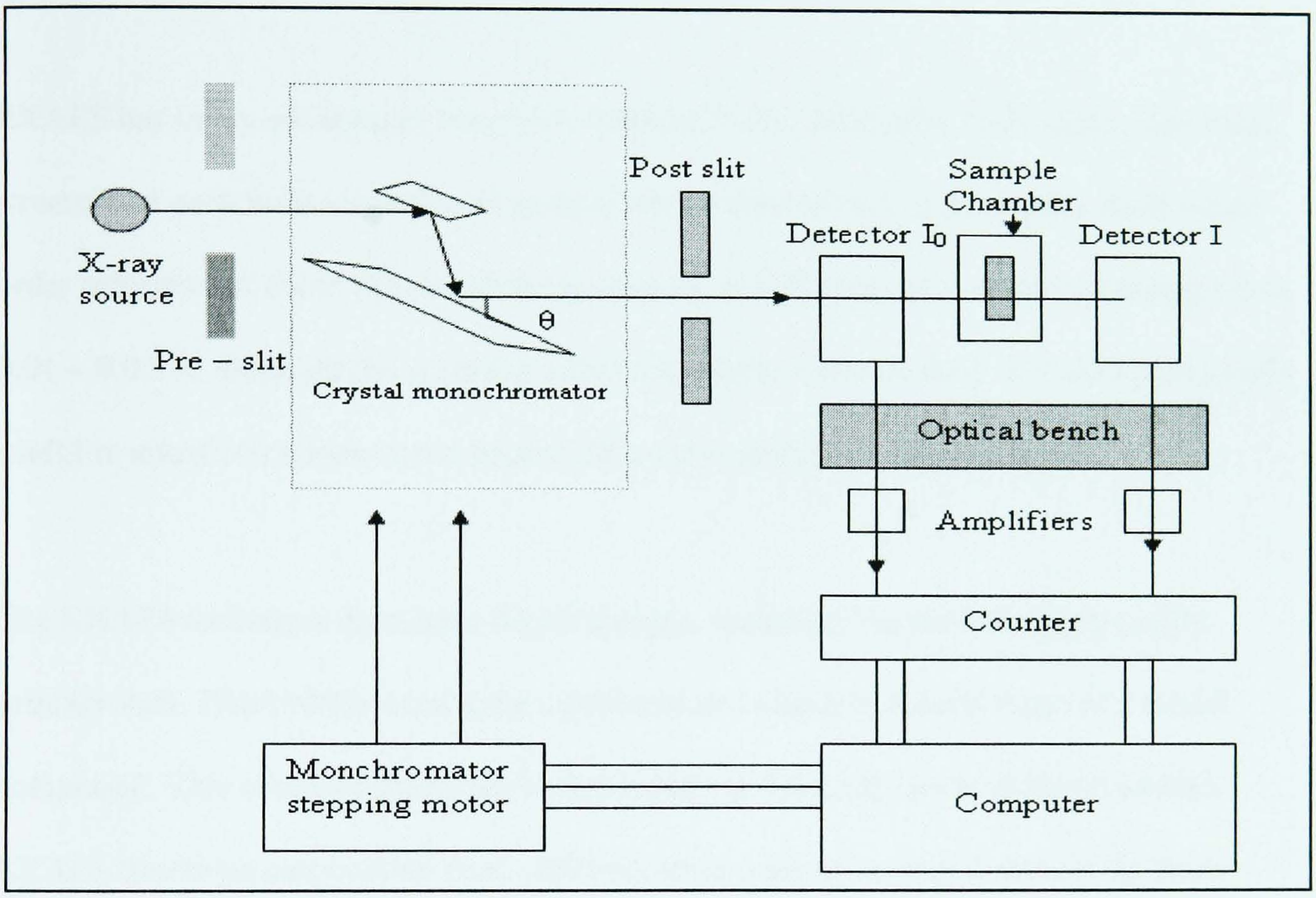

Figure 2.13 Typical experimental configuration of a transmission EXAFS experiment

Samples can be located in ovens, pressure chambers and vacuum chambers during measurement. One of the requirements for the sample is that it is uniformly thin and homogeneous. Ion chambers are used as detectors in the transmission mode as only a small fraction of the incident intensity is depleted by them. The ion chambers work on the principle of measuring the photoion current. Ion chambers have a gas mixture in them which can be readily adjusted to achieve the optimum detector absorption for the atom under investigation. The measured photo-currents are converted into voltages which are recorded by a computer which also controls the stepping motor movement for the monochromator. EXAFS are typically recorded between 800 and 1000 eV above the absorption edge.

EXAFS has many advantages over conventional X–ray diffraction techniques. The local structure of each individual atomic species can be determined, and provides short range order information about the absorbing species up to a distance of 6 Å with accuracy of *ca.* 0.01 – 0.03 Å; although the accuracy with outer shells is diminished. It is also particularly useful in situations where conventional diffraction methods cannot be used.

The EXAFS technique does have disadvantages, including the need for high quality primary data. Phase shifts need to be calculated and checked against those of a model compound. This creates difficulties in that model compounds can be difficult to find. EXAFS functions can overlap from different atom pairs at various distances. In these cases where there is fitting of multiple shells it is easy to overinterpret the data. Coordination numbers can only be ascertained to within an error of 10 – 30 %, increasing with shells at greater distances. One of the principal causes of error in the assignment of co-ordination number is multiple scattering effects. If atoms are arranged in a linear array, amplitude enhancement can be given to the outer shells which suggest a higher coordination number than is actually present. Further difficulties in assigning coordination number come from differentiating between a reduction in coordination number and an increase in thermal disorder, the Debye-Waller factor. For these reasons EXAFS should be used to complement other structural data and not used as the sole structural determination technique.

REFERENCES

1. A.R. West, *" Solid State Chemistry and Its Application "* John Wiley & Sons, Chichester, 1992
2. C. Kittel, *"Introduction to Solid State Physics",* John Wiley & Sons, New York, 7th ed., 1996
3. M.J.Buerger, *"X-ray Crytallography",* John Wiley & Sons, New York, 1942
4. W. Kraus and G. Nolze, *PowderCell for Windows V2.3,* 1999
5. H.P.Klug and L.E. Alexander, *"X-ray Diffraction Procedures for Polycrystalline and Amorphous Materials"* Wiley, New York, 1974
6. N.N. Greenwood and T.C.Gibb, *"Mössbauer Spectroscopy"Chapman and Hall,* London, 1971
7. D.P.E.Dickson and F.J. Berry, *"Mössbauer Spectroscopy"* Cambridge University Press, Cambridge, 1986
8. F.J. Berry, *"The Mössbauer Effect in Supported Microcrystallites",* Advances in Inorganic Chemistry and Radiochemistry, Vol. 21, Ed. H.J. Emeleus and A.G.Sharp, Academic Press, New York, 1978
9. N.W. Hurst, S.J.Gentry, A.Jones and B.D.McNicol, *Catal. Rev. Sci.Eng.,* 1982, **24**, 233
10. D.A.M.Monti and A.Baiker, *J. Catal.,* 1983, **83**, 323.
11. G. A. Waychunas, G. E. Brown and M. J. Apted, *Phys. Chem. Minerals,* 1986, **13,** 31
12. J. C. J. Bart and G.Vlaic, *Adv. Catalysis,* Vol 35, Academic Press, New York, 1987, p.1

13. D. G. Stearns and M. B. Stearns *"Extended X-ray Absorption fine Structure"* in Microscopic Methods in Metals, U. Gonser, ed., *Topics in Current Physics,* Vol 40, Springer-Verlag, Berlin-Heidelberg, 1986 p.153

14. G. A. Waychunas, M. J. Apted and G.E. Brown, *Phys. Chem. Minerals,* 1983, **10**, 1

15. P. A. Lee, P.H. Citrin, P. Eisenberger and B. M. Kincaid, *Reviews of Modern Physics,* 1981, **53**, 769

16. B. K. Teo and D. C. Joy *in "EXAFS Spectroscopy: Techniques and Application" Proceedings of 1979 meeting of the Materials Research Society,* November 26-30, 1979, Boston, Massachusetts, B.K. Teo and D. C. Joy, Plenum Press, New York, 1981

17. B. K. Teo *"EXAFS: Basic Principles and Data Analysis",* Springer-Verlag, Berlin-Heidelberg, 1986

Chapter 3

EXPERIMENTAL

Chapter 3

EXPERIMENTAL

3.1 PREPARATION OF MATERIALS

3.1.1 Perovskite-Related Phases

3.1.1.1 $La_{1-x}Sr_xFe_{1-y}Co_yO_3$ (Conventional Method)

Compounds of the type $La_{1-x}Sr_xFe_{1-y}Co_yO_3$ were prepared by grinding appropriate quantities of lanthanum (III) oxide, strontium (II) carbonate, α-iron(III) oxide and cobalt(II) oxide in an agate pestle and mortar followed by heating in air at 1250 °C (24h).

3.1.1.2 $La_{1-x}Sr_xFe_{1-y}Co_yO_3$ (Milling)

The materials were prepared by dry milling the reactant oxides in air using a Retsch PM 400 planetary ball mill with stainless steel balls and vials (250ml) at a milling speed of 200 rpm. The powder to ball mass ratio was 1:20.

3.1.1.3 $SrFe_{1-x}Co_xO_3$ (Conventional Method)

Compounds of the type $SrFe_{1-x}Co_xO_3$ were prepared by grinding appropriate quantities of strontium (II) carbonate, α-iron(III) oxide and cobalt(II) oxide in an agate pestle and mortar followed by heating in air at 1250 °C (24h).

3.1.1.4 $SrFe_{1-x}Sn_xO_3$(Conventional Method)

Compounds of the type $SrFe_{1-x}Sn_xO_3$ were prepared by grinding appropriate quantities of strontium (II) carbonate, α-iron(III) oxide and Tin(IV) oxide in an agate pestle and mortar followed by heating in air at 1250 °C (24h).

3.1.1.5 Ba_2SnO_4

The material was prepared by the solid state reaction of $BaCO_3$ and SnO_2, mixed in appropriate molar ratio in a pestle and mortar, and the heated at 1250°C for 24 hours in air before slowly cooling to room temperature

3.1.1.6 Fluorination of $La_{1-x}Sr_xFe_{1-y}Co_yO_3$

Fluorinated derivatives of $La_{1-x}Sr_xFe_{1-y}Co_yO_3$ were made by solid state reaction between this compound and poly(vinylidene difluoride) (PVF), $(-CH2-CF2-)_n-)$, in a molar ratio of 1:0.75. About 0.4g of the perovskite-related phase was heated with PVF in a boat crucible at temperatures of 400°C and 350 °C for 24 hours in a nitrogen gas flow.

3.1.1.7 Fluorination of $SrFe_{1-x}Co_xO_3$

Fluorinated derivatives of $SrFe_{1-x}Co_xO_3$ were made by solid state reaction between this compound and poly(vinylidene difluoride) (PVF) in a molar ratio of 1:0.75. About 0.4g of the perovskite-related phase was heated with PVF in a boat crucible at temperatures of 400°C for 24 hours in a nitrogen gas flow.

3.1.1.8 Fluorination of $SrFe_{1-x}Sn_xO_3$

Fluorinated derivatives of $SrFe_{1-x}Sn_xO_3$ were made by solid state reaction between this compoound and poly(vinylidene difluoride) (PVF) in a molar ratio of 1:0.75. About 0.4g of the perovskite-related phase was heated with PVF in a boat crucible at temperatures of 400°C for 24 hours in a nitrogen gas flow.

3.1.1.9 Fluorination of Ba_2SnO_4

Fluorinated Ba_2SnO_4 was made from a 1:1.5 molar ratio mixture of Ba_2SnO_4 (*ca.* 0.4g) and ZnF_2 in a boat crucible at 240°C for 24 hours in a nitrogen gas flow.

3.1.2 Rutile-Related Phases

3.1.2.1 Metal Antimonate (Conventional)

$FeSbO_4$ was formed by heating a mixture of α-Fe_2O_3 and Sb_2O_3 in air at 900°C (56h), cooling to room temperature and then grinding in a pestle and mortar before re-heating in air at 1000°C (48h). $VSbO_4$ was formed by heating a mixture of Sb_2O_3 and V_2O_5 at 600°C for 12 hours and then 750°C for 18 hours.

3.1.2.2 Metal Antimonate (Milling)

Mixtures of α-Fe_2O_3 or V_2O_5 and Sb_2O_3, with a transition metal to antimony ratio of 1:1, were dry milled in air or argon in a Retsch PM400 planetary ball mill using stainless steel vials (250ml) and balls at 200 rpm. The powder to ball weight ratio was 1:20.

3.2 TECHNIQUES

3.2.1 X-Ray Powder Diffraction

X-ray powder diffraction patterns were recorded at 298K with a Siemens D5000 diffractometer using Cu-Kα radiation. Lattice parameters were recorded using the program PowderCell for windows version 2.4.[1] The refinements of some X-ray powder diffraction patterns presented in Chapters 4 and 5 were performed using the programmes FullProf [2]and Maud[3].

3.2.2 Temperature Programmed Reduction

Temperature programmed reduction profiles were recorded from *ca.* 150 mg samples in flowing 10% H_2/ 90% N_2 (15-20ml/min) with the temperature being increased by 5°C/min.

3.2.3 X-Ray Absorption Spectroscopy

XANES and EXAFS measurements were performed at the Synchrotron Radiation Source at Daresbury Laboratory operating at an energy of 2.0 GeV and an average current of 200mA. Fe-, Co-K-edge were recorded at 298K in Station 7.1, Sn-K, La-L_{III} and Sr K-edges were recorded at 298K on station 9.2. The edge profiles were separated from the EXAFS data and, after subtraction of a linear pre-edge background, normalised to the edge step. The X-ray absorption edge was defined as the energy at which the normalised absorption was 0.5, i.e. the absorption at half-height of the edge step. The EXAFS oscillations were isolated after background subtraction of the raw data using the Daresbury program EXBACK and converted into *k* space. The data were weighted by k^3, where *k* is the photoelectron wave vector, to compensate for the diminishing amplitude of EXAFS at high *k*. The data were fitted using the Daresbury program EXCURV98.[4]

3.2.4 Mössbauer Spectroscopy

^{57}Fe Mössbauer spectra were recorded at 298K with a constant acceleration spectrometer in transmission geometry using a 400 M Bq ^{57}Co/Rh source. Measurements at 77K were performed with similar equipment in The University of Liverpool. The drive velocity was calibrated with the ^{57}Co/Rh source and a natural iron foil. All the isomer shift data are reported relative to that of metallic iron at room temperature.

^{121}Sb Mössbauer spectra were recorded at 77K in The University of Liverpool using a Ca $^{121}SnO_3$ source. The chemical isomer shift data are quoted relative to InSb as a standard.

^{119}Sn Mössbauer spectra were recorded at 77K with a constant acceleration spectrometer using a *ca.* 25 mCi $Ca^{119}SnO_3$ source. The ^{119}Sn Mössbauer chemical isomer shift data are quoted relative to SnO_2.

REFERENCES

1. W. Kraus and G. Nolze, *PowderCell for windows version 2.4,* Federal Institute for Materials Research and Testing Rudower Chaussee, Berlin, 2000
2. J. Rodríguez-Carvajal, *PROGRAM FULLPROF.2k, Version 1.9c,* LLB JRC, 5, 2001
3. L. Lutterotti, S. Matthies and H. -R. Wenk, *MAUD (Material Analysis Using Diffraction)*
4. N. Binsted, *EXCURV98,* CCLRC Daresbury Labaratory Computer Program, 1998

Chapter 4

RESULTS AND DISCUSSION: PEROVSKITE-RELATED PHASES: PREPARATION BY CONVENTIONAL- AND MILLING-TECHNIQUES AND STUDIES OF REDUCTION PROPERTIES

Chapter 4

RESULTS AND DISCUSSION: PEROVSKITE-RELATED PHASES: PREPARATION BY CONVENTIONAL- AND MILLING-TECHNIQUES AND STUDIES OF REDUCTION PROPERTIES

4.1. INTRODUCTION

This chapter reports on the:

1. Preparation of materials of the type $LaFe_{1-x}Co_xO_3$ by calcination and milling techniques,
2. Evaluation of the influence of cobalt on the reducibility of the perovskite-related phases,
3. Comparison between the reducibility of materials made by conventional- and milling-materials,
4. Preparation and examination of the reducibility of materials of the type $La_{0.5}Sr_{0.5}MO_3$ (M= Fe, Co) made by conventional methods.

4.2 $LaFe_{1-x}Co_xO_3$ (CONVENTIONAL PREPARATION)

The X-ray powder diffraction patterns recorded from $LaFe_{1-x}Co_xO_3$ (x = 0, 0.1, 0.5, 0.9, 1) are shown in Figure 4.1. The results show the materials are single phases. Transmission Electron microscopy showed all the powders to have a particle size of *ca.* 2 μm.

The X-ray powder diffraction patterns showed the perovskite-related $LaFe_{1-x}Co_xO_3$ to transform from the orthorhombic $LaFeO_3$- to the hexagonal $LaCoO_3$-type structure between x = 0.1 and x = 0.5 and are consistent with previous reports[1,2]. The lattice

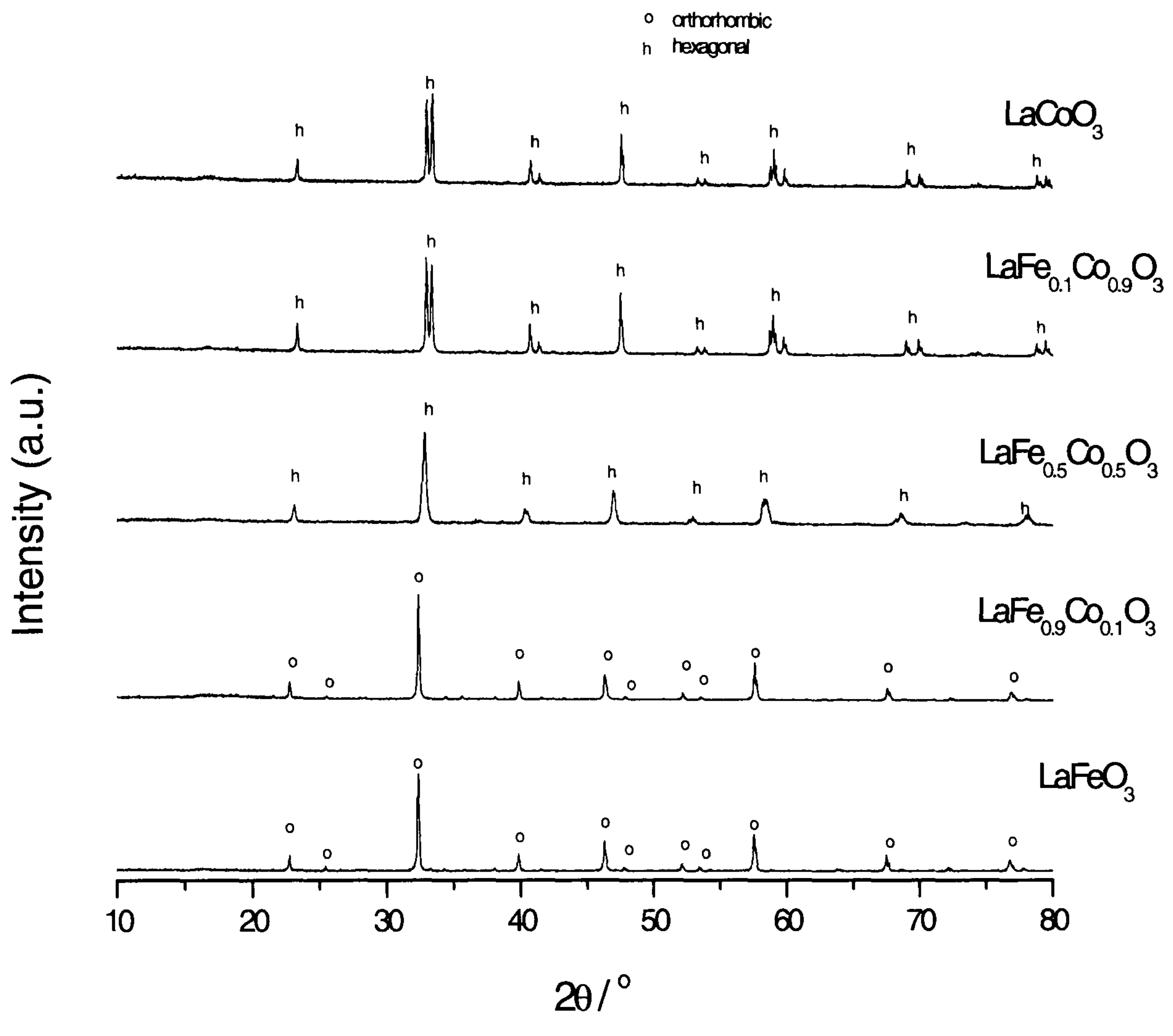

Figure 4.1 X-ray powder diffraction patterns recorded from $LaFe_{1-x}Co_xO_3$ (x = 0, 0.1, 0.5, 0.9, 1) made by conventional methods

parameters (Table 4.1) calculated according to the adoption of the orthorhombic or hexagonal unit cell were similar to those reported earlier[2].

Table 4.1. Lattice parameters for compounds of the type $LaFe_{1-x}Co_xO_3$

x	unit cell $^+$	*a* (Å) ±0.01	*b* (Å) ±0.01	*c* (Å) ±0.01
0.0	O	5.58	7.85	5.55
0.1	O	5.54	7.85	5.54
0.5	H	5.51		13.40
0.9	H	5.45		13.31
1.0	H	5.44		13.09

$^+$O = Orthorhombic, H = Hexagonal

$LaFeO_3$

The temperature programmed reduction (tpr) profile recorded from the compound $LaFeO_3$ (Figure 4.2) showed two broad peaks at *ca* 480 °C and 1150 °C. The

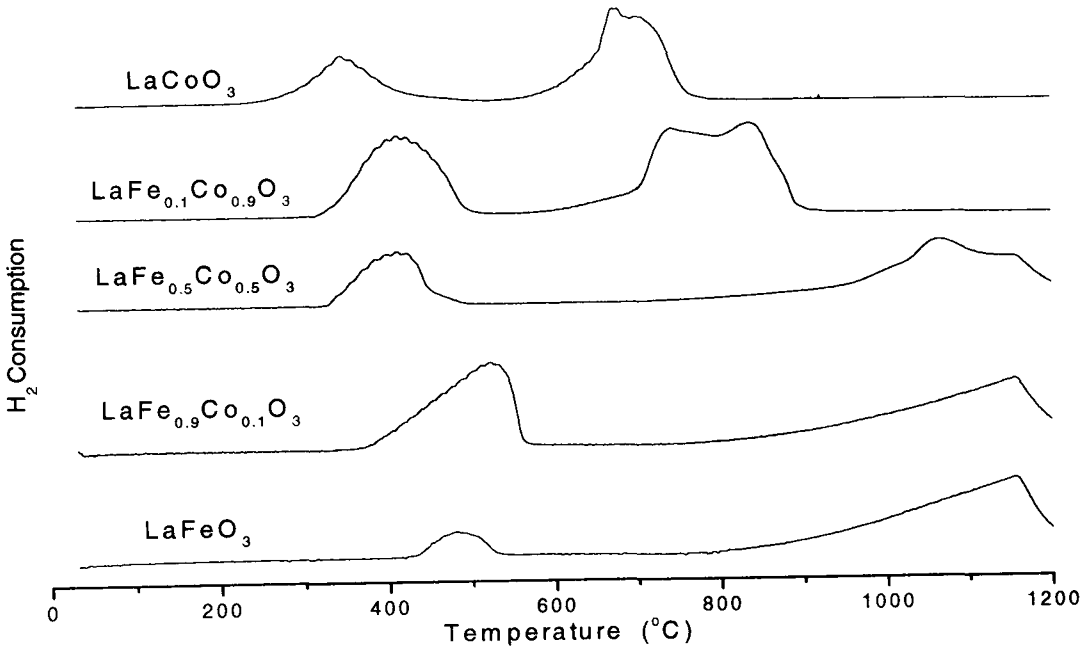

Figure 4.2 Temperature programmed reduction profiles recorded from $LaFe_{1-x}Co_xO_3$ (x = 0, 0.1, 0.5, 0.9, 1) made by conventional methods.

temperatures at which the peak maxima were observed were sensitive to the gas flow rate and hence all data reported here were recorded at a flow rate of 15-20 ml/min. The X-ray powder diffraction patterns recorded from reduced materials were of poor quality and difficult to interpret and are not shown in this thesis.

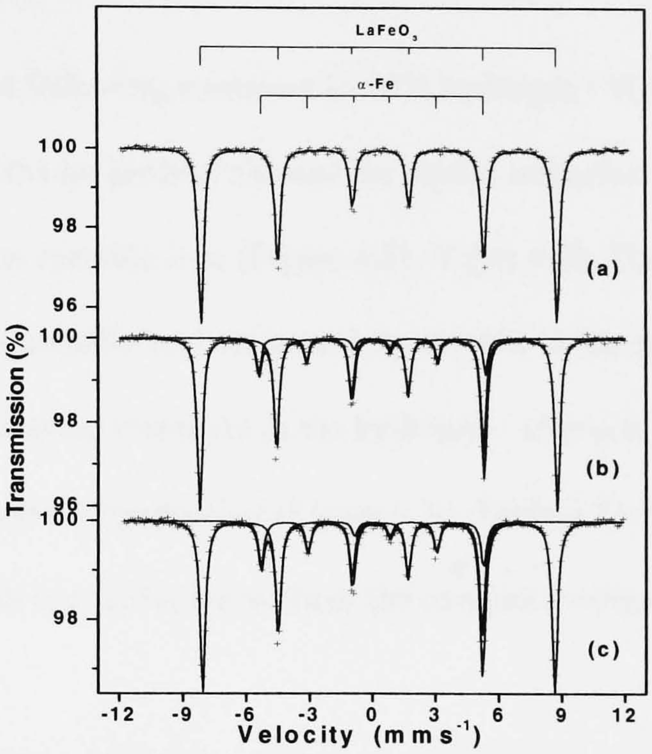

Figure 4.3 ^{57}Fe Mössbauer spectra recorded at 298 K from (a) LaFeO$_3$ made by conventional methods and following reduction at (b) 550°C and (c) 1200 °C.

Table 4.2 ^{57}Fe Mössbauer parameters recorded from LaFeO$_3$ made by conventional methods following treatment in 10% hydrogen/90% nitrogen.

	Assignment	$\delta \pm 0.01$ mms^{-1}	Δ* or $2\varepsilon^{\dagger} \pm$ 0.02 mms^{-1}	$H \pm 0.5$ T	Spectral Area ± 3 %
LaFeO$_3$	Fe^{3+}	0.36	-0.09	52.7	100
Following treatment in 10% hydrogen/90% nitrogen at 550°C	Fe^{3+} Fe^{0}	0.36 0.00	−0.07 0.00	52.3 33.0	84 16
Following treatment in 10% hydrogen/90% nitrogen at 1200°C	Fe^{3+} Fe^{0}	0.35 0.00	−0.07 0.00	52.4 33.2	78 22

* quadrupole split absorption

† magnetically split absorption

The ^{57}Fe Mössbauer spectra recorded from $LaFeO_3$ and following treatment under temperature programmed reduction conditions are shown in Figure 4.3. The ^{57}Fe Mössbauer parameters are collected in Table 4.2. The ^{57}Fe Mössbauer spectrum recorded from $LaFeO_3$ (Figure 4. 3a) was composed of a sextet pattern similar to that reported earlier[3].

The spectrum recorded following treatment in 10% hydrogen / 90% nitrogen at 550°C (after the first peak in the tpr profile) showed the partial reduction of the perovskite-related $LaFeO_3$ phase to metallic iron (Figure 4.3b, Table 4.2). The intensity of the sextet characteristic of metallic iron amounted to *ca.* 16% of the spectral area. The spectrum recorded following treatment in the hydrogen / nitrogen gas mixture at 1200°C (after the second peak in the tpr profile) (Figure 4.3c, Table 4.2) showed an increased amount of metallic iron (*ca.* 22%) but without the complete reduction of lanthanum orthoferrite.

The Fe K-edge XANES and EXAFS results are shown in Figures 4.4 and 4.5, respectively. The shape of the Fe K-edge XANES recorded from $LaFeO_3$ (Figure 4.4(i)a) was similar to that reported previously[4]. The positions of the edge at 7126.0 eV and that of the edge crest at 7130.4 eV are characteristic of the presence of trivalent iron[5]. The Fe K-edge XANES recorded from the samples following treatment in hydrogen and nitrogen (Figure 4. 4(i) b and c) showed the presence of a pre-edge feature at ca. 7114.2 eV which is close to the first inflexion point of the absorption edge of metallic iron. The intensity of this pre-edge feature increased with increasing temperature treatment in the reducing atmosphere. This is consistent with the ^{57}Fe Mössbauer spectroscopy results and is indicative that the extent of reduction to metallic iron increases with treatment under reducing conditions at increasing temperatures. The existence of an increasing contribution of metallic iron is more clearly seen in the first derivative of the absorption edge (Figure 4.4 (i) a'-c') which clearly shows changes in the region 7105-7115 eV in the data recorded from materials treated under reducing conditions particularly the appearance of a maximum at 7112.4 eV which can be associated with the presence of metallic iron.

The Fe K-edge EXAFS recorded from $LaFeO_3$ (Figure 4.5 (i)) were fitted according to the previously reported diffraction data[6] (Table 4.3). The results are in good agreement

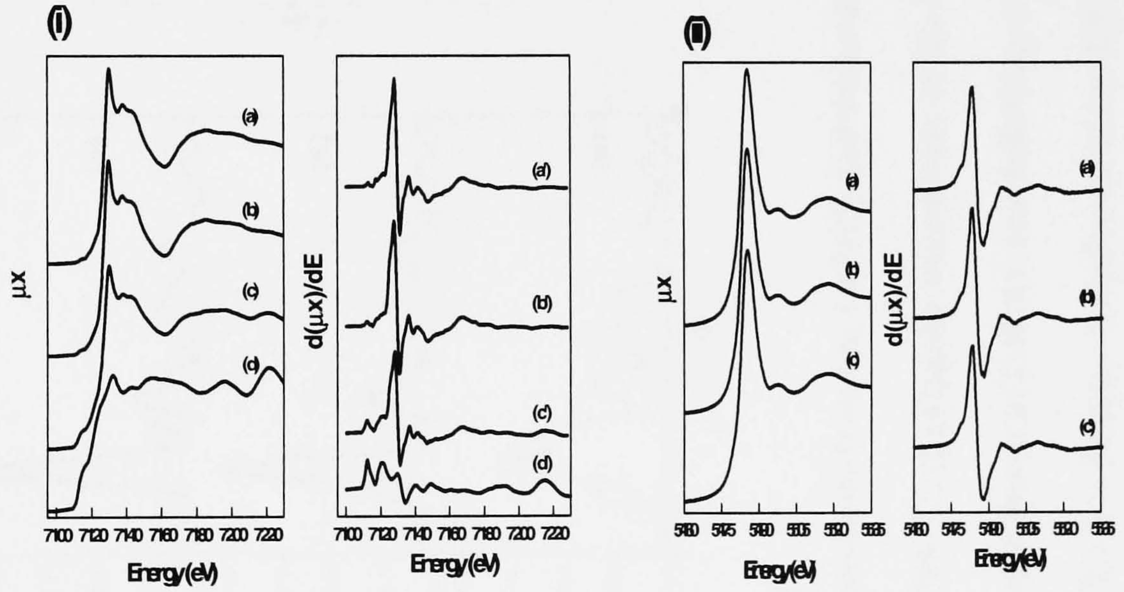

Figure 4.4 (i) Fe K-edge- and (ii) La L_{III}-edge- XANES recorded from (a) $LaFeO_3$ and following treatment in a 10% hydrogen / 90% nitrogen gas mixture at (b) 550 °C and (c) 1200 °C. (a'), (b') and (c') are the first derivative of (a), (b) and (c), respectively. The spectrum presented in (i) (d) corresponds to iron metal. (d') is the first derivative of (d).

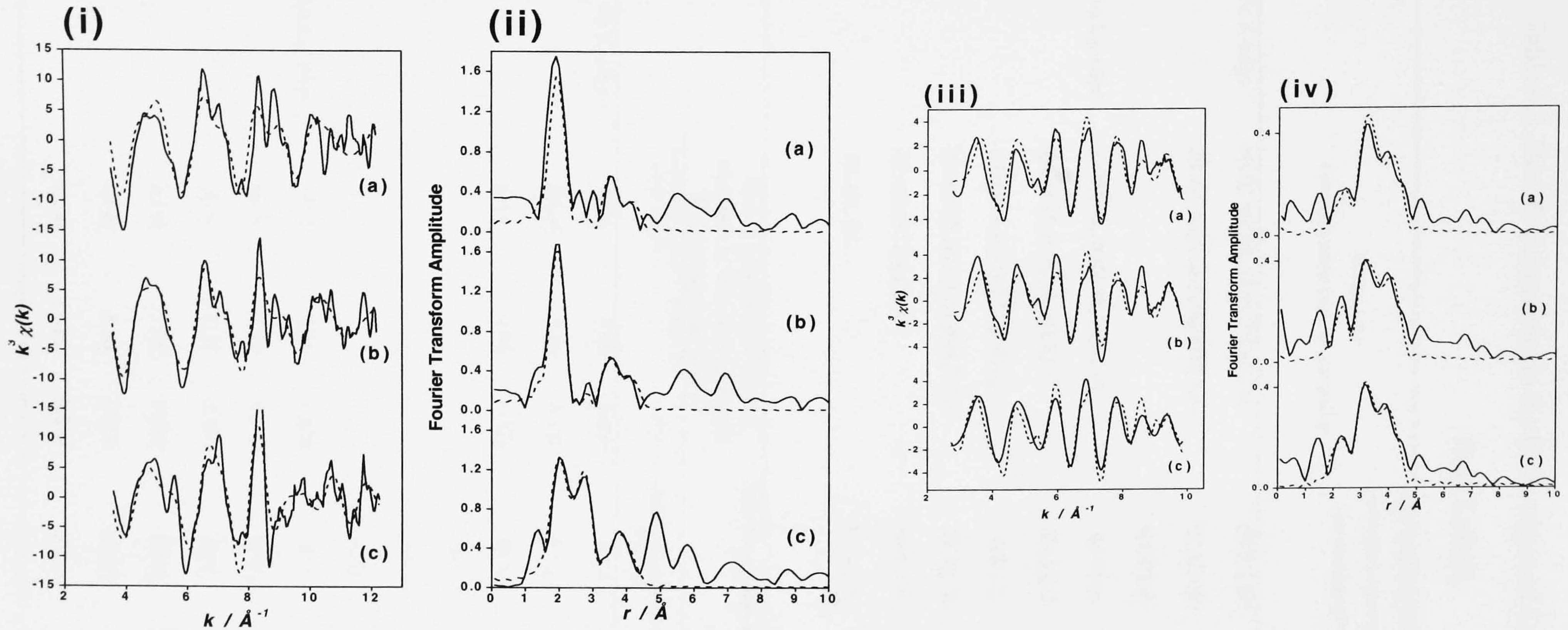

Figure 4.5 (i) Fe K-edge-EXAFS (raw data) recorded from (a) LaFeO$_3$ and following treatment in a hydrogen/nitrogen gas mixture at (b) 550 °C and (c) 1200 °C; (ii) Fourier transforms of the EXAFS data presented in (i). (iii) La L$_{III}$-edge- EXAFS (raw data) recorded from (a) LaFeO$_3$ and following treatment in a hydrogen/nitrogen gas mixture at (b) 550 °C and (c) 1200 °C; (iv) Fourier transforms of the EXAFS data presented in (iii). (The experimental data are indicated by a solid line and the fits to the data are indicated by a broken line.)

Table 4.3 Best fit parameters to the Fe K-edge and La L_{III}-edge EXAFS data recorded from $LaFeO_3$

	Diffraction data Coordination number [atom type] and distance[6]	Initial model for EXAFS Coordination number [atom type] and distance(Å)	Best fit parameters to $LaFeO_3$		
			Coordination number and [atom type]	d/ Å (±0.02)	$2\sigma^2$/ Å^2
Fe K-edge	6[O]2.00,2[La]3.28,2[La]3.39,	6[O] 2.00	6[O]	1.98	0.010
	2[La]3.43,2[La]3.54,6[Fe] 3.93	8[La] 3.41	8[La]	3.30	0.032
		6[Fe]3.93	6[Fe]	4.00	0.026
La L_{III}-edge	1[O]2.44,2[O]2.46,1[O]2.59,	3[O]2.46	3[O]	2.47	0.032
	2[O]2.65,2[O]2.80,1[O]3.03,	6[O]2.76	6[O]	2.71	0.050
	1[O]3.14,2[O]3.27,2[Fe]3.28,	3[O]3.22	3[O]	3.27	0.006
	2[Fe]3.39,2[Fe]3.43,2[Fe]3.54,	2[Fe]3.28	2[Fe]	3.36	0.029
	2[La]3.88, 2[La]3.94,	6[Fe]3.45	6[Fe]	3.43	0.042
	2[La]3. 98,	6[La]3.94	6[La]	3.90	0.023

	Best fit parameters following treatment in 10% hydrogen and 90% nitrogen at 550 °C			Best fit parameters following treatment in 10% hydrogen and 90% nitrogen at 1200 °C		
	Coordination number and [atom type]	d/ Å (±0.02)	$2\sigma^2$/ Å^2	Coordination number and [atom type	d/ Å (±0.02)	$2\sigma^2$/ Å^2
Fe K-edge	6[O]	1.99	0.090	6[O]	1.99	0.015
	8[La]	3.26	0.030	8[La]	3.26	0.048
	6[Fe]	3.98	0.020	6[Fe]	4.11	0.001
				2.5[Fe]	2.47	0.017
				1.5[Fe]	2.86	0.004
				6[Fe]	3.99	0.011
La L_{III}-edge	3[O]	2.45	0.020	3[O]	2.43	0.020
	6[O]	2.70	0.040	6[O]	2.67	0.030
	3[O]	3.24	0.020	3[O]	3.31	0.017
	2[Fe]	3.48	0.030	2[Fe]	3.52	0.005
	6[Fe]	3.36	0.030	6[Fe]	3.34	0.017
	6[La]	3.89	0.020	6[La]	3.89	0.030

with this model, the Fe K-edge EXAFS being dominated by a first coordination shell of 6 oxygen atoms at 1.98 Å (Figure 4.5(ii)a) which, given the XANES data, is consistent with an octahedrally coordinated Fe^{3+} species. The changes brought about by treatment in hydrogen and nitrogen are best appreciated by consideration of the Fe K-edge EXAFS (and the corresponding Fourier transform) recorded from the sample treated at 1200 °C (Figure 4.5(i)c, Table 4.3) which clearly showed a contribution from metallic iron (Fe-Fe distance at 2.47 Å (Figure 4.5(ii)c)) together with the $LaFeO_3$ contribution characterized by an Fe-O distance in the first coordination shell of 1.99 Å. The shells at *ca.* 3-3.5 Å correspond to Fe-La distances existing in the $LaFeO_3$ structure[6].

The La L_{III}-edge XANES (Figure 4.4(ii)) were similar to those recorded from La_2O_3 and were compatible with the presence of La^{3+}. The La L_{III}-edge EXAFS (Figure 4.5 (iii) and (iv)) were successfully fitted (Table 4.3) to a shell of 12 oxygen atoms according to the previously reported structural information[6] deduced from diffraction data. A distinctive feature of the La L_{III}-edge XANES and EXAFS recorded from $LaFeO_3$ following treatment in the hydrogen/nitrogen gas mixture is their similarity to the data recorded from the original material (Figures 4.4(ii)a-c and 4.5(iii) and (iv) a-c) indicative of the resistance of the trivalent lanthanum ion to a change in oxidation state or local coordination in the gaseous reducing atmospheres.

Hence the results recorded from Mössbauer spectroscopy, XANES and EXAFS show that treatment of $LaFeO_3$ in the hydrogen/nitrogen gas mixture results in partial reduction of Fe^{3+} which segregates from the structure to form metallic iron but without collapse of the perovskite-related structure and /or the reduction and segregation of lanthanum-containing phases.

$LaFe_{0.9}Co_{0.1}O_3$

The ^{57}Fe Mössbauer spectrum recorded from $LaFe_{0.9}Co_{0.1}O_3$ (Figure 4.6a, Table 4.4) (δ = 0.36 mms^{-1}, 2ε = -0.09 mms^{-1}, H = 51.5 T). was similar to that of $LaFeO_3$ (Table 4.2). The broader linewidth may reflect the introduction of cobalt into the cationic sublattice. The tpr profile recorded from $LaFe_{0.9}Co_{0.1}O_3$ is shown in Figure 4.2. The ^{57}Fe Mössbauer spectrum recorded after the first peak in the tpr profile (Figure 4.6b, Table 4.4) showed, besides the oxide contribution, an additional sextet with parameters (δ = 0.05 mms^{-1}, 2ε = 0.00 mms^{-1}, H = 36.1 T) that are compatible with the presence of *ca.* 10% Fe-Co alloy[8]. The results indicate that the Fe^{3+} and Co^{3+} in $LaFe_{0.9}Co_{0.1}O_3$ are both partially reduced and form an alloy. The ^{57}Fe Mössbauer spectrum recorded after the second reduction peak (Figure 4.6c, Table 4.4) showed the coexistence of metallic iron, an Fe-Co alloy, and the $LaFe_{0.9}Co_{0.1}O_3$ phase, with relative spectral areas of 16 %,

Table 4.4 ^{57}Fe Mössbauer parameters recorded from $LaFe_{0.9}Co_{0.1}O_3$ following treatment in 10% hydrogen/90% nitrogen

	Assignment	$\delta \pm 0.01$ mms^{-1}	Δ* or $2\varepsilon^{\dagger}$ ± 0.02 mms^{-1}	$H \pm 0.5$ T	Spectral Area ± 3 %
$LaFe_{0.9}Co_{0.1}O_3$	Fe^{3+}	0.36	-0.09	51.5	100
Following treatment in 10% hydrogen/90% nitrogen at 600°C	Fe^{3+}	0.37	−0.02	51.8	90
	Fe^0 (Fe-Co alloy)	0.05	0.00	36.1	10
Following treatment in 10% hydrogen/90% nitrogen at 1200°C	Fe^{3+}	0.37	0.01	51.7	65
	Fe^0 (Fe-Co alloy)	0.04	0.01	36.0	19
	Fe^0	0.00	0.00	33.6	16

* quadrupole split absorption
† magnetically split absorption

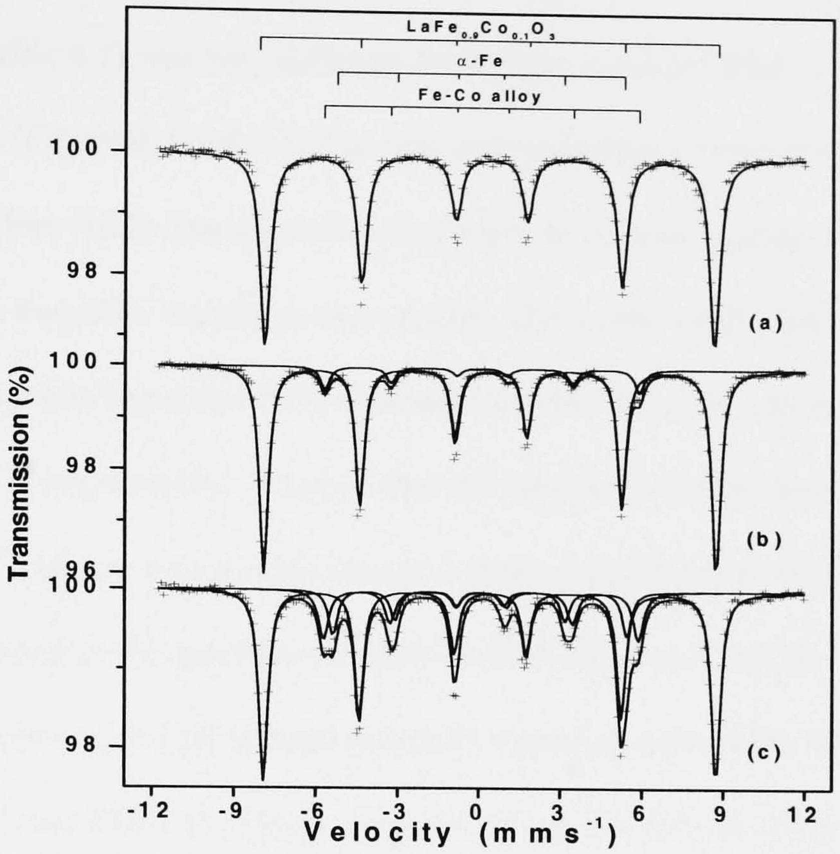

Figure 4.6 ^{57}Fe Mössbauer spectra recorded at 298 K from (a) $LaFe_{0.9}Co_{0.1}O_3$ and following treatment in hydrogen and nitrogen at (b) 600°C and (c) 1200°C.

19% and 65%, respectively. The result contrasts with that recorded from $LaFeO_3$ under reducing conditions in that the presence of cobalt appears to induce a greater degree of reduction, the segregation of both iron and cobalt, and the formation of metallic- and alloy- phases. However, it is interesting to note the stability of $LaFeO_3$ and $LaFe_{0.9}Co_{0.1}O_3$ to complete reduction in the hydrogen /nitrogen gas mixture at 1200 °C and that under these conditions reduction does not lead to total destruction of the oxide structure. The detailed fitted data were shown in Table 4.4.

$LaFe_{0.5}Co_{0.5}O_3$

The ^{57}Fe Mössbauer spectrum recorded at room temperature from $LaFe_{0.5}Co_{0.5}O_3$ (Figure 4.7a, Table 4.5) was very different from those recorded from $LaFeO_3$ and $LaFe_{0.9}Co_{0.1}O_3$. (Figure 4.3 and 4.6) The spectrum indicates a broad distribution of magnetic hyperfine fields characteristic of a system experiencing magnetic relaxation in the vicinity of a magnetic transition temperature. The isomer shift, quadrupole splitting and average magnetic hyperfine field obtained from the fit were 0.36 mms^{-1}, -0.03 mms^{-1} and 26.3T, respectively. It seems that the substitution of 50 % of the Fe^{3+} ions in $LaFeO_3$ by Co^{3+} induces a noticeable decrease in the magnetic ordering temperature. This was confirmed in the spectrum recorded at 80 K (Figure 4.7b) from the same material which showed a well-defined magnetic hyperfine pattern but with broadened linewidths and lower (49.7 T) average magnetic hyperfine field as compared with $LaFeO_3$ at room temperature (52.7 T, Table 4.2). The spectrum recorded at 10 K showed a sextet pattern with relatively broad lines and a magnetic hyperfine field of 51.1 T (Figure 4.7c).

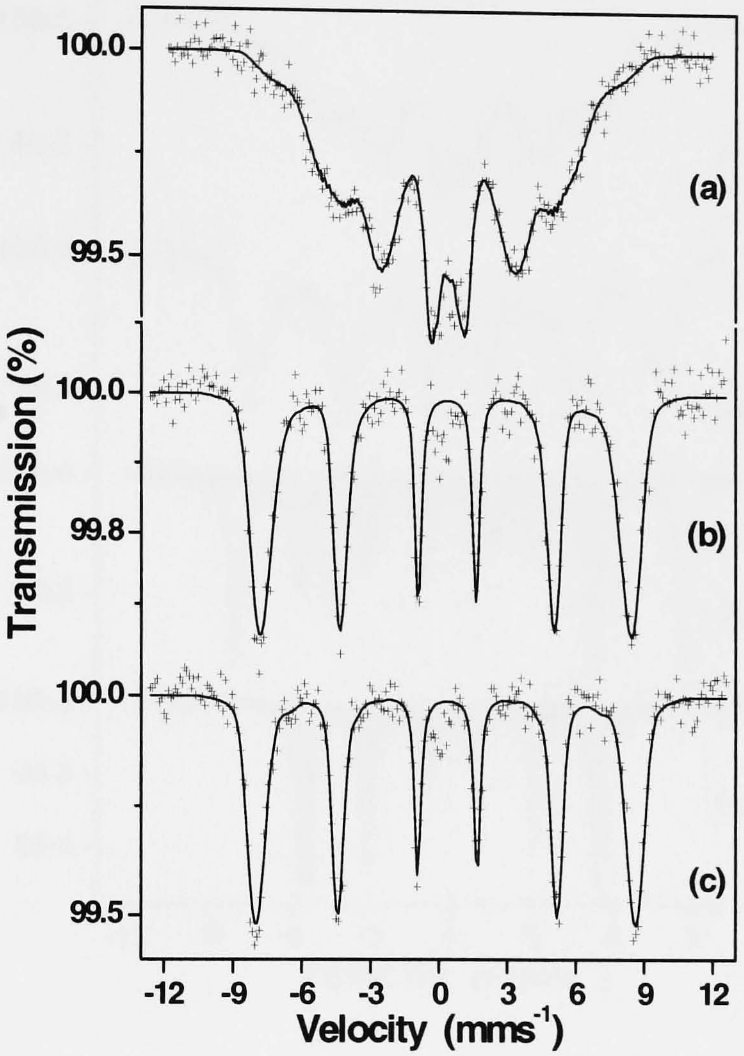

Figure 4.7 ^{57}Fe Mössbauer spectra recorded at 298, 80 and 10 K from $LaFe_{0.5}Co_{0.5}O_3$

The ^{57}Fe Mössbauer spectrum (Figure 4.8b, Table 4.5) recorded at 298 K from $LaFe_{0.5}Co_{0.5}O_3$ after treatment in the 10 % hydrogen/ 90% nitrogen gas mixture, i.e. after the first reduction peak in the profile (Figure 4.2), also showed a distribution of magnetic hyperfine fields. The broadness of the spectral lines and poor statistics

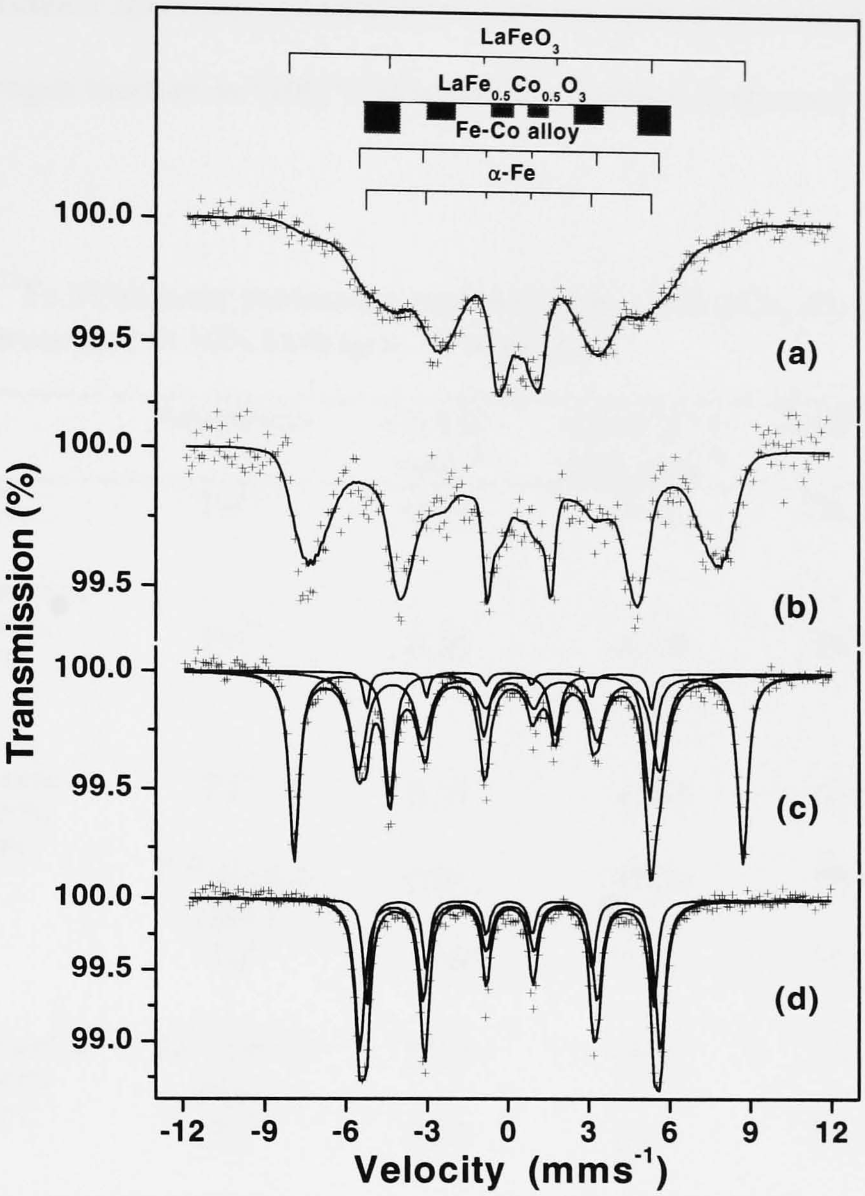

Figure 4.8 ^{57}Fe Mössbauer spectra recorded at 298 K from (a) $LaFe_{0.5}Co_{0.5}O_3$ and following reduction at (b) 500°C (c) 1000°C (d) 1200°C.

precluded the identification of a component corresponding to metallic iron. Whether or not iron and/or cobalt segregate from the material during the initial treatment in the reducing atmosphere is therefore unclear on the basis of Mössbauer spectroscopy data alone.

The ^{57}Fe Mössbauer spectrum recorded from material following treatment in the hydrogen/nitrogen mixture at 1000 °C (Figure 4.8c, Table 4.5) showed a sextet pattern (accounting for *ca.* 53% of the spectral area) with similar parameters to those of $LaFeO_3$ together with another broad sextet which was deconvoluted into two sextets: one characteristic of metallic iron (δ = 0.00 mms^{-1}, 2ε = 0.00 mms^{-1}, H = 33.0 T and Area= 6%) and a second more intense component (*ca.*41%) with Mössbauer parameters (δ = 0.04 mms^{-1}, 2ε = -0.04 mms^{-1} and H = 34.8 T) which are compatible with the presence of an iron-cobalt alloy[8]. The result indicates that treatment under reducing conditions at

Table 4.5 ^{57}Fe Mössbauer parameters recorded from $LaFe_{0.5}Co_{0.5}O_3$ following treatment in 10% hydrogen/ 90% nitrogen.

	Assignment	$\delta \pm 0.01$ mms^{-1}	Δ* or $2\varepsilon^{\dagger} \pm$ 0.02 mms^{-1}	$H \pm 0.5$ T	Spectral Area ± 3 %
$LaFe_{0.5}Co_{0.5}O_3$	Fe^{3+}	0.36	-0.03	26.3	100
Following treatment in 10% hydrogen/90% nitrogen at 500°C	Fe^{3+}	0.36	–0.19	36.7	90
Following treatment in 10% hydrogen/90% nitrogen at 1000°C	Fe^{3+}	0.37	–0.04	51.8	53
	Fe^{0} (Fe-Co alloy)	0.04	–0.04	34.8	41
	Fe^{0}	0.00	0.00	33.0	6
Following treatment in 10% hydrogen/90% nitrogen at 1200°C	Fe^{0} (Fe-Co alloy)	0.03	–0.01	35.7	67
	Fe^{0}	0.00	0.00	33.0	33

* quadrupole split absorption
† magnetically split absorption

1000°C induces the partial segregation of iron and cobalt from the perovskite-related oxide structure and the formation of metallic- and alloy-phases but without total destruction of the perovskite-related structure. The spectrum recorded from the material following further treatment in the hydrogen/nitrogen gas mixture at 1200°C (Figure 4.8d, Table 4.5) did not show any sextet component with isomer shift values which could be associated with an oxide species. It consisted of a sextet containing contributions from both metallic iron (*ca.*33%) and iron-cobalt alloy (*ca.* 67%). The magnetic hyperfine field obtained from the fit of the spectrum to the iron-cobalt alloy (35.7 T) was slightly higher than that observed in the case of the material formed at 1000°C indicating that the composition of this phase could be slightly different. The results demonstrate that in $LaFe_{0.5}Co_{0.5}O_3$, the Fe^{3+} and Co^{3+} ions in the perovskite-related structure are more susceptible to reduction than in the material of composition $LaFeO_3$ and, at high temperatures, their segregation to form metallic- and alloy- phases is accompanied by the collapse of the oxide structure.

The Fe K-edge XANES recorded from $LaFe_{0.5}Co_{0.5}O_3$ before and after tpr treatment are in good agreement with the Mössbauer data. The Fe K-edge XANES recorded from $LaFe_{0.5}Co_{0.5}O_3$ (Figure 4.9(i)a) is similar to that recorded from $LaFeO_3$ (position of the absorption edge 7126.0 eV) and is consistent with the presence of an Fe^{3+}-containing species. The Fe K-edge XANES recorded from the material treated at 500 °C in the hydrogen/nitrogen gas mixture (Figure 4.9(i)b) (i.e. after the first peak in the tpr profile, Figure 4.2) is also similar . However, close inspection of the first derivative of the absorption edge recorded from this sample (Figure 4.9(i) b') shows some small change in the region 7105-7115 eV that could be compatible with the presence of a small amount of Fe^0. The Fe K- absorption edge recorded from the material following treatment in hydrogen and nitrogen at 1000 °C (Figure 4.9(i)c)shows the presence of a pre-edge feature at *ca.* 7114.3 eV suggestive of the presence of Fe^0. Inspection of the first derivative of the absorption edge recorded from this material showed (Figure 4.9(i)c') that, although there are some oscillations compatible with the presence of Fe^{3+} within the perovskite-related structure, a considerable contribution from iron in the Fe^0 state is also present. Taken in conjunction with the Mössbauer spectroscopy data the results confirm the reduction of Fe^{3+} in the perovskite-related structure and the formation of metallic iron and the iron-cobalt alloy. The absorption edge in the Fe K-edge XANES recorded from the material treated at 1200 °C appears at 7112.4 eV (Figure 4.9(i)d). The position and shape of the edge features are compatible with the exclusive presence of Fe^0. It is interesting to note the characteristic maxima appearing in the first derivative of the absorption edge between 7105-7115 eV which lends support to the probability of Fe^0 in the spectra of the samples treated in hydrogen and nitrogen at 500 °C. The results clearly indicate that all the Fe^{3+} ions present in the original material are reduced to Fe^0 at 1200 °C in the reducing atmosphere and are consistent with the Mössbauer spectroscopy data.

The changes brought about by the tpr treatment are also well illustrated by the Fe K-edge EXAFS and their respective Fourier transforms (Figure 4.10 (i) and (ii)). The data recorded from pure $LaFe_{0.5}Co_{0.5}O_3$ (Table 4.6) were best fitted to a similar model to that used to fit the Fe K-edge EXAFS recorded from $LaFeO_3$. The shape and frequency of the EXAFS oscillations recorded from the material treated at 500 °C (Figure 4.10(i)b) are very similar to those of the original material. Consequently, the parameters obtained

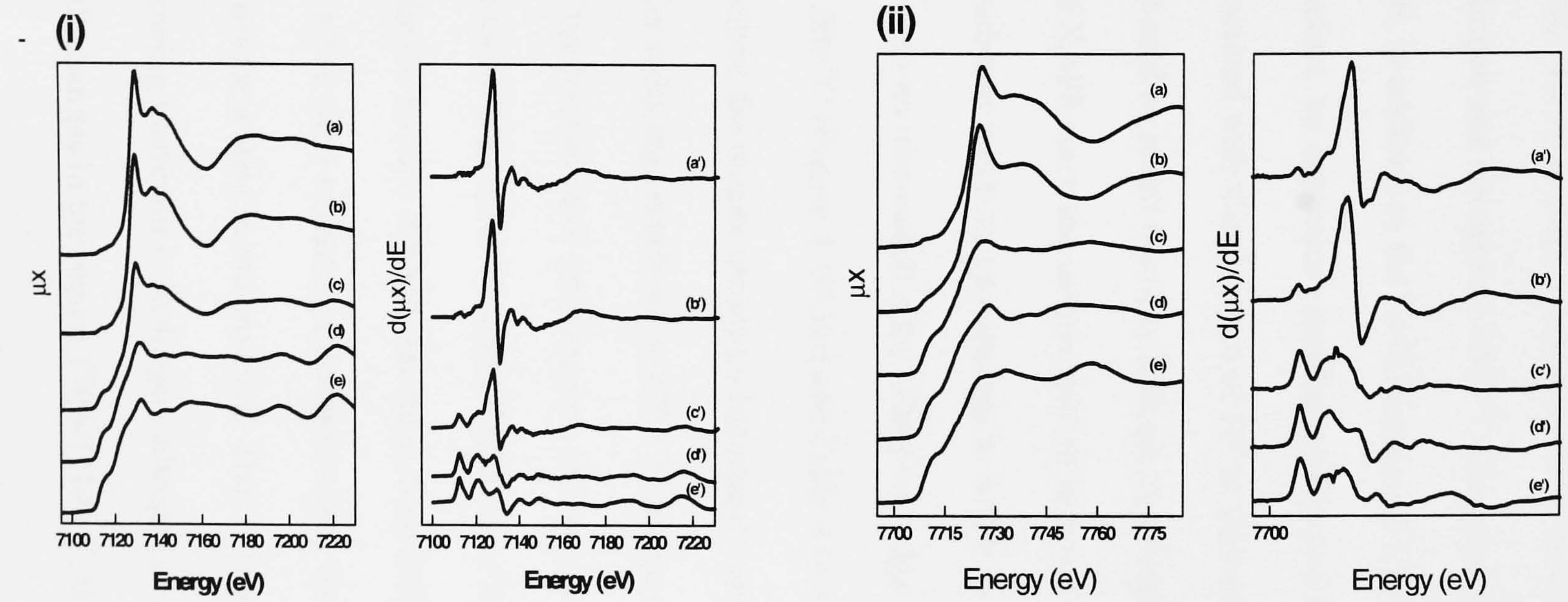

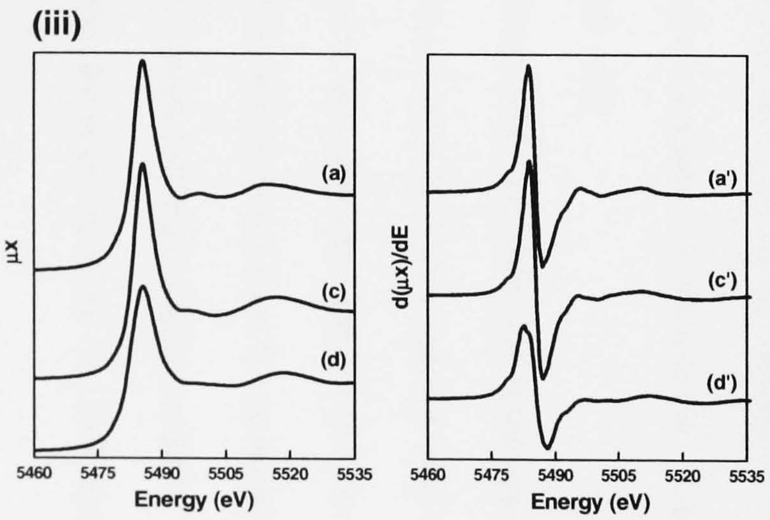

Figure 4.9 (i) Fe K-edge-, (ii) Co K-edge, and (iii) La L_{III}-edge-XANES recorded from (a) $LaFe_{0.5}Co_{0.5}O_3$ and following treatment in a hydrogen/nitrogen gas mixture at (b) 500 °C, (c) 1000 °C and (d) 1200 °C. (a'), (b'), (c') and (d') are the corresponding first derivative spectra of (a), (b), (c) and (d). The spectra presented in (i)(e) and (ii)(e) correspond to iron metal and cobalt metal, respectively. (e') is the corresponding first derivative of (e).

from the fit were also very similar. The small contribution from Fe^0 suggested by the XANES results appear not to be clearly reflected in the corresponding EXAFS. Indeed, attempts to fit the data with a contribution from Fe^0 did not significantly improve the goodness of the fit. The result implies that the extent of any reduction of iron is, at best, small. The Fe K-edge EXAFS recorded from the material following treatment in hydrogen and nitrogen at 1000 °C (Figure 4.10(i) c) showed in the first coordination shell, in addition to the Fe-O distance of 1.97 Å characteristic of Fe^{3+} in the perovskite structure, an important contribution due to a Fe-Fe/Co distance at 2.45 Å. This is associated with the presence of Fe^0 as shown by XANES and Mössbauer spectroscopy. It should be noted that it is difficult to distinguish between Fe-Fe and Fe-Co distances by EXAFS since the atomic radii of iron and cobalt are very similar. In this sense, Mössbauer spectroscopy appears to be the more sensitive technique to identify metallic iron and an iron-cobalt alloy. The Fe K-edge EXAFS recorded from the material treated at 1200 °C (Figure 4.10 (i) d and Table 4.6) was characteristic of a metallic phase and confirms the results shown by Mössbauer spectroscopy and XANES that treatment under reducing conditions at 1200 °C brings about the complete reduction of Fe^{3+} to Fe^0 and the formation of metallic iron and an iron-cobalt alloy.

The Co K-edge XANES and EXAFS show interesting trends. The position of the edge of the Co K-edge XANES recorded from $LaFe_{0.5}Co_{0.5}O_3$ at 7723.3 eV (Figure 4.9(ii) a and a') is close to that reported previously for $LaCoO_3$ [9] and confirms that cobalt is in the trivalent state in this material. The Co K-edge XANES recorded from the material following treatment in hydrogen/ nitrogen at 500 °C showed (Figure 4.9(ii) b and b') small changes in the region 7704-7714 eV. Given that the position of the first inflection

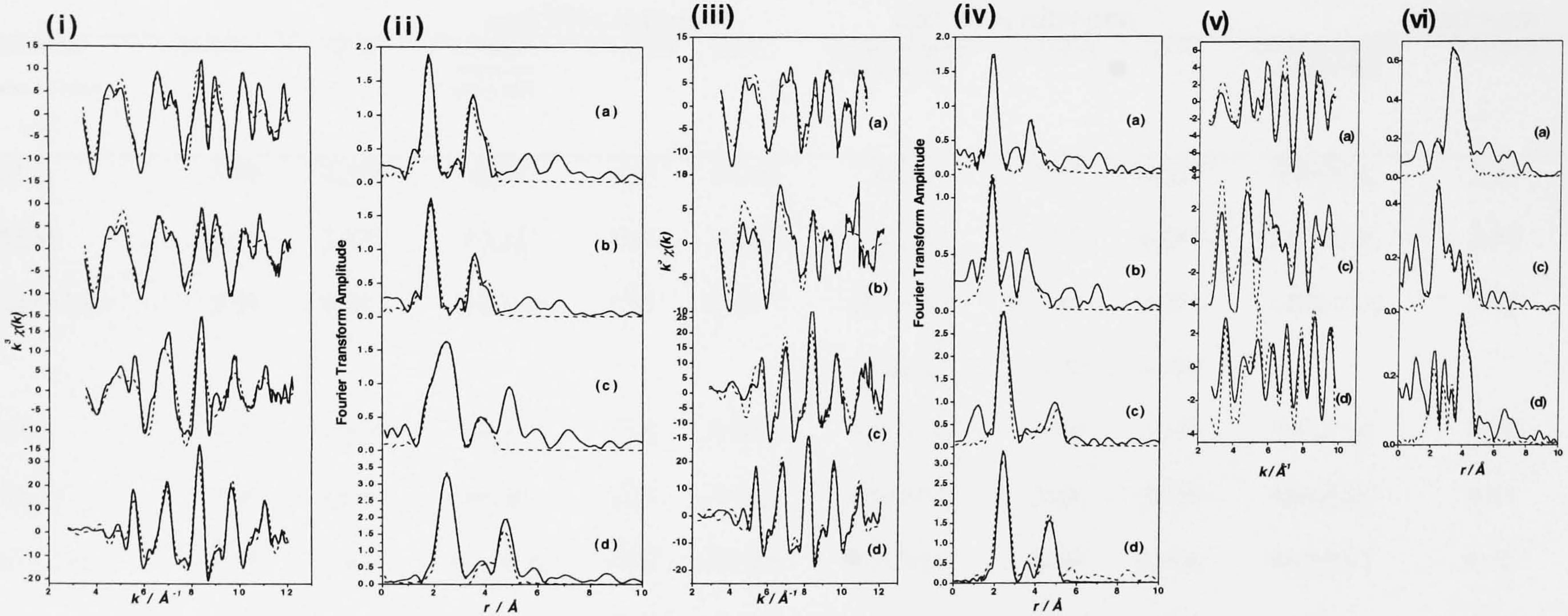

Figure 4.10 (i) Fe K-edge-EXAFS (raw data) recorded from $LaFe_{0.5}Co_{0\cdot 5}O_3$ (a) and following treatment in a hydrogen/nitrogen gas mixture at (b) 500 °C, (c) 1000 °C and (d) 1200°C; (ii) Fourier transforms of the EXAFS data presented in (i); (iii) Co K-edge-EXAFS (raw data) recorded from $LaFe_{0.5}Co_{0.5}O_3$ (a) and following treatment in a hydrogen/nitrogen gas mixture at (b) 500 °C, (c) 1000 °C and (d) 1200°C; (iv) Fourier transforms of the EXAFS data presented in (iii); (v) La L_{III}-edge- EXAFS recorded from $LaFe_{0.5}Co_{0.5}O_3$ (a) and following treatment in a hydrogen/nitrogen gas mixture at (c) 1000 °C and (d) 1200 °C; (vi) Fourier transforms of the EXAFS data presented in (v). (The experimental data are indicated by a solid line, the fits to the data are indicated by a broken line.)

Table 4.6. Best fit parameters to the Fe K-edge,Co K-edge and La L_{III}-edge EXAFS recorded from $LaFe_{0.5}Co_{0.5}O_3$ and following treatment in hydrogen and nitrogen at 500,1000 and 1200 °C

	$LaFe_{0.5}Co_{0.5}O_3$			$LaFe_{0.5}Co_{0.5}O_3$ treated at 500 °C in 10% hydrogen and 90% nitrogen			$LaFe_{0.5}Co_{0.5}O_3$ treated at 1000 °C in 10% hydrogen and 90% nitrogen			$LaFe_{0.5}Co_{0.5}O_3$ treated at 1200 °C in 10% hydrogen and 90% nitrogen		
	Coordination number and [atom type]	d/ Å (±0.02)	$2\sigma^2$/ Å^2	Coordination number and [atom type]	d/ Å (±0.02)	$2\sigma^2$/ Å^2	Coordination number and [atom type]	d/ Å(±0.02)	$2\sigma^2$/ Å^2	Coordination number and [atom type]	d/ Å(±0.02)	$2\sigma^2$/ Å^2
Fe K-edge	6[O]	1.98	0.008	6[O]	1.96	0.009	6[O]	1.97	0.017	8[Fe/Co]	2.48	0.014
	8[La]	3.30	0.020	8[La]	3.30	0.025	8[La]	3.23	0.067	6[Fe/Co]	2.83	0.020
	6[Fe/Co]	3.97	0.014	6[Fe/Co]	3.95	0.017	6[Fe/Co]	3.95	0.008	12[Fe/Co]	4.03	0.024
							8[Fe/Co]	2.45	0.010			
Co K-edge	6[O]	1.91	0.010	6[O]	1.96	0.016	9[Fe/Co]	2.45	0.016	9[Fe/Co]	2.49	0.014
	8[La]	3.29	0.044	8[La]	3.24	0.033	6[Fe/Co]	3.48	0.036	6[Fe/Co]	3.68	0.025
	6[Fe/Co]	3.93	0.004	6[Fe/Co]	3.95	0.022	9[Fe/Co]	4.30	0.024	9[Fe/Co]	4.38	0.020
La L_{III}-edge	3[O]	2.52	0.015	3.9[O]	2.55	0.020	4[O]	2.44	0.029	4[O]	2.43	0.028
	6[O]	2.76	0.018	6[O]	2.76	0.032	3[O]	2.69	0.020	3[O]	2.70	0.019
	3[O]	2.96	0.011	3[O]	2.98	0.021	12[La]	3.85	0.035	12[La]	3.85	0.036
	8[Fe/Co]	3.39	0.022	8[Fe/Co]	3.36	0.054	6[La]	4.19	0.027	6[La]	4.20	0.027
	6[La]	3.87	0.032	6[La]	4.26	0.030						

point on the cobalt foil edge was at 7708.9 eV the result is compatible with the partial reduction of Co^{3+} to Co^0. The first maximum in the first derivative of the Co K-edge data recorded from the material after treatment at 1000 and 1200 °C in hydrogen and nitrogen (Figure 4.9(ii) c' and d') and corresponding to the third and fourth peak in the tpr profile (Figure 4.2) occurs at 7708.4 eV, a value that corresponds to the position of the first maximum in the first derivative of the XANES recorded from metallic cobalt. Inspection of the first derivative of the absorption edge (Figure 4.9 (ii) c' and d') also shows that differences occur in the local structure around cobalt in the samples treated at 1000 °C and 1200 °C in hydrogen and nitrogen. This can be associated with the coexistence of Fe-Co alloy and metallic cobalt phases but with different concentrations in each sample. It is interesting to note that while there exists an oxide contribution in both the Mössbauer spectra and Fe K-edge XANES in the sample treated at 1000 °C in hydrogen and nitrogen, the Co K-edge XANES data show only Co^0 contributions. Hence, at 1000 °C, all the Co^{3+} appears to be reduced to Co^0 while a significant fraction of iron remains present as Fe^{3+}.

The Co-O distances obtained by fitting of the Co K-edge EXAFS recorded from $LaFe_{0.5}Co_{0.5}O_3$ (Figure 4.10 (iii)and (iv) and Table 4.6) are in excellent agreement with the EXAFS data recently reported on compounds of related composition [9]. Although analysis of the Co K-edge EXAFS recorded from these samples heated in hydrogen and nitrogen at 500 °C may show the presence of a small amount of Co^0, the data (Figure 4.10 (iii) b and Table 4.6) unequivocally indicate the presence of only Co^0 in the material treated in hydrogen and nitrogen at 1000 and 1200 °C and materials.

The position of the La L_{III}-edge recorded from $LaFe_{0.5}Co_{0.5}O_3$ (Figure 4.9(iii) a) was similar to that recorded from $LaFeO_3$ (Figure 4.4(ii)a). The position of the absorption edge did not change in samples following treatment in hydrogen and nitrogen and indicates that there is no reduction of La^{3+} although the attenuation of the small peak at *ca.* 5500 eV (Figure 4.9(iii) a-c) as the temperature of reduction increases suggests changes in the local environment of lanthanum. These changes are better appreciated by a consideration of the La L_{III}-edge EXAFS recorded from these samples (Figure 4.10 (v) and (vi)). The La L_{III}-edge EXAFS recorded from $LaFe_{0.5}Co_{0.5}O_3$ was fitted on the basis of recent EXAFS analysis of $LaCoO_3$[10]. The results are presented in Table 4.6. The Fourier transform of the EXAFS recorded from the sample treated in hydrogen and nitrogen at 1000 °C shows (Figure 4.10(vi) c) the disruption of the shell at 3-4.5 Å which is characteristic of the perovskite phase[10], the EXAFS being dominated by a first shell corresponding to La-O distances (Figure 4.10 (vi) c). The La L_{III}-edge EXAFS recorded from materials treated at 1200 °C gave very different EXAFS (Figure 4.10(v) d). The fit of these data (Table 4.6) is in excellent agreement with the presence of La_2O_3.

Summarizing, it seems that for the material of composition $LaFe_{0.5}Co_{0.5}O_3$ the tpr treatment induces first the reduction of Co^{3+} and Fe^{3+} to form an Fe-Co alloy as well as metallic cobalt and metallic iron phases. The complete reduction of Co^{3+} occurs at a lower temperature than the complete reduction of Fe^{3+}. The alloy- and metallic-phases segregate with the concomitant destruction of the perovskite structure and the formation of La_2O_3.

$LaFe_{0.1}Co_{0.9}O_3$

The ^{57}Fe Mössbauer spectrum recorded from $LaFe_{0.1}Co_{0.9}O_3$ (Figure 4.11a and Table 4.7) was composed of a single peak ($\delta = 0.36$ mms^{-1}) demonstrating that the substitution of 90 % of the Fe^{3+} by Co^{3+} ions induces the total collapse of the magnetic interactions at room temperature. The spectra recorded from the samples following treatment in hydrogen and nitrogen at 500 and 800 °C after the first and second peaks in the tpr profile(Figure 4.2) also showed a paramagnetic singlet (Figure 4.11 b and c). Treatment in the reducing gas mixture at 900 °C gave complete reduction to metallic iron (Figure 4.11 d). Hence cobalt enhances the susceptibility to reduction of iron in the cobalt-rich $La(Fe/Co)O_3$ phases such that, at the low temperature of 900 °C, metallic iron segregates from the structure.

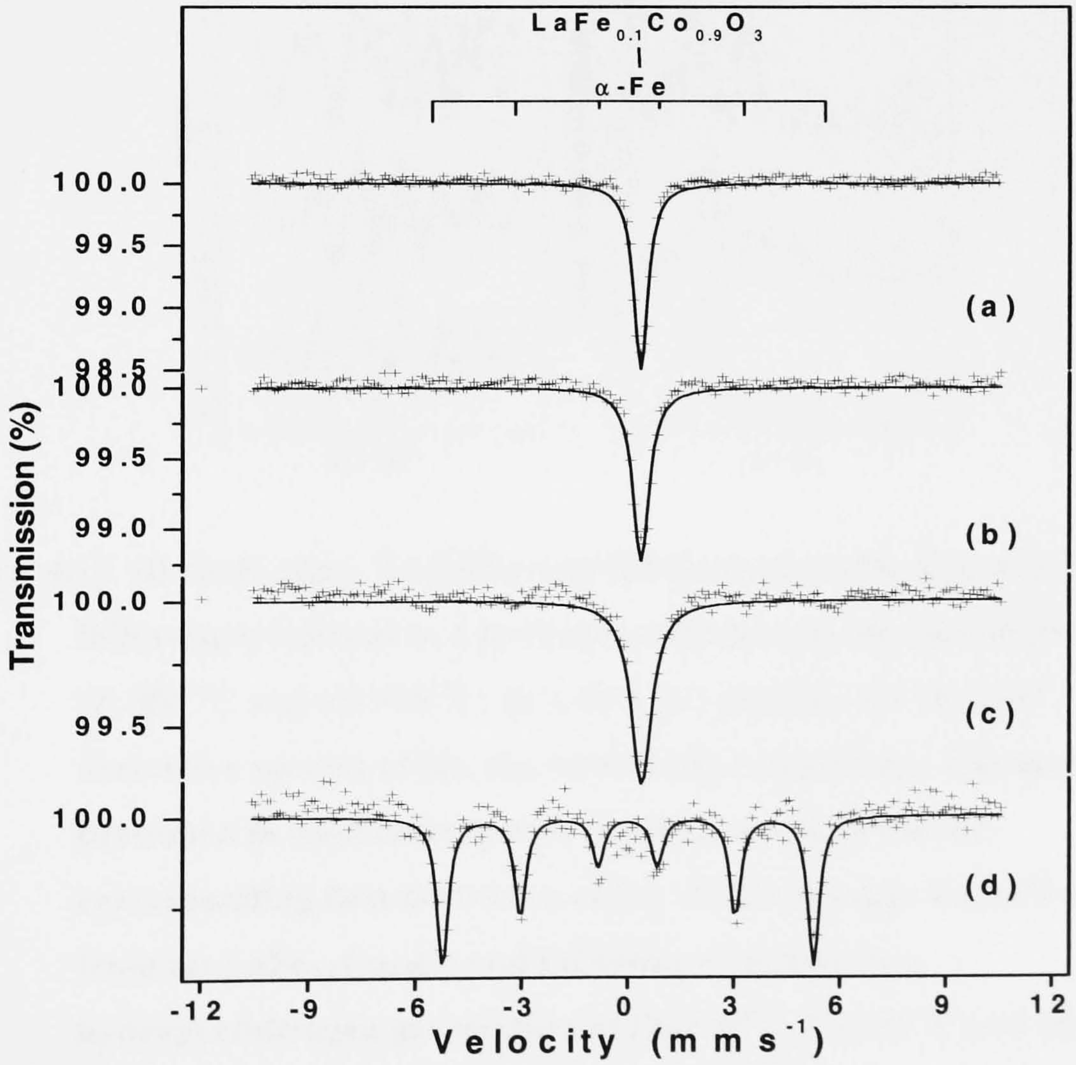

Figure 4.11 ^{57}**Fe Mössbauer spectra recorded from (a)** $LaFe_{0.1}Co_{0.9}O_3$ **and following reduction at (b) 500 °C (c) 800 °C (d) 900 °C.**

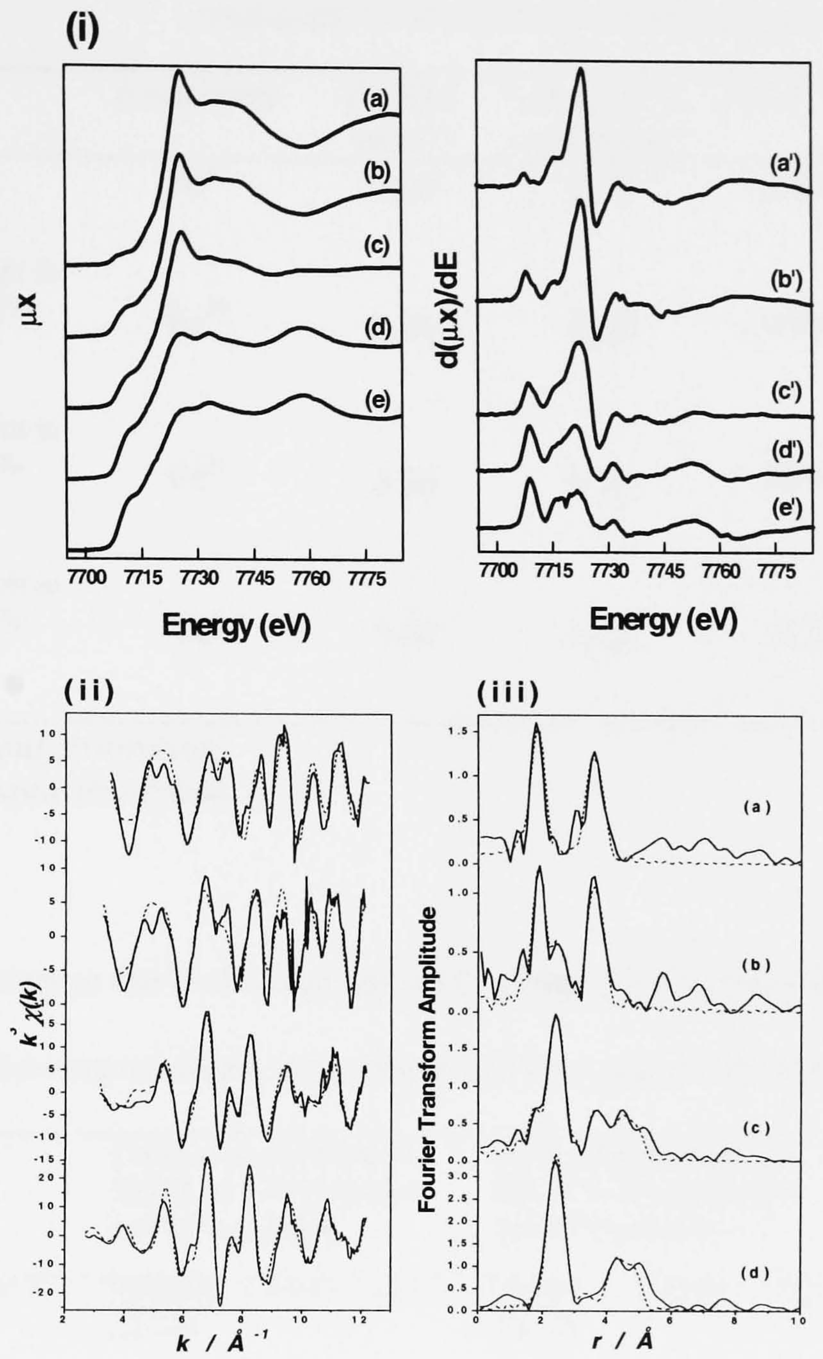

Figure 4.12 (i) Co K-edge- XANES recorded from (a) $LaFe_{0.1}Co_{0.9}O_3$ and following treatment in a hydrogen/nitrogen gas mixture at (b) 500 °C, (c) 800 °C and (d) 900 °C; (a'), (b'), (c') and (d') are the first derivative spectra of (a), (b), (c) and (d), respectively. The spectrum presented in (i)(e) corresponds to cobalt metal, (e') is the corresponding first derivative of (e). (ii) Co K-edge- EXAFS recorded from (a) $LaFe_{0.1}Co_{0.9}O_3$ and following treatment in a hydrogen/nitrogen gas mixture at (b) 500 °C, (c) 800 °C and (d) 900 °C; (iii) Fourier transforms. (The experimental data are indicated by a solid line, the fits to the data are indicated by a broken line.)

Table 4.7 ^{57}Fe Mössbauer parameters recorded from $LaFe_{0.1}Co_{0.9}O_3$ following treatment in 10% hydrogen/90% nitrogen

	Assignment	$\delta \pm 0.01$ mms^{-1}	Δ* or $2\varepsilon^{\dagger} \pm$ 0.02 mms^{-1}	$H \pm 0.5$ T	Spectral Area ± 3 %
$LaFe_{0.1}Co_{0.9}O_3$	Fe^{3+}	0.36	0.00	0.00	100
Following treatment in 10% hydrogen/90% nitrogen at 500°C	Fe^{3+}	0.36	0.00	0.00	100
Following treatment in 10% hydrogen/90% nitrogen at 800°C	Fe^{3+}	0.36	0.00	00.0	100
Following treatment in 10% hydrogen/90% nitrogen at 900°C	Fe^{0}	0.00	0.00	33.2	100

* quadrupole split absorption

† magnetically split absorption

Table 4.8. Best fit parameters to the Co K-edge and La L$_{III}$-edge EXAFS recorded from $LaFe_{0.1}Co_{0.9}O_3$ and following treatment in hydrogen and nitrogen at 500, 800, and 900 °C

	$LaFe_{0.1}Co_{0.9}O_3$			$LaFe_{0.1}Co_{0.9}O_3$ treated at 500 °C in 10% hydrogen and 90% nitrogen			$LaFe_{0.1}Co_{0.9}O_3$ treated at 800 °C in 10% hydrogen and 90% nitrogen			$LaFe_{0.1}Co_{0.9}O_3$ treated at 900 °C in 10% hydrogen and 90% nitrogen		
	Coordination number and [atom type]	d/ Å (±0.02)	$2\sigma^2$/ Å^2	Coordination number and [atom type]	d/ Å (±0.02)	$2\sigma^2$/ Å^2	Coordination number and [atom type]	d/ Å (±0.02)	$2\sigma^2$/ Å^2	Coordination number and [atom type]	d/ Å (±0.02)	$2\sigma^2$/ Å^2
Co K-edge	6[O]	1.88	0.012	5[O]	1.94	0.013	11.5[Co]	2.54	0.030	12[Co]	2.49	0.018
	8[La]	3.26	0.024	6[La]	3.28	0.022	5[Co]	3.57	0.010	6[Co]	3.49	0.033
	6[Co]	3.85	0.003	5[Co]	3.89	0.003	5[Co]	3.39	0.024	9[Co]	4.31	0.012
La L$_{III}$-edge	3[O]	2.42	0.004	3[O]	2.47	0.006	3.9[O]	2.50	0.003	6.5[O]	2.51	0.020
	6[O]	2.69	0.027	6[O]	2.74	0.008	6[O]	2.67	0.006	9[O]	2.68	0.036
	3[O]	2.93	0.012	3[O]	3.98	0.003	3[O]	2.89	0.003	1.5[Co]	3.98	0.019
	8[Co]	3.33	0.025	8[Co]	3.32	0.028	8[Co]	3.31	0.045	3.5[Co]	4.18	0.008
	6[La]	3.80	0.031	6[La	3.77	0.035	6[La]	4.17	0.021			

The Co K-edge- XANES and EXAFS (Figure 4.12, Table 4.8) showed that some Co^{3+} is reduced to Co^{o} by treatment in hydrogen/nitrogen at 500 °C and that more Co^{3+} is reduced at 800 °C. The La L_{III}-edge XANES and EXAFS (Table 4.8) indicated that the perovskite-related structure is largely destroyed by treatment in the reducing atmosphere at 800 °C and that lanthanum exists in a complex oxide matrix which resisted identification by X-ray powder diffraction.

Hence, in the cobalt-rich $LaFe/CoO_3$ materials, treatment in the reducing gaseous atmosphere induces the facile reduction of iron and cobalt to the metallic states at temperatures exceeding *ca.* 800°C with simultaneous destruction of the perovskite-related lattice.

$LaCoO_3$

The Co K-edge XANES and EXAFS data (Figures 4.13 and 4.14, Table 4.9) recorded from $LaCoO_3$ were similar to those recently reported from the material[9]. The results recorded from the material following treatment in hydrogen and nitrogen at 500 °C are very similar to the results recorded from the original materials except for a diminished amplitude of the EXAFS oscillations at both the Co K- and La L_{III}-edges. It seems that treatment at this temperature, rather than inducing the reduction of Co^{3+}, increases the extent of disorder in the materials. The data recorded from the material following treatment at 900 °C indicate the total reduction of Co^{3+} and the formation of metallic cobalt and La_2O_3 phases.

4.3 SUMMARY

Perovskite-related materials of composition $LaFe_{1-x}Co_xO_3$ prepared by conventional calcination methods are rendered more susceptible to reduction in a flowing mixture of hydrogen and nitrogen by the incorporation of cobalt. In iron-rich systems the limited reduction of iron and cobalt leads to the segregation of discrete metallic phases without destruction of the perovskite structure. In cobalt-rich systems the reduction of Co^{3+} to Co^{o} precedes complete reduction of Fe^{3+} and the segregation of alloy and metal phases is accompanied by destruction of the perovskite-related structure.

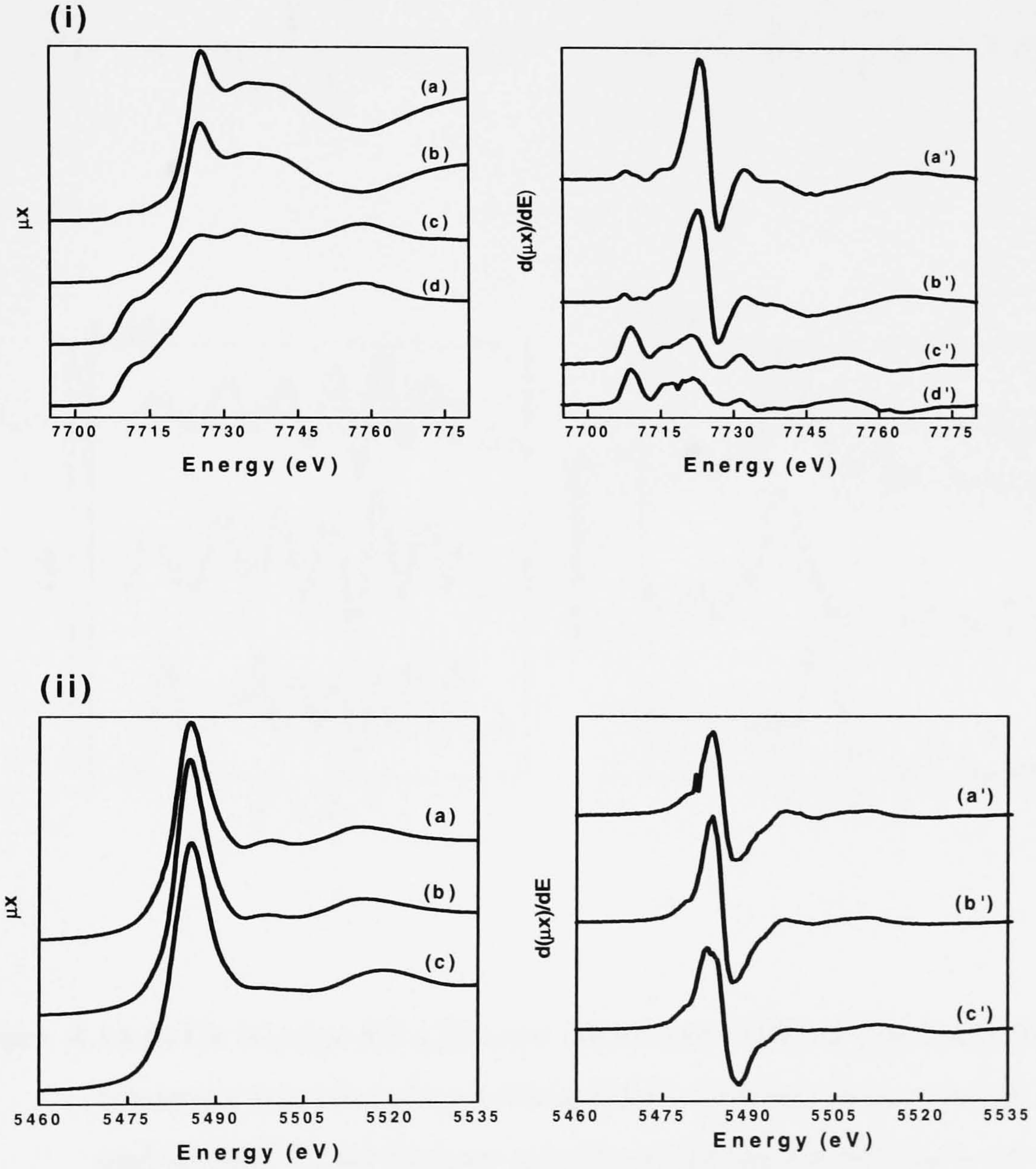

Figure 4.13 (i) Co K-edge- and (ii) La L_{III}-edge- XANES recorded from (a) $LaCoO_3$ and following treatment in a hydrogen/nitrogen gas mixture at (b) 500 °C and (c) 900 °C. The spectrum presented in (i)(d) corresponds to cobalt metal, (d') is the corresponding first derivative of (d). (a'), (b') and (c') are the first derivatives of (a), (b) and (c), respectively.

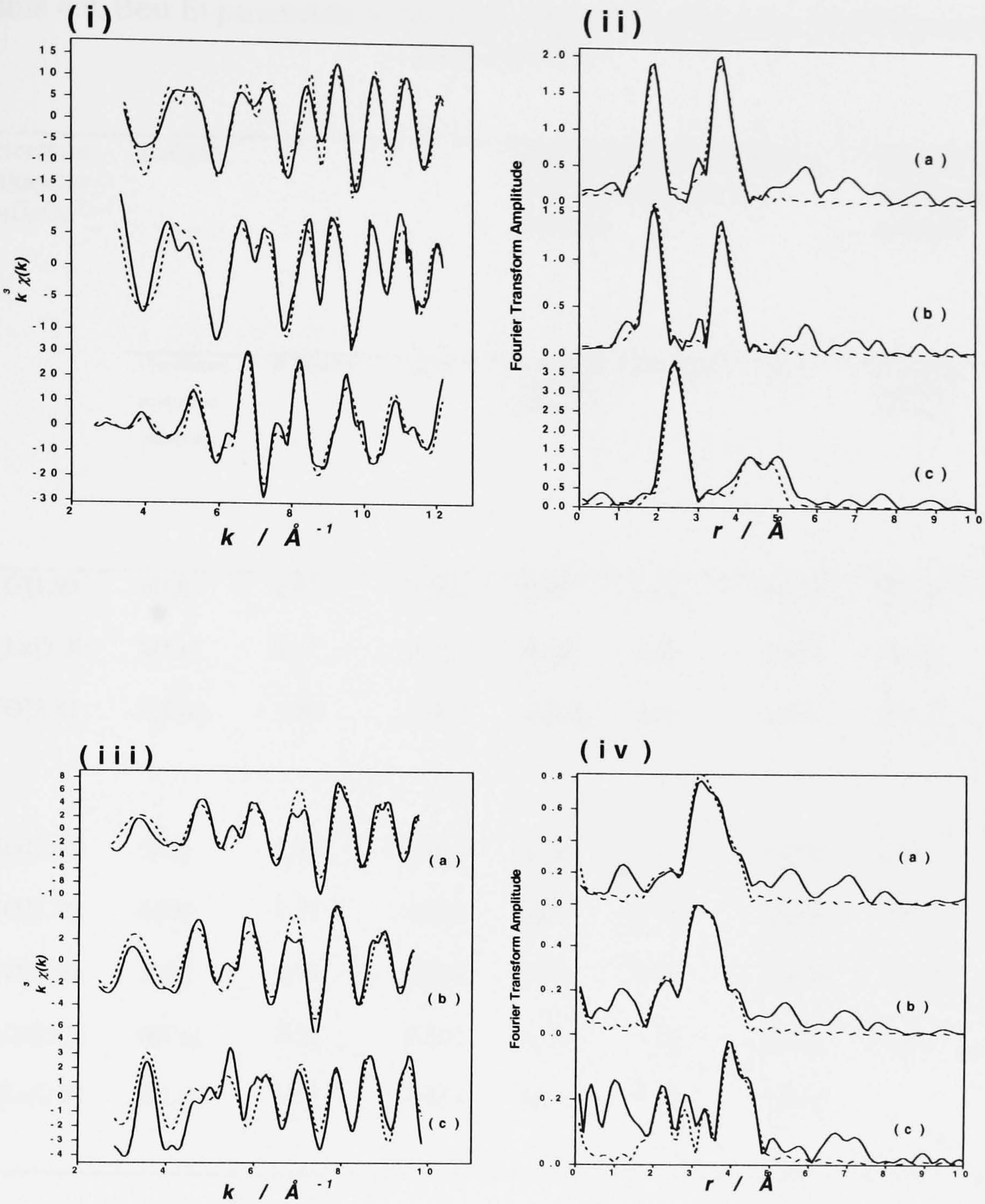

Figure 4.14 (i) Co K-edge-EXAFS (raw data) recorded from (a) $LaCoO_3$ and following treatment in a hydrogen/nitrogen gas mixture at (b) 500 °C and (c) 900 °C; (ii) Fourier transforms of the EXAFS data presented in (i); (iii) La L_{III}-edge- EXAFS recorded from (a) $LaCoO_3$ and following treatment in a hydrogen/nitrogen gas mixture at (b) 500 °C and (c) 900 °C; (iv) Fourier transforms of the EXAFS data presented in (iii) (The experimental data are indicated by a solid line, the fits to the data are indicated by a broken line.)

Table 4.9. Best fit parameters to the Co K-edge and La L_{III}-edge EXAFS recorded from $LaCoO_3$

	Literature values for $LaCoO_3$ [9]	$LaCoO_3$			$LaCoO_3$ treated at 500 °C in 10% hydrogen and 90% nitrogen			$LaCoO_3$ treated at 900 °C in 10% hydrogen and 90% nitrogen		
		Coordination number and [atom type]	d/ Å (±0.02)	$2\sigma^2$/ Å^2	Coordination number and [atom type]	d/ Å (±0.02)	$2\sigma^2$/ Å^2	Coordination number and [atom type]	d/ Å (±0.02)	$2\sigma^2$/ Å^2
Co K-edge	6[O]1.93	6[O]	1.92	0.009	6[O]	1.94	0.011	9[Co]	2.49	0.014
	8[La]3.30	8[La]	3.27	0.017	8[La]	3.28	0.025	6[Co]	3.50	0.027
	6[O]3.81	6[Co]	3.88	0.001	6[Co]]	3.91	0.002	9[Co]	4.32	0.009
La L_{III}-edge	3[O]2.43	3[O]	2.49	0.011	3[O]	2.52	0.005	4[O]	2.43	0.029
	6[O]2.69	6[O]	2.72	0.016	6[O]	2.76	0.006	3[O]	2.69	0.020
	3[O]3.00	3[O]	2.95	0.028	3[O]	2.98	0.0002	12[La]	3.84	0.036
	8[Co]3.31	6[Co]	3.32	0.019	8[Co]	3.34	0.024	6[La]	4.19	0.027
	6[La]3.81	6[La]	3.77	0.024	6[La]	3.79	0.042			

4.4 $LaFe_{1-x}Co_xO_3$ (MILLING PREPARATION)

The X-ray powder diffraction patterns recorded from a mixture of La_2O_3 and α-Fe_2O_3 (Figure 4.15) following mechanical milling showed a gradual broadening and simultaneous decrease in intensity of the lines characteristic of the reactant oxides during the first 20 hours of milling and the formation of a virtually amorphous

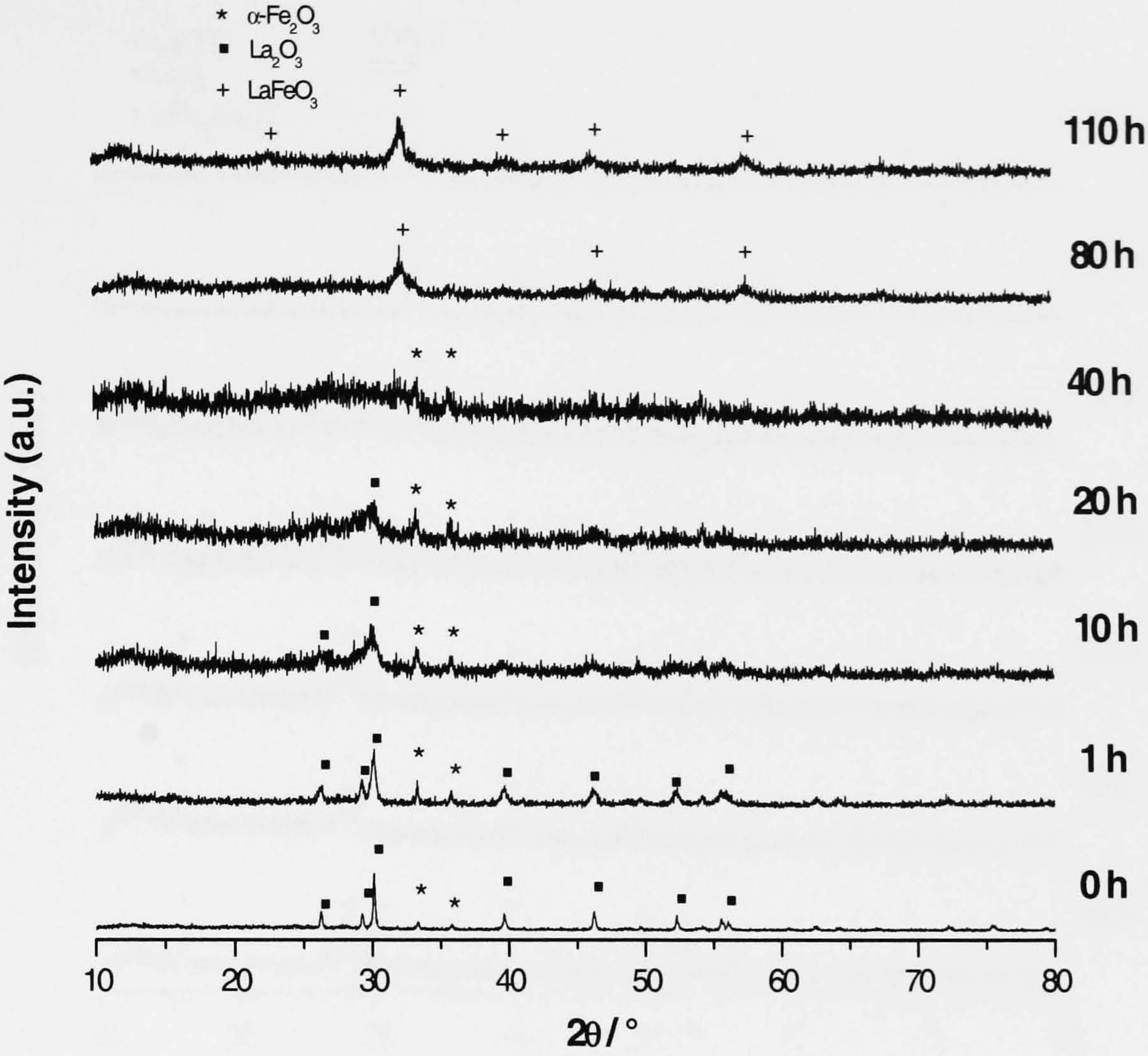

Figure 4.15 X-ray powder diffraction patterns recorded from mixtures of La_2O_3 and α-Fe_2O_3 after various periods of mechanical milling

material after 40 hours. The occurrence of a phase corresponding to $LaFeO_3$ was observed after milling for 80 hours with a particle size, determined from the X-ray powder diffraction data, of *ca.* 10nm which remained unchanged after milling for 110h. The milling of a mixture of La_2O_3, CoO and α-Fe_2O_3 was also followed by X-ray powder diffraction. The results (Figure 4.16) showed an initial contamination of

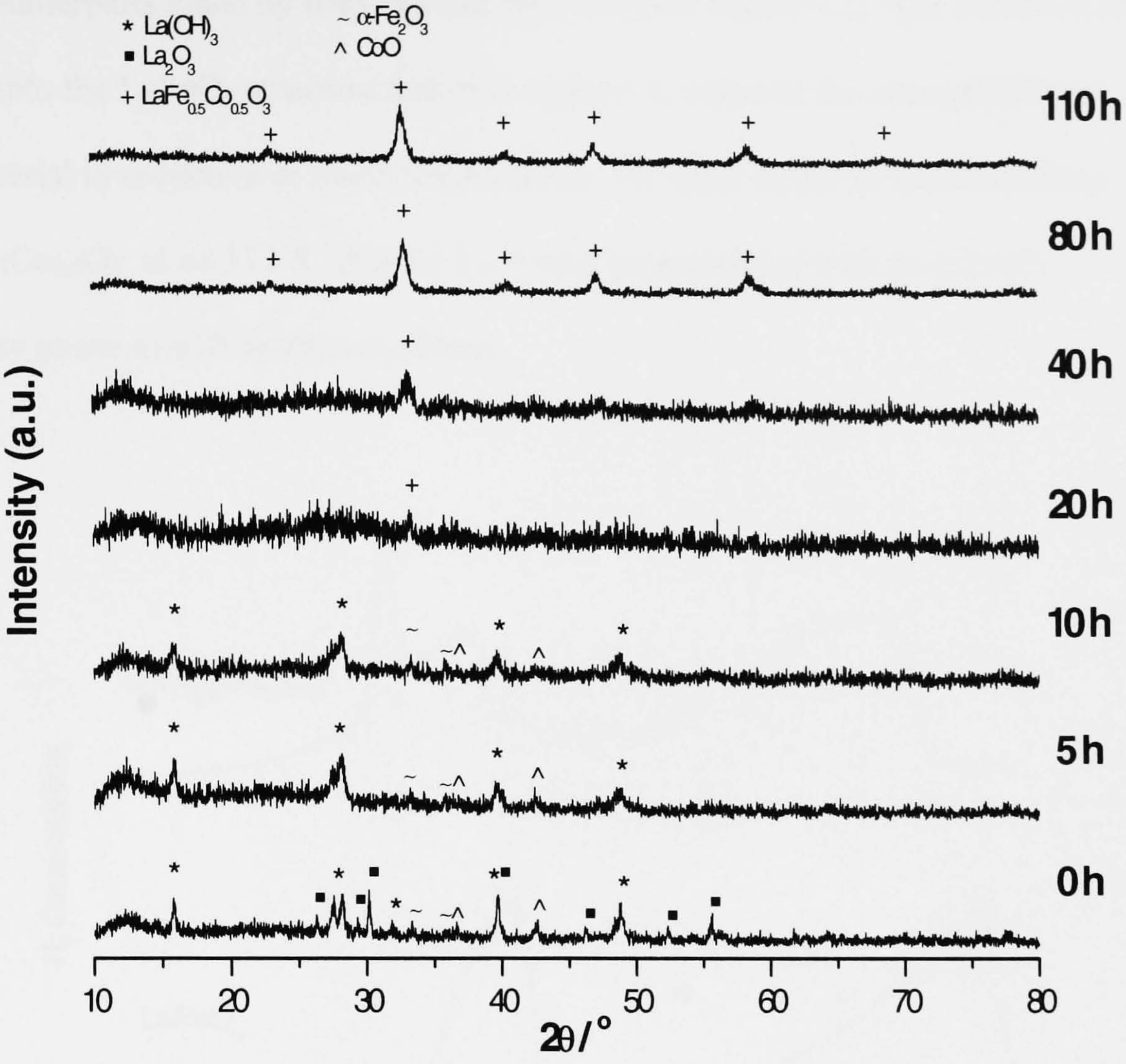

Figure 4.16 X-ray powder diffraction patterns recorded from mixtures of La_2O_3, CoO and α-Fe_2O_3 after various periods of mechanical milling

the La_2O_3 starting materials with $La(OH)_3$. The effect of milling was to give the more facile formation of the amorphous materials after only 20 hours of milling and the onset of formation of $LaFe_{0.5}Co_{0.5}O_3$ after 40 hours with a particle size of *ca.* 10 nm which remained unchanged after milling for 80 and 110 hours.

The temperature programmed reduction profiles recorded from $LaFeO_3$ and $LaFe_{0.5}Co_{0.5}O_3$ prepared by milling techniques are collected in Figure 4.17. The profiles show the onset of reduction to occur at lower temperatures as compared to their counterparts made by conventional methods (see Figure 4.2). The inclusion of cobalt into the $LaFeO_3$ structure therefore appears to enhance the susceptibility of the material to reduction at lower temperatures. The peak in the tpr recorded from $LaFe_{0.5}Co_{0.5}O_3$ at *ca.*370 °C (Figure 4.17) may be associated with an α-Fe_2O_3 impurity phase as will be discussed later.

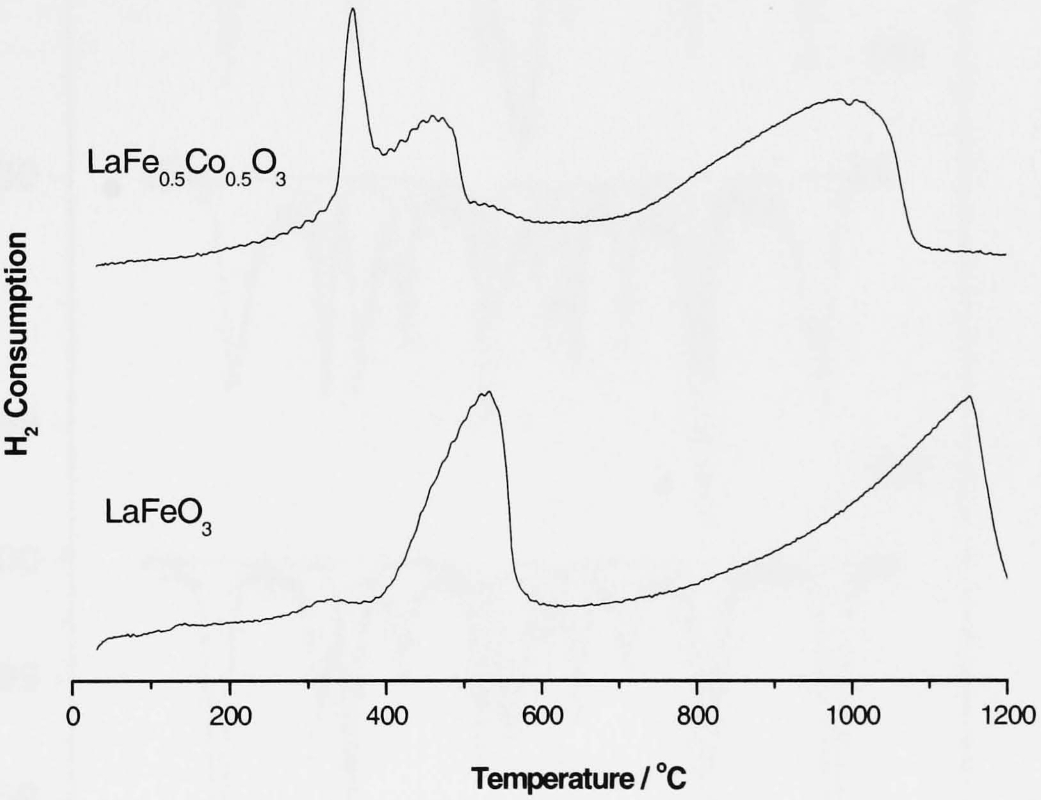

Figure 4.17 Temperature programmed reduction profiles record from compounds of the type $LaFe_{1-x}Co_xO_3$ prepared by milling

The ^{57}Fe Mössbauer spectrum recorded from $LaFeO_3$ prepared by milling techniques (Figure 4.18a and Table 4.10) contains a broadened sextet pattern showing a magnetic hyperfine field distribution accounting for *ca.* 66% of the spectral area

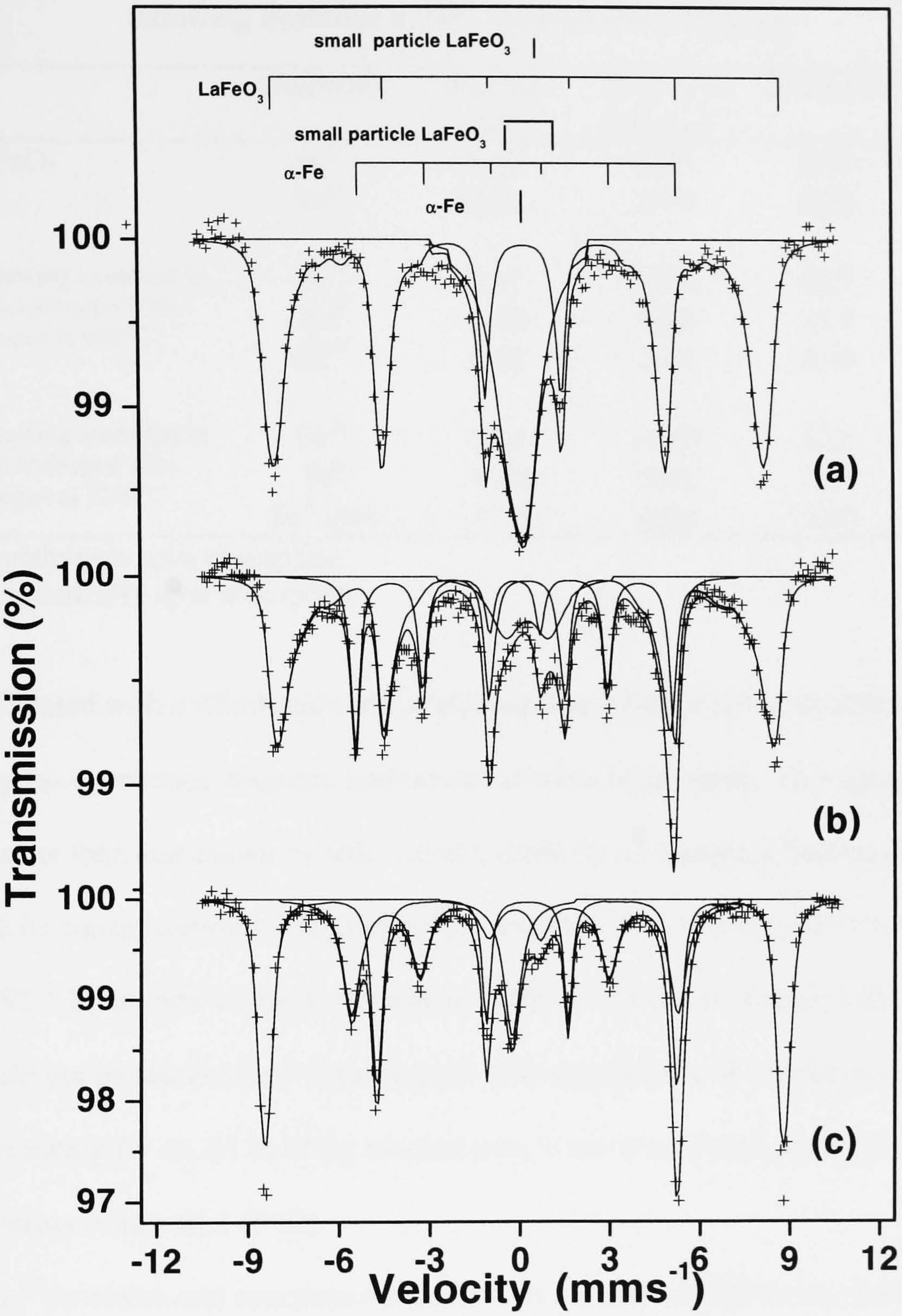

Figure 4.18 ^{57}**Fe Mössbauer spectra recorded from (a)** $LaFeO_3$ **formed by mechanical milling and after tpr treatment at (b) 600 °C and (c) 1200 °C.**

Table 4.10 ^{57}Fe Mössbauer parameters recorded from $LaFeO_3$ made by ball milling following treatment in 10% hydrogen/90% nitrogen

	Assignment	$\delta \pm 0.01$ mms^{-1}	Δ* or $2\varepsilon^{\dagger} \pm$ 0.02 mms^{-1}	$H \pm 0.5$ T	Spectral Area ± 3 %
$LaFeO_3$	Fe^{3+}	0.25	-0.15	48.9	66
	Fe^{3+}	0.09	0.59	0.00	34
Following treatment in 10% hydrogen/90% nitrogen at 600°C	Fe^{3+}	0.37	−0.03	48.7	61
	Fe^{0}	0.00	0.00	33.0	27
	Fe^{3+}	0.40	1.44	0.00	12
Following treatment in 10% hydrogen/90% nitrogen at 1200°C	Fe^{3+}	0.34	−0.07	53.5	55
	Fe^{0}	-0.03	0.01	33.7	35
	Fe^{0} spm	-0.13	0.00	0.00	10

* quadrupole split absorption

† magnetically split absorption

associated with a distribution of $LaFeO_3$ particles of different sizes albeit sufficiently large to experience magnetic interactions at room temperature. This spectrum is broader than that shown by bulk $LaFeO_3$ made by conventional heating (Figure 4.3a) and its corresponding average hyperfine magnetic field is lower (48.9 T, compared to 52.7 T). In view of the X-ray powder diffraction data, the broad singlet which could not be resolved into a quadrupole split absorption with confidence, and accounting for *ca.* 34 % of the spectral area, is associated with small particle superparamagnetic $LaFeO_3$.

The ^{57}Fe Mössbauer spectrum recorded from the material following treatment in hydrogen at 600 °C (Figure 4.18b) and after the first reduction peak in the tpr profile (Figure 4.17) continued to show the broadened sextet pattern associated with $LaFeO_3$ (H = 48.7 T) and accounting for *ca.* 61% of the spectral area, together with a narrow line sextet (H = 33.0T) characteristic of metallic ion (*ca.* 27% of spectral area) and a doublet (δ = 0.40 mms^{-1}, Δ = 1.44 mms^{-1}, *ca.* 12% spectral area) characteristic of Fe^{3+} in octahedral oxygen coordination associated with a remaining fraction of small particle lanthanum orthoferrite. The results indicate that treatment at 600 °C in a hydrogen/nitrogen gas mixture induces partial reduction of Fe^{3+} in the $LaFeO_3$ structure and its segregation to form metallic iron. The ^{57}Fe Mössbauer spectrum recorded from the material following treatment in the reducing atmosphere at 1200 °C (Figure 4.18c) and after the final peak in the tpr profile (Figure 4.17) showed a sharper-line sextet with parameters ($\delta = 0.34$ mms^{-1}, $2\varepsilon = -0.07$ mms^{-1}, $H = 53.5$ T, 55% of spectral area) that are more similar to those shown by bulk, well-crystallized $LaFeO_3$ and reflecting the sintering of the smaller particles at the higher temperature, a sextet corresponding to metallic iron ($H = 33.7$ T, 35% spectral area) and a singlet ($\delta =$ *ca.*-0.13 mms^{-1}, *ca.* 10%) which can be associated with the presence of small superparamagnetic metallic iron particles[11]. The results demonstrate that complete reduction of Fe^{3+} to metallic iron is not achieved even at the elevated temperature of 1200 °C, however, the extent of reduction is larger than that achieved when bulk $LaFeO_3$ made by conventional heating was treated under similar conditions (Figure 4.3) and presumably reflects the enhanced susceptibility to reduction of small particle $LaFeO_3$ made by milling.

The ^{57}Fe Mössbauer spectrum recorded from $LaFe_{0.5}Co_{0.5}O_3$ made by milling techniques (Figure 4.19a and Table 4.11) was dominated by a doublet ($\delta = 0.28$ mms^{-1}, $\Delta = 0.59$ mms^{-1}, *ca.* 71%) and a narrow-lined sextet pattern ($\delta = 0.38$ mms^{-1}, $2\varepsilon = -0.16$ mms^{-1}, $H = 51.9$T , *ca.* 29%). Given that X-ray powder diffraction showed the presence of a perovskite-related $LaFeO_3$-type structure similar to that made by conventional methods and previously identified as $LaFe_{0.5}Co_{0.5}O_3$, the dominant doublet is associated with superparamagnetic $LaFe_{0.5}Co_{0.5}O_3$. The sextet does not correspond to $LaFe_{0.5}Co_{0.5}O_3$ or $LaFeO_3$. However, in view of the reduction properties of the material (see below) this sextet is associated with an α-Fe_2O_3 impurity phase.

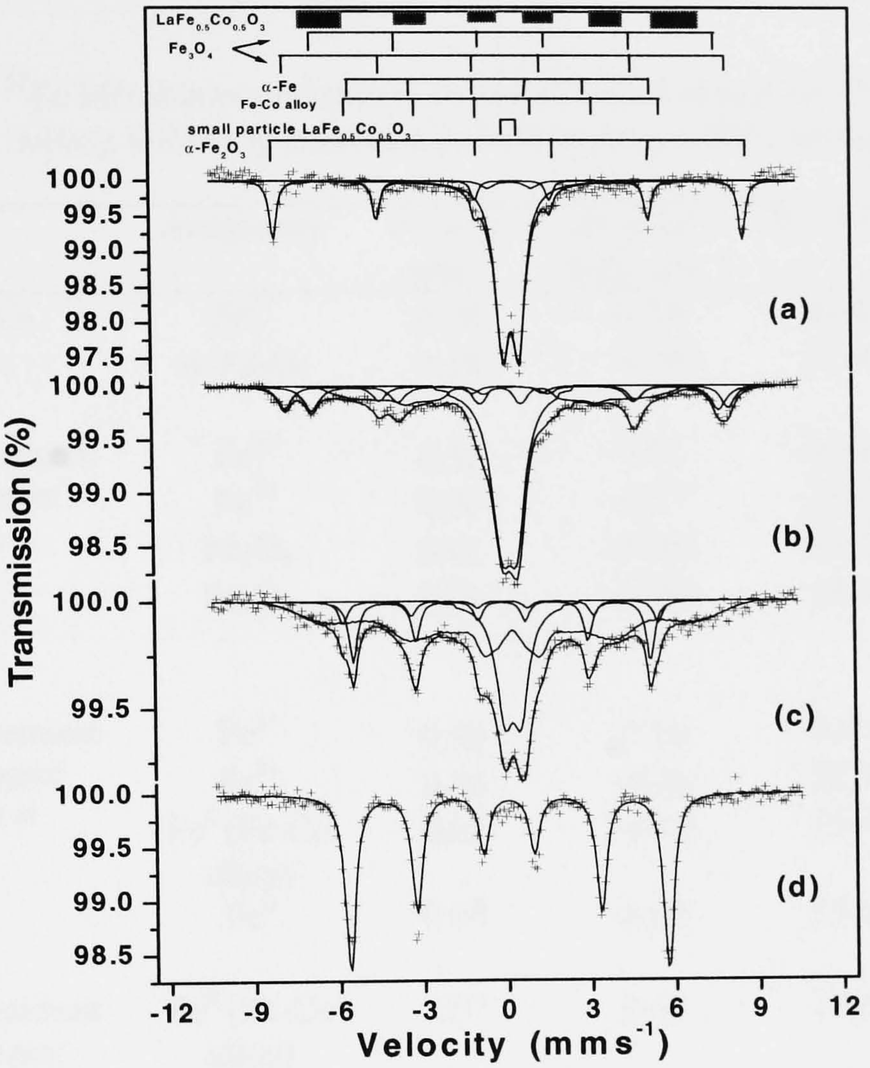

Figure 4.19 ^{57}Fe Mössbauer spectra recorded from (a) $LaFe_{0.5}Co_{0.5}O_3$ and after tpr treatment at (b) 400 °C, (c) 550 °C and (d) 1200 °C.

The ^{57} Fe Mössbauer spectrum recorded from $LaFe_{0.5}Co_{0.5}O_3$ following treatment in 10 % hydrogen and 90 % nitrogen at 400 °C (Figure 4.19b, Table 4.11) and after the first peak in the tpr profile (Figure 4.17) shows a broadened sextet pattern ($\delta = 0.35$

mms^{-1}, $2\varepsilon = -0.17$ mms^{-1}, $H = 25$ T , *ca.* 35%) similar to that of bulk $LaFe_{0.5}Co_{0.5}O_3$ made by conventional methods (Figure 4.8), together with the doublet observed in the original material and associated with small particle superparamagnetic

Table 4.11 ^{57}Fe Mössbauer parameters recorded from $LaFe_{0.5}Co_{0.5}O_3$ made by milling following treatment in 10% hydrogen/90% nitrogen

	Assignment	$\delta \pm 0.01$ mms^{-1}	Δ* or $2\varepsilon^{\dagger} \pm$ 0.02 mms^{-1}	$H \pm 0.5$ T	Spectral Area ± 3 %
$LaFe_{0.5}Co_{0.5}O_3$	Fe^{3+}	0.28	0.59	0.00	71
	α-Fe_2O_3	0.38	-0.16	51.9	29
Following treatment in 10% hydrogen/ 90% nitrogen at 400°C	Fe^{3+}	0.32	0.53	0.00	39
	Fe^{3+}	0.35	-0.17	25.0	35
	Fe_3O_4	0.61	-0.001	45.2	13
	Fe_3O_4	0.31	-0.001	49.1	13
Following treatment in 10% hydrogen/ 90% nitrogen at 550°C	Fe^{3+}	0.36	0.58	0.00	24
	Fe^{3+}	0.35	–0.04	28.3	55
	Fe^0 (Fe-Co alloy)	0.01	–0.06	35.0	6
	Fe^0	0.00	0.00	33.0	15
Following treatment in 10% hydrogen/ 90% nitrogen at 1200°C	Fe^0 (Fe-Co alloy)	0.07	0.00	35.4	100

* quadrupole split absorption
† magnetically split absorption

$LaFe_{0.5}Co_{0.5}O_3$ (*ca.* 40%) and two sextets characteristic of Fe_3O_4 resulting from reduction of the α–Fe_2O_3 impurity phase. Hence the features in the tpr profile recorded from $LaFe_{0.5}Co_{0.5}O_3$ at *ca.* 300 °C to 400 °C appear to be associated with the reduction of the impurity α–Fe_2O_3 phase and the development of large particle $LaFe_{0.5}Co_{0.5}O_3$ presumably reflecting the sintering of some of the small particles of this phase at 400 °C. The ^{57}Fe Mössbauer spectrum recorded from $LaFe_{0.5}Co_{0.5}O_3$

following treatment in the hydrogen and nitrogen gas mixture at 550 °C (Figure 4.19c) and after the second peak in the tpr profile (Figure 4.17) is composed of a broad sextet pattern (*ca.* 55% of spectral area) characteristic of large particle $LaFe_{0.5}Co_{0.5}O_3$ together with a doublet (*ca.* 24%) associated with superparamagnetic $LaFe_{0.5}Co_{0.5}O_3$, and two narrow sextets, one ($H = 33.0$ T,15%) corresponding to metallic iron and the other ($\delta = 0.01$ mms^{-1},$2\varepsilon = -0.06$ mms^{1}, $H = 35.0$ T , 6%) corresponding to an iron-cobalt alloy[8]. Following treatment in the hydrogen/nitrogen gas mixture at 1200 °C and after the final peak in the tpr profile (Figure 4.17) the ^{57}Fe Mössbauer spectrum (Figure 4.19d) shows a narrow line sextet ($\delta = 0.07$mms^{-1}, $2\varepsilon = 0.00$ mms^{-1}, $H = 35.4$ T) characteristic of an iron-cobalt alloy[8]. The XANES and EXAFS from materials made by milling methods were not recorded.

4.5 SUMMARY

Taken together the results show that small particle $LaFe_{1-x}Co_xO_3$ phases made by milling techniques are more susceptible to hydrogen reduction than their counterparts made by conventional techniques. This may reflect the smaller particle size of materials made by milling methods. The presence of cobalt enhances the reducibility of iron in the perovskite-related structure. In contrast to $LaFeO_3$ where the oxide structure at least was partially retained even after treatment in the reducing atmosphere at 1200 °C, treatment of $LaFe_{0.5}Co_{0.5}O_3$ in a reducing atmosphere leads to reduction of both Fe^{3+} and Co^{3+}, their segregation from the oxide matrix and the formation of an iron-cobalt alloy phase.

4.6 $La_{0.5}Sr_{0.5}MO_3$, (M = Fe, Co), (CONVENTIONAL PREPARATION)

$La_{0.5}Sr_{0.5}FeO_3$

The XRD pattern recorded from the compound $La_{0.5}Sr_{0.5}FeO_3$ is shown in Figure 4.20a. The pattern is characteristic of the cubic $SrFeO_3$-type structure. The tpr profile recorded from $La_{0.5}Sr_{0.5}FeO_3$ is shown in Figure 4.21. It shows a narrow peak at ca. 550°C and a broad peak starting at *ca* 800°C and extending up to 1200°C.

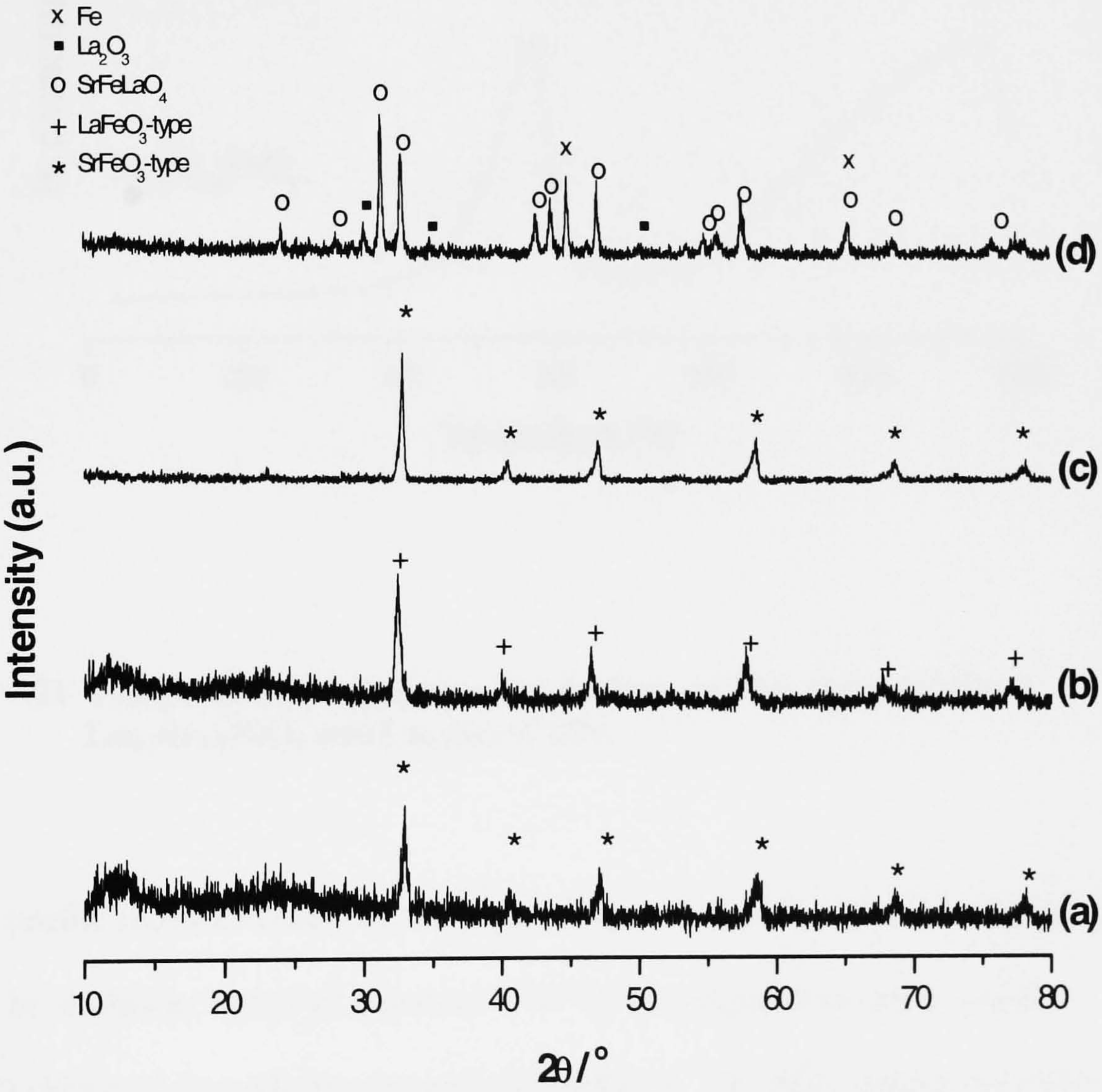

Figure 4.20 X-ray powder diffraction patterns recorded from (a) $La_{0.5}Sr_{0.5}FeO_3$ and following sequential treatment in (b) 10% hydrogen/90% nitrogen at 600°C, (c) heating in air at 600°C, (d) 10% hydrogen/ 90% nitrogen at 1200°C.

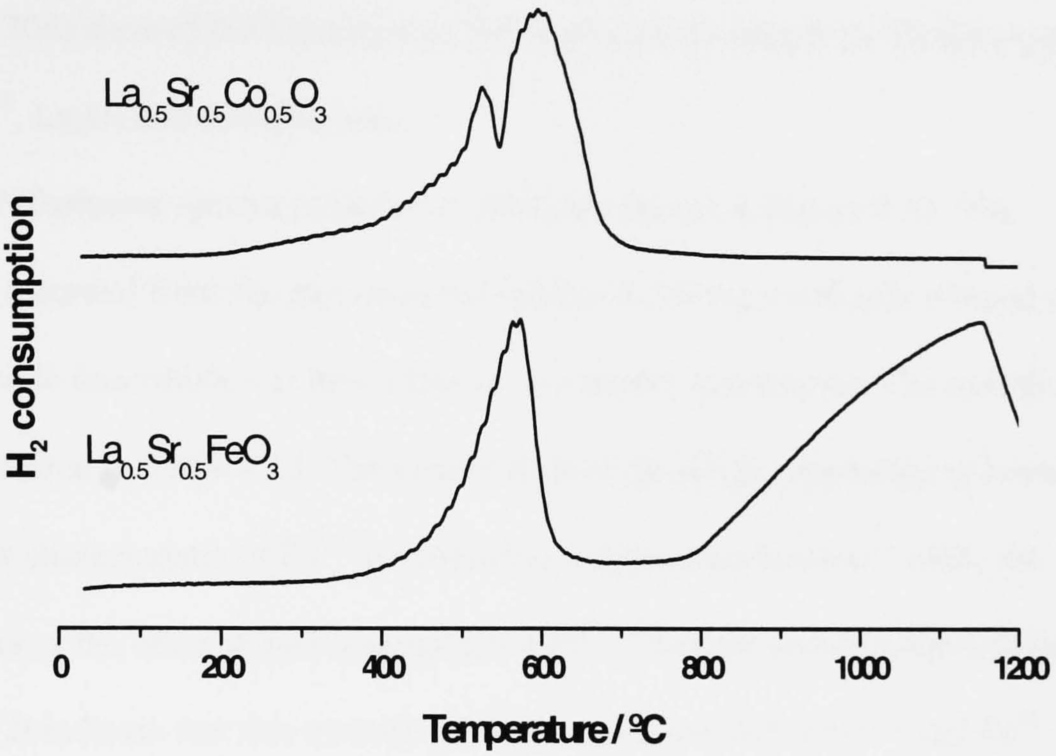

Figure 4.21 **Temperature programmed reduction profiles recorded from $La_{0.5}Sr_{0.5}FeO_3$ and $La_{0.5}Sr_{0.5}CoO_3$.**

The tpr profile recorded from $La_{0.5}Sr_{0.5}FeO_3$ (Figure 4.21) shows the first reduction peak to be shifted to higher temperature (570 °C) as compared to that in $LaFeO_3$ (480 °C) (Figure 4.2) made by conventional methods. The XRD pattern recorded from the material treated at 600°C in flowing hydrogen and nitrogen, i.e., after the first reduction peak (Figure 4.20b), shows all the XRD peaks to shift to lower angle. No evidence could be found for the presence of strontium oxide. These two XRD patterns can be indexed in the space group R-3c (No.167) with lattice parameters *a* = *b* = 5.489(1)Å, *c* = 13.378(1) Å for $La_{0.5}Sr_{0.5}FeO_3$ and *a* = *b* = 5.533(1) Å and *c*=13.503(1) Å for the material heated in hydrogen and nitrogen at 600°C. The XRD pattern recorded from the material after reheating in air at 600°C for 12 hours (Figure 4.20c) showed the product to return to the original $SrFeO_3$-type structure. The XRD pattern recorded from the material following treatment by tpr at 1200°C (Figure 4.20d) showed the formation of $SrFeLaO_4$ which adopts the K_2NiF_4-type structure[12], La_2O_3 and metallic iron.

The ^{57}Fe Mössbauer spectra recorded at 298K are shown in Figure 4.22. The spectrum recorded from the pure material (Figure 4.22a) showed only a broad central paramagnetic line which was best-fitted to two singlet absorptions. The results of the fit are collected in Table 4.12. The isomer shift of the singlet appearing at lower velocity is characteristic of Fe^{4+} in octahedral oxygen coordination[13] while the parameters of the other singlet correspond to Fe^{3+}. The data (relative spectral areas, Table 4.12) indicate that this material contains equal amounts of Fe^{4+} and Fe^{3+}.

Table 4.12 ^{57}Fe Mössbauer parameters recorded from $La_{0.5}Sr_{0.5}FeO_3$ following treatment in 10% hydrogen/90% nitrogen

	Assignment	$\delta \pm 0.01$ /mms^{-1}	*Δ or 2ε† 1± 0.02/mms^{-1}	$H \pm 0.5$/T	Spectral Area ± 3/%
$La_{0.5}Sr_{0.5}FeO_3$	Fe^{4+}	0.03	0	0	50
	Fe^{3+}	0.25	0	0	50
Following treatment in 10% hydrogen/90% nitrogen at 600°C	Fe^{3+}	0.27	−0.40	52.1	47
	Fe^{3+}	0.37	0.19	52.9	53
Following treatment in 10% hydrogen/90% nitrogen at 1200°C	Fe^{3+}	0.31	0.58	32.4	42
	Fe^0	0.00	0	33.2	51
	Fe^0	−0.08	0	0	7

* quadrupole split absorption
† magnetically split absorption

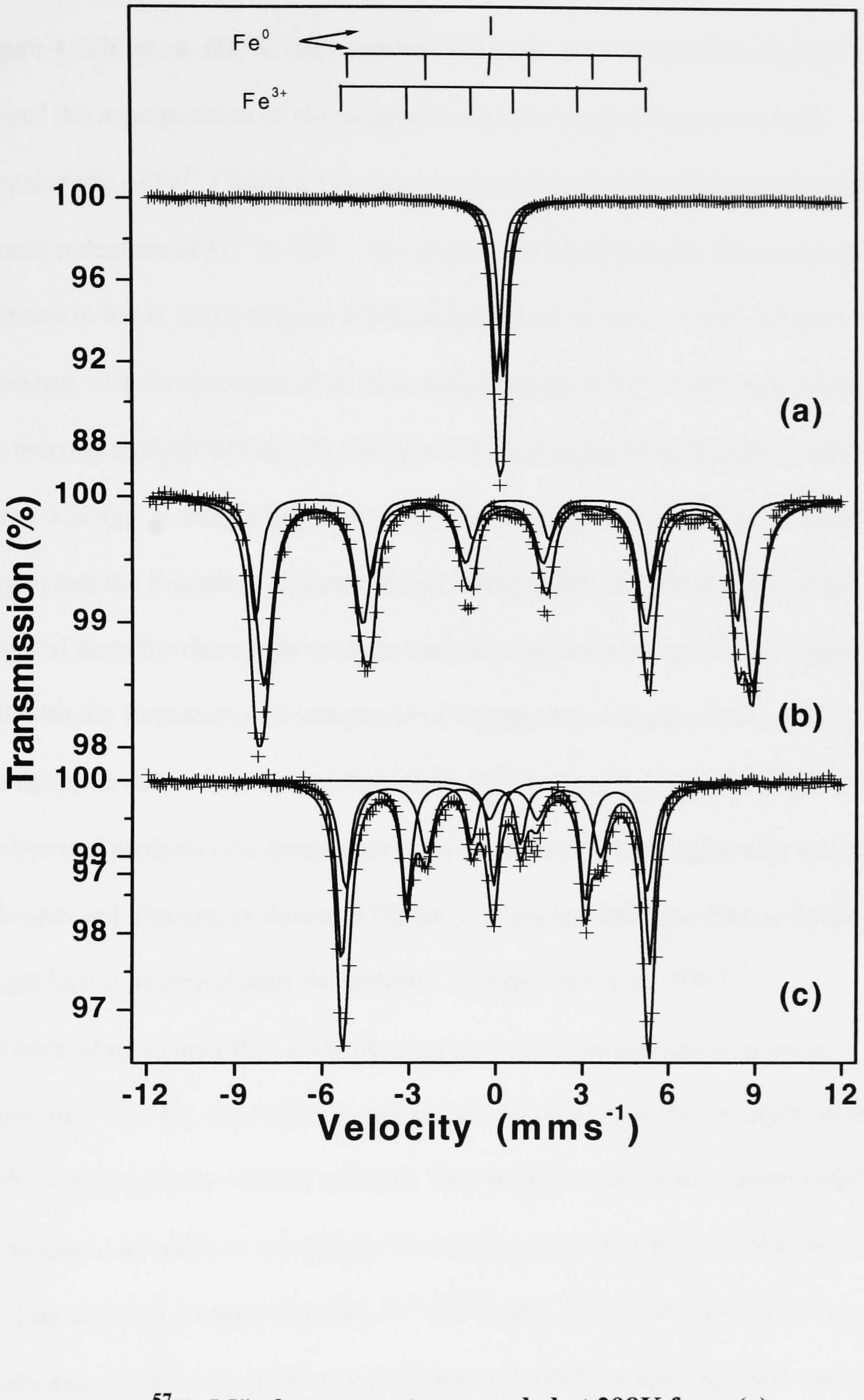

Figure 4.22 (a) ^{57}Fe Mössbauer spectra recorded at 298K from (a) $La_{0.5}Sr_{0.5}FeO_3$ and following treatment in 10% hydrogen/90% nitrogen at (b) 600 °C and (c) 1200 °C.

The spectrum recorded following treatment in flowing hydrogen and nitrogen (Figure 4.22b) at *ca.* 600°C (i.e. after the first peak in the tpr profile (Figure 4.21) showed the superposition of two magnetically split sextet components both characteristic of Fe^{3+} (Table 4.12) and demonstrating that low temperature treatment induces reduction of Fe^{4+} to Fe^{3+}. The shift in the X-ray powder diffraction peak positions to lower angle (Figure 4.20b) indicated an increase in unit cell parameters consistent with the presence of an increasing amount of Fe^{3+} with larger ionic radius. The thermal analysis of $La_{0.5}Sr_{0.5}FeO_3$ in 10% hydrogen /90% nitrogen is shown in Figure 4.23 (a). A weight decrease of *ca.* 2%, corresponding to a loss of lattice oxygen and the formation of a material of composition $La_{0.5}Sr_{0.5}FeO_{2.72}$, was observed from the thermogravimetric analysis (tga) curve at *ca.* 600 °C which agrees well with the formation of a compound of composition $La_{0.5}Sr_{0.5}FeO_{2.75}$ which can be calculated on the assumption that all the Fe^{4+} in $La_{0.5}Sr_{0.5}FeO_3$ is reduced to Fe^{3+}. The thermal analysis of a sample retrieved after the first peak following treatment in hydrogen and nitrogen is shown in Figure 4.23 (b) and indicates that no further weight loss is observed until the material is heated above *ca.* 700 °C.

It is interesting to note that while the pure material is paramagnetic at room temperature (298K), the material obtained after treatment in the tpr experiment at 600°C is magnetically ordered at 298K. This might be due to the different strength of the magnetic interactions existing in these compounds. It is known[14] that the Fe^{3+}-Fe^{3+} interaction is stronger than the Fe^{4+}-Fe^{4+}-and Fe^{4+}-Fe^{3+} interactions. Therefore, the absence of Fe^{4+} ions in the material heated at 600°C in hydrogen and nitrogen increases the strength of the superexchange interactions between the Fe ions which results in magnetic order at room temperature and, consequently, in the existence of a large hyperfine magnetic field.

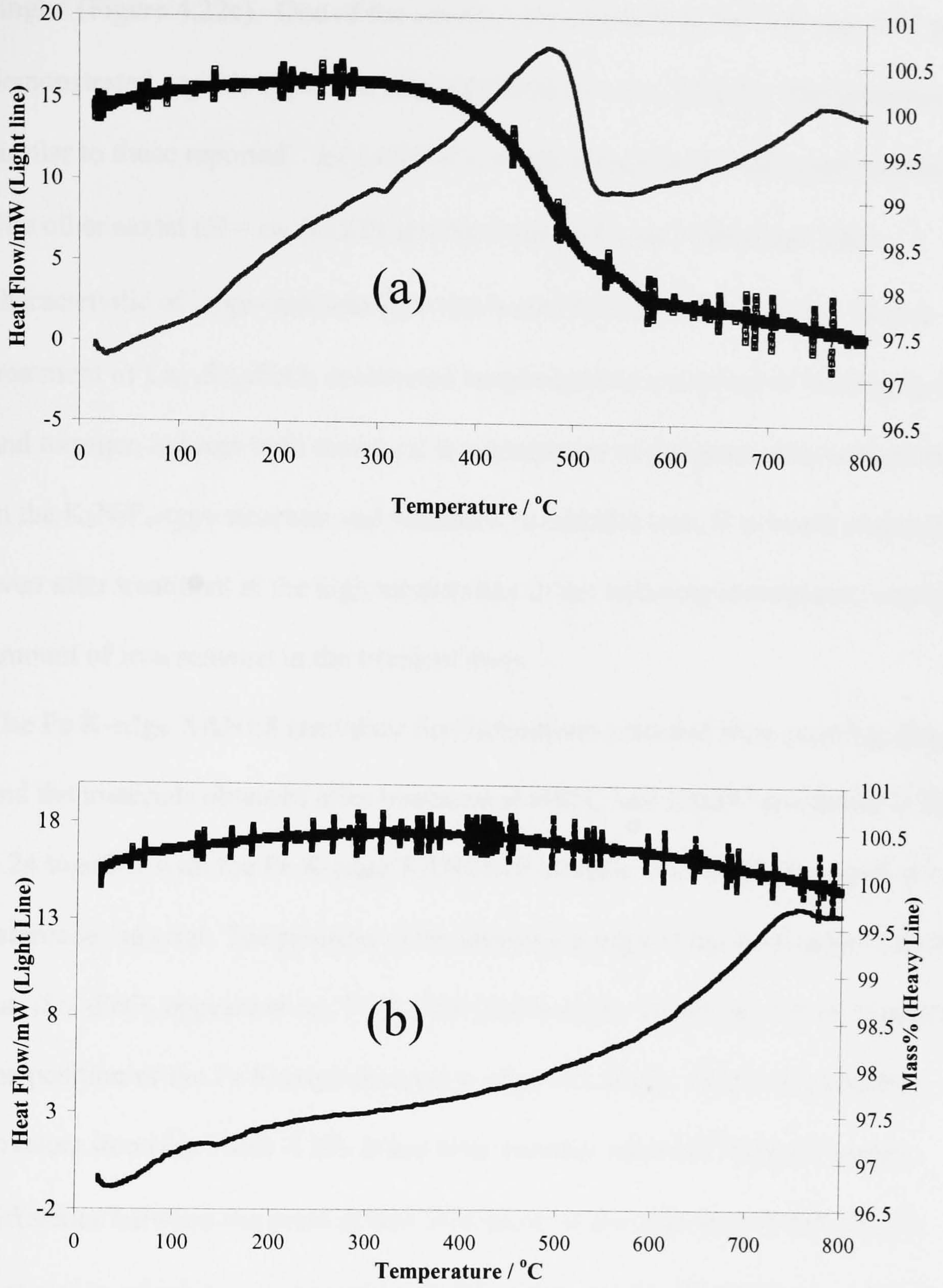

Figure 4.23 TGA (heavy line) and DSC (light line) curves in flowing hydrogen and nitrogen recorded from (a) $La_{0.5}Sr_{0.5}FeO_3$ and (b) $La_{0.5}Sr_{0.5}FeO_{3-\delta}$

.

The Mössbauer spectrum recorded from the material heated at *ca.* 1200°C that is, after the second peak in the tpr profile, showed the superposition of two sextets and a singlet (Figure 4.22c). One of the sextets, characteristic of Fe^{3+} (δ = *ca.* 0.31 mms^{-1}), demonstrated a small hyperfine magnetic field (H = *ca.* 32.4 T). The parameters are similar to those reported[17] for $LaSrFeO_4$ which adopts the K_2NiF_4-type structure. The other sextet (H = *ca.* 33.2T) and the singlet (δ = *ca.* -0.08 mms^{-1}) are characteristic of large- and small-particle metallic α-iron respectively. Hence treatment of $La_{0.5}Sr_{0.5}FeO_3$ at elevated temperature in a mixture of flowing hydrogen and nitrogen induces both structural rearrangement of the perovskite-related lattice to the K_2NiF_4-type structure and reduction to metallic iron. It is worth noting that, even after treatment at the high temperature in the reducing atmosphere, a noticeable amount of iron remains in the trivalent state.

The Fe K-edge XANES (and their first derivative) recorded from pure $La_{0.5}Sr_{0.5}FeO_3$ and the materials obtained after treatment at 600°C and 1200°C are shown in Figure 4.24 together with the Fe K-edge XANES of metallic iron which was used as a reference material. The position of the absorption edge in the Fe K-edge XANES of $La_{0.5}Sr_{0.5}FeO_3$ appears at *ca.* 7128.5 eV (Table 4.13). This is *ca.* 1.9 eV higher than the position of the Fe K-edge absorption edge of $LaFeO_3$ which only contains trivalent iron (see Table 4.13). It has been recently reported[16] that the energy difference between the point at half absorption of the edge step of $SrFeO_{3-\delta}$ (a material in which iron is primarily quadrivalent) and the first inflexion point in the Fe K-edge XANES of metallic Fe is *ca.* 14 eV. Inspection of Table 4.13 shows a similar energy difference for $La_{0.5}Sr_{0.5}FeO_3$ and metallic iron. The results are consistent with the presence of Fe^{4+} in this material as indicated by Mössbauer spectroscopy.

The position of the Fe K-absorption edge recorded from the material following treatment at 600°C shifts to 7127.4 eV, a value which is closer to that shown by

$LaFeO_3$. It is also interesting to note that the 1s→3d pre-edge feature at 7115.9 eV in the Fe K-edge XANES of pure $La_{0.5}Sr_{0.5}FeO_3$ shifts to 7114.6 eV in the Fe K-edge XANES of the material treated at 600°C. A shift of *ca.* 1.5 eV is also observed at the edge (Figure 4.24). All these changes are indicative of the reduction of Fe^{4+} to Fe^{3+}

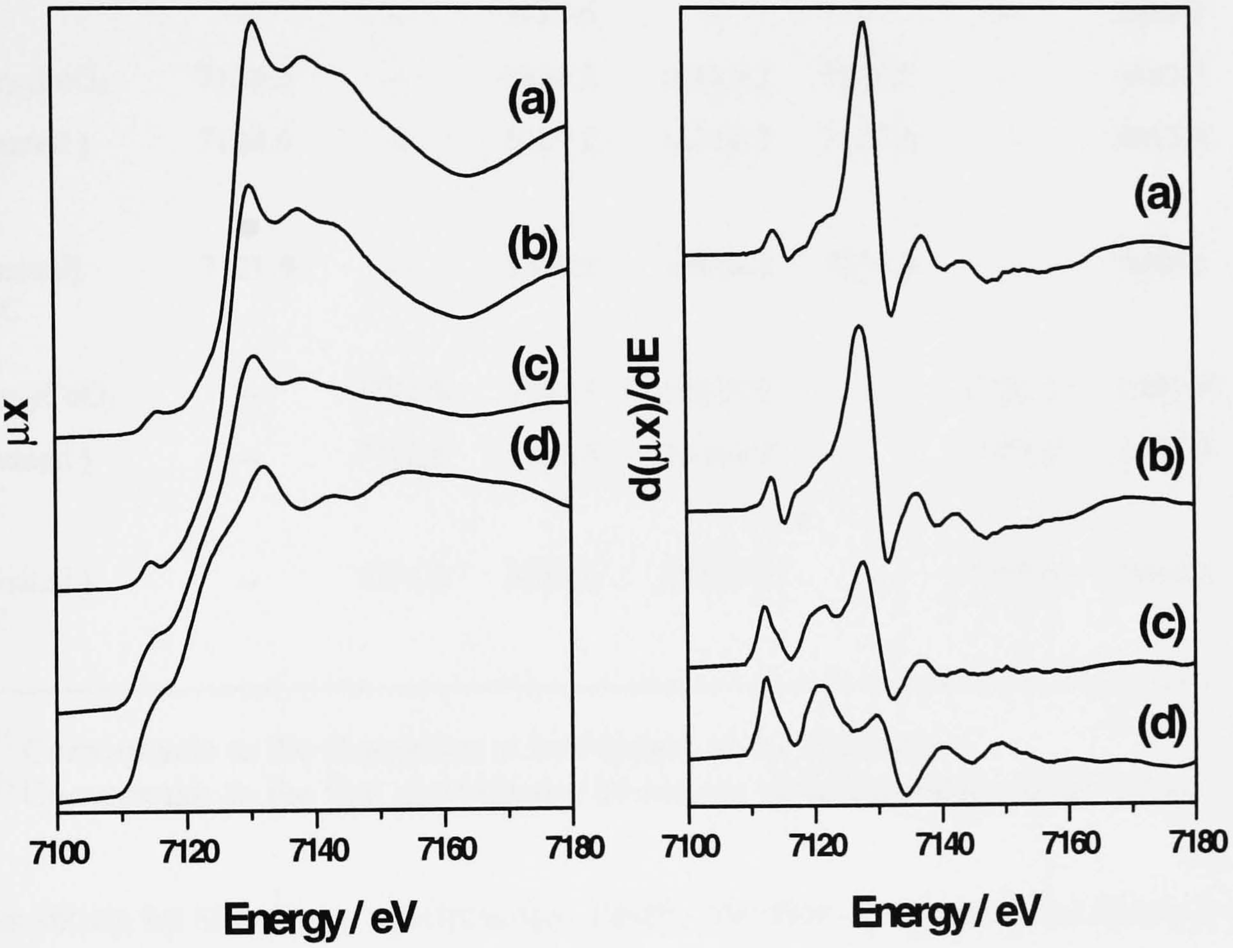

Figure 4.24 ***Left:*** **Fe K-edge XANES recorded from (a) $La_{0.5}Sr_{0.5}FeO_3$ and following treatment in 10% hydrogen/90% nitrogen at (b) 600°C and (c) 1200°C.** ***Right:*** **Corresponding first derivatives of the spectra on the left. (d) corresponds to iron metal.**

Table 4.13 X-ray Absorption Edge Positions Recorded from the X-ray Absorption Near Edge Structure

	Edge Position[1] (eV) ± 0.3				Edge Position[2] (eV) ± 0.3			
	Fe	Co	La	Sr	Fe	Co	La	Sr
Fe (metal foil)	7119.7	--	--	--	7112.3	--	--	--
Co (metal foil)	--	7716.0	--	--	--	7709.0	--	--
$LaFeO_3$	7125.5	--	5482.3	--	7126.6	--	5484.3	--
$LaCoO_3$	--	7720.6	--	--	--	7723.6	--	--
La_2O_3	--	--	5480.6	--	--	--	5484.3	--
$La_{0.5}Sr_{0.5}FeO_3$	7126.5	--	5480.2	16110.2	7128.5	--	5483.5	16102.5
(tpr treated) 600°C	7124.9	--	5480.2	16110.2	7127.4	--	5483.4	16104.3
(tpr treated) 1200°C	7121.9	--	5480.2	16110.2	7112.3	--	54832	16103.8
$La_{0.5}Sr_{0.5}CoO_3$	--	7721.8	5480.5	16110.0	--	7724.2	5483.9	16105.1
(tpr treated) 520°C	--	7716.6	5480.8	16110.2	--	7709.0	5483.9	16105.0
(tpr treated) 800°C	--	7716.2	5481.0	16110.2	--	7709.0	5484.2	16104.9

[1] Corresponds to the absorption at half-height of the edge step
[2] Corresponds to the first most intense maximum in the derivative of the XANES

as shown by Mössbauer spectroscopy. Finally, the first most intense maximum in the derivative of the Fe K-edge XANES of the material treated at 1200°C appears at 7112.3 eV, a value which matches the position of the Fe K-edge of metallic iron. Inspection of Figure 4.24 also shows that the Fe K-edge XANES of this material contains some features compatible with the presence of Fe^{3+} (peak in the first derivative at 7127.4 eV) which corresponds to the presence (evidenced by both XRD and ^{57}Fe Mössbauer spectroscopy) of the Fe^{3+}-containing phase $SrLaFeO_4$.

Table 4.14 Best fit parameters to the Fe K-edge Sr K-edge and La L_{III}-edge EXAFS recorded from $La_{0.5}Sr_{0.5}FeO_3$

	$La_{0.5}Sr_{0.5}FeO_3$			$La_{0.5}Sr_{0.5}FeO_3$ treated at 600 °C in 10% hydrogen and 90% nitrogen			$La_{0.5}Sr_{0.5}FeO_3$ treated at 1200 °C in10% hydrogen and 90% nitrogen		
	Coordination number and [atom type]	d/ Å (±0.02)	$2\sigma^2$/ Å^2	Coordination number and [atom type]	d/ Å (±0.02)	$2\sigma^2$/ Å^2	Coordination number and [atom type]	d/ Å (±0.02)	$2\sigma^2$/ Å^2
Fe K-edge	3[O]	1.865	0.006	6[O]	1.942	0.01	4[O]	1.963	0.019
	3[O]	1.983	0.004	0.5[La]	2.913	0.004	2[O]	2.197	0.012
	0.5[La]	3.052	0.009	0.5[Sr]	3.223	0	4.5[Fe]	2.484	0.013
	0.5[Sr]	3.219	0.001	7[La]	3.202	0.03			
	7[La]	3.217	0.03	6[Fe]	3.947	0.02			
	6[Fe]	3.939	0.009						
Sr K-edge	3[O]	2.557	0.01	3[O]	2.537	0.02	1[O]	2.391	0
	6[O]	2.750	0.02	6[O]	2.758	0.05	4[O]	2.589	0.004
	3[O]	3.322	0.001	3[O]	3.299	0.001	4[O]	2.793	0.01
	2[Fe]	3.512	0.04	2[Fe]	3.441	0.03	4[Fe]	3.240	0.023
	6[Fe]	3.321	0.02	6[Fe]	3.272	0.04			
	6[Sr]	3.960	0.05	6[Sr]	3.919	0.05			
La L_{III}-edge	3[O]	2.588	0.007	3[O]	2.530	0.02	1[O]	2.440	0.003
	6[O]	2.813	0.03	6[O]	2.741	0.04	4[O]	2.626	0.0
	3[O]	3.488	0.004	3[O]	3.468	0.05	4[O]	2.845	0.002
	2[Fe]	3.466	0.008	2[Fe]	3.544	0.01	4[Fe]	3.287	0.024
	6[Fe]	3.339	0.01	6[Fe]	3.351	0.02			
	6[Sr]	4.044	0.05	6[Sr]	4.056	0.05			

Summarizing, the movement to lower energy of the Fe K-edge XANES (clearly observed in Figure 4.24 and Table 4.13 if the criterion of defining the position of the edge at the energy at half-absorption of the edge step is taken) with increasing treatment in the hydrogen/nitrogen gas mixture is consistent with enhanced reduction of iron. In contrast to the variation of the Fe K- X-ray absorption edge positions, the La L_{III}-edge- and Sr K-edge-X-ray absorption edge positions do not change significantly with treatment in the flowing mixture of hydrogen and nitrogen being characteristic of La^{3+} and Sr^{2+} respectively (Table 4.13).

The Fe K-edge EXAFS are shown in Figure 4.25. The fitting of the data recorded from the reduced materials was complicated by the multiphasic nature of the products, hence Table 4.14 contains only the best fit parameters to the region 0-3Å. The first peak corresponding to six oxygen atoms in the Fourier transform of the data recorded from $La_{0.5}Sr_{0.5}FeO_3$ (Figure 4.25a) was located at *ca.* 1.924 Å which is shorter than the distance (1.98-2.00 Å) for the six oxygen atoms which coordinate iron in $LaFeO_3$[6]. This is consistent with the presence of Fe^{4+} in $La_{0.5}Sr_{0.5}FeO_3$ as shown by ^{57}Fe Mössbauer spectroscopy. A better fit was obtained by refining the first shell oxygen coordination to three oxygen atoms at 1.865 Å, a distance which is characteristic of Fe^{4+} [18], and three at 1.983 Å characteristic of Fe^{3+}-O distance, and which reflects the equal amount of Fe^{4+} and Fe^{3+} in this material.

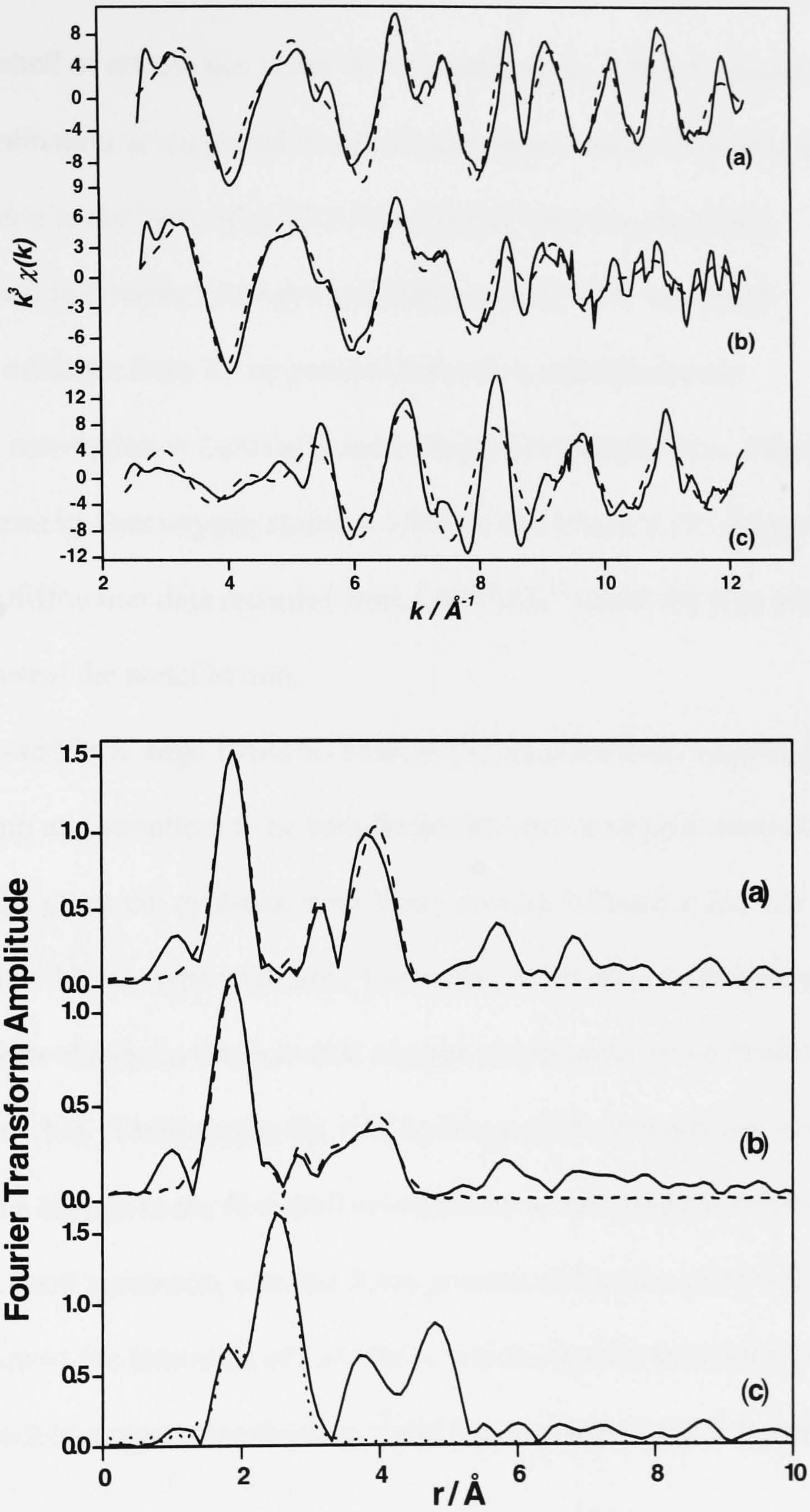

Figure 4.25 *Top:* Fe K-edge EXAFS recorded from (a) $La_{0.5}Sr_{0.5}FeO_3$ and following treatment in 10% hydrogen/90% nitrogen at (b) 600°C and (c) 1200°C. *Bottom:* The corresponding Fourier transforms of the above EXAFS. (The experimental data are indicated by a solid line, and the fits to the data are indicated by a broken line.)

Following treatment in hydrogen and nitrogen at 600°C the Fe K-edge EXAFS showed the first shell of six oxygen atoms to be located at *ca.* 1.942 Å consistent with Fe^{3+}-O coordination as suggested by Mössbauer spectroscopy. The first shell coordination of iron in the Fe K-edge EXAFS recorded from $La_{0.5}Sr_{0.5}FeO_3$ following treatment in flowing hydrogen and nitrogen at 1200°C was fitted according to the evidence from X-ray powder diffraction and Mössbauer spectroscopy for conversion to $LaSrFeO_4$ and reduction to metallic iron. Hence the coordination of iron by four oxygen atoms at 1.963 Å and two at 2.197 Å agrees well with the neutron diffraction data recorded from $LaSrFeO_4$[12] whilst the iron atoms at *ca.* 2.484 Å represent the metallic iron.

The La L_{III}-edge-and Sr K-edge EXAFS (Table 4.14) recorded from $La_{0.5}Sr_{0.5}FeO_3$ showed lanthanum and strontium to be coordinated by twelve oxygen atoms as would be expected given the evidence from X-ray powder diffraction that the material adopts the $SrFeO_3$-type structure. The material treated in hydrogen at *ca.* 600°C showed little change in the first shell oxygen coordination of lanthanum and strontium (Table 4.14). Treatment in the 10% hydrogen/90% nitrogen gas mixture at 1200 °C induced a change in the first shell coordination to nine oxygen atoms (Table 4.14). This is in good agreement with the X-ray powder diffraction pattern (Figure 4.20d) which showed the formation of $LaSrFeO_4$, which contains lanthanum and strontium in nine-fold oxygen coordination,[12] and the presence of small amounts of La_2O_3.

$La_{0.5}Sr_{0.5}CoO_3$

The XRD pattern recorded from the compound $La_{0.5}Sr_{0.5}CoO_3$ is shown in Figure 4.26. The pattern is characteristic of the $SrCoO_3$-type structure (Figure 4.26 (a)). The tpr profile recorded for $La_{0.5}Sr_{0.5}CoO_3$ (Figure 4.21) shows the second peak to move to much lower temperature as compared to $La_{0.5}Sr_{0.5}FeO_3$. The XRD pattern recorded from the material treated at 520°C, i.e. after the first reduction peak in the tpr profile (Figure 4.21), showed very broad lines which indicate a marked decrease in the crystallinity of this material. After tpr treatment at 800°C, the material had decomposed to SrO, La_2O_3 and metallic cobalt (Figure 4.26).

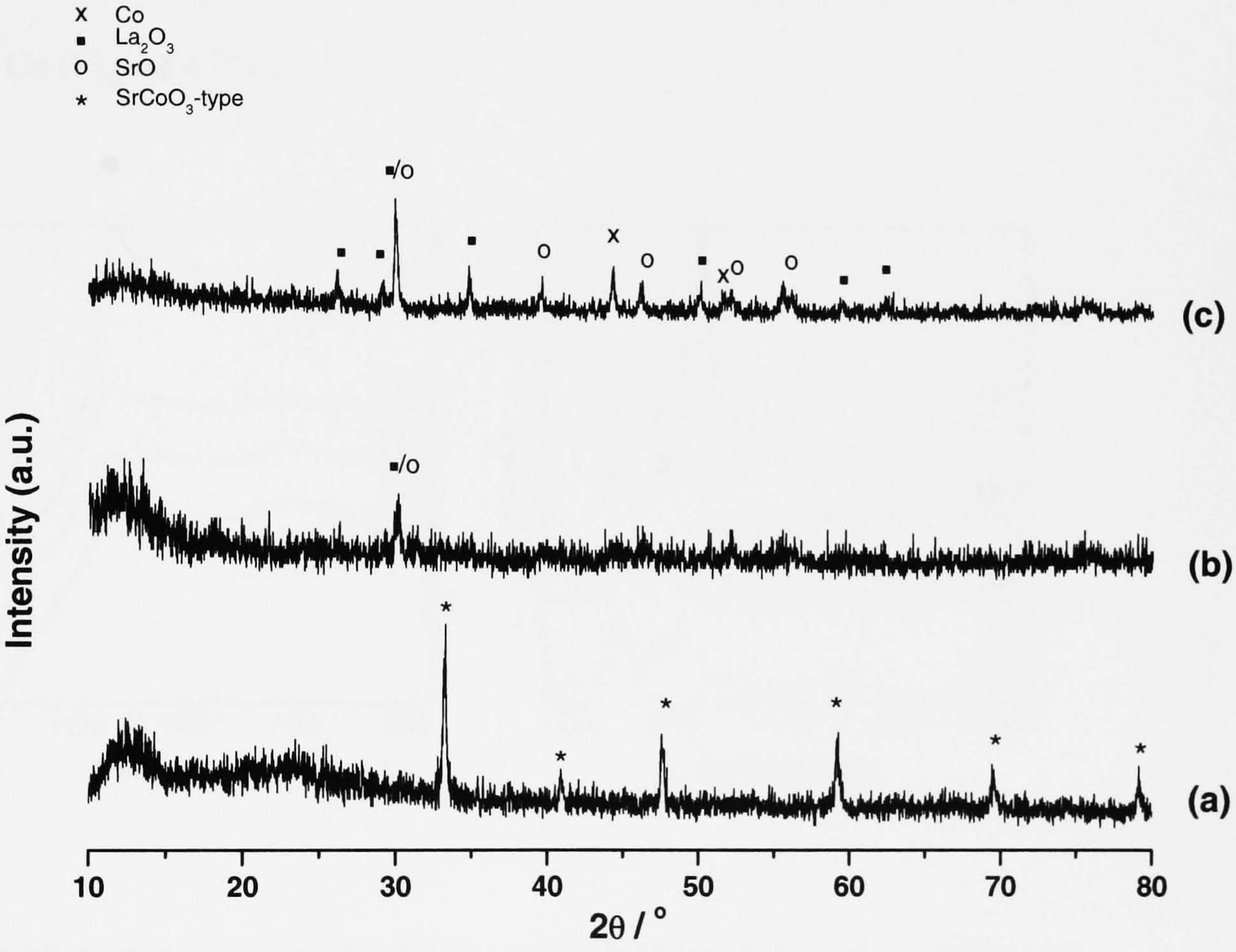

Figure 4.26 X-ray powder diffraction patterns recorded from (a) $La_{0.5}Sr_{0.5}CoO_3$ and following sequential treatment in (b) 10% hydrogen/90% nitrogen at 520°C (c) 10% hydrogen/90% nitrogen at 800°C.

The edge position at 7724.2 eV of the Co K-edge XANES recorded from $La_{0.5}Sr_{0.5}CoO_3$ (Figure 4.27a, Table 4.13) is *ca.* 0.6 eV higher than the edge position of the Co K-edge XANES recorded from $LaCoO_3$ made by the conventional method which contained only Co^{3+}. The energy at half-absorption of the edge step (Table

4.13) correlates well with recently published XANES data for $La_{0.5}Sr_{0.5}CoO_3$[19,20] and reflects the presence in this compound of Co^{4+} and Co^{3+}. The Co K-edge XANES recorded when the material was heated in flowing hydrogen and nitrogen at 520°C was almost identical to that recorded from metallic Co (Figure 4.27b and 4.27d). This demonstrates that, under these mild conditions, the formation of metallic cobalt is readily achieved. The Co K-edge XANES recorded from the material heated at the higher temperature of 800°C also showed the presence of metallic Co (Figure 4.27c).

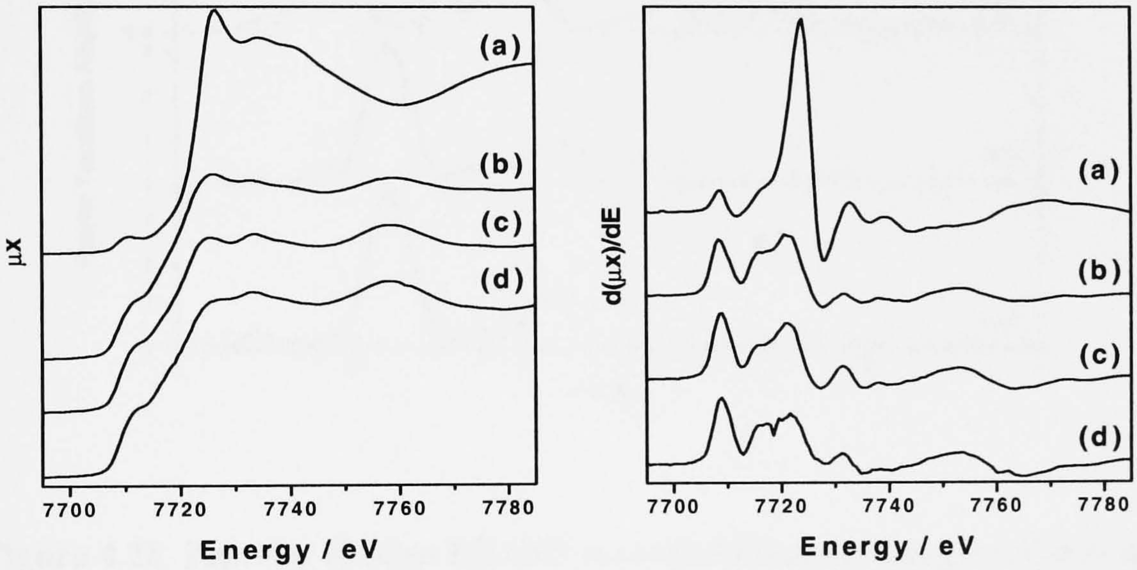

Figure 4.27 ***Left:*** **Co K-edge XANES recorded from (a) $La_{0.5}Sr_{0.5}CoO_3$ and following treatment in flowing 10% hydrogen/90% nitrogen at (b) 520°C, (c) 800°C.** ***Right:*** **Corresponding first derivatives of the spectra on the left, (d) XANES recorded from metallic cobalt.**

The Co K-edge EXAFS (Figure 4.28, Table 4.15) endorsed the result showing that the coordination of cobalt by six oxygen atoms in the pure material (Figure 4.28a, Table 4.15) at 1.90 Å, which is close to that reported previously[19,20], changed to coordination by cobalt atoms in the reduced phases (Figure 4.28b, c; Table 4.15).

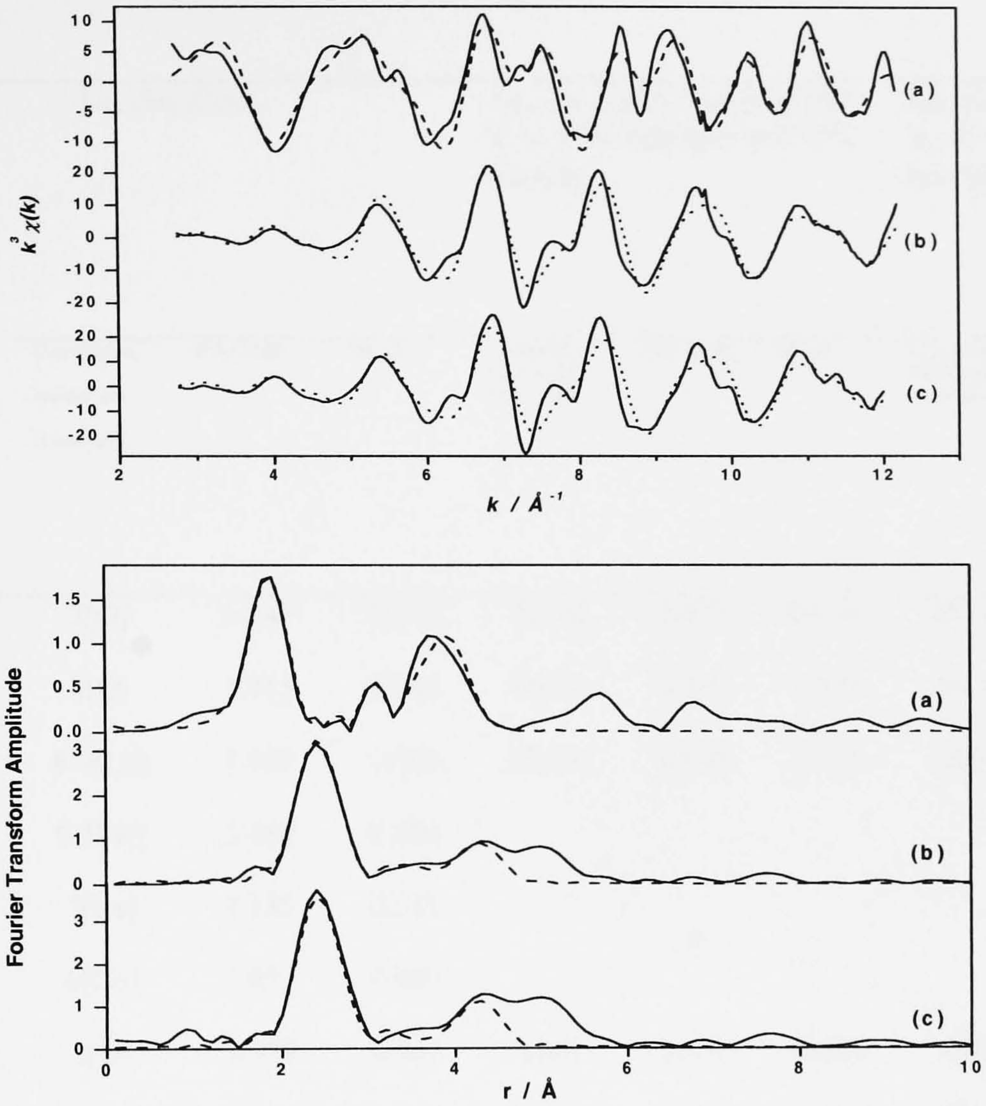

Figure 4.28 ***Top:*** **Co K-edge EXAFS recorded from (a) $La_{0.5}Sr_{0.5}CoO_3$ and following treatment in flowing 10% hydrogen/90% nitrogen at (b) 520°C, (c) 800°C.** ***Bottom:*** **The corresponding Fourier transforms of the above EXAFS. (The experimental data are indicated by a solid line, and the fits to the data are indicated by a broken line.)**

Table 4.15 Best fit parameters to the Co K-edge Sr K-edge and La L$_{III}$-edge EXAFS recorded from La$_{0.5}$Sr$_{0.5}$CoO$_3$

	La$_{0.5}$Sr$_{0.5}$CoO$_3$			La$_{0.5}$Sr$_{0.5}$CoO$_3$ treated at 520 °C in 10% hydrogen and 90% nitrogen			La$_{0.5}$Sr$_{0.5}$CoO$_3$ treated at 800 °C in 10% hydrogen and 90% nitrogen		
	Coordination number and [atom type]	d/ Å (±0.02)	$2\sigma^2$/ Å^2	Coordination number and [atom type]	d/ Å (±0.02)	$2\sigma^2$/ Å^2	Coordination number and [atom type]	d/ Å (±0.02)	$2\sigma^2$/ Å^2
Co K-edge	3[O]	1.849	0.005	8[Co]	2.479	0.014	8[Co]	2.477	0.012
	3[O]	1.955	0.004	6[Co]	3.492	0.028	6[Co]	3.446	0.035
	0.5[La]	3.029	0.008	12[Co]	4.308	0.018	12[Co]	4.300	0.015
	0.5[Sr]	3.168	0.009						
	7[La]	3.185	0.031						
	6[Co]	3.892	0.009						
Sr K-edge	3[O]	2.576	0.003	6[O]	2.551	0.024	6[O]	2.571	0.021
	6[O]	2.776	0.014	4[Sr]	3.544	0.041	12[Sr]	3.606	0.045
	3[O]	3.280	0.003						
	2[Co]	3.538	0.030						
	6[Co]	3.300	0.018						
	6[Sr]	3.921	0.037						
La L$_{III}$-edge	3[O]	2.547	0.002	4[O]	2.530	0.004	4[O]	2.523	0.0035
	6[O]	2.735	0.019	3[O]	2.741	0.006	3[O]	2.669	0.0067
	3[O]	3.411	0.008	6[Sr]	3.884	0.05	6[Sr]	3.847	0.053
	2[Co]	3.397	0.023	6[Sr]	4.177	0.023	6[Sr]	4.177	0.021
	6[Co]	3.302	0.012						
	6[Sr]	3.942	0.047						

The X-ray absorption edge position of the La L_{III}-edge and Sr K-edges obtained from the XANES data (Table 4.13) did not change with increasing treatment in the reducing environment.

The La L_{III}-edge EXAFS recorded from $La_{0.5}Sr_{0.5}CoO_3$ (Figure 4.29a, Table 4.15) showed the lanthanum to be coordinated to twelve oxygen atoms in the

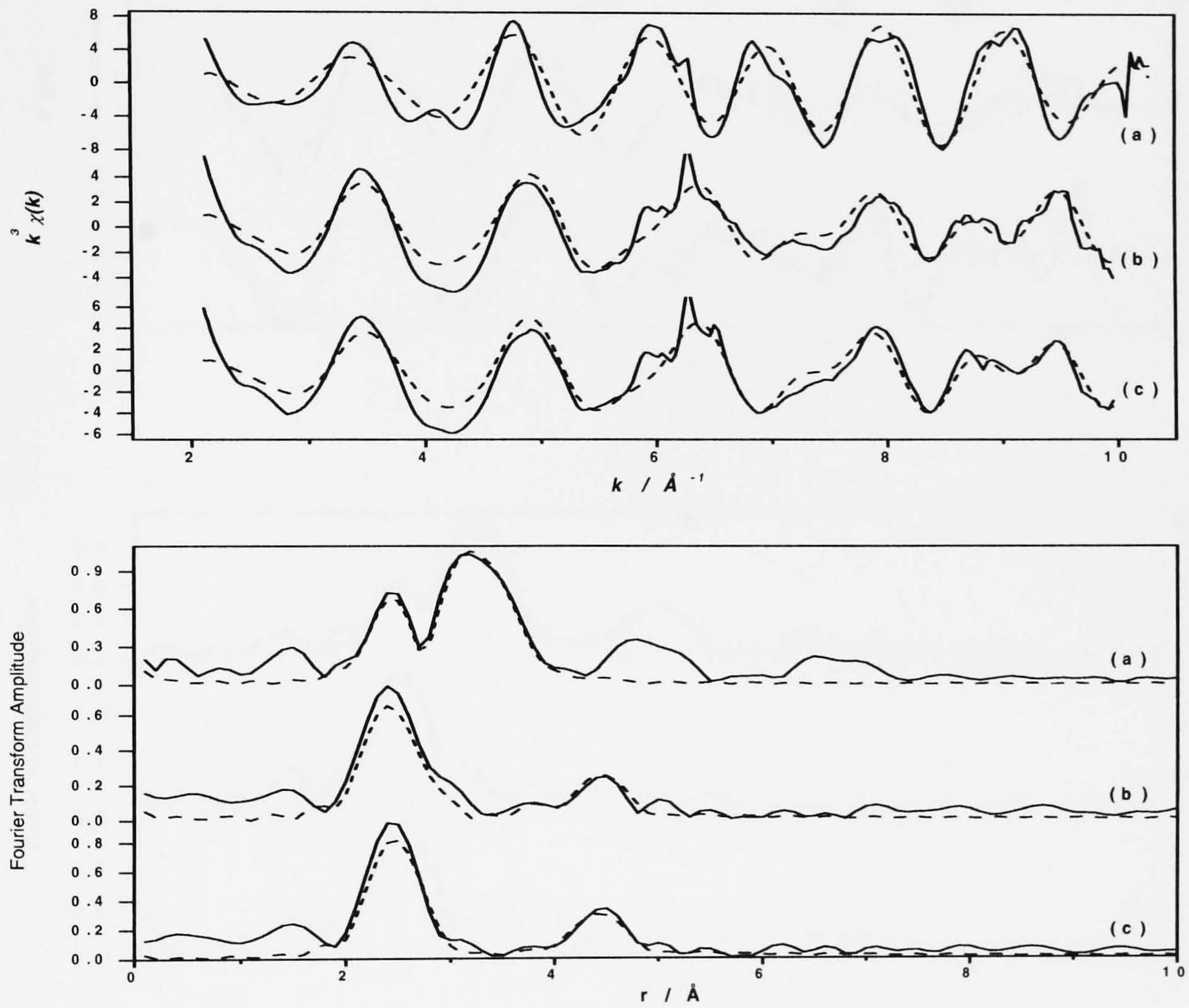

Figure 4.29 ***Top:*** **La L_{III}-edge EXAFS recorded from (a) $La_{0.5}Sr_{0.5}CoO_3$ and following treatment in flowing 10% hydrogen/90% nitrogen at (b) 520 °C, (c) 800 °C.** ***Bottom:*** **The corresponding Fourier transforms of the above EXAFS. (The experimental data are indicated by a solid line, and the fits to the data are indicated by a broken line.)**

perovskite-related structure[9]. Treatment at 520°C and 800°C in flowing 10 % hydrogen and 90 % nitrogen gave seven-fold oxygen coordination characteristic of La_2O_3[21] (Figure 4.29b, c, Table 4.15).

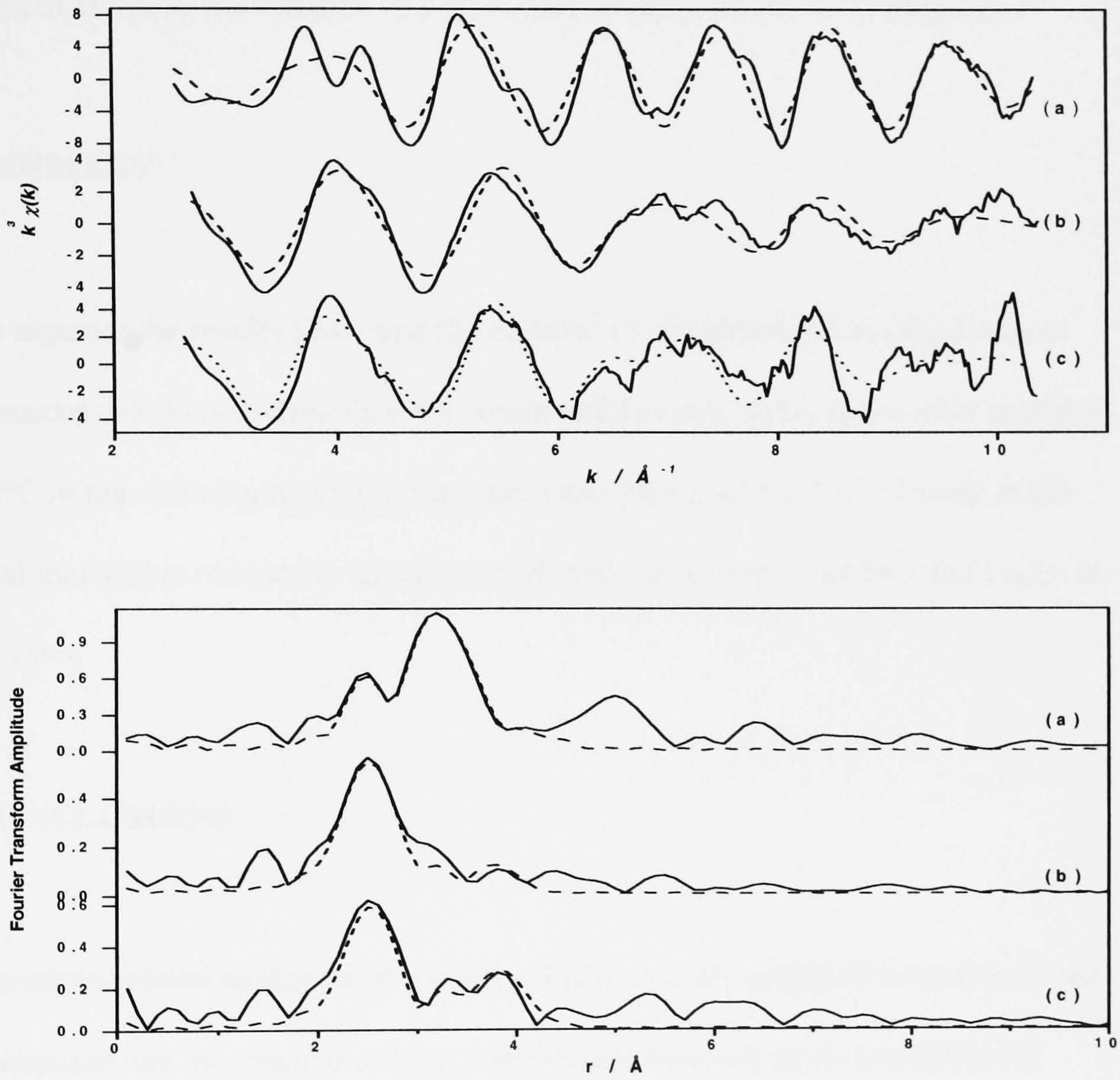

Figure 4.30 ***Top:*** **Sr K-edge EXAFS recorded from (a) $La_{0.5}Sr_{0.5}CoO_3$ and following treatment in flowing 10% hydrogen/90% nitrogen at (b) 520 °C, (c) 800°C.** ***Bottom:*** **The corresponding Fourier transforms of the above EXAFS. (The experimental data are indicated by a solid line, and the fits to the data are indicated by a broken line.)**

The Sr K-edge EXAFS recorded from $La_{0.5}Sr_{0.5}CoO_3$ (Figure 4.30a, Table 4.15) showed the strontium to be coordinated to twelve oxygen atoms in the perovskite-related structure. The data recorded following treatment in hydrogen and nitrogen at 800°C (Figure 4.30b, c Table 4.15) showed the strontium atom to be coordinated to six oxygen atoms at the distance of 2.57 Å characteristic of the SrO structure.

4.7 SUMMARY

Taken together the results show that the material of composition $La_{0.5}Sr_{0.5}CoO_3$ is more susceptible to reduction than the compound $La_{0.5}Sr_{0.5}FeO_3$ since, after heating at 520°C in the reducing hydrogen/nitrogen atmosphere, all the Co^{3+} present in the original material is reduced to metallic cobalt and the formation of SrO and La_2O_3 is also occurs.

4.8 CONCLUSIONS

1. Perovskite-related phases of composition $LaFe_{1-x}Co_xO_3$ prepared by conventional calcination and mechanical milling methods are rendered more susceptible to reduction in a flowing mixture of hydrogen and nitrogen by the incorporation of cobalt.
2. In iron-rich systems the limited reduction of iron and cobalt leads to segregation of discrete metallic phases without destruction of the perovskite structure.
3. In cobalt-rich systems the reduction of Co^{3+} to Co^0 precedes complete reduction of Fe^{3+} and the segregation of alloy and metal phases is accompanied by destruction of the perovskite-related structure.

4. Similar phases made by milling techniques are of smaller particle size and are more susceptible to hydrogen reduction than their counterparts made by conventional techniques.
5. Materials of the type $La_{0.5}Sr_{0.5}MO_3$, (M = Fe, Co) made by calcination methods are more susceptible to reduction when the transition metal M is cobalt rather than iron.

REFERENCES

1. Y. Sadaoka, E. Traversa, P. Nunziante, and M. Sakamoto, *J. Alloys Compounds,* 1997, **261**, 182
2. E. Traversa, P. Nunziante, M. Sakamoto, Y. Sodoaka, and R. Montanar, *Mater. Res. Bull.,* 1998, **33**, 673
3. M. Eibschitz, S. Shtrikmand, and D. Treves, *Phys. Rev.,* 1967, **156,** 562
4. B. Buffat and M. H. Tuilier, *Solid State Comm.,* 1987, **64**, 401
5. N. Binsted, G. N. Greaves and C. M. B. Henderson, *J. Phys. Coll C8*, 1986, **12,** C8-837
6. H. Falcon, A. E. Goeta, G. Punte and R. E. Carbonio, *J. Solid State Chem.*, 1997, **133**, 379
7. P. Eisenberger and B. Lengeler, *Phys. Rev.,* 1980, **22**, 3551
8. V. Carles, C. Laurent, M. Brieu, and A. Rousset, *J. Mater. Chem.,* 1999, **9**, 1003
9. P. Porta, S. de Rossi, M. Faticanti, G. Minelli, I. Pettiti, L. Lisi, and M.Turco, *J. Solid State Chem.*, 1999, **146**, 291
10. S. Colonna, S. de Rossi, M. Faticanti, I. Pettiti, L.Lisi, and P.Porta, *J. Mol. Catal A: Chem.*, 2002, **180**, 161
11. B. S. Clausen, S. Morup, P. Nielsen, N. Traen, and H. Topsoe, *J. Phys. E Sci. Ins.,* 1979, **19**, 439
12. J. L. Soubeyroux, P. Courbin, L. Fournes, D. Fruchart and G. Le Flem, *J. Solid State Chem.*, 1980, **31**, 313
13. L. Fournès, A. Wattiaux, A. Demourgues, P. Bezdicka, J. C. Grenier, M. Pouchard and J. Etourneau, *J. Phys. IV, Colloque C1,* 1997, **7,** C1-353
14. T. C. Gibb, *J. Chem. Soc. Dalton Trans.*, 1985, 1455

15. J. B. Yang, W. B. Yelon, W. J. James, Z. Chu, M. Kornecki, Y. X. Xie, X.D. Zhou, H. U. Anderson, A. G. Joshi and S. K. Malik, *Phys. Rev.*, 2002, **B66,** 184415

16. G. M. Veith, I. D. Fawcett, M. Greenblatt. M. Croft and I. Nowik, *Int. J. Inorg. Mater.,* 2000, **2,** 513

17. G. A. Waychunas, M. J. Apted and G. E. Brown, *Phys. Chem. Minerals,* 1983, **10,** 1

18. M. Holzapfel, O. Proux, P. Strobel, C. Darie, M. Borowski and M. Morcrette, *J. Mater. Chem.,* 2004, **14,** 102

19. A. C. Masset , O. Toulemonde , D. Pelloquin , E. Suard , A. Maignan , F. Studer, M. Hervieu , C. Michel, *Int. J. Inorg. Mat.*, 2000, **2,** 687

20. J. E. Sunstrom IV, K. V. Ramanujachary, and M. Greenblatt, *J. Solid State Chem.,* 1998, **139,** 388

21. F. Ali, A.V. Chadwick, and M. E. Smith, *J. Mater. Chem.,* 1997, **7,** 285

Chapter 5

RESULTS AND DISCUSSION: FLUORINATION OF PEROVSKITE-RELATED PHASES

Chapter 5

RESULTS AND DISCUSSION: FLUORINATION OF PEROVSKITE-RELATED PHASES

5.1 INTRODUCTION

The work described in Chapter 5 reports on:

1. Characterisation of perovskite-related materials of the type $La_{1-x}Sr_xFe_{1-y}Co_yO_3$, $SrFe_{1-x}Co_xO_3$ and $SrFe_{1-x}Sn_xO_3$ made by conventional methods, their fluorination by reaction with poly(vinyldene difluoride) and the characterisation of the fluorinated derivatives.
2. Fluorination of the K_2NiF_4-type phase Ba_2SnO_4 by reaction with ZnF_2.

5.2 $La_{1-x}Sr_xFe_{1-y}Co_yO_3$

The fluorination of several perovskite-related phases of the type $La_{1-x}Sr_xFe_{1-y}Co_yO_3$ made by conventional calcination methods (Chapter 3) was attempted. It was found that the presence of strontium was necessary for successful fluorination. Hence, fluorination experiments were performed on some representative strontium-containing samples in the $La_{1-x}Sr_xFe_{1-y}Co_yO_3$ system by reaction of the pure oxide with poly(vinylidene fluoride). The X-ray powder diffraction patterns recorded from materials of composition $La_{1-x}Sr_xFe_{1-y}Co_yO_3$ and their fluorinated derivatives are shown in Figure 5.1. The patterns show that fluorination induces a shift in peak position to lower angle corresponding to an increase in unit cell size. As also shown in Figure 5.1, heating the fluorinated samples subsequently in air at 400°C for 2 hours resulted in no further

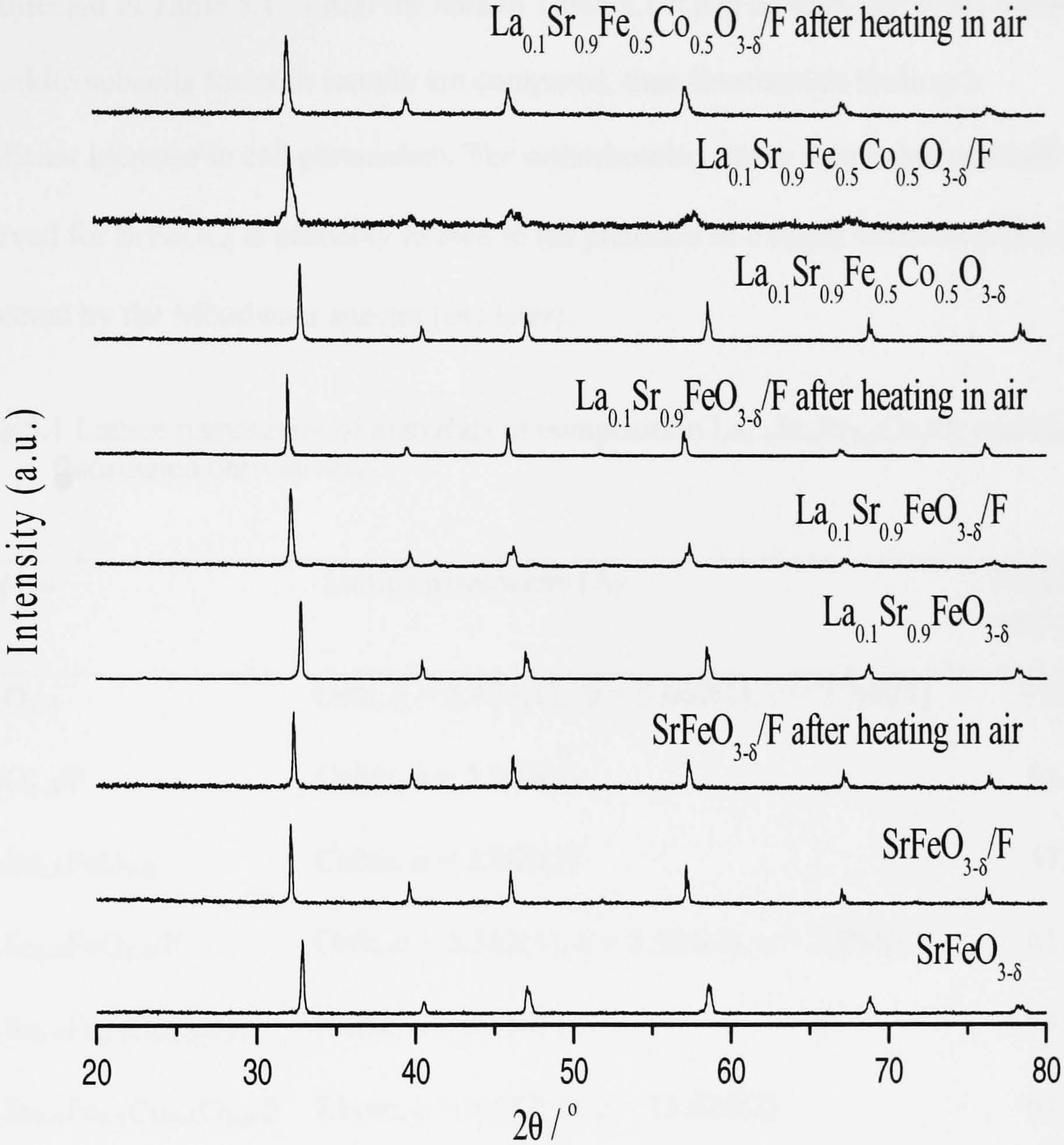

Figure 5.1 X-ray powder diffraction patterns recorded from materials of composition $La_{1-x}Sr_xFe_{1-y}Co_yO_3$ and their fluorinated derivatives, and after heating the fluorinated derivatives in air at 400 °C for 2 hours.

changes in peak position, consistent with the partial replacement of oxygen by fluorine, rather than a simple reduction in oxygen content.

The lattice parameters recorded from the pure oxides and their fluorinated derivatives are collected in Table 5.1. From the data in Table 5.1 it can be seen that if the primitive perovskite subcells for each sample are compared, then fluorination leads to a significant increase in cell parameters. The orthorhombic rather than cubic unit cell observed for $SrFeO_{3-\delta}$ is probably related to the presence of oxygen deficiency (δ) as supported by the Mössbauer spectra (see later).

Table 5.1 Lattice parameters of materials of composition $La_{1-x}Sr_xFe_{1-y}Co_yO_3$ and their fluorinated derivatives.

Samples	Lattice parameters (Å)	Primitive cell volumes (Å^3)
$SrFeO_{3-\delta}$	Orth, $a = 5.474(1)$, $b = 5.469(1)$, $c = 7.706(1)$	57.6
$SrFeO_{3-\delta}/F$	Cubic, $a = 3.956(1)$	61.9
$La_{0.1}Sr_{0.9}FeO_{3-\delta}$	Cubic, $a = 3.865(1)$	57.7
$La_{0.1}Sr_{0.9}FeO_{3-\delta}/F$	Orth, $a = 5.562(1)$, $b = 5.584(1)$, $c = 7.904(1)$	61.3
$La_{0.1}Sr_{0.9}Fe_{0.5}Co_{0.5}O_{3-\delta}$	Cubic, $a = 3.854(1)$	57.2
$La_{0.1}Sr_{0.9}Fe_{0.5}Co_{0.5}O_{3-\delta}/F$	Rhom, $a = 5.582(1)$, $c = 13.626(2)$	61.2

The X-ray absorption edge data recorded from materials of the type $La_{1-x}Sr_xFe_{1-y}Co_yO_3$, their fluorinated derivatives and appropriate standards are shown in Figure 5.2 and the edge position are collected in Table 5.2. The La L_{III}- and Sr K-edge X-ray absorption edge positions of all the materials did not change upon fluorination and were characteristic of La^{3+} in $LaFeO_3$ and Sr^{2+} in $SrFeO_{3-\delta}$. The results show that fluorination

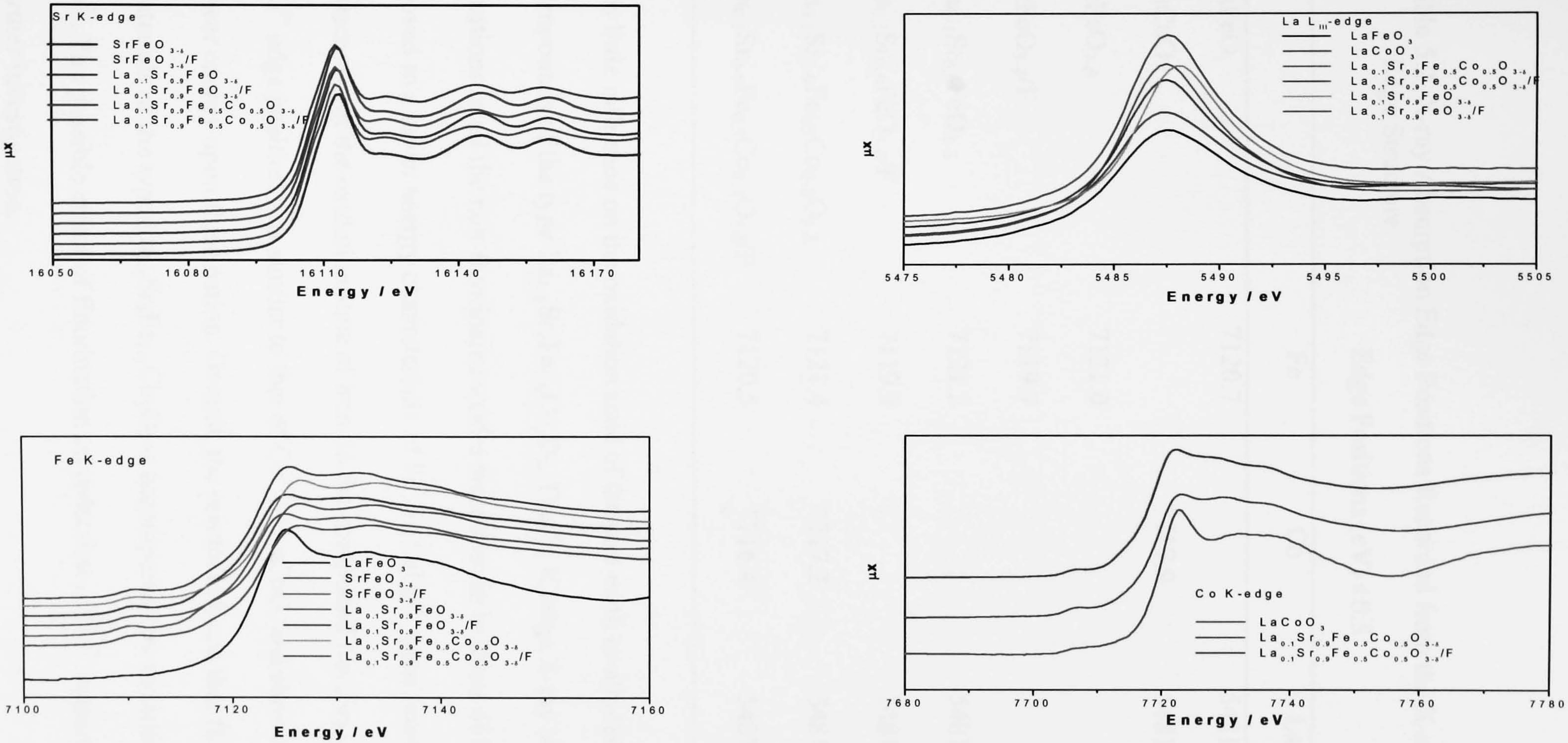

Figure 5.2 The X-ray absorption edge data recorded from materials of the type $La_{1-x}Sr_xFe_{1-y}Co_yO_3$ and their fluorinated derivatives.

Table 5.2 X-ray Absorption Edge Positions Recorded from the X-ray Absorption Near Edge Structure

Edge Positions (eV) ±0.5

	Fe	Co	La	Sr
$LaFeO_3$	7120.7		5481.5	
$LaCoO_3$		7717.9	5481.5	
$SrFeO_{3-\delta}$	7121.0			16110.4
$SrFeO_{3-\delta}/F$	7119.7			16110.4
$La_{0.1}Sr_{0.9}FeO_{3-\delta}$	7121.2		5481.2	16110.3
$La_{0.1}Sr_{0.9}FeO_{3-\delta}/F$	7119.9		5481.2	16110.3
$La_{0.1}Sr_{0.9}Fe_{0.5}Co_{0.5}O_{3-\delta}$	7121.4	7717.2	5481.7	16110.1
$La_{0.1}Sr_{0.9}Fe_{0.5}Co_{0.5}O_{3-\delta}/F$	7120.5	7716.4	5481.3	16110.3

has little influence on the oxidation state of the rare earth or alkaline earth element in compounds of the type $La_{1-x}Sr_xFe_{1-y}Co_yO_3$. The Fe K-edge X-ray absorption edge positions in all the non-fluorinated oxides were similar to those of Fe^{4+} in $SrFeO_{3-\delta}$ and moved to a lower energy characteristic of Fe^{3+} in $LaFeO_3$ upon fluorination indicative of a decrease in the oxidation state of iron. In the compound $La_{0.1}Sr_{0.9}Fe_{0.5}Co_{0.5}O_{3-\delta}$ the Co^{3+} edge position was similar to that of Co^{3+} in $LaCoO_3$ and showed a small shift to a lower energy upon fluorination. Overall, the results indicate that fluorination of materials of the type $La_{1-x}Sr_xFe_{1-y}Co_yO_3$ is accompanied by reduction of the Fe^{4+} ion to Fe^{3+}. The possible effect of fluorination on reduction of Co^{3+} requires confirmation and further investigation.

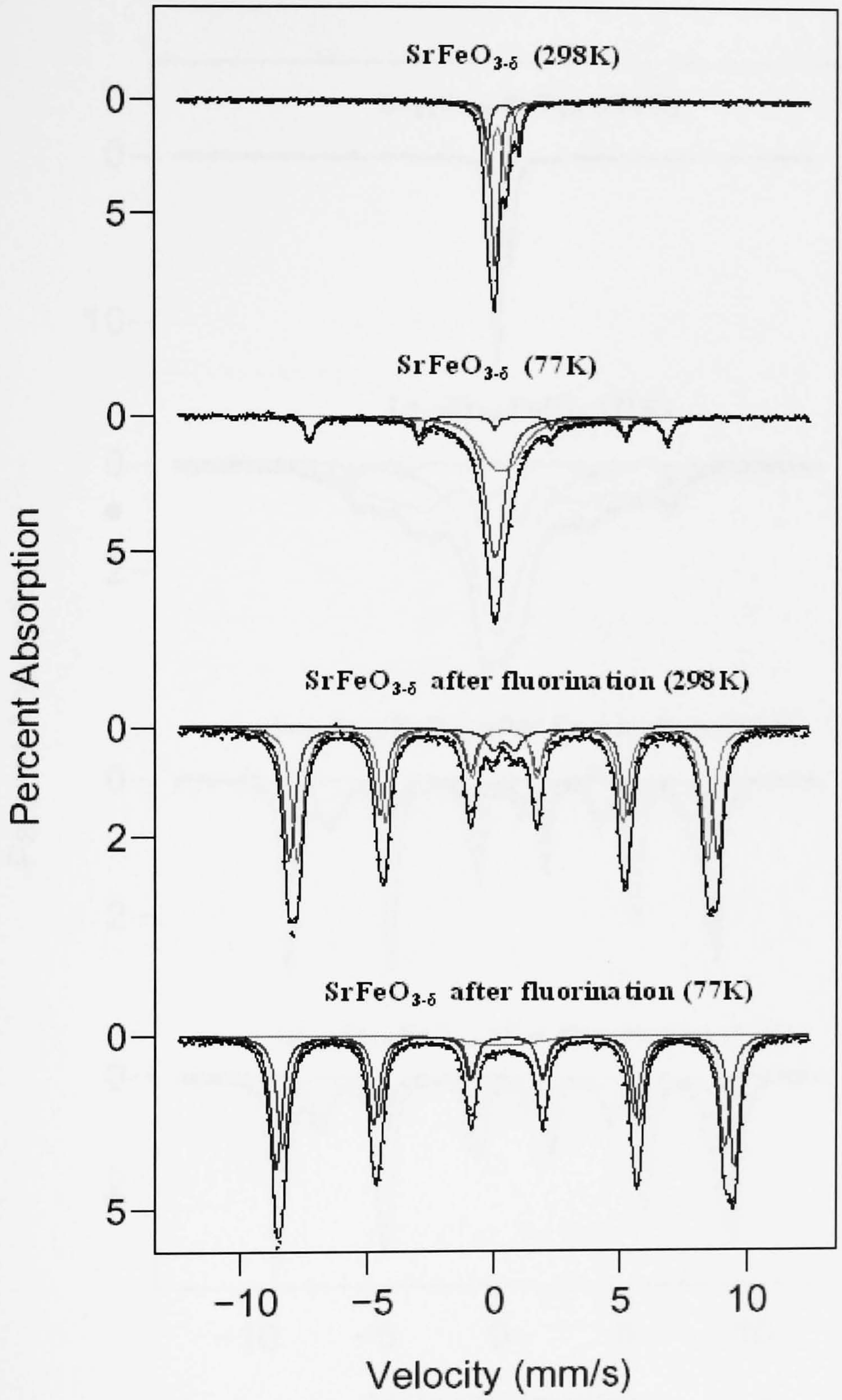

Figure 5.3 ^{57}Fe Mössbauer spectra recorded from SrFeO$_{3-\delta}$ at 298 K and 77K and following fluorination and recorded at 298 K and 77 K.

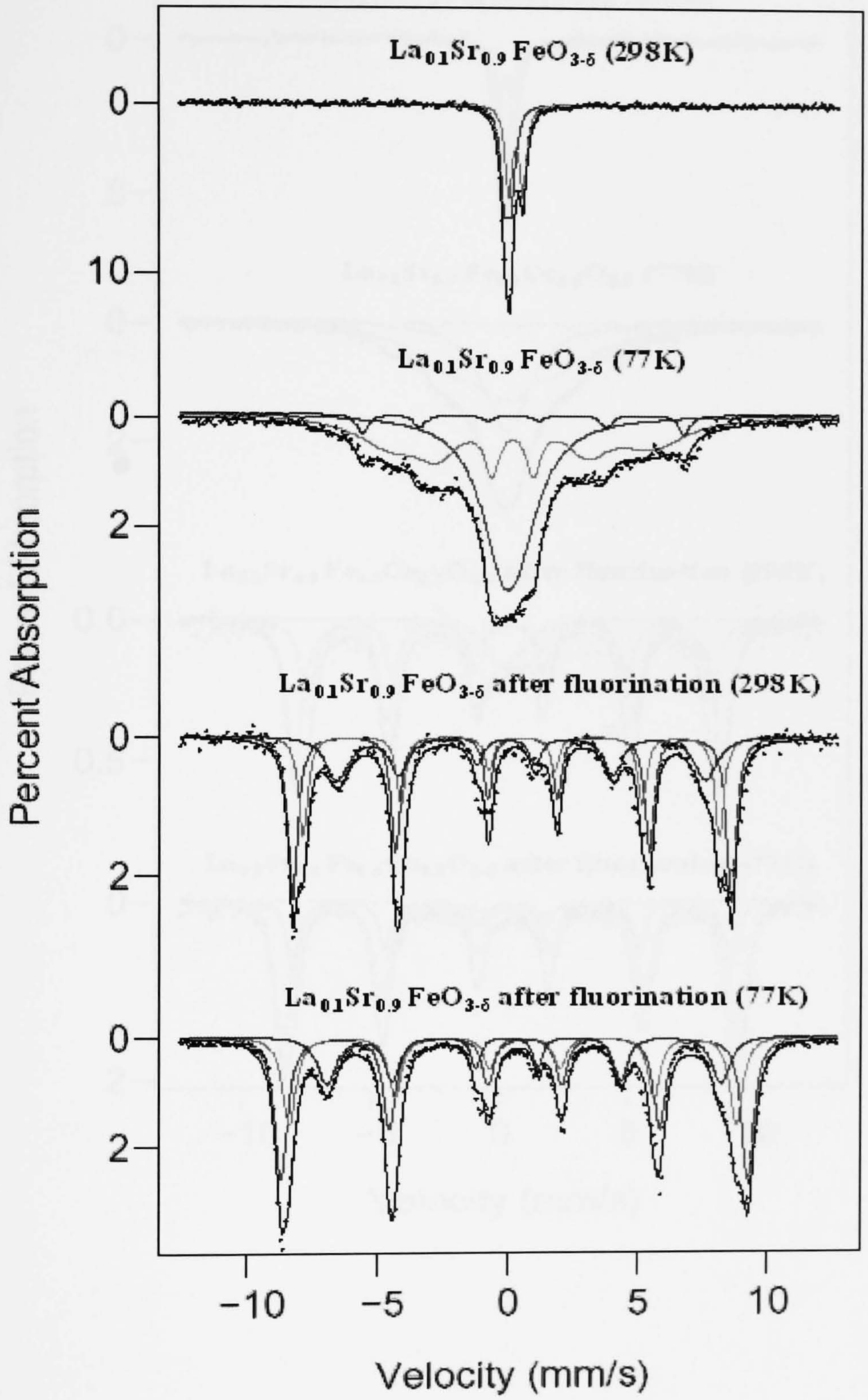

Figure 5.4 ^{57}**Fe Mössbauer spectra recorded from** $La_{0.1}Sr_{0.9}FeO_{3-\delta}$ **at 298 K and 77K and following fluorination and recorded at 298 K and 77 K.**

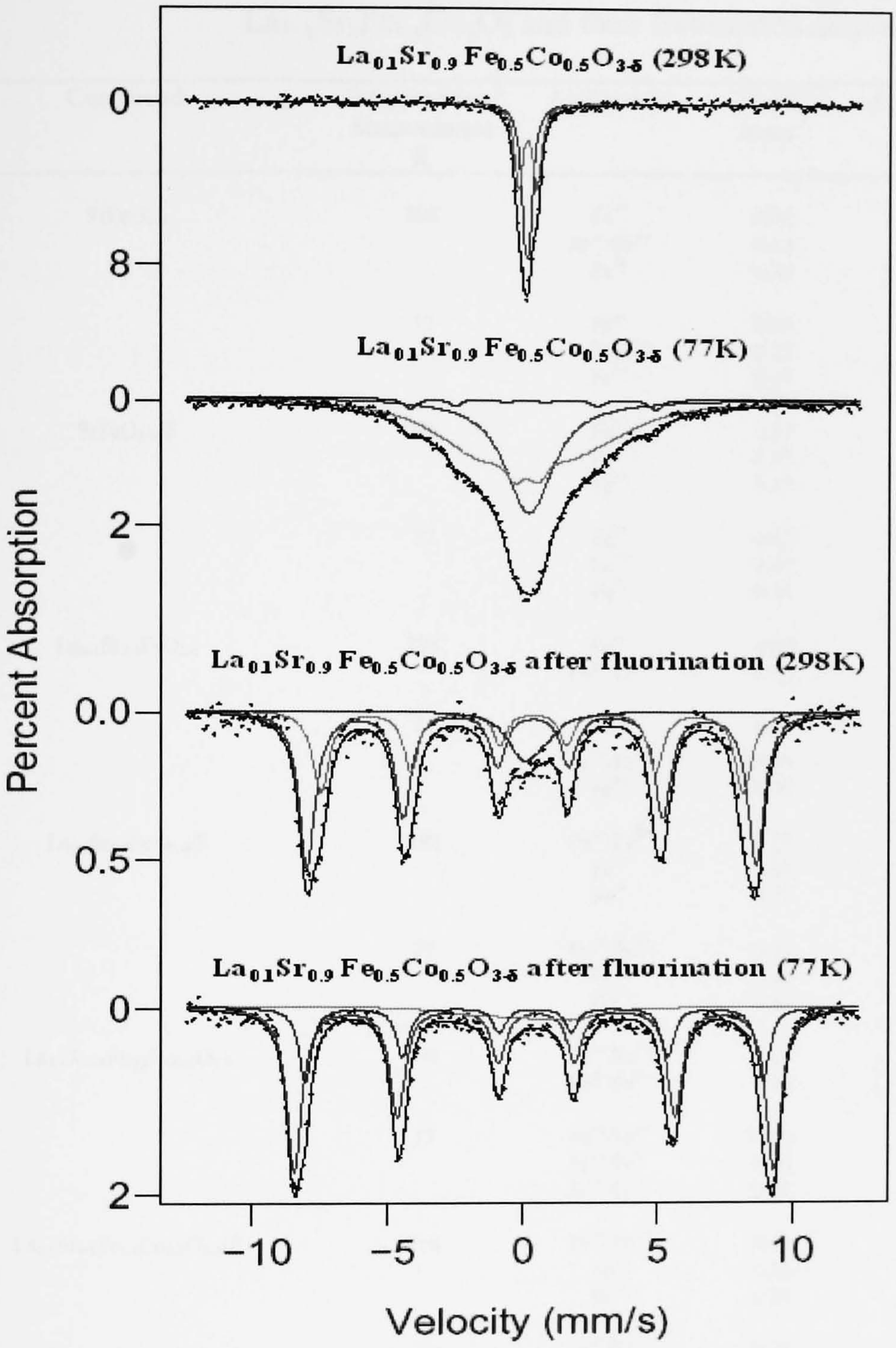

Figure 5.5 ^{57}**Fe Mössbauer spectra recorded from** $La_{0.1}Sr_{0.9}Fe_{0.5}Co_{0.5}O_{3-\delta}$ **at 298 K and 77K and following fluorination and recorded at 298 K and 77 K.**

Table 5.3 ^{57}Fe Mössbauer parameters recorded from materials of composition $La_{1-x}Sr_xFe_{1-y}Co_yO_3$ and their fluorinated derivatives

Compound	Temperature of Measurement K	Assignment	δ±0.05 /mms^{-1}	Δ or 2ε± 0.10 /mms^{-1}	H± 0.5 /T	Area± 5 %
$SrFeO_{3-\delta}$	298	Fe^{4+}	0.04	0.12	0	44
		Fe^{4+}/Fe^{3+}	0.14	0.69	0	38
		Fe^{3+}	0.35	1.26	0	18
	77	Fe^{4+}	0.04	0.26	0	47
		Fe^{4+}/Fe^{3+}	0.27	-0.68	3.4	38
		Fe^{3+}	0.47	-1.33	43.6	15
$SrFeO_{3-\delta}/F$	298	Fe^{3+}	0.37	-0.01	52.3	45
		Fe^{3+}	0.37	-0.05	50.1	45
		Fe^{3+}	0.37	-0.01	4.5	10
	77	Fe^{3+}	0.47	0.01	56.1	43
		Fe^{3+}	0.46	-0.09	54.1	49
		Fe^{3+}	0.44	0.00	1.8	8
$La_{0.1}Sr_{0.9}FeO_{3-\delta}$	298	Fe^{4+}	-0.02	0.26	0	53
		Fe^{4+}/Fe^{3+}	0.28	0.54	0	47
	77	Fe^{4+}	0.05	0.26	2.0	48
		Fe^{4+}/Fe^{3+}	0.34	0.35	31.0	47
		Fe^{3+}	0.40	0.40	38.2	5
$La_{0.1}Sr_{0.9}FeO_{3-\delta}/F$	298	Fe^{4+}/Fe^{3+}	0.23	0.60	44.0	32
		Fe^{3+}	0.39	-0.39	52.1	43
		Fe^{3+}	0.35	-0.40	49.4	25
	77	Fe^{4+}/Fe^{3+}	0.31	0.68	46.9	24
		Fe^{3+}	0.49	-0.36	55.5	46
		Fe^{3+}	0.44	-0.43	53.1	30
$La_{0.1}Sr_{0.9}Fe_{0.5}Co_{0.5}O_{3-\delta}$	298	Fe^{4+}/Fe^{3+}	0.11	0.16	0	52
		Fe^{4+}/Fe^{3+}	0.14	0.67	0	48
	77	Fe^{4+}/Fe^{3+}	0.20	0.00		36
		Fe^{4+}/Fe^{3+}	0.20	0.15	16.3	60
		Fe^{4+}/Fe^{3+}	0.20	0.24	28.0	4
$La_{0.1}Sr_{0.9}Fe_{0.5}Co_{0.5}O_{3-\delta}/F$	298	Fe^{4+}/Fe^{3+}	0.21	0.40	2.5	10
		Fe^{3+}	0.35	-0.03	51.4	59
		Fe^{3+}	0.36	-0.03	48	31
	77	Fe^{4+}/Fe^{3+}	0.31	-0.50	12.8	7
		Fe^{3+}	0.47	-0.06	54.9	67
		Fe^{3+}	0.45	-0.01	52.4	26

The ^{57}Fe Mössbauer spectra recorded from $SrFeO_{3-\delta}$, $La_{0.1}Sr_{0.9}FeO_{3-\delta}$, $La_{0.1}Sr_{0.9}Fe_{0.5}Co_{0.5}O_{3-\delta}$ and their fluorinated derivatives are illustrated in Figures 5.3, 5.4 and 5.5 respectively. The ^{57}Fe Mössbauer parameters are collected in Table 5.3.

$SrFeO_{3-\delta}$

The spectrum recorded at 298K was best fitted to a doublet (δ = *ca.* 0.04 mms^{-1}, Δ = *ca.* 0.12 mms^{-1}) similar to that previously reported[1] for Fe^{4+} in $SrFeO_3$ together with a doublet (δ = *ca.* 0.14 mms^{-1}, Δ = *ca.* 0.69 mms^{-1}).The component with chemical isomer shift δ 0.14 mms^{-1} is intermediate between that characteristic of an Fe^{3+} species (δ = *ca.* 0.35 mms^{-1}) and an Fe^{4+} species (δ = *ca.* 0.04 mms^{-1}) and would require a description as representing an ion of mean charge. Such a description may imply charge sharing between neighbouring Fe^{3+} and Fe^{4+} ions with a time scale smaller than 10^{-8} seconds at 298 K. The results are very similar to those previously[2] recorded from the oxygen deficient variant of Fe^{4+}-containing $SrFeO_{3-\delta}$. The spectrum also contained a quadrupole split absorption (δ = *ca.* 0.35 mms^{-1}, Δ = *ca.* 1.26 mms^{-1}) characteristic of an Fe^{3+}-containing impurity phase. The spectrum recorded at 77K showed a doublet (δ = *ca.* 0.04 mms^{-1}, Δ = *ca.* 0.26 mms^{-1}) characteristic of Fe^{4+} with two sextet patterns, one (δ = *ca.* 0.27 mms^{-1}, 2ε = *ca.* -0.68 mms^{-1}, H = 3.4 T) characteristic of the mixture of Fe^{4+} and Fe^{3+} and the other, (δ = *ca.* 0.47 mms^{-1}, 2ε = *ca.* -1.33 mms^{-1}, H = 43.6 T), characteristic of the Fe^{3+}-containing impurity phase, which was not visible in the XRD pattern, and so is presumed to be due to an amorphous impurity. The calculation of the oxygen deficiency of $SrFeO_{3-\delta}$ can be estimated from the Mössbauer spectral components at 298 K (Table 5.3) if the contribution of the Fe^{3+}-containing impurity phase is deducted. The strontium ion was assigned as Sr^{2+} on the basis of the XANES data(see earlier). Half of the mixed Fe^{4+}/Fe^{+3} species was associated with Fe^{4+} which . together with the contribution characteristic of Fe^{4+}, implies that *ca.* 77% of the iron is present as Fe^{4+}. The remaining iron was associated with Fe^{3+}. So that in terms of charge balance:

$$\underset{\{Sr^{2+}\}}{2} + [(\underset{\{Fe^{3+}\}}{0.23 \times 3}) + (\underset{\{Fe^{4+}\}}{0.77 \times 4})] = \underset{\{O^{2-}\}}{(3 - \delta) \times 2}$$

such that $\delta = 0.12$. Hence, the composition of $SrFeO_{3-\delta}$ might approximate more closely to $SrFeO_{2.88}$.

The evidence from Mössbauer spectroscopy for only Fe^{3+} in the fluorinated derivative of $SrFeO_{3-\delta}$ and which may be assumed to adopt the formulation $SrFeO_{3-x}F_x$ enabled a very approximate estimate of the fluorine content. Hence:

$$\underset{\{Sr^{2+}\}}{2} + (\underset{\{Fe^{3+}\}}{1.00 \times 3}) = \underset{\{O^{2-}\}}{(3 - x) \times 2} + \underset{\{F^{-}\}}{x}$$

such that x = 1 and the material is formulated as $SrFeO_2F$. Accurate analysis of the fluorine content in this compound, and of other fluorinated compounds reported in this thesis, will be the subject of a subsequent project.

The ^{57}Fe Mössbauer spectrum recorded at 298 K from the fluorinated derivative was best fitted to the superposition of two sextet patterns together with a profile which can be fitted to a hyperfine field of *ca.* 4.5 T; all components had chemical isomer shifts characteristic of Fe^{3+}. The spectrum recorded at 77K was similar with the component of smallest hyperfine field appearing as a broadened singlet. The results are consistent with fluorination inducing the reduction of Fe^{4+} in the $SrFeO_3$-related phase to Fe^{3+}. The results endorse the evidence from XANES for fluorination inducing the reduction of Fe^{4+} to Fe^{3+}. The predominance of complex magnetically split hyperfine patterns recorded from the fluorinated materials reflects the interaction between Fe^{3+} ions which

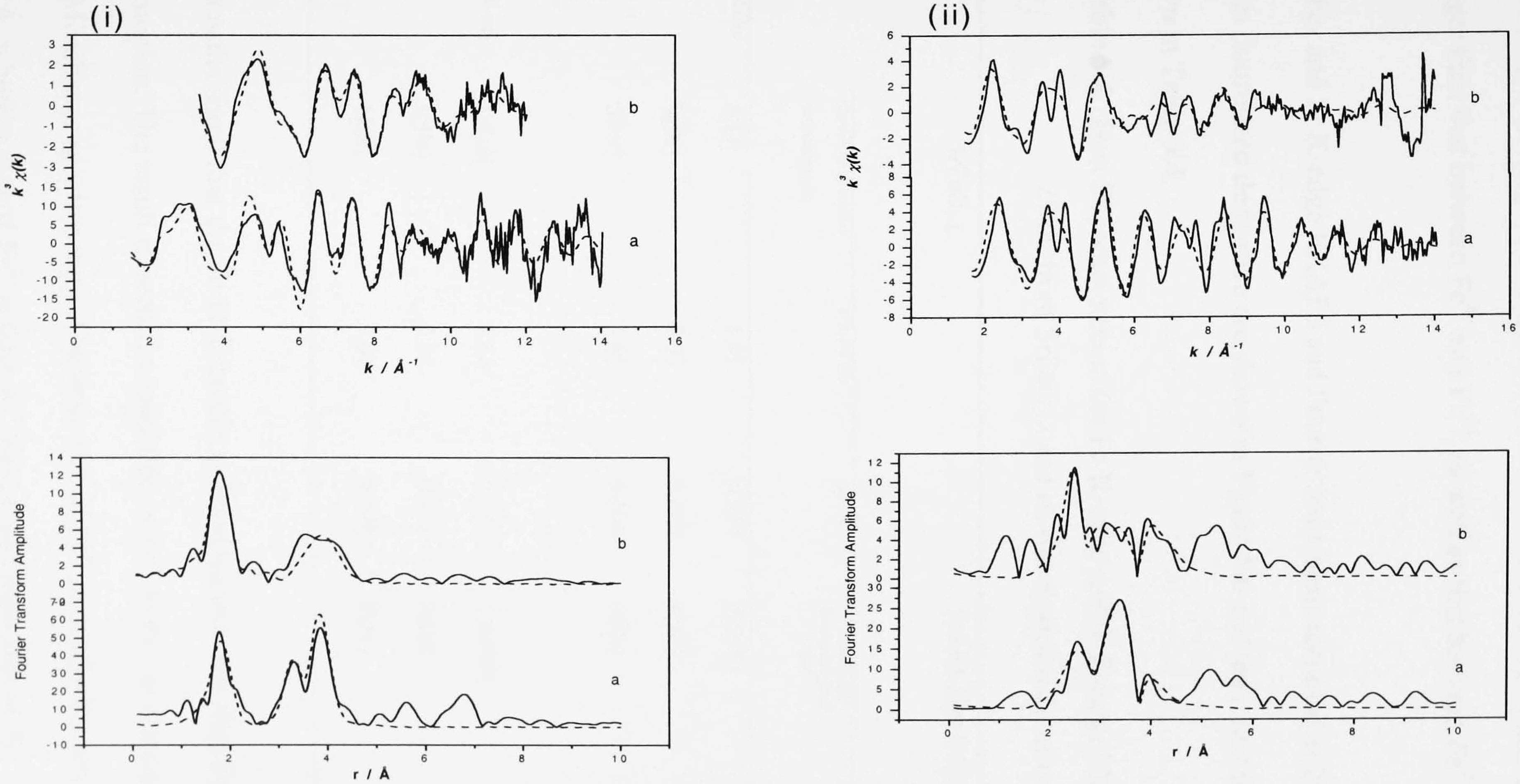

Figure 5.6 (i)Fe- and (ii) Sr K-edge EXAFS and Fourier transforms recorded at 298K from (a) $SrFeO_{3-\delta}$ and (b) its fluorinated derivative. (The experimental data are shown by a solid line.)

are not possible in oxides containing Fe^{4+}. According to the superexchange theory of Goodenough,[3] the superexchange interaction between $3d^5(Fe^{3+})$ and $3d^5(Fe^{3+})$ ions is stronger than that between Fe^{4+} and Fe^{3+}, as well as that between Fe^{4+} and Fe^{4+} ions.

The Fe- and Sr K-edge EXAFS and Fourier transforms recorded at 298K from $SrFeO_{3-\delta}$ and its fluorinated derivative are shown in Figure 5.6 and their best fit parameters are shown in Table 5.4.

Table 5.4 Best fit parameters to the Fe K-edge and Sr K-edge EXAFS recorded at 298K from $SrFeO_{3-\delta}$ and its fluorinated derivative

	$SrFeO_{3-\delta}$			$SrFeO_{3-\delta}$ after fluorination		
	Coordination number and [atom type]	d/ Å (±0.02)	$2\sigma^2$/ Å^2	Coordination number and [atom type]	d/ Å (±0.02)	$2\sigma^2$/ Å^2
Fe K-edge	6[O]	1.91	0.037	6[O/F]	1.92	0.041
	8[Sr]	3.31	0.025	8[Sr]	3.34	0.062
	6[Fe]	3.82	0.020	6[Fe]	3.76	0.038
Sr K-edge	12[O]	2.64	0.051	12[O/F]	2.59	0.020
	8[Fe]	3.34	0.021	8[Fe]	3.39	0.050
	6[Sr]	3.84	0.026	6[Sr]	3.92	0.032

The results show that the Fe-O distances in $SrFeO_{3-\delta}$ increase slightly in length upon fluorination. The result reflects the reduction of Fe^{4+} to Fe^{3+} as shown by both XANES and Mössbauer spectroscopy. The ionic size of Fe^{4+} in octahedral oxygen coordination is 0.58 Å whereas that of Fe^{3+} is 0.64 Å.[4] Hence the larger size of Fe^{3+} would be expected to lead to an enlargement of the Fe-O distance. The Fe-Sr distance also shows an increase. The Sr-O distances appear to show a shortening on fluorination although the subsequent Sr-Fe and Sr-Sr distances appear to increase.

$La_{0.1}Sr_{0.9}FeO_{3-\delta}$

The ^{57}Fe Mössbauer spectrum recorded at 298K was composed of a doublet (δ = -0.02 mms^{-1}, Δ = 0.26 mms^{-1}) characteristic of Fe^{4+} and another doublet (δ = 0.28 mms^{-1}, Δ = 0.54 mms^{-1}) characteristic of the presence of a mixed Fe^{4+}/Fe^{3+} species. The oxygen deficiency of $La_{0.1}Sr_{0.9}FeO_{3-\delta}$ was estimated from the Mössbauer spectral components at 298K (Table 5.3), assuming the Fe^{4+}/Fe^{+3} component to be a mixture of half Fe^{4+} and half Fe^{3+}. Hence:

$$\underset{\{La^{3+}\}}{0.1 \times 3} + \underset{\{Sr^{2+}\}}{0.9 \times 2} + [\underset{\{Fe^{3+}\}}{(0.235 \times 3)} + \underset{\{Fe^{4+}\}}{(0.765 \times 4)}] = \underset{\{O^{2-}\}}{(3-\delta)} \times 2$$

such that $\delta = 0.07$. Hence, the composition of $La_{0.1}Sr_{0.9}FeO_{3-\delta}$ might approximate more closely to $La_{0.1}Sr_{0.9}FeO_{2.93}$. The spectrum recorded at 77K showed three magnetically split components illustrating magnetic order from the Fe^{3+}-containing components at low temperature. Fluorination gave a material from which the ^{57}Fe Mössbauer spectrum at 298K showed three magnetically split components, one (δ = 0.23 mms^{-1}, 2ε = 0.60 mms^{-1}, H = 44 T) characteristic of a mixture of Fe^{3+} and Fe^{4+}, whilst the other two sextet patterns corresponding to ca. 68% of the spectral area, were characteristic of Fe^{3+}. The presence of *ca.* 32% mixed Fe^{4+}/Fe^{3+} indicates that fluorination has not resulted in complete reduction to Fe^{3+} in this case. This may be related to thermally induced loss of poly(vinylidene difluoride) before the full fluorination can occur. The possibility of increasing the fluorine content in this compound will be the subject of a further project. The results demonstrate the reduction of most of the Fe^{4+} to Fe^{3+} as a result of fluorination and the concomitant inducement of magnetic order. The spectrum recorded at 77K was amenable to similar analysis. From an analysis of the spectral areas of the two components in the Mössbauer spectrum at 298K a composition of $La_{0.1}Sr_{0.9}FeO_{2.26}F_{0.74}$ (assuming a formula of $La_{0.1}Sr_{0.9}FeO_{3-x}F_x$) can be deduced as follows.

$$\underset{\{La^{3+}\}}{0.1 \times 3} + \underset{\{Sr^{2+}\}}{0.9 \times 2} + [\underset{\{Fe^{3+}\}}{(0.84 \times 3)} + \underset{\{Fe^{4+}\}}{(0.16 \times 4)}] = \underset{\{O^{2-}\}}{(3-x) \times 2} + \underset{\{F^{-}\}}{x}$$

such that x = 0.74.

The Fe K-, Sr K- and La L_{III}-edge EXAFS and Fourier transforms recorded at 298K from $La_{0.1}Sr_{0.9}FeO_{3-\delta}$ and its fluorinated derivative are shown in Figure 5.7 and their best fit parameters are shown in Table 5.5. The results show the Fe-O distances in $La_{0.1}Sr_{0.9}FeO_{3-\delta}$ to increase slightly upon fluorination as a result of reduction of Fe^{4+} to Fe^{3+}. The Fe-La/Sr distance also increases. The Sr-O and La-O distances appear to decrease (as also observed when $SrFeO_{3-\delta}$ was fluorinated) although the Sr-Fe distance become longer (as also observed when $SrFeO_{3-\delta}$ was fluorinated) and the La-Fe distance decreases.

Table 5.5 Best fit parameters to the Fe K-, Sr K- and La L_{III}-edge EXAFS recorded from $La_{0.1}Sr_{0.9}FeO_{3-\delta}$ and its fluorinated derivative.

	$La_{0.1}Sr_{0.9}FeO_{3-\delta}$			$La_{0.1}Sr_{0.9}FeO_{3-\delta}$ after fluorination		
	Coordination number and [atom type]	d/ Å (±0.02)	$2\sigma^2$/ Å^2	Coordination number and [atom type]	d/ Å (±0.02)	$2\sigma^2$/ Å^2
Fe K-edge	6[O]	1.90	0.046	6[O/F]	1.92	0.022
	8[La/Sr]	3.34	0.033	8[La/Sr]	3.46	0.067
	6[Fe]	3.95	0.015	6[Fe]	3.95	0.041
Sr K-edge	12[O]	2.66	0.053	12[O/F]	2.60	0.024
	8[Fe]	3.34	0.021	8[Fe]	3.40	0.054
	6[Sr/La]	3.84	0.030	6[Sr/La]	3.94	0.038
La L_{III}-edge	12[O]	2.871	0.020	12[O/F]	2.703	0.016
	8[Fe]	3.570	0.006	8[Fe]	3.391	0.018
	6[Sr/La]	3.965	0.010	6[Sr/La]	3.793	0.007

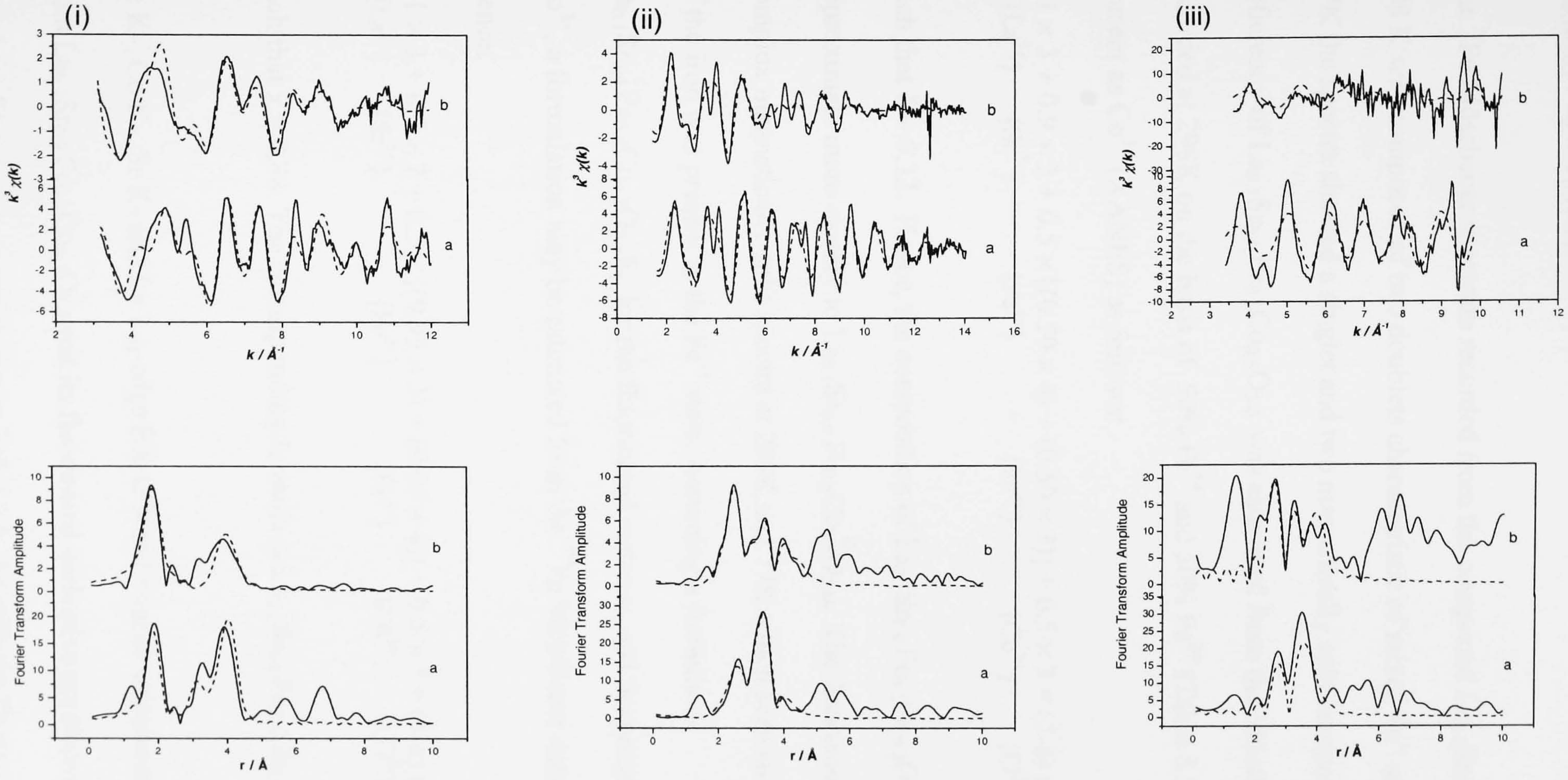

Figure 5.7 (i)Fe K-, (ii) Sr K- and (iii) La L_{III}-edge EXAFS and Fourier transforms recorded at 298K from (a) $La_{0.1}Sr_{0.9}FeO_{3-\delta}$ and (b) its fluorinated derivative. (The experimental data are shown by a solid line.)

$La_{0.1}Sr_{0.9}Fe_{0.5}Co_{0.5}O_{3-\delta}$

The ^{57}Fe Mössbauer spectrum recorded from the compound $La_{0.1}Sr_{0.9}Fe_{0.5}Co_{0.5}O_{3-\delta}$ at 298 K was composed of two doublets characteristic of mixed Fe^{4+} and Fe^{3+} species. At 77K the spectra showed a singlet and two magnetically split components. The oxygen deficiency of $La_{0.1}Sr_{0.9}Fe_{0.5}Co_{0.5}O_{3-\delta}$ was estimated from the Mössbauer spectrum recorded at 298K on the basis of 50% Fe^{4+} and 50% Fe^{3+} (Table 5.3) and cobalt being present as Co^{3+} (XANES) as follows:

$$\underset{\{La^{3+}\}}{0.1 \times 3} + \underset{\{Sr^{2+}\}}{0.9 \times 2} + 0.5 \times [\underset{\{Fe^{4+}\}}{(0.50 \times 4)} + \underset{\{Fe^{3+}\}}{(0.50 \times 3)}] + \underset{\{Co^{3+}\}}{0.5 \times 3} = \underset{\{O^{2-}\}}{(3-\delta) \times 2}$$

such that $\delta = 0.32$. Hence, the composition of $La_{0.1}Sr_{0.9}Fe_{0.5}Co_{0.5}O_{3-\delta}$ might approximate more closely to $La_{0.1}Sr_{0.9}Fe_{0.5}Co_{0.5}O_{2.68}$. The fluorinated materials gave complex magnetically split spectra at 298K and 77K which both showed that *ca.* 95 % of the iron was present in the Fe^{3+} state. Assuming a formula of $La_{0.1}Sr_{0.9}Fe_{0.5}Co_{0.5}O_{3-x}F_x$ for the fluorinated material, and the presence of cobalt as Co^{3+}, a formulation may be estimated from the ^{57}Fe Mössbauer data recorded at 298K. Hence:

$$\underset{\{La^{3+}\}}{0.1 \times 3} + \underset{\{Sr^{2+}\}}{0.9 \times 2} + 0.5 \times [\underset{\{Fe^{3+}\}}{(0.95 \times 3)} + \underset{\{Fe^{4+}\}}{(0.05 \times 4)}] + \underset{\{Co^{3+}\}}{0.5 \times 3} = \underset{\{O^{2-}\}}{(3-x) \times 2} + \underset{\{F^{-}\}}{x}$$

such that x = 0.88. The corresponding formula is $La_{0.1}Sr_{0.9}Fe_{0.5}Co_{0.5}O_{2.12}F_{0.88}$.

Fe K-, Co K-, Sr K- and La L_{III}-edge EXAFS and Fourier transforms recorded at 298K from $La_{0.1}Sr_{0.9}Fe_{0.5}Co_{0.5}O_{3-\delta}$ and its fluorinated derivative are shown in Figure 5.8 and their best fit parameters are shown in Table 5.6. As with the fluorination of

$La_{0.1}Sr_{0.9}FeO_{3-\delta}$ and $SrFeO_{3-\delta}$ the first oxygen shell coordination around iron increases in distance upon fluorination reflecting the reduction of Fe^{4+} to Fe^{3+}. There is also an increase in the Fe-La/Sr distances and Fe-Fe/Co distances following fluorination. The Co K-edge data also showed small increases in Co-O, Co-La/Sr and Co-Fe/Co distances upon fluorination which also are consistent with the increase in unit cell size which accompanied fluorination. The Sr-O and La-O distances decreased in the fluorinated materials whereas the Sr-Fe/Co and Sr-Sr/La distances increase and the La-Fe/Co and La-Sr/La distances decreased.

Table 5.6 Best fit parameters to the Fe K-, Co K-, Sr K- and La L_{III}-edge EXAFS from $La_{0.1}Sr_{0.9}Fe_{0.5}Co_{0.5}O_{3-\delta}$ and its fluorinated derivative

	$La_{0.1}Sr_{0.9}Fe_{0.5}Co_{0.5}O_{3-\delta}$			$La_{0.1}Sr_{0.9}Fe_{0.5}Co_{0.5}O_{3-\delta}$ after fluorination		
	Coordination number and [atom type]	d/ Å (±0.02)	$2\sigma^2$/ Å^2	Coordination number and [atom type]	d/ Å (±0.02)	$2\sigma^2$/ Å^2
Fe K-edge	6[O]	1.91	0.015	6[O/F]	1.96	0.026
	8[La/Sr]	3.36	0.064	8[La/Sr]	3.49	0.072
	6[Fe/Co]	3.85	0.022	6[Fe/Co]	4.01	0.061
Co K-edge	6[O]	1.88	0.036	6[O/F]	1.89	0.006
	8[La/Sr]	3.34	0.034	8[La/Sr]	3.38	0.044
	6[Fe/Co]	3.93	0.007	6[Fe/Co]	3.94	0.018
Sr K-edge	12[O]	2.65	0.049	12[O/F]	2.60	0.021
	8[Fe/Co]	3.33	0.024	8[Fe/Co]	3.38	0.049
	6[Sr/La]	3.85	0.039	6[Sr/La]	3.91	0.034
La L_{III}-edge	12[O]	2.76	0.050	12[O/F]	2.64	0.007
	8[Fe/Co]	3.50	0.015	8[Fe/Co]	3.32	0.010
	6[Sr/La]	3.90	0.034	6[Sr/La]	3.77	0.005

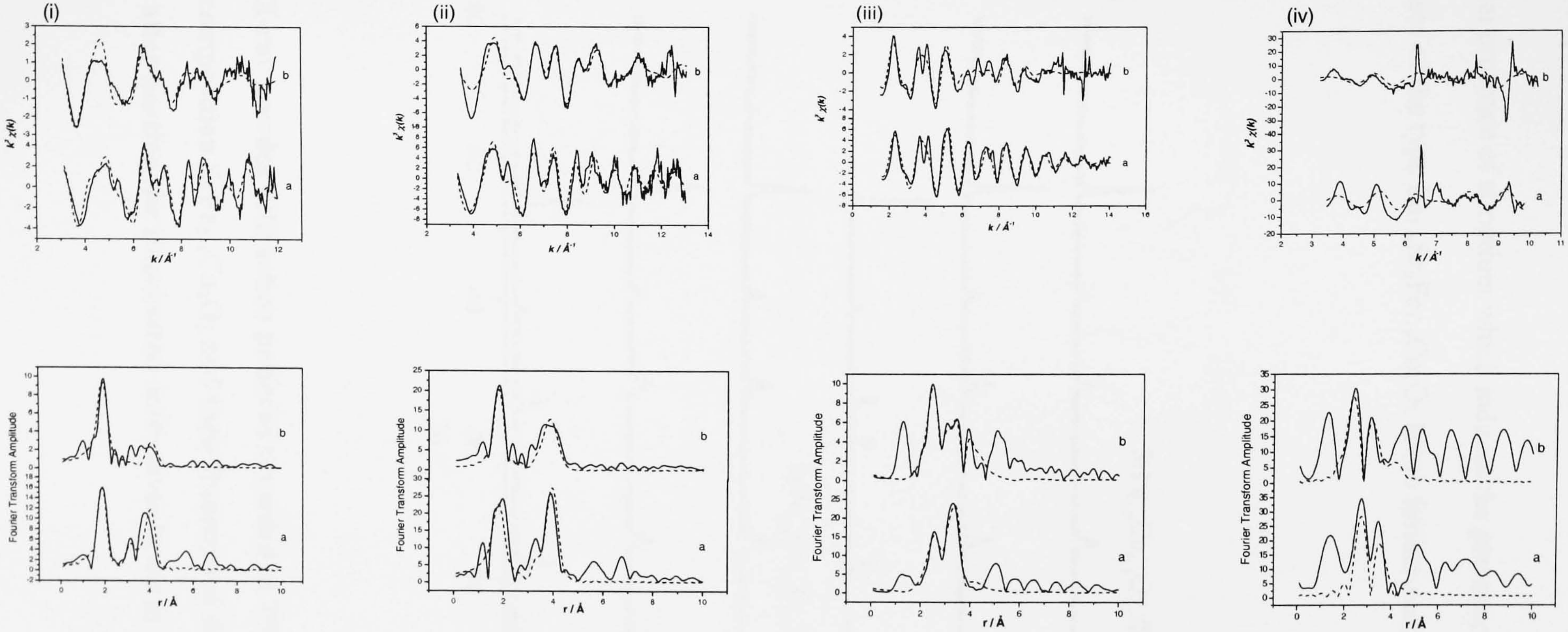

Figure 5.8 (i)Fe K-, (ii) Co K-, (iii) Sr K-edge and (iv) La L_{III}-edge EXAFS and Fourier transforms recorded at 298K from (a) $La_{0.1}Sr_{0.9}Fe_{0.5}Co_{0.5}O_{3-\delta}$ and (b) its fluorinated derivative. (The experimental data are shown by a solid line.)

5.3 $SrFe_{1-x}Co_xO_3$

The essential presence of strontium which induces the presence of Fe^{4+} in perovskite-related phases of the type $La_{1-x}Sr_xFe_{1-y}Co_yO_3$ led to further consideration of the

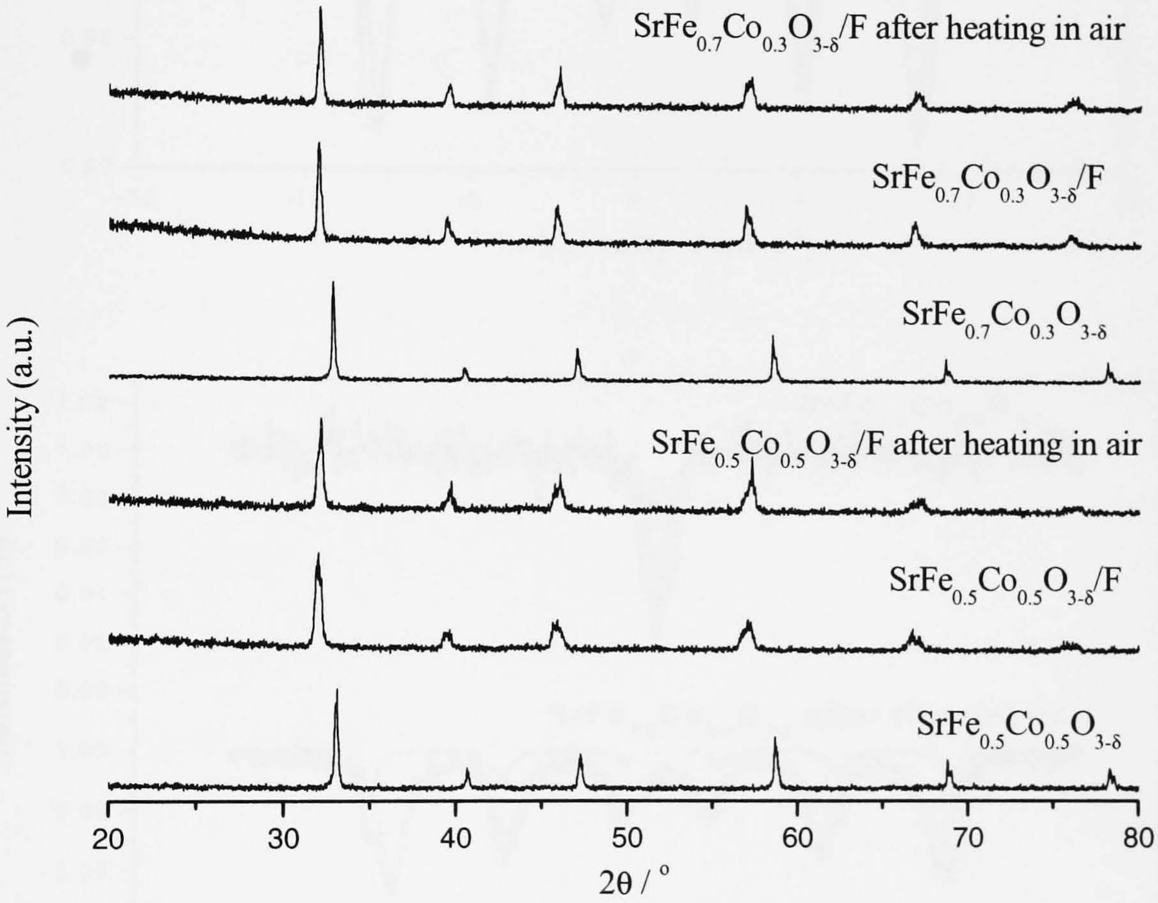

Figure 5.9 X-ray powder diffraction patterns recorded at 298K from materials of composition $SrFe_{1-x}Co_xO_3$ and their fluorinated derivatives, and after heating the fluorinated derivatives in air at 400 °C for 2 hours.

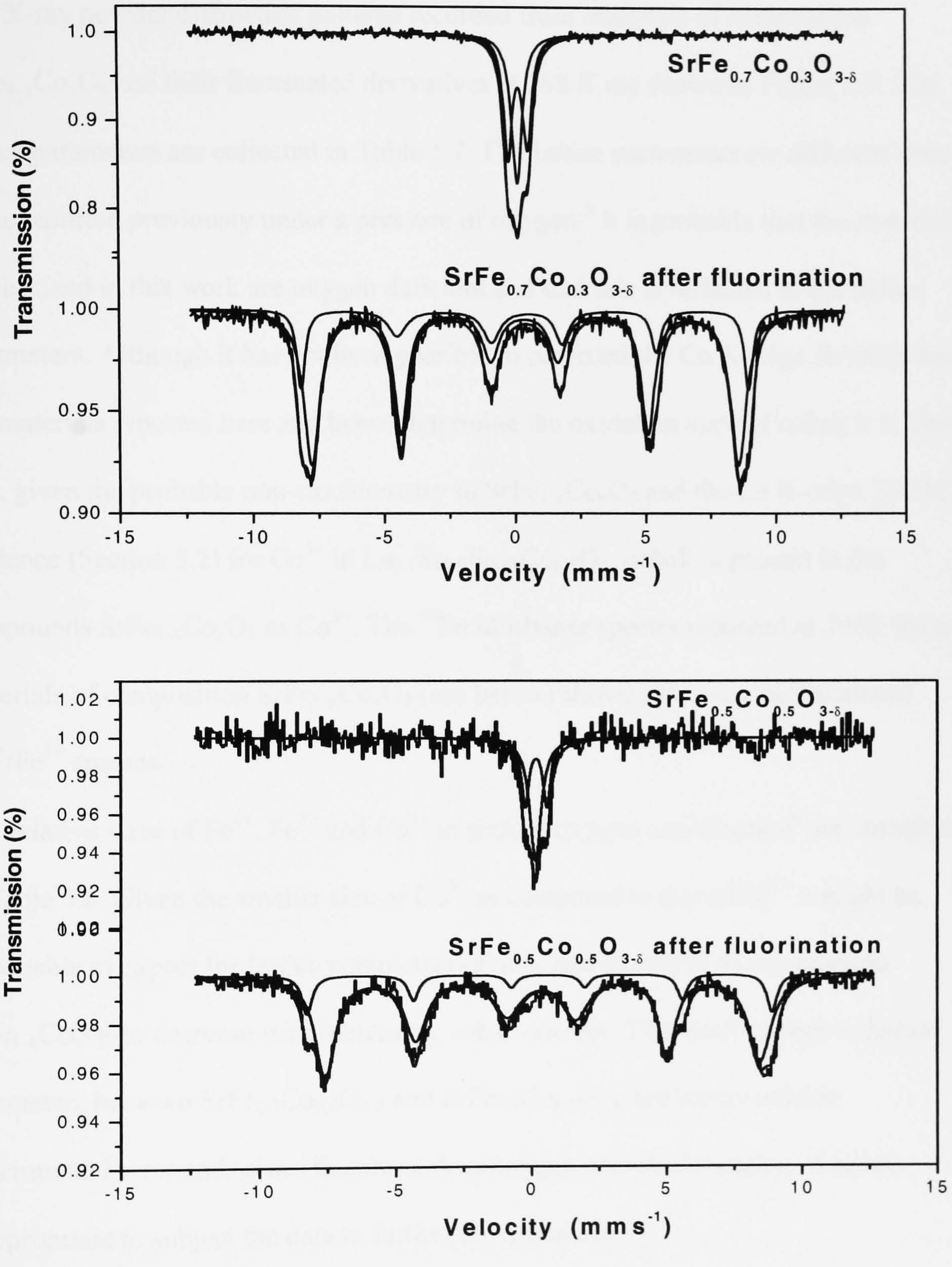

Figure 5.10 ^{57}Fe Mössbauer spectra recorded from materials of composition $SrFe_{1-x}Co_xO_3$ and their fluorinated derivatives at 298 K.

possibility of fluorination of other non-lanthanum-containing structurally related phases. The X-ray powder diffraction patterns recorded from materials of composition $SrFe_{1-x}Co_xO_3$ and their fluorinated derivatives at 298 K are shown in Figure 5.9. The lattice parameters are collected in Table 5.7. The lattice parameters are different from those reported previously under a pressure of oxygen.[5] It is probable that the materials synthesized in this work are oxygen deficient and that this is reflected in the lattice parameters. Although it has not been possible to recorded the Co K-edge XANES from the materials reported here and hence determine the oxidation state of cobalt it is likely that, given the probable non-stochiometry in $SrFe_{1-x}Co_xO_3$ and the Co K-edge XANES evidence (Section 5.2) for Co^{3+} in $La_{0.1}Sr_{0.9}Fe_{0.5}Co_{0.5}O_3$, cobalt is present in the compounds $SrFe_{1-x}Co_xO_3$ as Co^{3+}. The ^{57}Fe Mösbauer spectra recorded at 298K from materials of composition $SrFe_{1-x}Co_xO_3$ (see below) showed the presence of mixed Fe^{4+}/Fe^{3+} species.

The relative sizes of Fe^{4+}, Fe^{3+} and Co^{3+} in sixfold oxygen coordination[4] are contained in Table 5.8. Given the smaller size of Co^{3+} as compared to that of Fe^{3+} it might be reasonable to expect the lattice parameters of pure mixed oxides of composition $SrFe_{1-x}Co_xO_3$ to decrease with increasing cobalt content. The small change in lattice parameters between $SrFe_{0.7}Co_{0.3}O_{3-\delta}$ and $SrFe_{0.5}Co_{0.5}O_{3-\delta}$ are barely outside experimental error and, given factors such as oxygen non-stochiometry, it seems inappropriate to subject the data to further interpretation.

Table 5.7 Lattice parameters recorded from materials of composition $SrFe_{1-x}Co_xO_3$ and their fluorinated derivatives

Samples	Lattice parameters (Å)	Primitive cell volumes (Å^3)
$SrFe_{0.7}Co_{0.3}O_{3-\delta}$	Cubic a = 3.870(1)	57.9
$SrFe_{0.7}Co_{0.3}O_{3-\delta}/F$	Orth. a = 5.592(1), b = 5.578(1), c = 7.891(1)	61.5
$SrFe_{0.7}Co_{0.3}O_{3-\delta}/F$ (following heating at 400°C in air)	Orth. a = 5.596(1), b= 5.622(1), c = 7.906 (1)	62.1
$SrFe_{0.5}Co_{0.5}O_{3-\delta}$	Cubic a = 3.873(1)	58.0
$SrFe_{0.5}Co_{0.5}O_{3-\delta}/F$	Orth. a = 5.577(1), b = 5.578(1), c= 7.891(1)	61.3
$SrFe_{0.5}Co_{0.5}O_{3-\delta}/F$ (following heating at 400°C in air)	Orth. a = 5.592(1), b = 5.618(1), c = 7.876 (1)	61.8

Table 5.8 Ionic radii for Fe^{4+}, Fe^{3+} and Co^{3+} in six fold oxygen coordination[4]

	Ionic radii (Å)
Fe^{4+},	0.58
Fe^{3+}	0.64
Co^{3+}	0.61

The lattice parameters for the compounds of the type of $SrFe_{1-x}Co_xO_3$ increased when the pure oxides were fluorinated as shown in Table 5.7. This result is consistent with fluorination causing a reduction in the oxidation state of the iron (see below) with a consequent increase in bond distances and unit cell parameters. Heating the samples in air at 400 °C for 2 hours resulted in no further changes to the X-ray diffraction powder patterns (Figure 5.9) and a small change in lattice parameters (Table 5.7) possibly due to the presence of some un-reacted poly(vinyldene difluoride), which reacts further on heating in air and so produces a phase with higher fluorine content. This is to be the subject of further investigation.

The ^{57}Fe Mössbauer spectra recorded at 298K from $SrFe_{0.7}Co_{0.3}O_{3-\delta}$, $SrFe_{0.5}Co_{0.5}O_{3-\delta}$ and their fluorinated derivatives are shown in Figure 5.10. The ^{57}Fe Mössbauer parameters are collected in Table 5.9. Both pure oxides could be fitted to a doublet with chemical isomer shift δ of *ca.* 0.16 mms^{-1} and a singlet with chemical isomer shift δ of *ca.* 0.13 mms^{-1}. The values of the chemical isomer shifts are intermediate between that characteristic of an Fe^{3+} species ($\delta =$ *ca.* 0.35 mms^{-1}) and an Fe^{4+} species ($\delta =$ *ca.* 0.04 mms^{-1}) and, as in the case of materials of the type $La_{1-x}Sr_x\,Fe_{1-y}Co_yO_3$ (Section 5.2), require a description in terms of an ion of mean charge. Such a description may imply charge sharing between neighbouring Fe^{3+} and Fe^{4+} ions. An attempt was made to calculate the oxygen deficiency of $SrFe_{0.7}Co_{0.3}O_{3-\delta}$ from the amount of Fe^{4+} and Fe^{3+} detected by the Mössbauer spectroscopy and assuming the presence of Co^{3+}:

$$\underset{\{Sr^{2+}\}}{2} + \underset{\{Fe^{4+}\}}{0.35\times 4} + \underset{\{Fe^{3+}\}}{0.35\times 3} + \underset{\{Co^{3+}\}}{0.30\times 3} = \underset{\{O^{2-}\}}{(3-\delta)\times 2}$$

such that $\delta = 0.32$. Hence, the composition of $SrFe_{0.7}Co_{0.3}O_{3-\delta}$ might approximate more closely to $SrFe_{0.7}Co_{0.3}O_{2.68}$.

The calculation of the oxygen deficiency of $SrFe_{0.5}Co_{0.5}O_{3-\delta}$ can be performed in a similar fashion from Mössbauer spectral components as follows:

$$\underset{\{Sr^{2+}\}}{2} + \underset{\{Fe^{4+}\}}{0.25\times 4} + \underset{\{Fe^{3+}\}}{0.25\times 3} + \underset{\{Co^{3+}\}}{0.50\times 3} = \underset{\{O^{2-}\}}{(3-\delta)\times 2}$$

such that δ = 0.37. Hence, the composition of $SrFe_{0.5}Co_{0.5}O_{3-\delta}$ might approximate more closely to $SrFe_{0.5}Co_{0.5}O_{2.63}$.

Fluorination resulted in both samples giving magnetically split Mössbauer spectra at 298K with chemical isomer shift *δ ca.* 0.35-0.47 mms^{-1} characteristic of Fe^{3+} in magnetically ordered materials. The results are similar to those recorded from materials of the type $La_{1-x}Sr_x Fe_{1-y}Co_yO_3$ (Section 5.2) and demonstrate that fluorination induces reduction of the Fe^{4+} species to Fe^{3+}. The complex magnetically split hyperfine patterns recorded from the fluorinated materials reflect the interaction between Fe^{3+} ions which are not possible in oxides containing Fe^{4+}. (Section 5.2)

Table 5.9 ^{57}Fe Mössbauer parameters recorded from materials of composition $SrFe_{1-x}Co_xO_3$ and their fluorinated derivatives

Compounds	Assignment	δ±0.05 /mms^{-1}	Δ or 2ε± 0.10 /mms^{-1}	H± 0.5 /T	Area± 5 %
$SrFe_{0.7}Co_{0.3}O_{3-\delta}$	Fe^{4+}/ Fe^{3+}	0.17	0.74	0	56
	Fe^{4+}/ Fe^{3+}	0.14	0	0	44
$SrFe_{0.7}Co_{0.3}O_{3-\delta}$/F	Fe^{3+}	0.35	0.06	49.8	70
	Fe^{3+}	0.47	-0.13	52.8	30
$SrFe_{0.5}Co_{0.5}O_{3-\delta}$	Fe^{4+}/ Fe^{3+}	0.15	0.80	0	42
	Fe^{4+}/ Fe^{3+}	0.13	0	0	58
$SrFe_{0.5}Co_{0.5}O_{3-\delta}$/F	Fe^{3+}	0.37	0.03	49.8	85
	Fe^{3+}	0.44	-0.15	53.2	15

Given the ^{57}Mössbauer spectral evidence for only Fe^{3+} in the fluorinated samples and assuming the presence of Co^{3+}, the fluorinated phases might be considered to approach a formulation of $SrFe_{1-x}Co_xO_2F$.

5.4 $SrFe_{1-x}Sn_xO_3$

X-ray powder diffraction patterns recorded at 298K from materials of composition $SrFe_{1-x}Sn_xO_3$ and their fluorinated derivatives at 298 K are shown in Figure 5.11 and the lattice parameters, together with those of $SrFeO_{3-\delta}$ for comparative purpose, are collected in Table 5.10. The X-ray powder diffraction data showed $SrFe_{0.7}Sn_{0.3}O_{3-\delta}$ and $SrFe_{0.5}Sn_{0.5}O_{3-\delta}$ to be orthorhombic and the results indicate a general increase in unit cell size with increasing tin content. Given that the ionic size of Sn^{4+} (0.69 Å) in six-fold oxygen coordination[4] is larger than that of octahedrally coordinated Fe^{3+}(0.64 Å) (Table 5.8) then the expansion of the unit cell can be associated with the incorporation of increasing amounts of the larger Sn^{4+} ion. The expansion of the unit cell in compounds

Table 5.10 Lattice parameters for materials of composition $SrFe_{1-x}Sn_xO_3$ and their fluorinated derivatives

Samples	Lattice parameters (Å)	Primitive Cell Volumes (Å^3)
$SrFeO_{3-\delta}$	Orth, $a = 5.474(1)$, $b = 5.469(1)$, $c = 7.706(1)$	57.6
$SrFe_{0.7}Sn_{0.3}O_{3-\delta}$	Orth, $a = 5.580(1)$, $b = 5.576(1)$, $c = 7.825(1)$	60.8
$SrFe_{0.7}Sn_{0.3}O_{3-\delta}/F$	Orth, $a = 5.644(1)$, $b = 5.643(1)$, $c = 7.973(1)$	63.4
$SrFe_{0.7}Sn_{0.3}O_{3-\delta}/F$ (following heating at 400°C in air)	Orth, $a = 5.648(2)$, $b = 5.646(7)$, $c = 7.935(4)$	63.2
$SrFe_{0.5}Sn_{0.5}O_{3-\delta}$	Orth, $a = 5.578(1)$, $b = 5.653(1)$, $c = 7.989(1)$	62.9
$SrFe_{0.5}Sn_{0.5}O_{3-\delta}/F$	Orth, $a = 5.674(1)$, $b = 5.653(1)$, $c = 8.026(1)$	64.3
$SrFe_{0.5}Sn_{0.5}O_{3-\delta}/F$ (following heating at 400°C in air)	Orth, $a = 5.681(4)$, $b = 5.640(2)$, $c = 8.027(9)$	64.3

of the type $SrFe_{1-x}Sn_xO_3$ upon fluorination, and which remained unchanged after heating at 400 °C in air, reflects the reduction of iron to Fe^{3+} upon fluorination (see later) and demonstrates that fluorination involves substitution on the oxygen sublattice as opposed to simple oxygen loss.

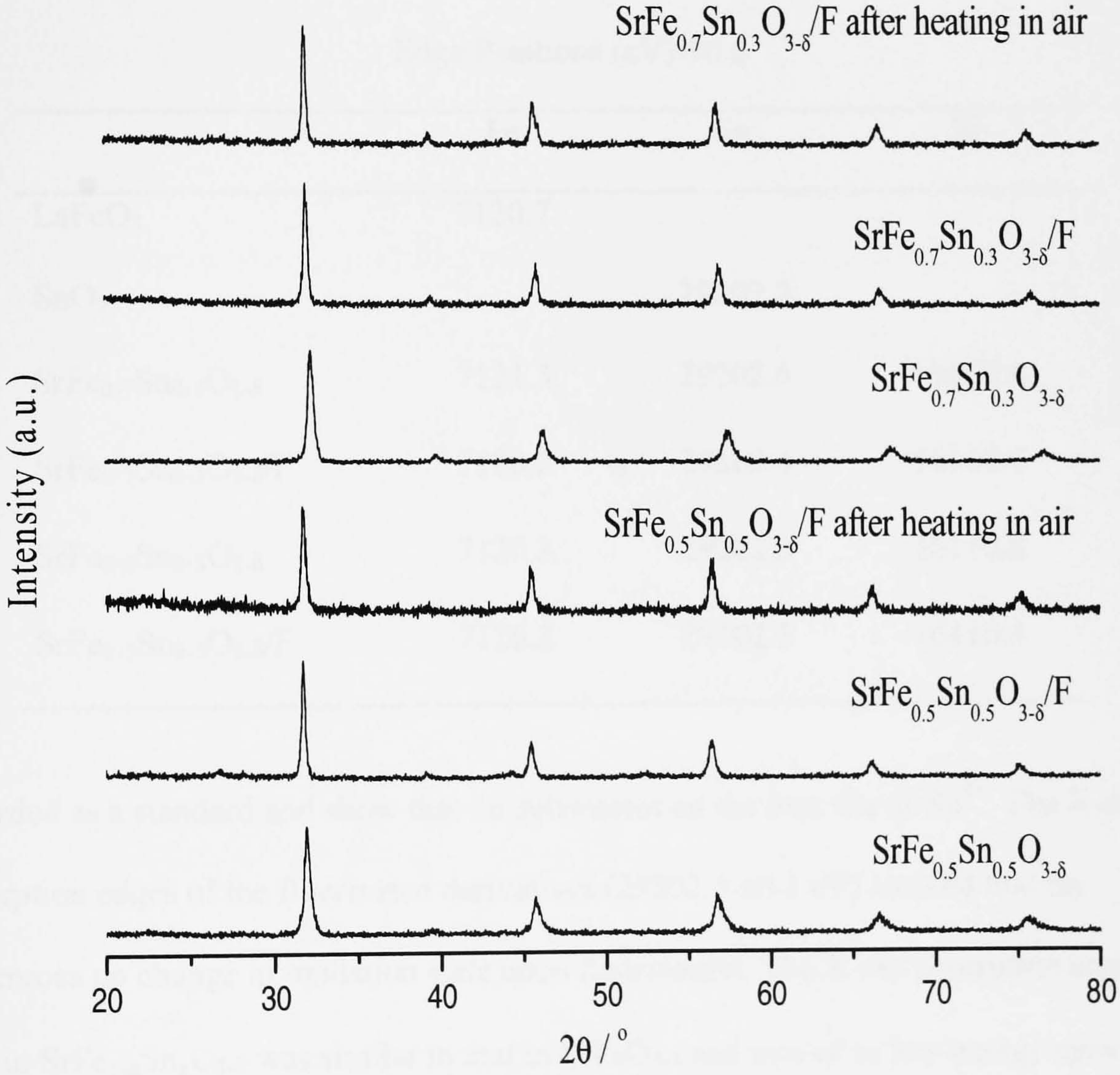

Figure 5.11 X-ray powder diffraction patterns recorded from materials of composition $SrFe_{1-x}Sn_xO_3$ and their fluorinated derivatives at 298 K, and after heating the fluorinated derivatives in air at 400 °C for 2 hours.

The X-ray absorption edge positions (Figure 5.12 and Table 5.11) of tin in compounds of the type $SrFe_{1-x}Sn_xO_3$ (29202.6±0.1eV) were deduced from the Sn K-edge X-ray absorption near edge structure (XANES) and were identical to those of tin dioxide recorded as a standard and show that tin substitutes on the iron site as Sn^{4+}. The X-ray absorption edges of the fluorinated derivatives (29202.5 ±0.1 eV) showed that tin undergoes no change in oxidation state upon fluorination. The X-ray absorption edge of iron in $SrFe_{1-x}Sn_xO_{3-\delta}$ was similar to that in $SrFeO_{3-\delta}$ and moved to low energy upon fluorination. The Sr K-edge absorption edge showed no change on fluorination.

Table 5.11 X-ray Absorption Edge Positions Recorded from the X-Ray Absorption Near Edge Structure from $SrFe_{1-x}Sn_xO_3$ and their fluorinated derivatives

Edge Positions (eV) ±0.5

	Fe	Sn	Sr
$LaFeO_3$	7120.7		
SnO_2		29202.2	
$SrFe_{0.7}Sn_{0.3}O_{3-\delta}$	7121.3	29202.6	16110.4
$SrFe_{0.7}Sn_{0.3}O_{3-\delta}/F$	7120.2	29202.4	16110.4
$SrFe_{0.5}Sn_{0.5}O_{3-\delta}$	7120.8	29202.6	16110.8
$SrFe_{0.5}Sn_{0.5}O_{3-\delta}/F$	7120.2	29202.5	16110.4

The ^{57}Fe Mössbauer spectra recorded from materials of composition $SrFe_{1-x}Sn_xO_3$ and their fluorinated derivatives at 298 K are shown in Figure 5.13. The ^{57}Fe Mössbauer parameters are showed in Table 5.12.

Table 5.12 ^{57}Fe Mössbauer parameters recorded at 298K from materials of composition $SrFe_{1-x}Sn_xO_3$ and their fluorinated derivatives

Compound	Assignment	$\delta\pm0.05$ /mms^{-1}	Δ or $2\varepsilon\pm0.10$ /mms^{-1}	$H\pm0.5$ /T	Area$\pm$ 5 %
$SrFe_{0.7}Sn_{0.3}O_{3-\delta}$	Fe^{5+}	-0.05	0.43		42
	Fe^{3+}	0.32	0.82		58
$SrFe_{0.7}Sn_{0.3}O_{3-\delta}/F$	Fe^{3+}	0.29	-0.22	42	37
	Fe^{3+}	0.38	0.90		63
$SrFe_{0.5}Sn_{0.5}O_{3-\delta}$	Fe^{5+}	-0.07	0.43		26
	Fe^{3+}	0.32	0.87		74
$SrFe_{0.5}Sn_{0.5}O_{3-\delta}/F$	Fe^{3+}	0.39	1.01		100

The ^{57}Fe Mössbauer spectra recorded from $SrFe_{0.7}Sn_{0.3}O_{3-\delta}$ and $SrFe_{0.5}Sn_{0.5}O_{3-\delta}$ were different from those recorded from materials of type $La_{1-x}Sr_xFe_{1-y}Co_yO_3$ or $SrFe_{1-x}Co_xO_3$ in that they were composed of two doublets one of which (δ = *ca.* -0.05 or -0.07 mms^{-1}, Δ = *ca.* 0.43 mms^{-1}) was similar to that previously[2] attributed to Fe^{5+} in the compound $La_{1-x}Sr_xFeO_3$ recorded at 4.2K. The other (δ = *ca.* 0.32 mms^{-1}, Δ = *ca.* 0.87 mms^{-1}) was characteristic of the remaining iron content being in the form of Fe^{3+}. The observation of Fe^{5+} in $SrFe_{0.7}Sn_{0.3}O_{3-\delta}$ is surprising since, assuming the presence of Sr^{2+}, it would be reasonable to expect that substitution of Sn^{4+} by Fe^{4+} would require no charge balance on the cationic sub lattice. The results imply that the presence of Sn^{4+} causes disproportion of Fe^{4+} into Fe^{5+} and Fe^{3+}. The reason for this behaviour at 298K awaits further investigation at low temperature and further structural characterisation. An attempt was made to estimate the oxygen deficiency of $SrFe_{0.7}Sn_{0.3}O_{3-\delta}$ from the Mössbauer spectral components associated with the Fe^{5+} and Fe^{3+} species and assuming the presence of Sn^{4+} as follows:

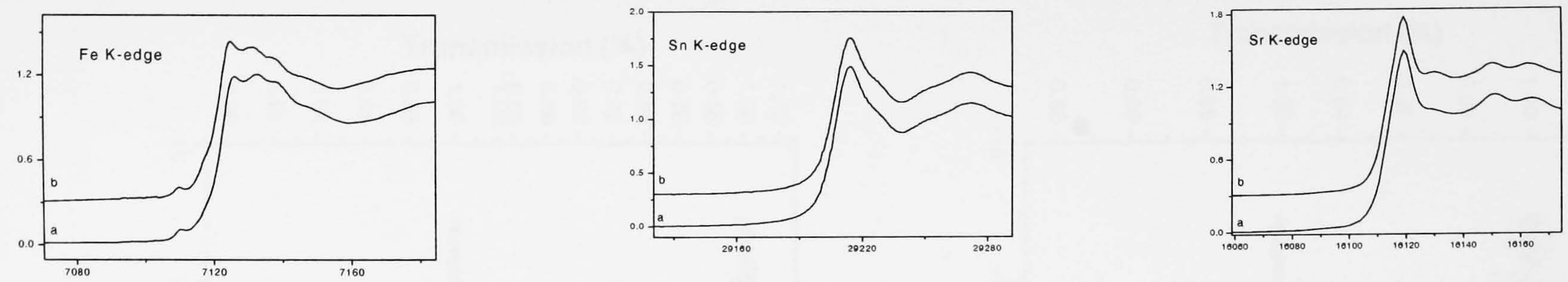

Figure 5.12a Fe K-, Sn K- and Sr K-edge X-ray absorption edge data recorded from (a) SrFe$_{0.7}$Sn$_{0.3}$O$_{3-\delta}$ and (b) its fluorinated derivative

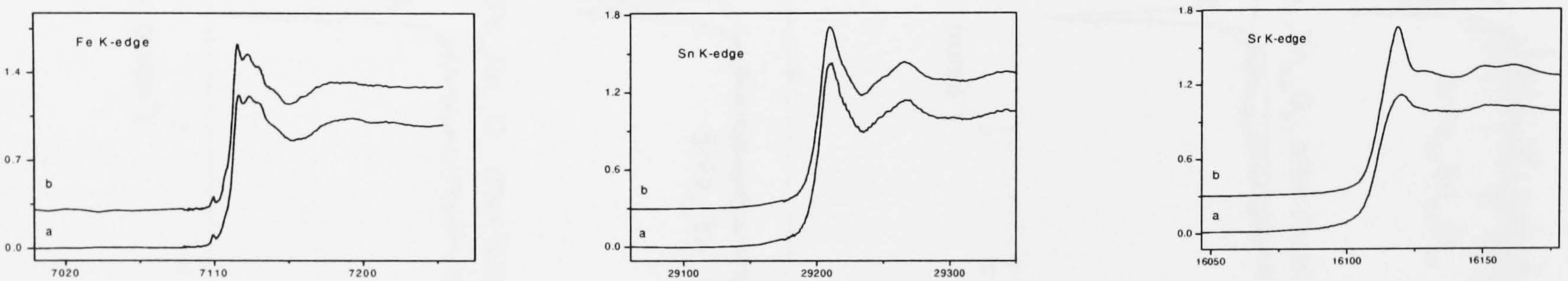

Figure 5.12b Fe K-, Sn K- and Sr K-edge X-ray absorption edge data recorded from (a) SrFe$_{0.5}$Sn$_{0.5}$O$_{3-\delta}$ and (b) its fluorinated derivative.

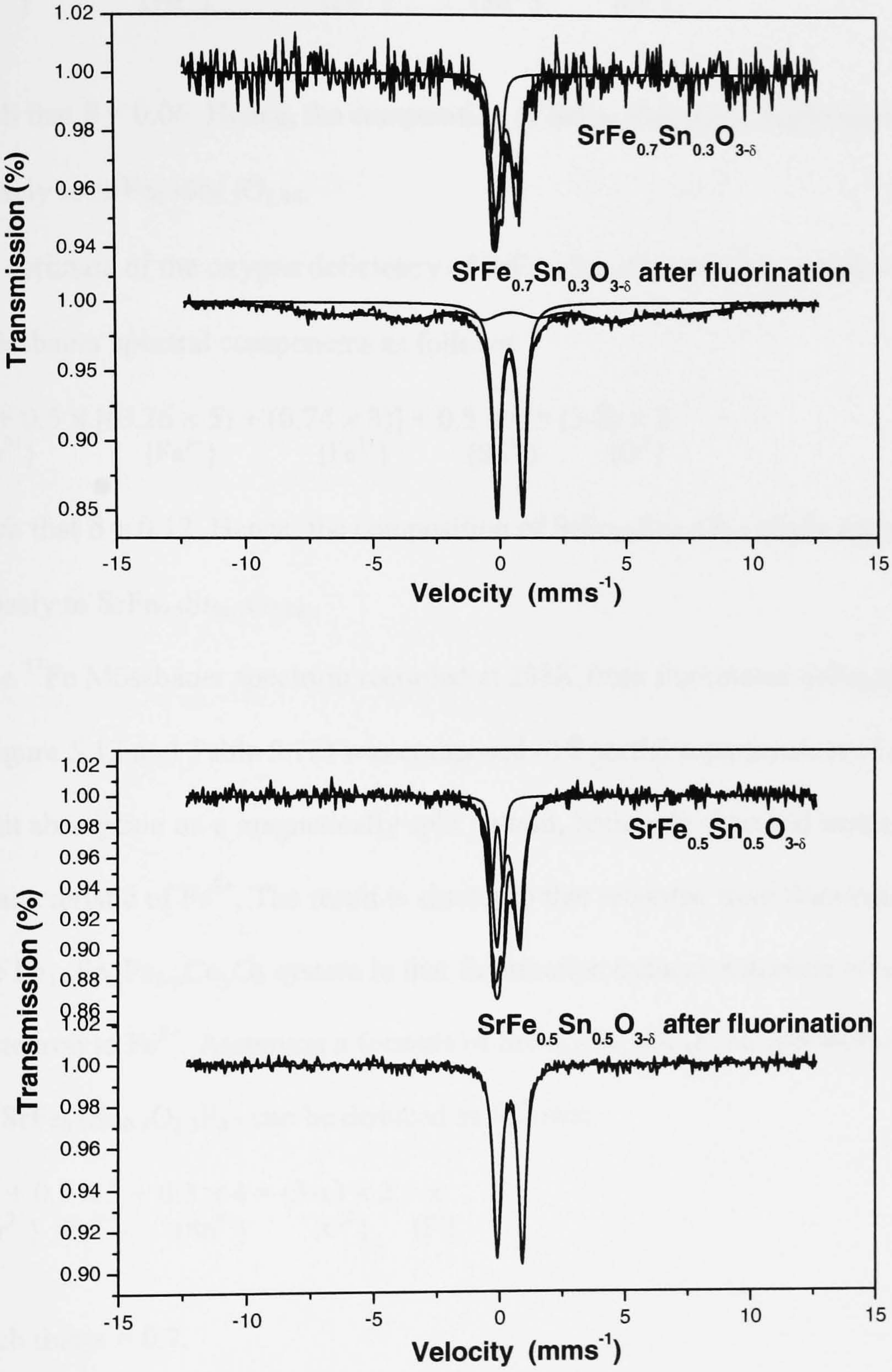

Figure 5.13 ^{57}Fe Mössbauer spectra recorded from materials of composition SrFe$_{1-x}$Sn$_x$O$_3$ and their fluorinated derivatives at 298 K.

$$\underset{\{\mathrm{Sr^{2+}}\}}{2} + 0.7 \times [(\underset{\{\mathrm{Fe^{5+}}\}}{0.42 \times 5}) + (\underset{\{\mathrm{Fe^{3+}}\}}{0.58 \times 3})] + \underset{\{\mathrm{Sn^{4+}}\}}{0.3 \times 4} = \underset{\{\mathrm{O^{2-}}\}}{(3-\delta) \times 2}$$

such that $\delta = 0.06$. Hence, the composition of $\mathrm{SrFe_{0.7}Sn_{0.3}O_{3-\delta}}$ might approximate more closely to $\mathrm{SrFe_{0.7}Sn_{0.3}O_{2.94}}$.

An estimate of the oxygen deficiency of $\mathrm{SrFe_{0.5}Sn_{0.5}O_{3-\delta}}$ can be carried out from the Mössbauer spectral components as follows:

$$\underset{\{\mathrm{Sr^{2+}}\}}{2} + 0.5 \times [(\underset{\{\mathrm{Fe^{5+}}\}}{0.26 \times 5}) + (\underset{\{\mathrm{Fe^{3+}}\}}{0.74 \times 3})] + \underset{\{\mathrm{Sn^{4+}}\}}{0.5 \times 4} = \underset{\{\mathrm{O^{2-}}\}}{(3-\delta) \times 2}$$

such that $\delta = 0.12$. Hence, the composition of $\mathrm{SrFe_{0.5}Sn_{0.5}O_{3-\delta}}$ might approximate more closely to $\mathrm{SrFe_{0.5}Sn_{0.5}O_{2.88}}$.

The ^{57}Fe Mössbauer spectrum recorded at 298K from fluorinated $\mathrm{SrFe_{0.7}Sn_{0.3}O_{2.94}}$ (Figure 5.13 and Table 5.12) was composed of a partial superposition of a quadrupole split absorption on a magnetically split pattern, both with chemical isomer shifts characteristic of $\mathrm{Fe^{3+}}$. The result is similar to that recorded from fluorinated phases in the $\mathrm{La_{1-x}Sr_x\,Fe_{1-y}Co_yO_3}$ system in that fluorination induces reduction of high oxidation state iron to $\mathrm{Fe^{3+}}$. Assuming a formula of $\mathrm{SrFe_{0.7}Sn_{0.3}O_{3-x}F_x}$ an approximate composition of $\mathrm{SrFe_{0.7}Sn_{0.3}O_{2.3}F_{0.7}}$ can be deduced as follows:

$$\underset{\{\mathrm{Sr^{2+}}\}}{2} + \underset{\{\mathrm{Fe^{3+}}\}}{0.7 \times 3} + \underset{\{\mathrm{Sn^{4+}}\}}{0.3 \times 4} = \underset{\{\mathrm{O^{2-}}\}}{(3-x) \times 2} + \underset{\{\mathrm{F^{-}}\}}{x}$$

such that $x = 0.7$.

Fluorinated $\mathrm{SrFe_{0.5}Sn_{0.5}O_{3-\delta}}$ (Figure 5.13, Table 5.12) gave a simple quadrupole split Mössbauer specrum at 298 K characteristic of a single paramagnetic $\mathrm{Fe^{3+}}$ species. An approximate composition of $\mathrm{SrFe_{0.5}Sn_{0.5}O_{2.5}F_{0.5}}$ was deduced as follows:

$$\underset{\{Sr^{2+}\}}{2} + \underset{\{Fe^{3+}\}}{0.5 \times 3} + \underset{\{Sn^{4+}\}}{0.5 \times 4} = \underset{\{O^{2-}\}}{(3-x) \times 2} + \underset{\{F^{-}\}}{x}$$

such that x = 0.5. Overall, the results are similar to those recorded from the other fluorinated perovskite-related oxides examined in this work in that the higher oxidation state of iron is reduced upon fluorination to Fe^{3+}. However, it is clear that the Mössbauer spectrum of $SrFe_{0.5}Sn_{0.5}O_{2.5}F_{0.5}$ shows no magnetic order at 298 K and this suggests that the extent of magnetic interaction between Fe^{3+} species decreases as the tin content increases. The reasons for this will be the subject of further investigation.

Fe-, Sn- and Sr K-edge EXAFS and Fourier transforms recorded at 298K from compositions of the type $SrFe_{1-x}Sn_xO_3$ and their fluorinated derivatives are shown in Figure 5.14 and their best fit parameters are shown in Table 5.13. The results show that the Fe-O distances in $SrFe_{0.7}Sn_{0.3}O_{3-\delta}$ increase slightly in length upon fluorination due to the reduction of the oxidation state of iron. The Fe-Sr distances (based on the Sr K-edge data) increase and the Fe-Fe/Sn distances tended to decrease. The Sn-O distances in $SrFe_{0.5}Sn_{0.5}O_{3-\delta}$ showed a small increase on fluorination, the Sr-O distances decreased on fluorination, the Sr-Fe, Sr-Sn and Sr-Sr distances all increased on fluorination.

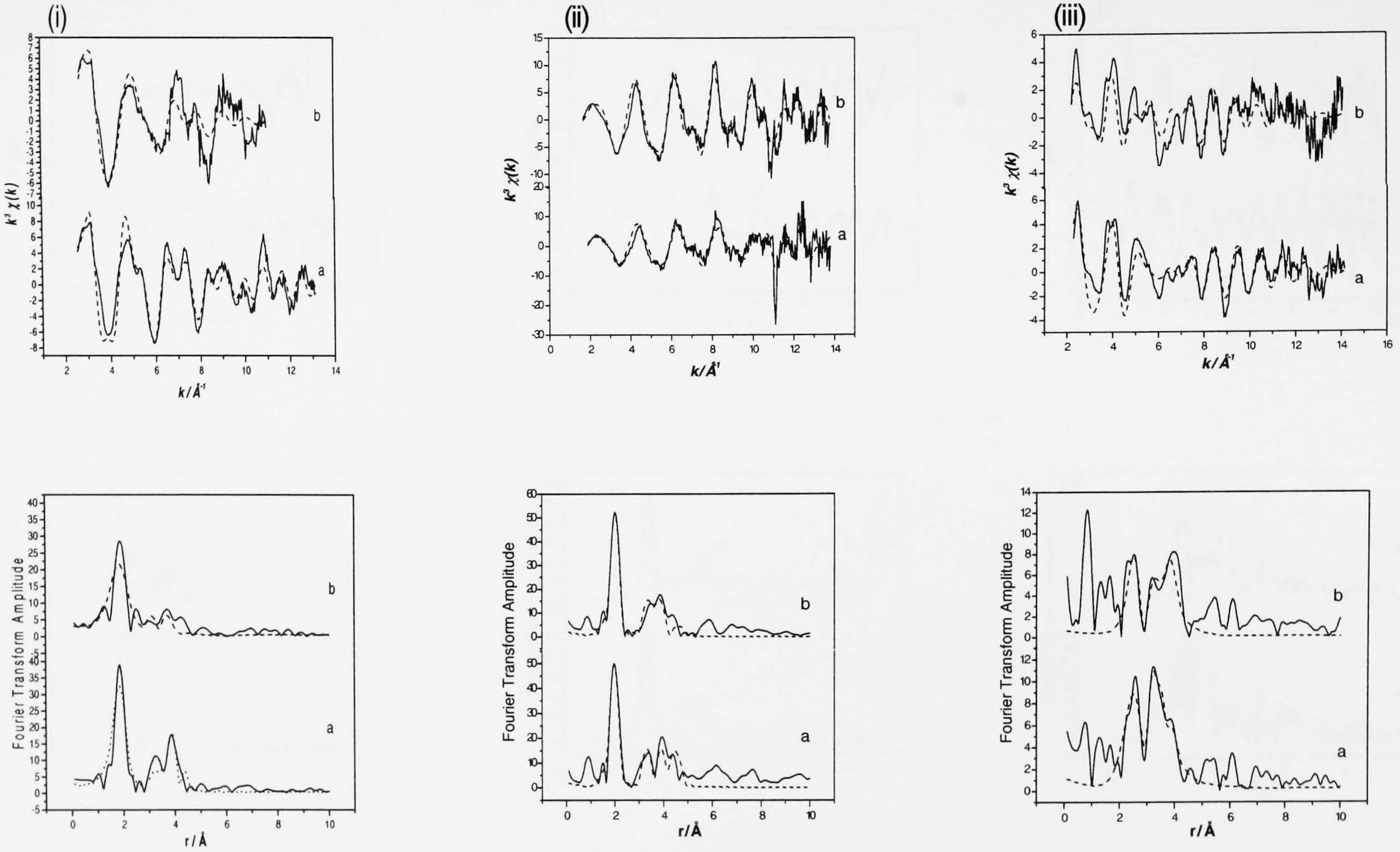

Figure 5.14b (i)Fe K-, (ii) Sn K- and Sr K-edge EXAFS and Fourier transforms recorded at 298K from (a) $SrFe_{0.5}Sn_{0.5}O_{3-\delta}$ and (b) its fluorinated derivative. (The experimental data are shown by a solid line.)

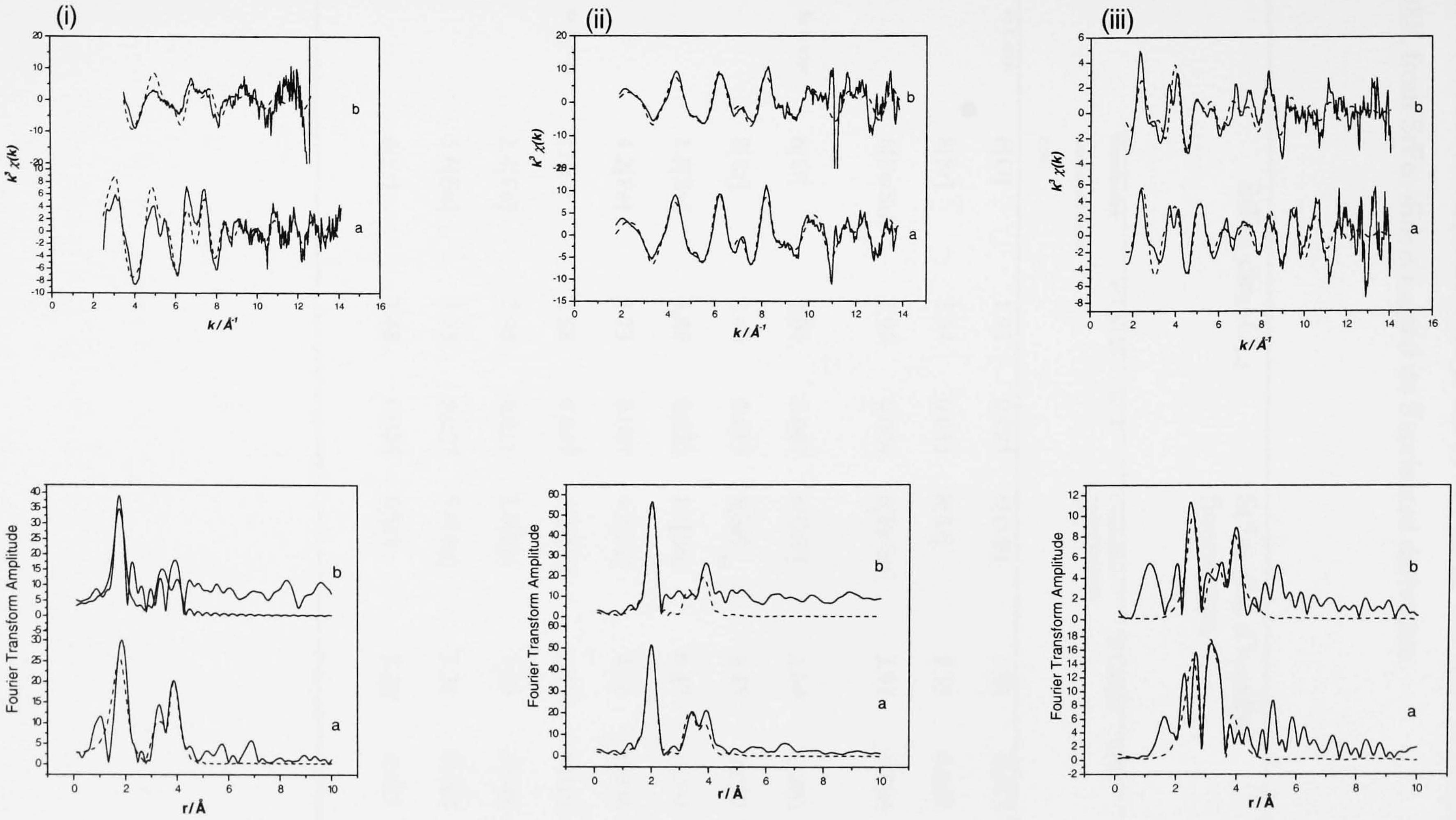

Figure 5.14a (i)Fe K-, (ii) Sn K- and Sr K-edge EXAFS and Fourier transforms recorded at 298K from (a) SrFe$_{0.7}$Sn$_{0.3}$O$_{3-\delta}$ and (b) its fluorinated derivative. (The experimental data are shown by the solid line.)

Table 5.13a Best fit parameters to the Fe K-, Sn K- and Sr K-edge EXAFS recorded at 298K from $SrFe_{0.7}Sn_{0.3}O_{3-\delta}$ and its fluorinated derivative.

	$SrFe_{0.7}Sn_{0.3}O_{3-\delta}$			$SrFe_{0.7}Sn_{0.3}O_{3-\delta}$ after fluorination		
	Coordination number and [atom type]	d/ Å (±0.02)	$2\sigma^2$/ Å^2	Coordination number and [atom type]	d/ Å (±0.02)	$2\sigma^2$/ Å^2
Fe K-edge	6[O]	1.92	0.025	6[O/F]	1.94	0.043
	8[Sr]	3.34	0.033	8[Sr]	3.35	0.059
	6[Fe/Sn]	3.99	0.009	6[Fe/Sn]	3.93	0.024
Sn K-edge	6[O]	2.04	0.007	6[O/F]	2.04	0.006
	8[Sr]	2.46	0.015	8[Sr]	3.45	0.020
	1.8[Sn]	4.49	0.023	1.8[Sn]	4.42	0.032
	4.2[Fe]	3.73	0.007	4.2[Fe]	3.72	0.006
Sr K-edge	12[O]	2.68	0.047	12[O/F]	2.59	0.019
	2.4[Fe]	2.96	0.021	2.4[Fe]	3.03	0.048
	5.6[Sn]	3.15	0.027	5.6[Sn]	3.31	0.044
	6[Sr]	3.48	0.026	6[Sr]	3.58	0.027

Table 5.13b Best fit parameters to the Fe K-, Sn K- and Sr K-edge EXAFS recorded at 298K from $SrFe_{0.5}Sn_{0.5}O_{3-\delta}$ and its fluorinated derivative

	$SrFe_{0.5}Sn_{0.5}O_{3-\delta}$			$SrFe_{0.5}Sn_{0.5}O_{3-\delta}$ after fluorination		
	Coordination number and [atom type]	d/ Å (±0.02)	$2\sigma^2$/ Å^2	Coordination number and [atom type]	d/ Å (±0.02)	$2\sigma^2$/ Å^2
Fe K-edge	6[O]	1.90	0.028	6[O/F]	1.95	0.049
	8[Sr]	3.37	0.040	8[Sr]	3.38	0.045
	6[Fe/Sn]	4.03	0.012	6[Fe/Sn]	3.74	0.068
Sn K-edge	6[O]	2.02	0.009	6[O/F]	2.05	0.007
	8[Sr]	2.44	0.019	8[Sr]	3.48	0.018
	3[Sn]	4.38	0.004	3[Sn]	4.45	0.014
	3[Fe]	3.72	0.004	3[Fe]	3.74	0.005
Sr K-edge	12[O]	2.63	0.066	12[O/F]	2.56	0.025
	4[Fe]	2.98	0.046	4[Fe]	3.02	0.046
	4[Sn]	3.19	0.032	4[Sn]	3.28	0.032
	6[Sr]	3.53	0.024	6[Sr]	3.57	0.024

5.5 SUMMARY

Iron in oxides in the $La_{1-x}Sr_xFe_{1-y}Co_yO_3$, $SrFe_{1-x}Co_xO_3$ and $SrFe_{1-x}Sn_xO_3$ systems is formed in an oxidation state higher than +3. Fluorination is accompanied by a reduction in the oxidation state of iron to Fe^{3+}. The fluorinated materials are magnetically ordered. The accurate analysis of the fluorine content and the characterisation the structural and magnetic properties of the materials is to be the subject of the further investigation.

5.6 Ba_2SnO_4

The fluorination of Ba_2SnO_4 by poly(vinylidene difluoride) was not successful.

The X-ray powder diffraction patterns recorded from the K_2NiF_4-related compound Ba_2SnO_4 and its fluorinated derivative, which was formed by reaction of the pure oxide with zinc fluoride at 240°C in nitrogen gas, are shown in Figure 5.15. The pattern recorded from the compound Ba_2SnO_4 was identical to that reported in the literature[4] with lattice parameters $a = b = 4.140(1)$, $c = 13.309(1)$ Å. The fluorinated phase showed a shift in line position to lower angle and the calculated lattice parameters $a = b = 4.080(1)$, $c = 16.330(1)$ Å showed a significant enlargement of the unit cell along the

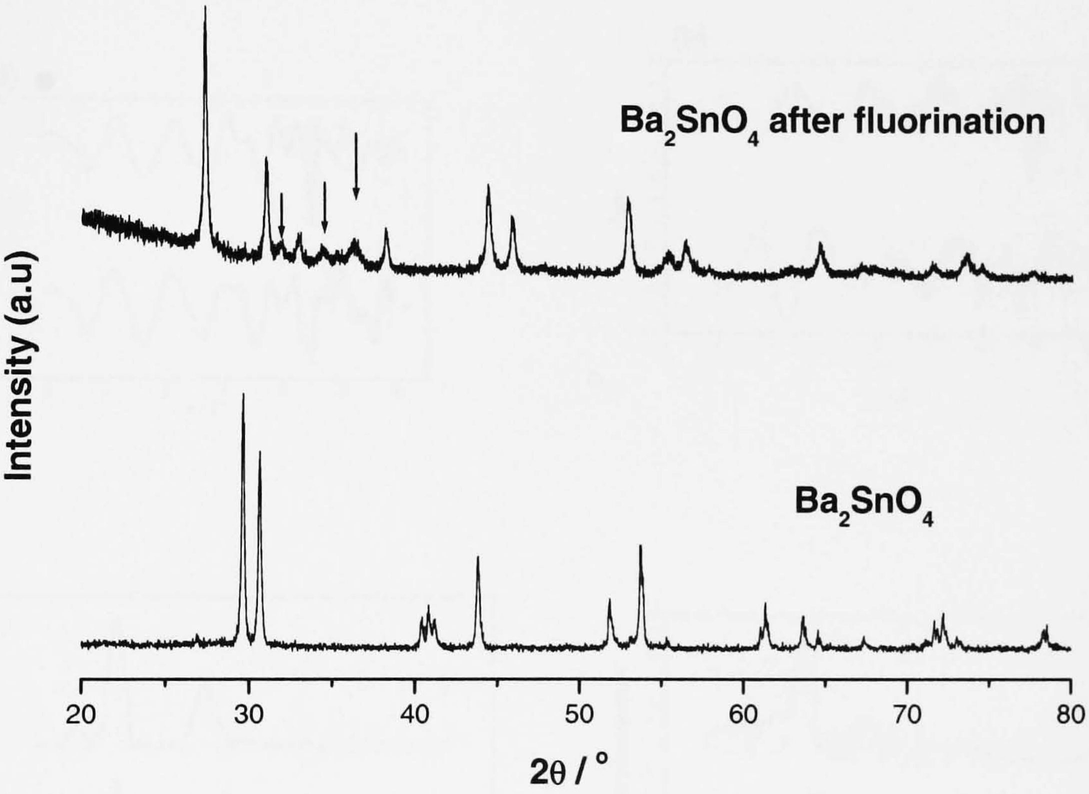

Figure 5.15 X-ray powder diffraction patterns recorded from Ba_2SnO_4 and its fluorinated derivative. (Arrows indicate peaks characteristic of zinc oxide)

c-axis. The pattern also shows the presence of zinc oxide formed as impurity from the reaction of ZnF_2 with Ba_2SnO_4

The Sn- and Ba- K-edge EXAFS recorded at 298K from Ba_2SnO_4 and its fluorinated derivative are shown in Figure 5.16. The best fit parameters are collected in Table 5.14.

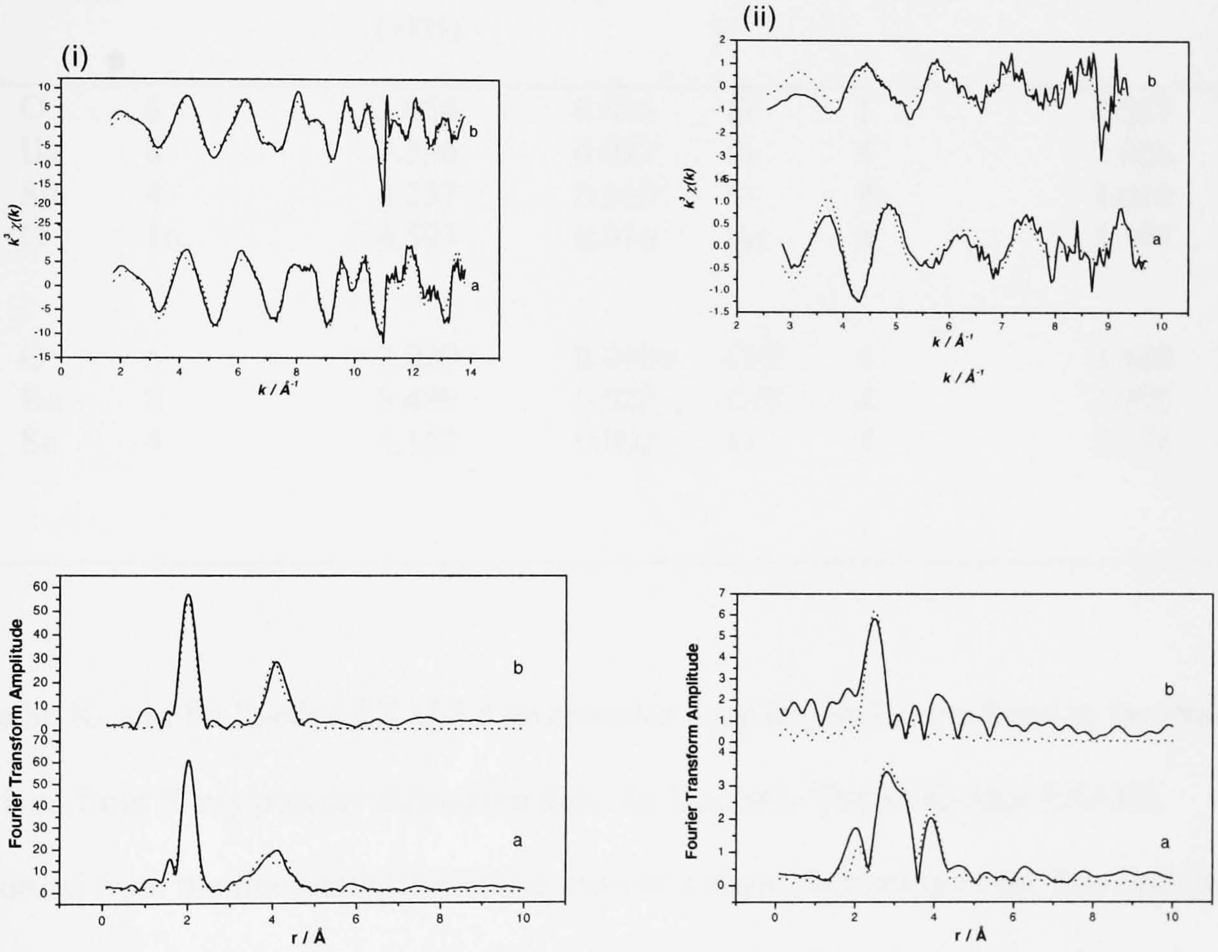

Figure 5.16 (i) Sn-, and (ii) Ba- K-edge EXAFS and Fourier transforms recorded at 298K from (a) Ba_2SnO_4 and (b) its fluorinated derivative. (The experimental data are shown by a solid line.)

Table 5.14 Best fit parameters to the Sn K-edge and Ba K-edge EXAFS recorded at 298 K from Ba_2SnO_4 and its fluorinated derivative

Compounds	Sn K-edge				Ba K-edge			
	Atom type	Coordination number	Tin-atom distance Å (±1%)	$2\sigma^2$(Å^2) (±10%)	Atom type	Coordination number	Barium-atom distance Å (±1%)	$2\sigma^2$(Å^2) (±10%)
Ba_2SnO_4	O	6	2.054	0.006	O	1	2.553	0.012
	Ba	8	3.556	0.027	O	4	2.806	0.012
	Sn	4	4.237	0.010	O	4	3.010	0.015
	O	16	4.593	0.016	Sn	4	3.597	0.041
Ba_2SnO_4/F	O	6	2.029	0.010	O/F	4	2.640	0.014
	Ba	8	3.499	0.028	O/F	4	2.908	0.016
	Sn	4	4.152	0.002	O	4	3.178	0.035

The Sn K- and Ba K-edge EXAFS data recorded from Ba_2SnO_4 were fitted to the model derived from X-ray powder diffraction data[7] for Ba_2SnO_4. The Sn K-edge EXAFS recorded from the fluorinated derivative showed a slight shortening of the first shell tin-oxygen distances upon fluorination. The Ba K-edge EXAFS recorded from fluorinated Ba_2SnO_4 were fitted to two shells of four oxygen or fluorine atoms at 2.640 and 2.908 Å and to a third shell of four oxygen atoms at 3.178 Å. The changes follow the same pattern as that observed when the K_2NiF_4-related compound Ba_2ZrO_4 was fluorinated[8].

The ^{119}Sn Mössbauer spectrum recorded from Ba_2SnO_4 at 77K (Figure 5.17) was composed of a single absorption, δ=0.22(1) mms^{-1}. The spectrum recorded from the fluorinated compound (Figure 5.17) was similar but with a smaller chemical isomer shift, δ=0.12(1) mms^{-1}, indicative of the electron withdrawing effect of fluorine

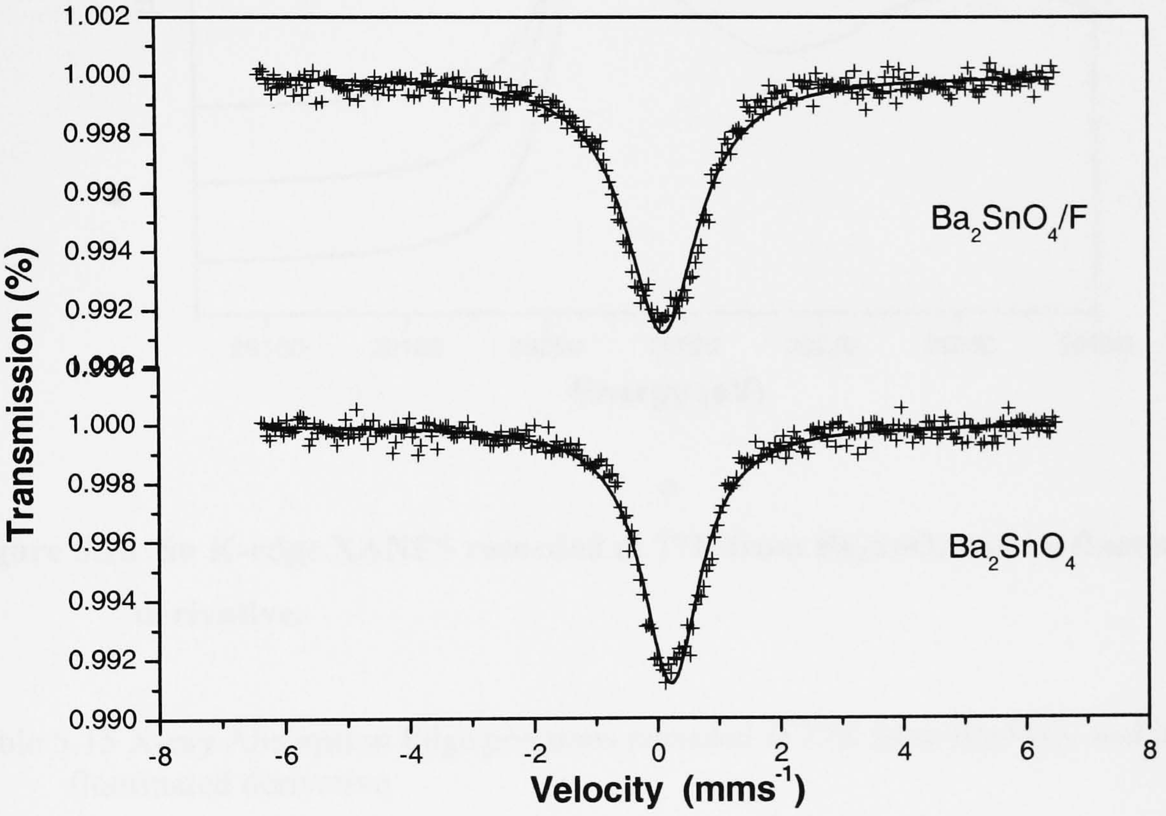

Figure 5.17 ^{119}Sn Mössbauer spectra recorded from Ba_2SnO_4 and its fluorinated derivative.

on the electron density around Sn^{4+}. This result was endorsed by the Sn K-edge XANES (Figure 5.18, Table 5.15), also recorded at 77K, which showed the X-ray absorption edge position of Ba_2SnO_4 to be identical to that of tin dioxide. The X-ray absorption edge position of the fluorinated derivative of Ba_2SnO_4 was observed to be at a higher

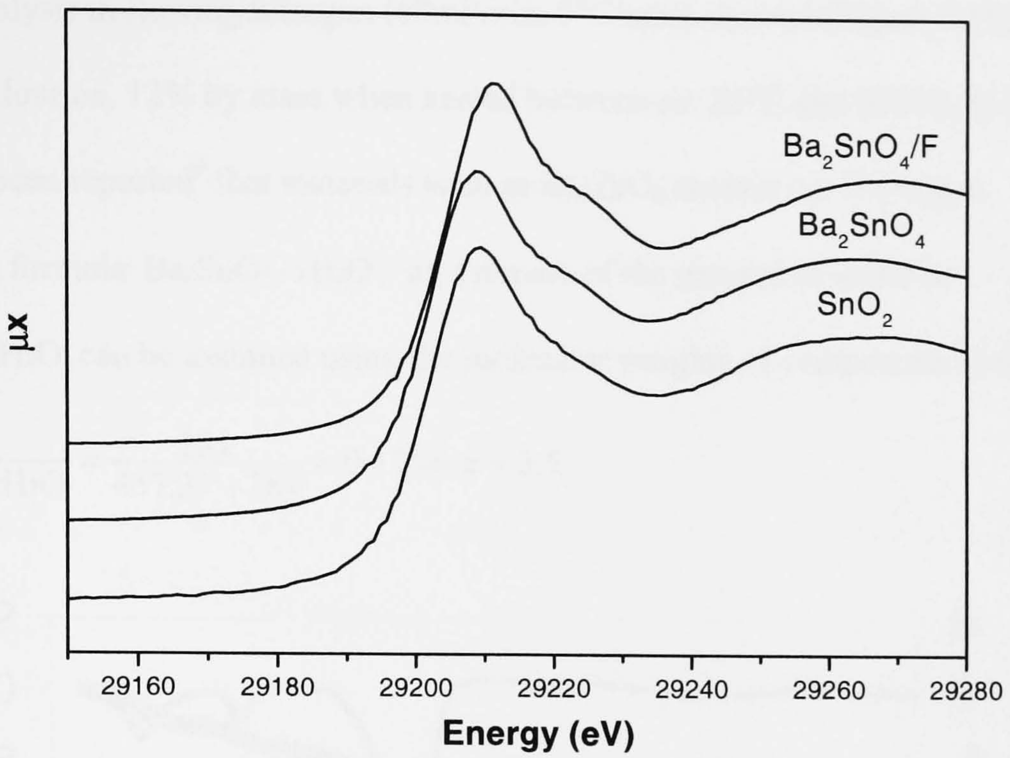

Figure 5.18 Sn K-edge XANES recorded at 77K from Ba_2SnO_4 and its fluorinated derivative.

Table 5.15 X-ray Absorption Edge positions recorded at 77K from Ba_2SnO_4 and its fluorinated derivative

Compounds	X-ray Absorption Edge Position (eV) ±0.2
Sn metal	29200.0
SnO_2	29202.3
Ba_2SnO_4	29202.3
Ba_2SnO_4/F	29205.7

energy consistent with electronegative fluorine withdrawing electron density from Sn^{4+}. Thermal analysis in flowing nitrogen (60ml/min, 5°C/min) showed (Figure 5.19) Ba_2SnO_4 to lose *ca.* 12% by mass when heated between *ca.* 25°C and 600°C. It has previously been reported[9] that materials such as Ba_2ZrO_4 contain *ca.* 9% water. Assuming a formula $Ba_2SnO_4 \cdot xH_2O$, an estimate of the amount of water in $Ba_2SnO_4 \cdot xH_2O$ can be assumed using the molecular weights of compounds as follows:

$$\frac{xH_2O}{Ba_2SnO_4 \cdot xH_2O} = \frac{18x}{457.37 + 18x} = 0.12 \Rightarrow x \approx 3.5$$

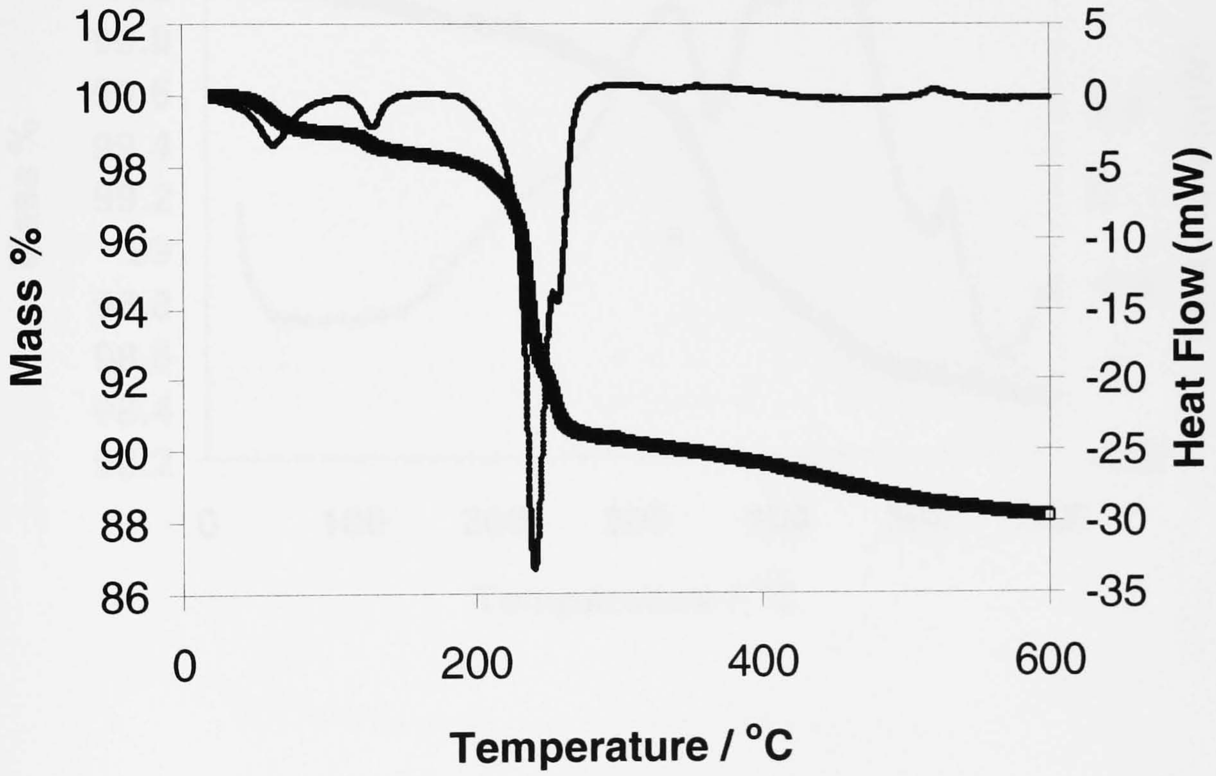

Figure 5.19 Thermal analysis of Ba_2SnO_4 in flowing nitrogen (60 ml/min, 5°C/min). The solid line indicates the tga data, the thin line indicates the dta data

Thermal analysis of Ba_2SnO_4/F (Figure 5.20) showed the material to lose *ca.* 1.6% by mass when heated in nitrogen between *ca.* 25°C and 600°C. The result is similar to the 2.0% mass loss which was observed by the thermal analysis of Ba_2ZrO_4/F[8] in air, which is consistent with a loss of approximately 0.5 mol H_2O. Assuming a formula $Ba_2SnO_3F_2 \cdot xH_2O$ the water content x in $Ba_2SnO_3F_2 \cdot xH_2O$ may be estimated as:

$$\frac{xH_2O}{Ba_2SnO_3F_2 \cdot xH_2O} = \frac{18x}{479.37 + 18x} = 0.016 \Rightarrow x \approx 0.4$$

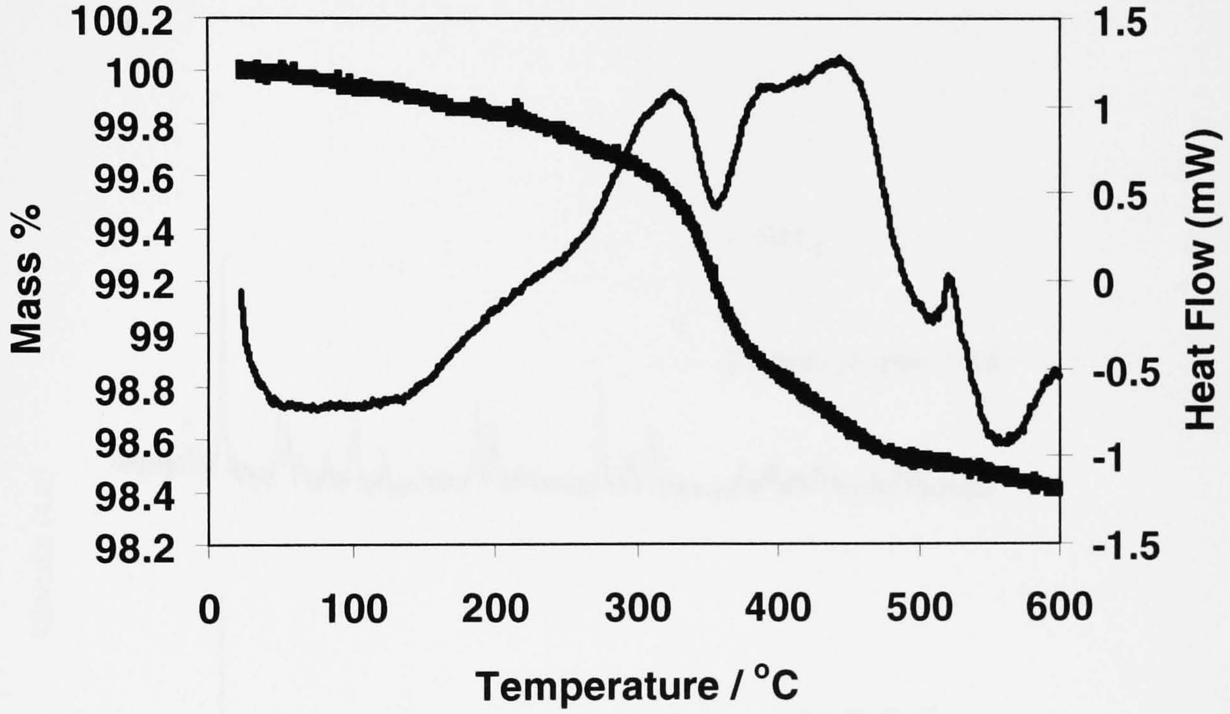

Figure 5.20 **Thermal analysis of Ba_2SnO_4/F in flowing nitrogen (60 ml/min, 5°C/min). The solid line indicates the tga data, the thin line indicates the dta data.**

The X-ray powder diffraction patterns recorded from Ba_2SnO_4/F and following heating at 600°C (Figure 5.21) showed a shift in the X-ray powder diffraction peaks to higher angle characteristic of a smaller unit cell. The lattice parameters changed ($a = b =$ 4.080(1), $c =$ 16.330(1) Å) for Ba_2SnO_4/F to $a = b =$ 4.058(1), $c =$ 16.442(1) Å for the material following heating at 600°C. There was an overall reduction in unit cell volume from 271.8 $Å^3$ to 270.5 $Å^3$ which could be consistent with the loss of water.

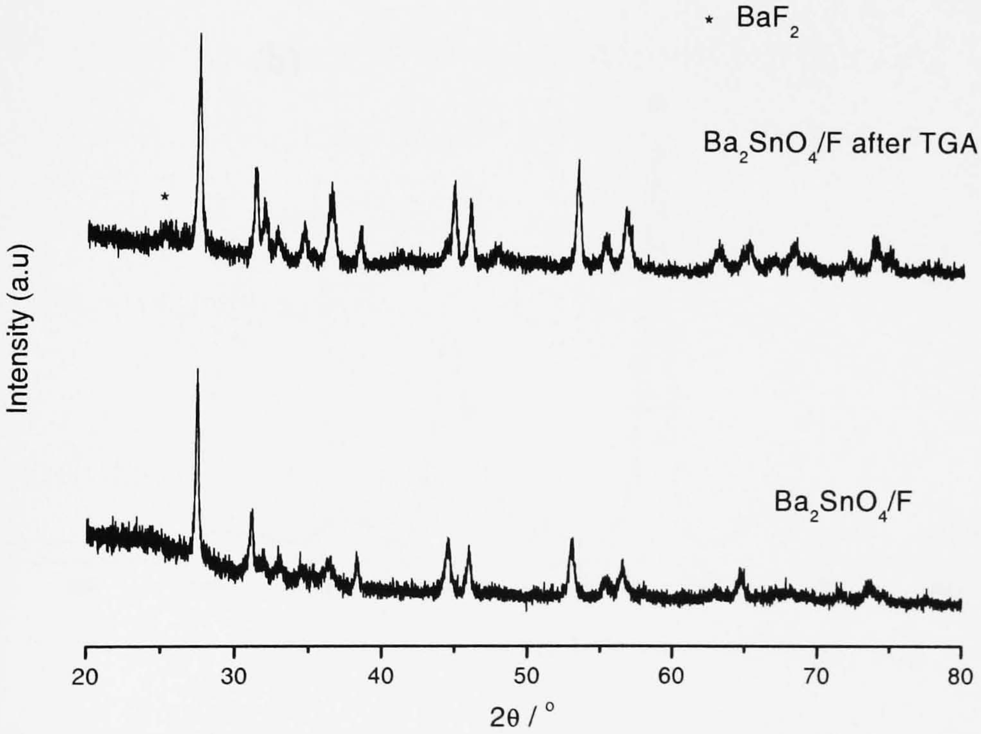

Figure 5.21 X-ray powder diffraction patterns recorded from Ba_2SnO_4/F before and after thermal analysis at 600 °C.

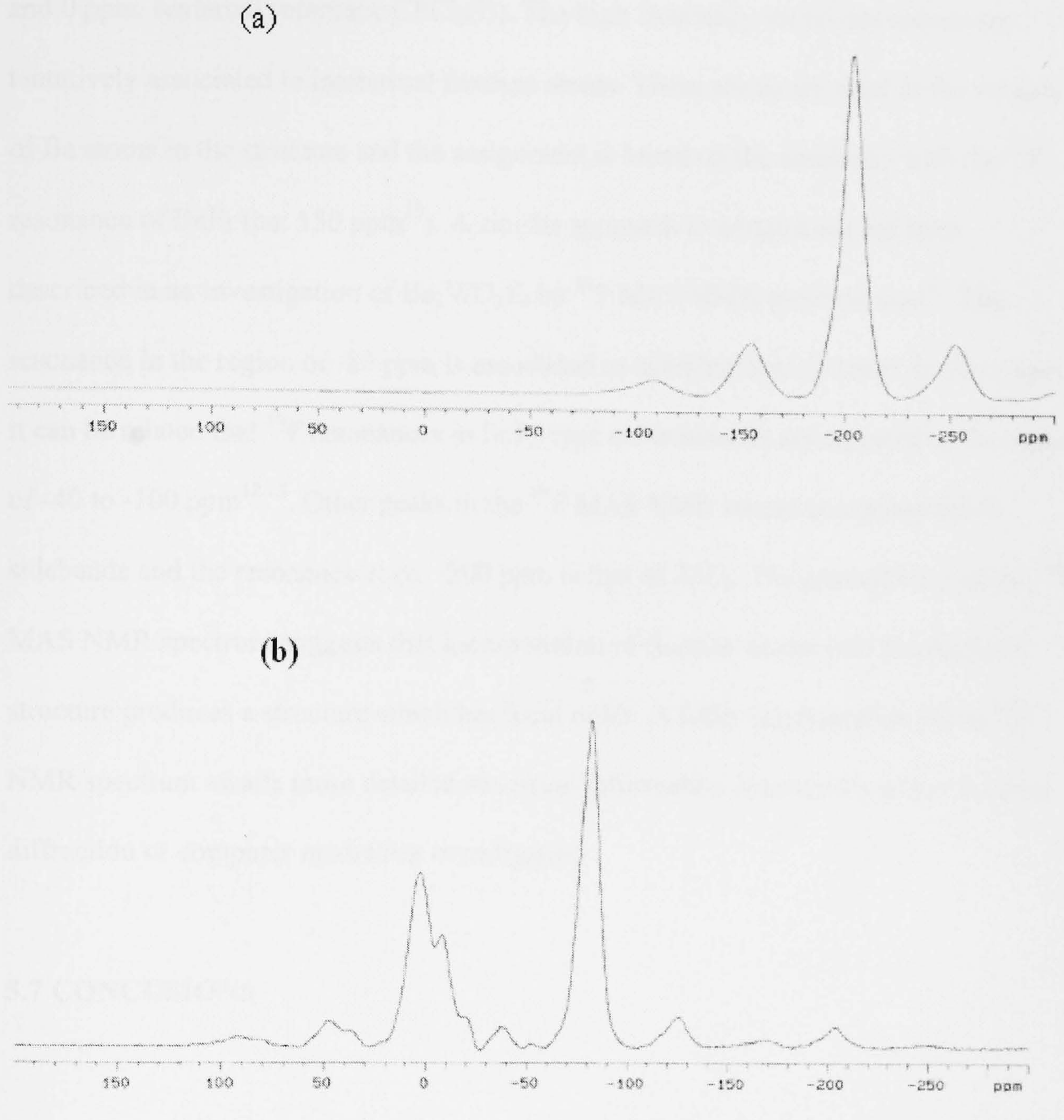

Figure 5.22 ^{19}F MAS nmr spectra recorded from (a)ZnF$_2$ and (b) fluorinated Ba$_2$SnO$_4$.

A preliminary ^{19}F MAS NMR study has been carried out on the fluorinated Ba$_2$SnO$_4$ derivative. The ^{19}F MAS NMR spectrum recorded at 282.1 MHz using a single pulse sequence is shown in Figure 5.22. There are two sets of resonances in the region of -80 and 0 ppm. (external reference $CFCl_3(l)$). The high frequency set of resonances are tentatively associated to interstitial fluorine atoms. These atoms are sited in the vicinity of Ba atoms in the structure and the assignment is based on the similarity with the ^{19}F resonance of BaF_2 (*ca.* 150 ppm[10]). A similar approach to assignment has been described in an investigation of $Ba_2WO_3F_4$ by ^{19}F MAS NMR spectroscopy[11]. The resonance in the region of -80 ppm is associated to substitutional fluorine. In this respect it can be related that ^{19}F resonances in SnF_2-type environments are reported in the region of -40 to -100 ppm[12,13]. Other peaks in the ^{19}F MAS NMR spectrum correspond to sidebands and the resonance at *ca.* -200 ppm is that of ZnF_2. The general form of the ^{19}F MAS NMR spectrum suggests that incorporation of fluorine atoms into the Ba_2SnO_4 structure produces a structure which has local order. A fuller interpretation of the ^{19}F NMR spectrum awaits more detailed structural information obtained by either neutron diffraction or computer modelling investigation.

5.7 CONCUSIONS

Perovskite-related compounds of composition $La_{1-x}Sr_x Fe_{1-y}Co_yO_{3-\delta}$ and $SrFe_{1-x}Co_xO_{3-\delta}$ which contain Fe^{4+} were fluorinated by a reaction with poly(vinylidene difluoride). The Fe^{4+} was reduced to Fe^{3+}. The fluorinated materials were magnetically ordered. Compounds of the type $SrFe_{1-x}Sn_xO_3$ were found to contain both Fe^{5+} and Fe^{3+}. Fluorination resulted in the reduction of the high oxidation state iron to Fe^{3+} and, in iron-rich systems the fluorinated materials were magnetically ordered.

The fluorination of K_2NiF_4-related Ba_2SnO_4 has been obtained by a reaction with ZnF_2 and resulted in an expansion of the unit cell along the *c*-axis. The materials appear to contain water. Fluorine appears to occupy both substitutional and interstitial sites. The fluorine content of all these materials requires accurate analysis. The investigation of the structural properties of the solids by neutron diffraction is planned as a part of a further investigation of these materials as are further studies of changes in cationic oxidation state by Mössbauer spectroscopy and XANES.

REFERENCES

1. U. Shimony and J. M. Knudsen, *Phys. Rev.,* 1966, **144**, 361
2. A. D. Al-Rawwas, C. E. Johnson, M. F. Thomas, S. E. Dann and M. T. Weller *Hyperfine Interactions,* 1994, **93,** 1521
3. J. B. Goodenough, *In Magnetism and The Chemical Bond,* edited by F. Albert Cotton (Interscience,London,1963), Vol. 1, p.15414.
4. R. D. Shannon, *Acta Cryst.,* 1976, **A32,** 751
5. A. Maignan, C. Martin, N. Nguyen and B. Raveau, *Solid State Sci.,* 2001, **3**, 57
6. ASTM Index Card No. 120665
7. M. A. Green, K. Prassides, P. Day and J. K. Stalick, *Synthetic Metals,* 1995, **71**, 1617
8. P. R. Slater and R. K. B. Gover, *J. Mater. Chem.,* 2001, **11**, 2035
9. R. V. Shpanchenko, E. V. Antipov and L. M. Kovba, *Zh. Neorg. Khim.*, 1993, **38**, 599
10. J. J. Kiczenski and J. F. Stebbins, *J. Non-cryst. Solid*, 2002, **306,** 160
11. L-S Du, F. Wang and C. P. Erey, *J. Solid State Chem.,* 1998, **140**, 285
12. S. Chaudhuri, F. Wang and C. P. Erey, *J. Am. Chem. Soc.,* 2002, **124,** 11746
13. M. Le Floch-Durund, U. H and C.Muller, *J. Phys.,* 1982, **43,** 107

Chapter 6

RESULTS AND DISCUSSION: METAL ANTIMONATES

Chapter 6

RESULTS AND DISCUSSION: METAL ANTIMONATES

6.1 INTRODUCTION

This Chapter reports on the:

1. Preparation of iron- and vanadium-antimonate by milling techniques,
2. Characterisation of the products,
3. Phase transitions in antimony oxides induced by mechanically milling.

6.2 IRON ANTIMONATE

The X-ray powder diffraction patterns recorded from a mixture of α-Fe_2O_3 and Sb_2O_3

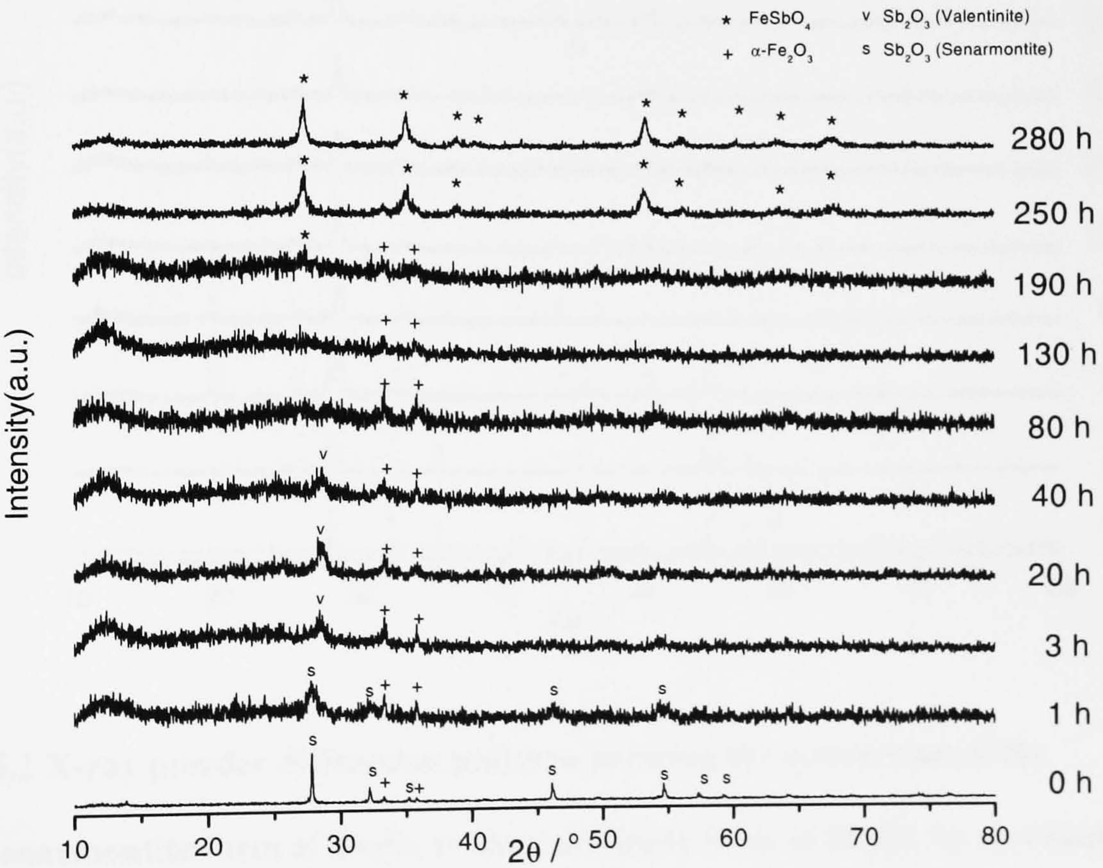

Figure 6.1 X-ray powder diffraction patterns recorded from a mixture of α-Fe_2O_3 and Sb_2O_3 following mechanical milling in air for various periods of time.

following mechanical milling in air for various periods of time are collected in Figure 6.1. The X-ray powder diffraction pattern recorded from the unmilled mixture showed it to contain corundum-related α-Fe_2O_3 and the senarmontite phase of Sb_2O_3. Milling for 3 hours resulted in the onset of conversion of senarmontite to the valentinite modification of Sb_2O_3. This observation is interesting because senarmontite has long been known [1] to be the stable form of Sb_2O_3 at temperatures below 570 °C. In separate experiments (Figure 6.2) it was found that the cubic senarmontite form of Sb_2O_3 was

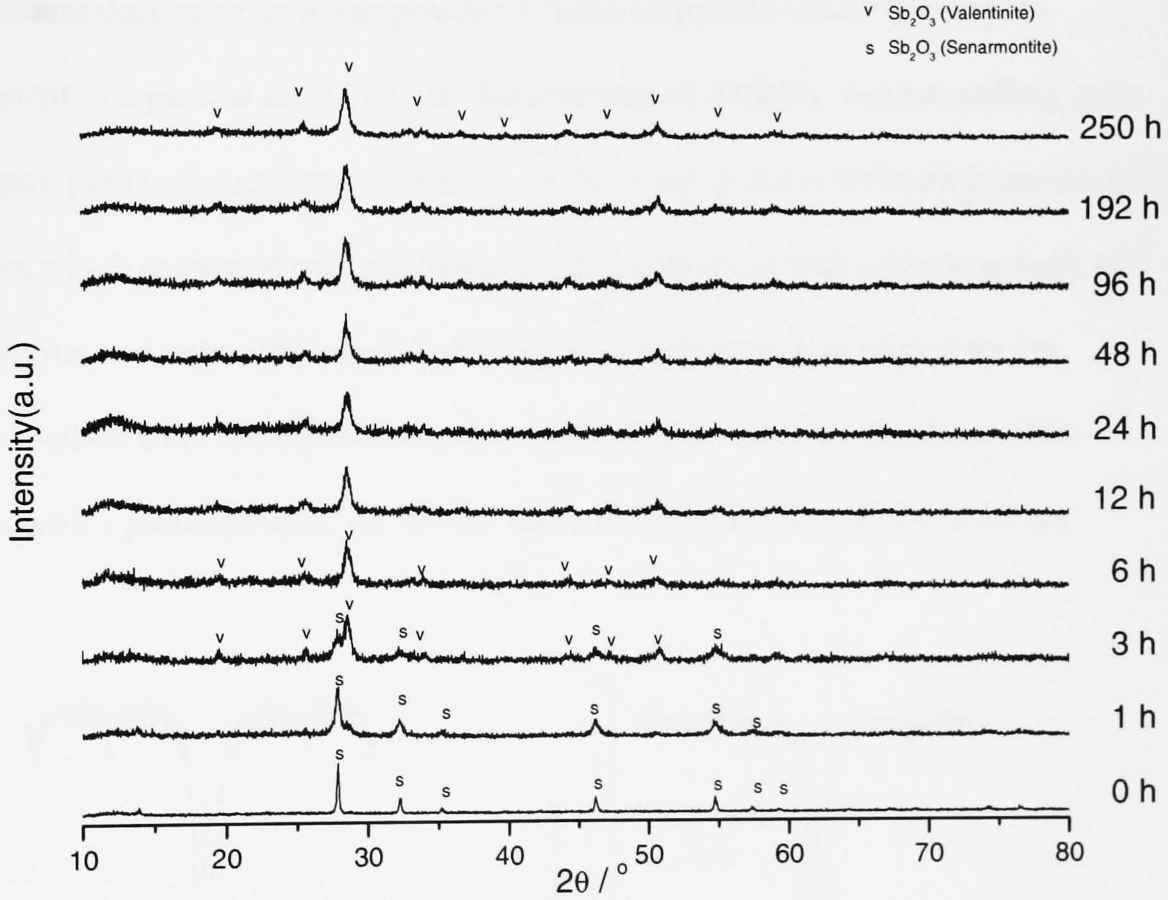

Figure 6.2 X-ray powder diffraction patterns showing the conversion of the senarmontite form of Sb_2O_3 to the valentinite form of Sb_2O_3 by mechanical milling in air.

completely converted to the orthorhombic valentinite form of Sb_2O_3 by mechanical milling in air for only 6 hours. No evidence was found for oxidation to Sb_2O_4 even after 250 hours of milling.

Both results demonstrate that milling is a facile means of inducing phase transitions in Sb_2O_3. X-ray powder diffraction showed that continued milling of the mixture of α-Fe_2O_3 and Sb_2O_3 (Figure 6.1) resulted in a broadening of the diffraction peaks and, after 80 hours of milling, the formation of a nearly amorphous material. After 190 hours of milling the mixture gave an X-ray powder diffraction pattern which showed the development of a peak at *ca.* 27.27° 2θ characteristic of $FeSbO_4$. Further milling gave rise to more peaks characteristic of $FeSbO_4$ in the X-ray powder diffraction pattern with intensities which increased with continued milling consistent with particle growth and crystallisation and, after 280 hours, $FeSbO_4$ with a particle size estimated by the Scherrer method from the diffraction peak width of *ca.*20 nm was observed. This contrasts with a particle size of *ca.* 40 nm when $FeSbO_4$ was formed by heating a

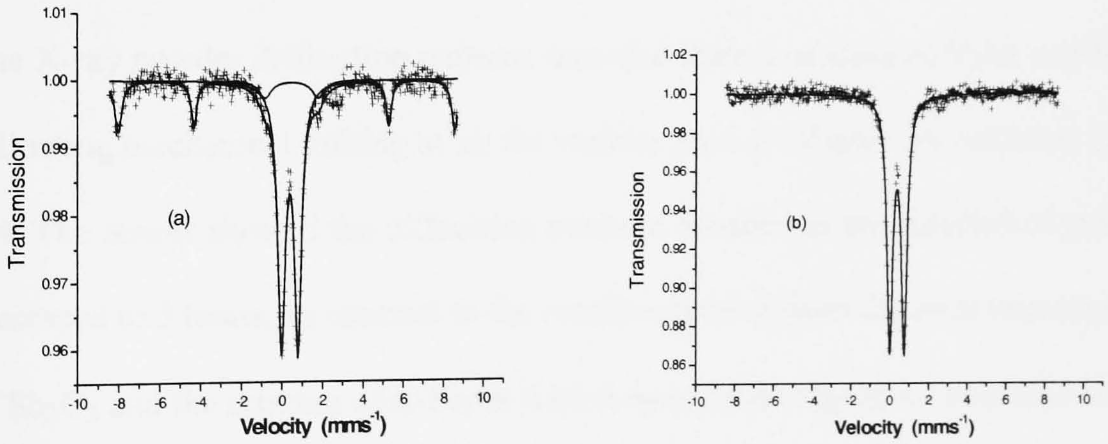

Figure 6.3 The ^{57}Fe Mössbauer spectra recorded from $FeSbO_4$ prepared by (a) milling techniques (b) calcination methods.

mixture of α-Fe_2O_3 and Sb_2O_3 in air at 900°C (56h), cooling to room temperature and grinding in a pestle and mortar before heating in air at 1000°C (48h).

The ^{57}Fe Mössbauer spectrum recorded from $FeSbO_4$ made by milling techniques in air is shown in Figure 6.3a. The spectrum contains two components. The first, a quadrupole split absorption (δ = 0.38 mms^{-1}, Δ = 0.81 mms^{-1}) is characteristic of Fe^{3+} in $FeSbO_4$[2] and implying a formation $Fe^{3+}Sb^{5+}O_4$,The sextet pattern (δ = 0.38 mms^{-1}, 2ε =-0.09 mms^{-1}, H = 51 T) is characteristic of an α-Fe_2O_3 impurity phase (*ca.* 27 %) and suggests that the reaction does not go to completion in the ball mill. Presumably the small particle of the impurity phase contributed to its absence in the X-ray diffraction pattern.

The ^{57}Fe Mössbauer spectrum recorded from $FeSbO_4$ made by conventional calcination is shown in Figure 6.3b and represents Fe^{3+} in $FeSbO_4$.[2] The ^{57}Fe Mössbauer spectra therefore indicate a formulation $Fe^{3+}Sb^{5+}O_4$ for iron antimonate.

6.3 VANADIUM ANTIMONATE

The X-ray powder diffraction patterns recorded from a mixture of V_2O_5 and Sb_2O_3 following mechanical milling in air for various periods of time are collected in Figure 6.4. The results showed the diffraction peaks to broaden as the duration of milling was increased to 3 hours. In contrast to the results recorded from the pure senarmontite form of Sb_2O_3 and the mixture of α-Fe_2O_3 with senarmontite Sb_2O_3, no evidence was found for the conversion of senarmontite to the valentinite form of Sb_2O_3. Instead, the peak broadening was consistent with the rapid formation of a poorly crystalline mixture of

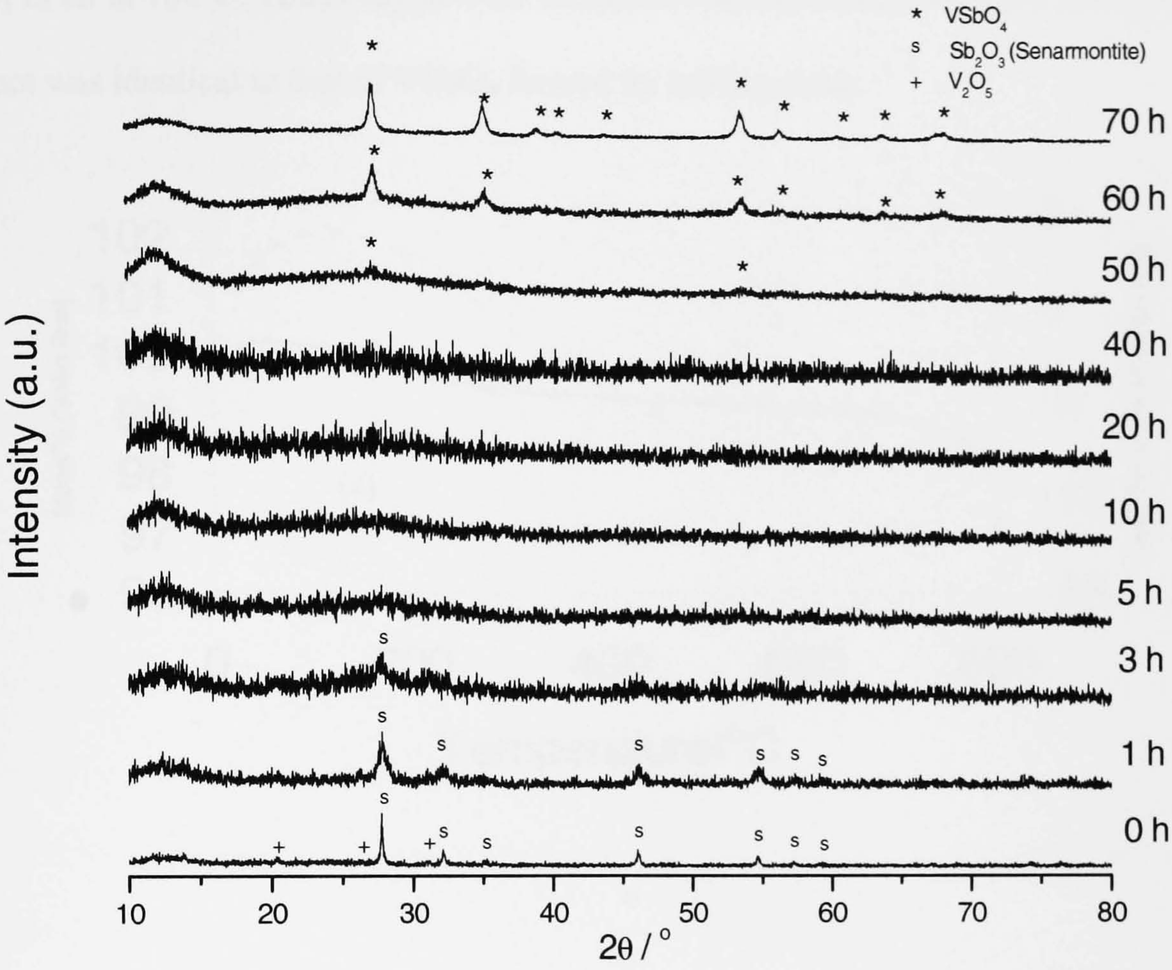

Figure 6.4 X-ray powder diffraction patterns recorded from a mixture of V_2O_5 and Sb_2O_3 following mechanical milling in air for various periods of time.

Sb_2O_3 and V_2O_5 which remained amorphous to X-rays until milled for 50 hours when peaks characteristic of $VSbO_4$ were observed. The appearance of $VSbO_4$ after 60 hours milling indicates that the reaction between V_2O_5 and Sb_2O_3 in the ball mill is more rapid than that between α-Fe_2O_3 and Sb_2O_3 under similar conditions. The crystallite size, determined from the X-ray powder diffraction data of $VSbO_4$ formed after 70 hours of milling, of *ca.*23 nm was similar to that of $FeSbO_4$ formed after 280 hours of milling, but smaller than that of $VSbO_4$, *ca.* 50nm, made by heating a mixture of V_2O_5 and

Sb_2O_3 in air at 750°C. The X-ray powder diffraction pattern of the vanadium antimonate product was identical to that of $VSbO_4$ formed by milling in air.

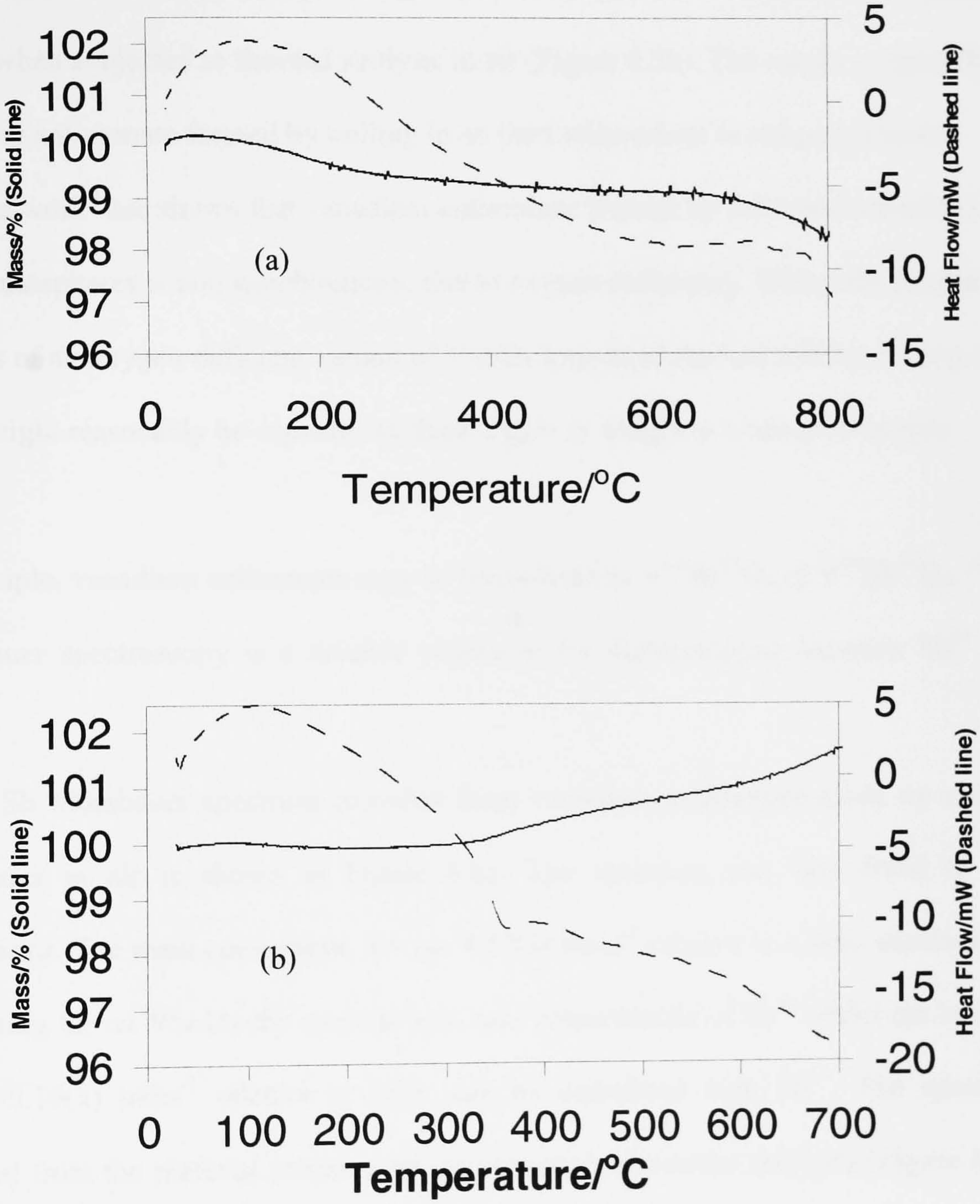

Figure 6.5 TGA (solid line) and DSC (dashed line) curves recorded from $VSbO_4$ made by milling in (a) air and (b) argon.

Thermal analysis in air showed that the vanadium antimonate formed by ball milling in air underwent a small weight loss as it was heated to 800°C (Figure 6.5a) In contrast, vanadium antimonate formed by milling V_2O_5 and Sb_2O_3 for 70 hours in argon gained weight when subjected to thermal analysis in air (Figure 6.5b). The results suggest that vanadium antimonate formed by milling in an inert atmosphere is oxygen deficient. Previous work[3] has shown that vanadium antimonate formed by calcination methods in inert atmospheres is non stoichiometric due to oxygen deficiency. Hence the thermal analysis of an oxygen-deficient variant of $VSbO_4$ formed in the ball mill by milling in argon might reasonably be expected to show a gain in weight as a result of oxygen uptake.

In principle, vanadium antimonate may be formulated as $V^{3+}Sb^{5+}O_4$ or $V^{5+}Sb^{3+}O_4$. ^{121}Sb Mössbauer spectroscopy is a suitable technique for distinguishing between Sb^{3+} and Sb^{5+}.

The ^{121}Sb Mössbauer spectrum recorded from vanadium antimonate made by milling techniques in air is shown in Figure 6.6a. The spectrum was best fitted to two absorptions. The main component, $\delta = ca.\ 8.57(3)$ mms^{-1} relative to a InSb standard and accounting for *ca.* 96±1% the spectral area, was characteristic of Sb^{5+} whilst the other, $\delta = ca.\ -5.10(1)$ mms^{-1} relative to InSb, can be associated with Sb^{3+}. The spectrum recorded from the material prepared by conventional calcination methods (Figure 6.6b) was very similar with *ca.* 99% the spectrum corresponding to Sb^{5+} ($\delta = ca.\ 8.57(3)$ mms^{-1} relative to InSb). The results demonstrate that antimony in vanadium antimonate is predominantly present as Sb^{5+} so that the formulation $V^{3+}Sb^{5+}O_4$ can be formulated.

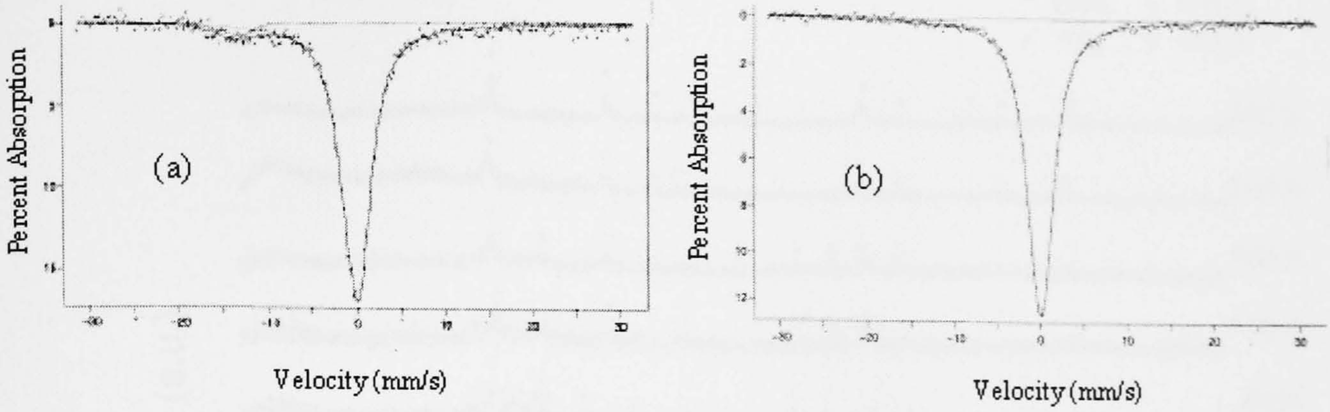

Figure 6.6 The ^{121}Sb Mössbauer spectra recorded from vanadium antimonate prepared by (a) milling techniques (b) calcination methods

6.4 THE CONVERSION OF α-Sb_2O_4 TO β-Sb_2O_4

A mixture of V_2O_5 and α-Sb_2O_4 was also mechanically milled under identical conditions. The results (Figure 6.7) also showed the onset of formation of $VSbO_4$ after 110 hours of milling. However, of greater interest was the appearance of a peak at 27.6° 2θ in the X-ray powder diffraction pattern recorded from the mixture after milling for 5 hours which is characteristic of β-Sb_2O_4. The result is unexpected since α-Sb_2O_4 is only converted to the β-polymorph at 1130°C[4] by a mechanism described[4] in terms of the dissociation of α-Sb_2O_4 into Sb_2O_3 which recombines with oxygen and condenses as β-Sb_2O_4. The conversion of α- to β-Sb_2O_4 by mechanical milling was therefore subjected to further examination.

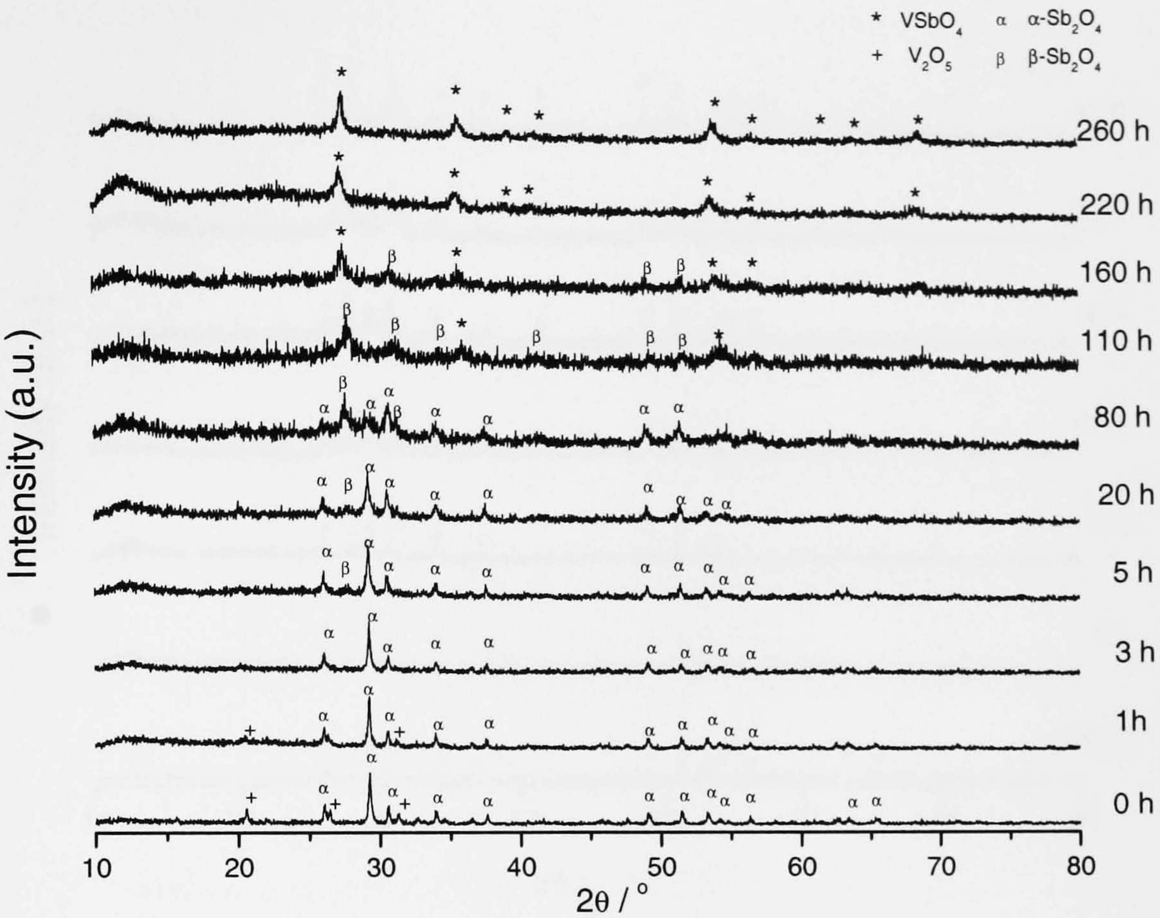

Figure 6.7 X-ray powder diffraction patterns recorded from a mixture of V_2O_5 and α-Sb_2O_4 following mechanical milling in air for various periods of time.

The X-ray powder diffraction patterns recorded after milling α-Sb_2O_4 for different periods of time in air are collected in Figure 6.8. After 3 hours of milling a peak at 27.6° 2θ characteristic of β-Sb_2O_4 appeared. The X-ray powder diffraction pattern characteristic of β-Sb_2O_4 developed with further milling and was accompanied by a decrease in the intensity of the pattern characteristic of α-Sb_2O_4. After 20 hours of milling the X-ray powder diffraction pattern showed nearly complete conversion to β-Sb_2O_4 with a crystallite size, estimated by the Scherrer method from the X-ray powder

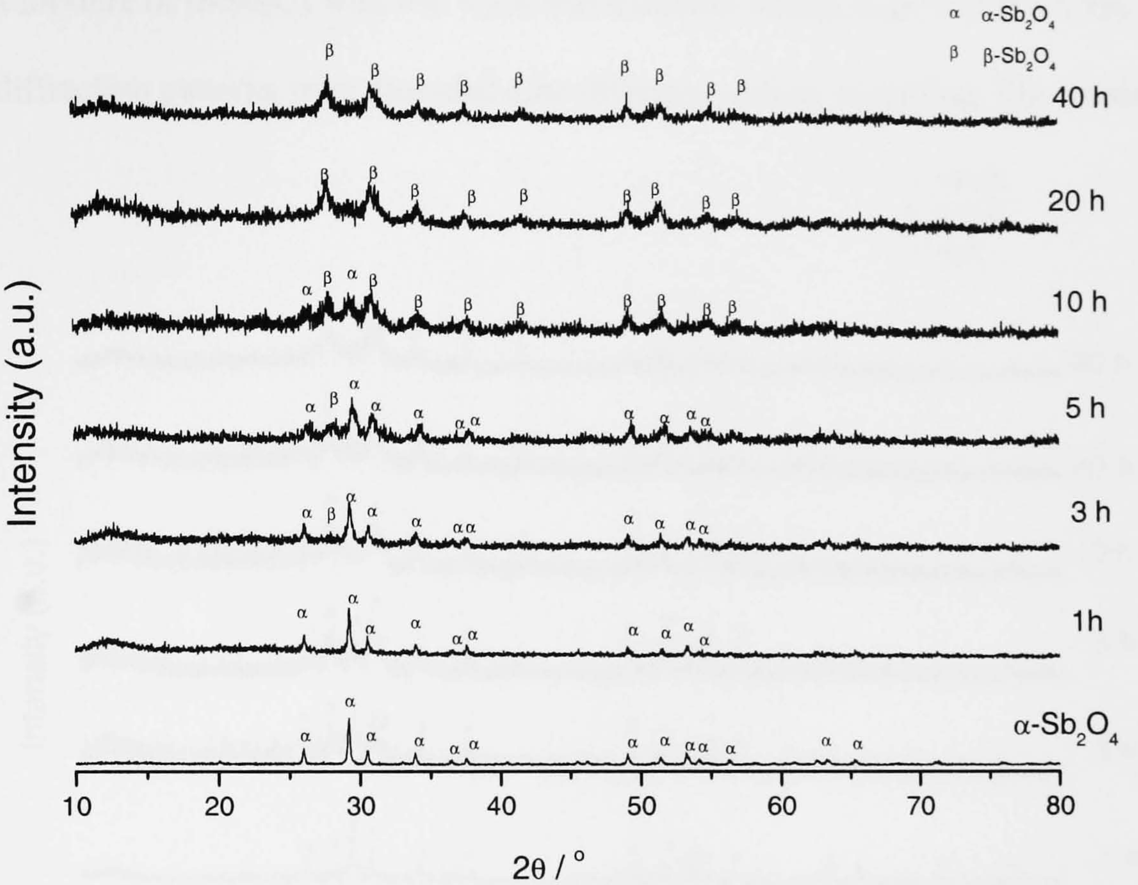

Figure 6.8 X-ray powder diffraction patterns recorded from α-Sb_2O_4 following mechanical milling in air for various periods of time.

diffraction data, of *ca.*15 nm. A similar result was obtained when α-Sb_2O_4 was milled in an atmosphere of argon for 20 hours. Hence the results suggest that mechanical milling facilitates the α- to β-Sb_2O_4 phase transformation in the solid state.

However, it has also been shown[3] that the calcination of α-Sb_2O_4 containing a small amount of V_2O_5 lowers the temperature of the α- to β-Sb_2O_4 phase transformation to *ca.*

810°C. A mixture of α-Sb_2O_4 with 4% V_2O_5 was therefore milled in air and the X-ray powder diffraction patterns were recorded after different periods of milling. The results are collected in Figure 6.9. The results show the onset of formation of β-Sb_2O_4 after only 1 hour and, with further milling, the decrease in intensity of peaks corresponding to α-Sb_2O_4 and V_2O_5 and the development of the pattern characteristic of β-Sb_2O_4. After 20 hours of milling the pattern showed nearly complete conversion of α-Sb_2O_4 to β-Sb_2O_4 with a crystallite size determined from the X-ray powder diffraction data of *ca.* 15

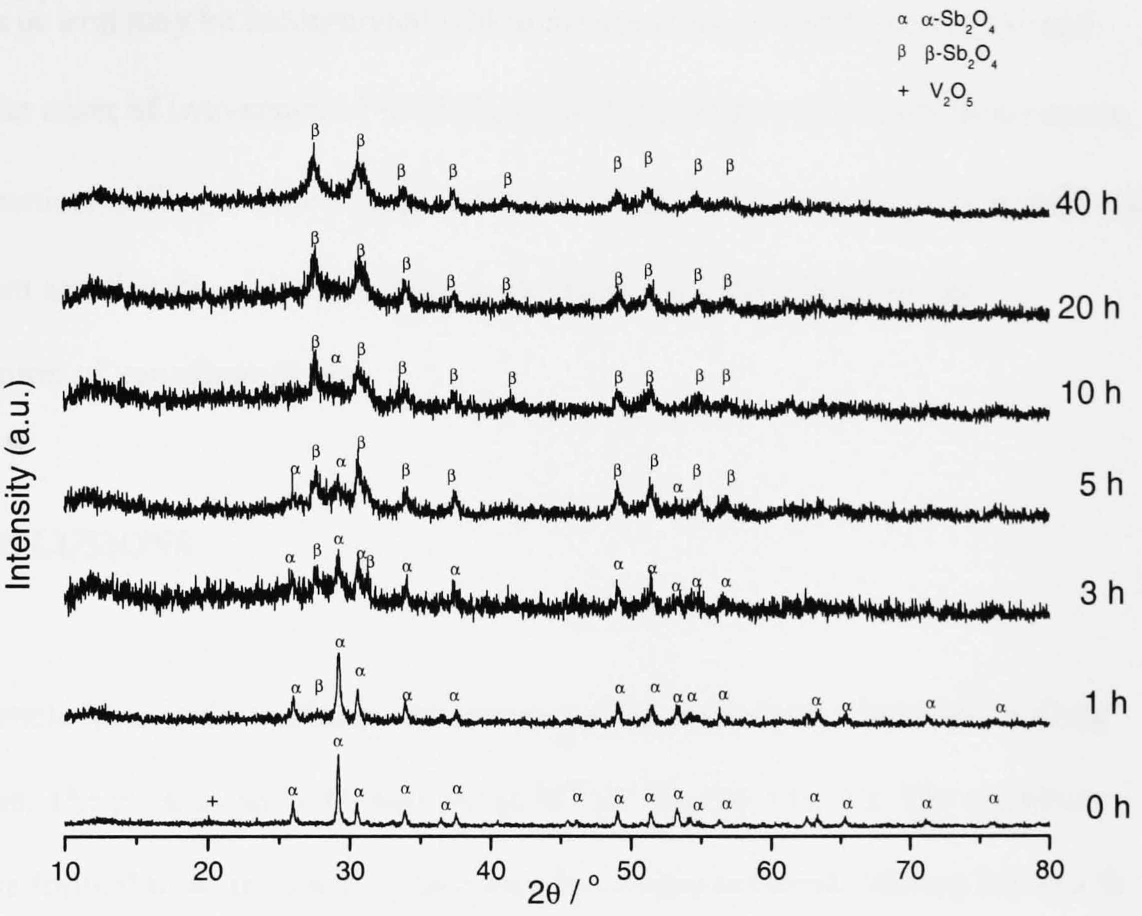

Figure 6.9 X-ray powder diffraction patterns recorded from a mixture of α-Sb_2O_4 and 4% V_2O_5 following mechanical milling in air for various periods of time.

nm. The milling of a mixture of α-Sb_2O_4 with 4% α-Fe_2O_3 for 20 hours was subsequently also found to induce the conversion of α- to β-Sb_2O_4. Presumably vanadium or iron may be incorporated within the structure as found previously[3] and induces the onset of conversion of α-Sb_2O_4 to β-Sb_2O_4. Hence the results demonstrate that mechanical milling is able to induce the conversion of α- to β-Sb_2O_4 by a solid state mechanism and that the phase transition is rendered even more facile by the incorporation of vanadium or iron.

6.5 CONCLUSIONS

Small particle iron- and vanadium- antimonate can be made by mechanically milling techniques. The phases can be formulated as $M^{3+}Sb^{5+}O_4$ (M = Fe, V). The vanadium animonate formed in an inert atmosphere may be oxygen deficient. Milling induces the phase transformation of the cubic senarmontite form of Sb_2O_3 to the orthorhombic valentinite Sb_2O_3 form and also the conversion of α-Sb_2O_4 to β-Sb_2O_4. The evaluation of the catalytic properties of the small particle antimonates made by milling methods will be the subject of separate investigation.

REFERENCES

1. E. J. Robert and F. Fenwick, *J. Amer. Chem. Soc.,* 1928, **50**, 2125

2. F. J. Berry, J. G. Holden, M. H. Loretto and D. S. Urch, *J. Chem. Soc., Dalton Trans.,*1987, 1727

3. F. J. Berry, M. E. Brett and W. R. Patterson, *J. Chem. Soc, Dalton Trans.,* 1983, 13

4. D. Rogers and A. C. Skapski, *Proc. Chem. Soc.,* London, 1964, 400